

Tribology and the Triboelectric Effect

A study into the influence of tribological factors on frictional electrification

Joshua Louis Armitage

Submitted in accordance with the requirements for the degree of
Doctor of Philosophy (Ph.D.) in Integrated Tribology

The University of Leeds
Institute for Functional Surfaces (iFS)
School of Mechanical Engineering, Faculty of Engineering

Dec 2022

Intellectual Property Statement

The candidate confirms that the work submitted is their own, except where work which has formed part of jointly-authored publications has been included. The contribution of the candidate and the other authors to this work has been explicitly indicated below. The candidate confirms that appropriate credit has been given within the thesis where reference has been made to the work of others.

1. *An investigation into the influence of tribological parameters on the operation of sliding triboelectric nanogenerators*

CRedit authorship contribution statement: **J.L. Armitage**: Conceptualization, Methodology, Software, Formal analysis, Investigation, Data curation, Writing - original draft, Visualization, Project administration. **A. Ghanbarzadeh**: Software, Validation, Resources, Writing - review & editing, Supervision. **C. Wang**: Conceptualization, Resources, Supervision. **A. Neville**: Conceptualization, Methodology, Resources, Writing - review & editing, Visualization, Supervision, Project administration, Funding acquisition.

2. *Investigating the Influence of Friction and Material Wear on Triboelectric Charge Transfer in Metal–Polymer Contacts*

Authorship contribution statement: All authors contributed to the study conception and design. Material preparation, data collection and data analysis were performed by **J.L. Armitage**. The first draft of the manuscript was written by **J.L. Armitage** and all authors commented on previous versions of the manuscript. All authors read and approved the final manuscript.

This copy has been supplied on the understanding that it is copyright material and that no quotation from the thesis may be published without proper acknowledgement.

The right of Joshua Louis Armitage to be identified as Author of this work has been asserted by them in accordance with the Copyright, Designs and Patents Act 1988.

© 2022 The University of Leeds and Joshua Louis Armitage

Acknowledgements

I would like to express my sincere gratitude to Prof. Anne Neville for her crucial guidance, motivation, and endless inspiration throughout the entirety of this project and my research as a whole. I would like to extend this gratitude to my current supervisors Ali Ghanbarzadeh and Mike Bryant for guiding me through the final stages of this PhD, and for providing invaluable feedback during the drafting of my publications.

I would also like to thank my fellow cohorts at the Centre for Doctoral Training in Integrated Tribology (iT-CDT) and the Institute for Functional Surfaces (iFS) for their substantial support in the office, labs, and during many conference presentations and attendances.

Special thanks to Michael Huggan, Jordan Thomas, Ryan Smith, Phys Moore, Robert Guest and Paul Kilburn for their guidance and input during the manufacturing of the UMT-TENG peripherals, and for all preliminary machining and additive manufacturing of parts.

Special thanks to Hardy Boocock from the Electronic Services Workshop for designing and assembling the feedback ammeter, as well as for assisting with testing and noise reduction.

Special thanks to Professor Zhong Lin Wang and the staff at the Beijing Institute for Nanoenergy and Nanosystems (BINN) for allowing Anne and myself to visit their facilities, whilst also providing valuable discussions and insight into the research on TENG devices.

Special thanks to Professor Mojtaba Ghadiri of the University of Leeds, School of Chemical and Process Engineering, and Tatsushi Matsuyama of Soka University, for their discussions regarding the triboelectric charging of pharmaceutical powders in addition to inviting me to present my research at the international workshop on the static-tribo-electricity of powders (STEP).

Special thanks to Professor Sohini Kar Narayan at Cambridge University for allowing Anne and myself to visit her research group and have valuable discussions regarding the electrical optimisation of material surfaces.

Special thanks for Professor Laurence Marks of the McCormick School of Engineering at Northwestern University for his advice and insight into his research on the flexoelectric influence of triboelectric charging.

And of course, a massive thank you to anyone who reads this in pursuit of a greater understanding of the complex phenomenon that is frictional electrification.

Preface

Tribology in itself is often described as an interdisciplinary field. This research builds on this already expanding topic through incorporating concepts from a wide range of additional subjects. The triboelectric effect has been shown to bring together concepts from tribology, condensed matter physics, and electronic engineering; to describe a phenomenon that influences so many previously unconsidered mechanisms such as galvanic corrosion and surface liquephobicity. This research was derived from my desire to apply my passion for engineering and physics to something that can ultimately benefit society. This quickly became a drive to further understand the often overlooked physical phenomenon of triboelectric charge transfer, in order to optimise its potential for green applications in self-powered sensing technologies. One particular moment which motivated me was when my late supervisor – Professor Anne Neville OBE – told me that after spending her highly decorated career studying the wear and degradation of materials, it would be great if someone could find a way to use it for something positive. The ultimate aim of this study was to investigate triboelectric charging as a positive use for friction, in contrast to most research in tribology.

Table of Contents

Intellectual Property Statement	1-2
Acknowledgements.....	1-3
Preface.....	1-4
Table of Contents	1-5
Abstract	1-9
Table Scientific and Numerical Constants.....	1-10
Table of Notations	1-11
Table of Properties	1-12
Chapter 1 – Overview of The Triboelectric Effect and Applications	1-17
1.1 Terminology	1-17
1.2 Historical	1-18
1.3 The Triboelectric Series.....	1-19
1.4 Charge Transfer Mechanisms	1-20
1.4.1 Electron Transfer	1-21
1.4.1.a Work Function	1-21
1.4.1.b Fermi Gas Model.....	1-27
1.4.1.c Ultraviolet Photoelectron Spectroscopy	1-32
1.4.1.d Thermionic Emission Spectroscopy.....	1-34
1.4.1.e Atomic Force Microscopy Methodologies	1-35
1.4.1.e.i Lateral Force Microscopy	1-37
1.4.1.e.ii Electrostatic Force Microscopy.....	1-37
1.4.1.e.iii Kelvin Probe Force Microscopy	1-38
1.4.1.f Semi-metals, Semi-conductors, and Insulators	1-40
1.4.1.g Electron Affinity and Electronegativity.....	1-42
1.4.1.h Surface State Model.....	1-49
1.4.1.i Surface Energy and Surface Tension	1-52
1.4.1.j Molecular Ion State Model.....	1-56
1.4.1.k Electron-Phonon Interactions.....	1-59
1.4.1.l Mechano-ions and radicals	1-62
1.4.1.m Flexoelectricity	1-63
1.4.2 Ion Transfer.....	1-66
1.4.3 Material Transfer.....	1-69
1.5 Contributing Factors	1-70
1.5.1 Surface Composition.....	1-70

1.5.2 Contact Force and Surface Roughness.....	1-72
1.5.3 Temperature	1-75
1.5.4 Ambient Medium	1-76
1.5.5 Friction	1-77
1.6 Applications of the Triboelectric Effect	1-78
1.6.1 Implications	1-78
1.6.2 Benefits	1-78
1.6.2 Triboluminescence	1-79
1.6.3 Triboelectric Nanogenerators	1-80
1.6.3.a Device Geometries.....	1-82
1.6.3.b Electrical Properties	1-86
Chapter 2 – The Freestanding TENG Apparatus	2-94
2.1 Methodology	2-94
2.1.1 The F-TENG Contact.....	2-94
2.1.2 Electronic Measurements	2-99
2.1.2.a Feedback Ammeter Design	2-100
2.1.2.b Measurement Circuit	2-103
2.1.3 Data Processing.....	2-104
2.1.4 Sample Preparation	2-106
2.1.5 Testing procedure	2-122
2.1.5.a Feedback Ammeter and Oscilloscope Configuration.....	2-122
2.1.5.b Feedback Ammeter and myDAQ Configuration	2-122
2.1.5.c Belt Driven Actuation and Electrometer Configuration.....	2-123
2.2 Results & Discussion	2-124
2.2.1 Current Measurements	2-124
2.2.1.a Feedback Ammeter and Oscilloscope Configuration.....	2-124
2.2.1.b Feedback Ammeter and myDAQ Configuration	2-127
2.2.2 Triboelectric Charge Measurements.....	2-133
2.2.2.a Hand Held Actuation and Feedback Ammeter	2-133
2.2.2.b Belt Driven Actuation and Electrometer	2-141
2.2.2.b.i Influence of Surface Composition	2-141
2.2.2.b.ii Influence of Surface Roughness	2-145
2.3 Conclusions	2-150
Chapter 3 – The UMT-TENG Apparatus: Tribological and Electronic Response.....	3-152
3.1 Methodology	3-152

3.1.1 UMT-TENG Contact.....	3-152
3.1.2 Tribological Measurements.....	3-155
3.1.3 Electronic Measurements	3-156
3.1.4 Data Processing.....	3-159
3.1.5 Sample Preparation	3-159
3.1.6 Testing Procedure.....	3-163
3.2 Results and Discussion	3-163
3.2.1 Friction measurements	3-163
3.2.1.a Influence of Polymer Composition	3-166
3.2.1.b Influence of Electrode Composition	3-166
3.2.1.c Influence of Surface Roughness	3-166
3.2.1.d Influence of Applied Load	3-167
3.2.1.e Wear Analysis	3-167
3.2.2 Electronic Output Measurements	3-170
3.2.2.a Current and Voltage Measurements	3-170
3.2.2.b Microscale ESD Observations	3-175
3.2.2.c Triboelectric Charge Measurements	3-180
3.2.2.c.i Influence of Polymer Composition.....	3-182
3.2.2.c.ii Influence of Electrode Composition.....	3-182
3.2.2.c.iii Influence of Surface Roughness.....	3-182
3.2.2.c.iv Influence of Applied Load	3-183
3.2.3 Comparison of Tribological & Electronic Measurement Results.....	3-183
3.3 Conclusions	3-187
Chapter 4 – The UMT-TENG Apparatus: Friction and Semi-Analytical Model	4-188
4.1 Methodology	4-188
4.1.1 Contact Geometry	4-188
4.1.2 Electronic Measurements	4-189
4.1.3 Sample Preparation	4-190
4.1.4 Testing Procedure.....	4-191
4.2 Results and Discussion	4-192
4.2.1 Friction Response	4-192
4.2.1.a Reciprocating Frequency	4-193
4.2.1.b Applied Load	4-194
4.2.2 Electric Response	4-194
4.2.2.a Reciprocating Frequency	4-195

4.2.2.b Electrostatic Charge Dissipation	4-195
4.2.2.c Applied Load	4-197
4.3 Semi-Analytical Model	4-198
4.3.1 Theory	4-199
4.3.1.a Charge Saturation Value.....	4-199
4.3.1.b Flexoelectric Contribution	4-200
4.3.1.c Friction Contribution	4-201
4.3.1.d Material Wear Contribution	4-202
4.3.1.e Full Equation	4-203
4.3.2 Data Fitting.....	4-203
4.4 Conclusions	4-207
Chapter 5 – Summary.....	5-209
Appendix A: Additional Analysis Techniques.....	5-212
5.1 Atomic Force Microscopy Study	5-212
5.1.2 Methodology	5-212
5.1.2 Results and Discussion.....	5-213
5.1.3 Conclusions	5-215
Appendix B: The Terminologies of Potential.....	5-217
Index of Figures.....	5-219
Index of Tables	5-224
Index of Equations	5-225
Bibliography.....	5-226

Abstract

The triboelectric effect has long been understood as the phenomenon of electric charge transfer resulting from mechanical contact. Although this has long been observed in a multitude of circumstances, ranging from daily life to specific engineering applications, a significant knowledge gap remains regarding the mechanisms that describe triboelectric charge transfer. Research into the triboelectric effect has however seen a recent surge in the previous decade, owing to the conception of the triboelectric nanogenerator (TENG) and its subsequent applications in energy recycling and self-powered sensing.

Existing research now entails various models for predicting the output of TENG devices from an electrical engineering standpoint, in addition to qualitatively describing the mechanisms that drive triboelectric charging. However, many of these models fall short with regards to describing the role of tribological factors in these physical mechanisms. Similarly, the field of tribology has only recently begun to expand its interests into triboelectric phenomena.

This research plays a key part in discerning the influence of tribology on triboelectric mechanisms and applications. Factors such as surface composition, contact topography, normal and tangential forces, and relative motion are determined, as well as the effects of material wear and the presence of contaminating media. This is achieved primarily through the modification of a mechanical testing apparatus with the integration of a high-impedance electronic measurement circuit for the correlation of mechanical and electrical measurements. Ultimately, a semi-analytical model is also constructed using these data as a way of providing a stepping stone towards a fundamental understanding of all aspects of the triboelectric effect.

Table Scientific and Numerical Constants

Symbol	Definition	Unit / Value
i	Imaginary unit, equal to $\sqrt{-1}$. Not to be confused with i subscript for denoting arbitrary objects.	Dimensionless
e	Euler's number, $\sum_{n=0}^{\infty} \frac{1}{n!} \approx 2.71828\dots$	Dimensionless
q_e	Elementary electric charge ($1.6e^{-19}$ Coulombs).	Coulomb (C)
h	Planck's constant ($6.62607\dots e^{-34}$ Joule seconds).	Joule second (J s)
\hbar	Planck's reduced constant ($h/2\pi \approx 1.05457\dots e^{-34}$ Joule seconds).	Joule second (J s)
m_e	Electron mass ($9.10938\dots e^{-31}$ kilograms).	Kilogram (kg)
m_u	Atomic mass unit. ($1.66054\dots e^{-27}$ kilograms). Also a unit of measurement defined as the Dalton (Da, u).	Kilogram (kg)
ϵ_0	Permittivity of free space, vacuum permittivity ($8.85419\dots e^{-12}$ Farad metre ⁻¹).	Farad metre ⁻¹ (F m ⁻¹)
k_B	Boltzmann's constant ($1.38065\dots e^{-23}$ Joules kelvin ⁻¹). Associates particle kinetic (thermal) energy with temperature within a gas of particles.	Joule kelvin ⁻¹ (J K ⁻¹)
A_0	Richardson constant (Equal to $1.20173\dots e^6$ Coulombs second ⁻¹ metre ⁻² kelvin ⁻²).	Coulomb second ⁻¹ metre ⁻² kelvin ⁻² (C s ⁻¹ m ⁻² K ⁻²)
g	Gravitational acceleration (equal to approximately 9.8 metres second ⁻²)	Metre second ⁻² (m s ⁻²)
δ_{ij}	The Kronecker delta. Equal to 1 when i is equal to j , and 0 everywhere else.	Dimensionless

Table of Notations

Symbol	Definition
$\langle a \rangle$	Averaged or rms value of an arbitrary property a .
$ a $	Absolute magnitude of an arbitrary property a .
\vec{a}	An arbitrary vector quantity of a .
\hat{a}	A unitary vector or operator (e.g. \hat{r} and \hat{H} respectively).
a'	A modified or perturbed value of an arbitrary property a .
a^*	An effective or equivalent value of an arbitrary property a through some approximation.
a_i	Value of an arbitrary property a corresponding to an arbitrary object or property i .
$a(i)$	An arbitrary property a as a function of another arbitrary property i .
Δa	Spatial gradient, or finite change, in an arbitrary property a .
$\nabla^2 a$	Laplace operator ('Laplacian') of an arbitrary property a . Described as the divergence of the gradient of a scalar function on Euclidean (position) space.
$\partial a, da$	Infinitesimal change, in an arbitrary property a .

Table of Properties

Symbol	Definition	Unit / Value
N_i	Number (of a given object i).	Dimensionless
\vec{r}	Position vector, expressed in any form of spatial coordinate (Cartesian, Spherical etc.)	Metre (m) / radian (rad)
x, y, z	Cartesian coordinates. The direction z is often used to describe distances and separations orthogonal to the plane of surfaces.	Metre (m)
r, θ, φ	Spherical coordinates; radial distance (r), polar angle (θ), and azimuthal angle (φ) respectively.	Metre (m), radian (rad), radian (rad)
r, θ, z	Cylindrical coordinates; radial distance (r), polar angle (θ), and Cartesian z coordinate respectively.	Metre (m), radian (rad), metre (m)
$T_{r,\theta,z \rightarrow x,y,z}$	Coordinate transformation matrix (e.g. cylindrical to Cartesian etc.).	Unitless 2D matrix
$L, l(t)$	Length of an object. Time dependant length.	Metre (m)
$\langle d \rangle$	Average distance. Specifically the separation distance of excess charges within a volume of bulk material. Usually in the order of microns (10^{-6} metre).	Metre (m)
R	Radius of a circular or spherical object.	Metre (m)
a	Hertzian contact radius.	Metre (m)
θ	Angle. Often stated in degrees ($\frac{180}{\pi}$ radians).	Radian (rad)
S_a, S_q	Arithmetic mean roughness, centre-line roughness. Root mean square (rms) roughness.	Metre (m)
S_p, S_v, S_z	Maximum peak height, maximum valley depth, roughness height range.	Metre (m)
$S_{\Delta a}, S_{\Delta q}$	Arithmetic mean gradient. Root mean square gradient.	Dimensionless
S_{sk}, S_{ku}	Surface skewness. Surface kurtosis.	Dimensionless
\vec{k}	Wave-vector. Spatial frequency.	Metre ⁻¹ (m ⁻¹)
A	Area.	Metre ² (m ²)
V	Volume.	Metre ³ (m ³)
n_i	Volumetric number density or concentration (of a given object i).	Metre ⁻³ (m ⁻³)
t	Time.	Second (s)

τ	Time constant, e.g. a timescale for a particular mechanism.	Second (s)
f	Frequency, often defined in units Hertz (Hz).	Second ⁻¹ (s ⁻¹)
Δf	Frequency bandwidth.	Second ⁻¹ (s ⁻¹)
ω	Angular frequency.	Radian second ⁻¹ (rad s ⁻¹)
\vec{v}	Velocity vector.	Metre second ⁻¹ (m s ⁻¹)
$\langle \vec{v}_d \rangle$	Drift velocity of a collection of particles.	Metre second ⁻¹ (m s ⁻¹)
\vec{a}	Acceleration vector.	Metre second ⁻² (m s ⁻²)
m	Mass.	Kilogram (kg)
M	Atomic mass number.	Dimensionless
ρ	Volumetric mass density.	Kilogram metre ⁻³ (kg m ⁻³)
\vec{p}	Momentum vector.	Kilogram metre second ⁻¹ (kg m s ⁻¹)
F	Absolute magnitude of force acting in a particular direction. Force may also be expressed as a vector quantity.	Newton (N), Kilogram metre second ⁻² (kg m s ⁻²)
μ	Friction coefficient.	Dimensionless
P	Pressure. Force exerted per unit area. Also referred to as mechanical stress.	Pascal (Pa), Newton metre ⁻² (N m ⁻²)
σ	Mechanical stress. Analogous to pressure.	Pascal (Pa)
Y	Elastic modulus. Young's modulus.	Pascal (Pa)
Y^*	Equivalent elastic modulus of an interface.	Pascal (Pa)
G	Shear modulus.	Pascal (Pa)
ν	Poisson's compressibility ratio.	Dimensionless
ϵ	Material strain.	Dimensionless

E	Energy. A measure of work.	Joule (J), Newton metre (N m)
E_K	Kinetic energy.	Joule (J)
T	Temperature. A measure of the average kinetic energy of particles in a substance.	Kelvin (K)
U	Internal energy of a thermodynamic system.	Joule (J)
G	Gibb's free energy. The maximum amount of non-volume-expansion work that can be performed on a closed thermodynamic system. Equal to product of entropy (S) and temperature (T), subtracted from enthalpy (H).	Joule (J)
F	Helmholtz free energy. The useful work obtainable from a closed thermodynamic system at a constant temperature (T). Equal to product of entropy (S) and temperature (T), subtracted from the internal energy (U).	Joule (J)
H	Enthalpy. The summation of a thermodynamic system's internal energy with the product of its pressure (P) and volume (V).	Joule (J)
S	Entropy. A physical measure of disorder for a thermodynamic state or system.	Joule kelvin ⁻¹ (J K ⁻¹)
$\bar{\mu}$	Fermi level, Fermi potential, electrochemical potential energy. Often stated in units of electronvolt.	Joule (J)
ϕ	Work function, chemical potential relative to vacuum, often stated in units of electronvolt (eV, 1.6e ⁻¹⁹ Joules).	Joule (J), kilogram metre ² second ⁻² (kg m ² s ⁻²)
ϕ^*	Effective work function, often assigned to dielectric surfaces and stated in units of electronvolt.	Joule (J)
ϕ'	Effective perturbed interfacial work function. Often stated in units of electronvolt.	Joule (J)
μ_{int}	Internal chemical potential energy, chemical potential energy. Often stated in units of electronvolt (eV, 1.60218...e ⁻¹⁹ Joules).	Joule (J)
μ_{ext}	External potential energy.	Joule (J)
E_{vac}	Vacuum level, vacuum potential energy. Often stated in units of electronvolt.	Joule (J)
E_F	Fermi energy. Often stated in units of electronvolt.	Joule (J)

E_0	Ground-state energy of a quantum system. Often stated in units of electronvolt.	Joule (J)
E_{HOMO}	Energy of the highest occupied molecular orbital relative to the vacuum level. Often stated in units of electronvolt.	Joule (J)
E_{LUMO}	Energy of the lowest unoccupied molecular orbital relative to the vacuum level. Often stated in units of electronvolt.	Joule (J)
E_{EA}, χ	Electron affinity. Often stated in units of electronvolt.	Joule (J)
E_{IP}	Ionisation potential. 1 st Ionisation energy. Often stated in units of electronvolt.	Joule (J)
γ	Interfacial energy.	Joule metre ⁻² (J m ⁻²)
$g(E)$	Density of (electron) states per unit energy and volume as a function of (electron) energy.	Joule ⁻¹ metre ⁻³ (J ⁻¹ m ⁻³)
$f(E)$	Fermi-Dirac state occupancy distribution as a function of energy.	Probabilistic
$b(E)$	Bose-Einstein state occupancy distribution as a function of energy.	Probabilistic
Q	Electric charge.	Coulomb (C)
σ	Surface charge density.	Coulomb metre ⁻² (C m ⁻²)
ρ_q	Volumetric charge density.	Coulomb metre ⁻³ (C m ⁻³)
\vec{I}, I	Electric current vector, electric current magnitude.	Ampere (amp, A), Coulomb second ⁻¹ (C s ⁻¹)
\vec{J}_i, J_i	Electric current density vector, pointed orthogonally to the cross-sectional area or surface (i) in question. Absolute magnitude of electric current density.	Coulomb second ⁻¹ metre ⁻² (C s ⁻¹ m ⁻²)
V	Electric potential difference, voltage.	Volt (V)
V_{CPD}	Volta potential, contact potential difference (CPD).	Volt (V)
R	Electrical resistance.	Ohm (Ω)
\vec{E}	Electric field vector.	Volt metre ⁻¹ (V m ⁻¹)
\bar{P}	Electric polarisation density magnitude.	Coulomb metre ⁻² (C m ⁻²)

C	Capacitance.	Farad (F), coulomb ² second ² kilogram ⁻¹ metre ⁻² (C ² s ² kg ⁻¹ m ⁻²)
μ_{ijkl}	Flexoelectric coefficient tensor.	Joule metre (J m)
ε	Absolute permittivity, electric polarizability. Often stated relative to the permittivity of free space (ε_0)	Farad metre ⁻¹ (F m ⁻¹), Coulomb ² second ² kilogram ⁻¹ metre ⁻³ (C ² s ² kg ⁻¹ m ⁻³)
ψ	Wavefunction of a quantum system.	Metre ^{-3/2} (m ^{-3/2})
ρ	Spatial probability density.	Metre ⁻³ (m ⁻³)
β	Resonance integral constant. Describes the resonance between two wavefunctions.	Dimensionless
n, l, m_l, m_s	Principle, azimuthal, magnetic, and spin quantum numbers.	Dimensionless
\hat{H}	Hamiltonian operator. Denoting the energy of a quantum system.	Operator
X	Denotes an atomic species.	Object
C_i, ζ, ξ	Arbitrary scaling constants.	Dimensionless
λ_R	Material specific constant relevant for thermionic emission.	Dimensionless
Q	Quality factor. A dimensionless constant which correlates to a signal-no-noise ratio.	Dimensionless

Chapter 1 – Overview of The Triboelectric Effect and Applications

The triboelectric effect is the physical phenomenon that describes the transference of electric charge between two contacting media without the presence of an external driving potential. The exact nature of such an interface, as well as the nature of the involved charge carriers, can vary and be applied to a wide variety of circumstances and applications. Before describing the methodologies and findings of in this research, a comprehensive overview of the triboelectric effect is required in order to provide context.

1.1 Terminology

The exact terminology pertaining to the triboelectric effect is varied, with terms relating to different and similar aspects of the phenomenon. The term '*triboelectric charger transfer*' will refer to all cases of charge transference resulting from triboelectric phenomena. One prominent aspect of studies into the triboelectric effect is that of '*contact electrification*'. Contact electrification is known as the phenomenon describing the transference of electric charge between media as they are brought into physical contact, usually under a minimal normal load and without the presence of a net tangential load. A '*normal load*' is described as the component of force applied to the interface which is perpendicular to the plane of the interface within the context of mechanics, whereas a '*tangential load*' is described as the component of force applied to the interface in a specific direction that is parallel to the plane of the interface. Owing to the nature of contacting rough surfaces, tangential stresses are present on the asperity level in addition to the compressive stresses applied by the normal load. When a large enough net tangential force is applied to the contact, such that the onset of kinetic friction is reached, the term '*contact electrification*' is often replaced by '*frictional electrification*' or '*triboelectric charging*'. Within the context of this work, '*contact electrification*' will refer to triboelectric charge transfer across an interface without relative tangential motion i.e. '*non-sliding*', and '*frictional electrification*' will refer to triboelectric charge transfer across an interface with relative tangential motion. The mechanisms that govern triboelectric charge transfer across rolling contacts, as well as solid-liquid interfaces, are beyond the scope of these investigations but are hypothesised in further discussion. These terms are not to be confused with '*triboelectrification*' which has been used in many recent publications pertaining to the growing use of triboelectric applications in the engineering industry rather than any physical mechanism (Chen and Wang, 2017).

1.2 Historical

The etymology of the word '*triboelectric*' has roots in Greece, being derived from a combination of the Greek words τρίβος '*tribos*' and ἤλεκτρον '*elektron*', meaning '*to rub*' and '*amber*' respectively. The electrostatic properties of amber are first mentioned by Plato (Plato, 360BC) and later by Theophrastus (Theophrastus, 300BC). These properties are later questioned by Plutarch (Plutarch, 100AD), who likened these electrostatic properties to the ferromagnetic properties exhibited by magnetite lodestones. Despite the first use of the term '*tribo-electricity*' not being until the early 20th century (Khvolson et al., 1906; Shaw, 1917), the triboelectric effect itself has been observed since antiquity. It has widely been suggested that the first recording of the electrostatic charging of materials was by the presocratic philosopher Thales of Miletus, who is credited in many reputable publications for carrying out experiments and observations of electrostatic charging from the rubbing of amber against a multitude of counter-materials (Keithley, 1999). This particular notion has since been discredited (Iversen and Lacks, 2012); with Thales instead being credited by Aristotle for having discussed the nature of a soul, and magnetism as a motive force (Aristotle, 350BC). It is therefore likely that the comments of Plato on the triboelectric effect are instead the earliest to be recorded.

Regardless of the origin of scientific study into the triboelectric effect, what is inherently clear is that the triboelectric effect has been present in daily life for thousands of years. The first distinction between electrostatic and magnetic forces are recorded in the second book of William Gilbert's '*De Magnete*' where a rubbed amber stick is shown to attract various organic matter and water, whereas magnetism is shown to only attract ferrous objects (Gilbert, 1600). It was from this point on academic interest into electrostatics, and most notably triboelectrics, was somewhat reinvigorated. Scientific observations of triboelectric charging and potential applications further developed throughout the 17th and 18th centuries.

The first recorded observations of triboelectric charge transfer between materials other than amber are those by Otto von Guericke, who rubbed a globe of sulphur by hand to generate an electrostatic charge (von Guericke, 1672). The replacement of the sulphur globe with one composed of silicate glass was proposed by Newton (Newton, 1704) and implemented by Hawksbee (Hawksbee, 1709), who performed and recorded numerous observations of triboelectric phenomena using a rotating ball-on-plate apparatus in a vacuum environment. These experiments were also among the first to record the phenomenon known as '*triboluminescence*', a phenomenon related to the triboelectric effect that is further explained in 1.6.2 Triboluminescence. A variation of this apparatus was used by Georg Matthias Bose, with the addition of an electrically isolated metal bar known as a '*prime conductor*', as a method of storing triboelectrically generated charges. The application of this prime conductor, in addition to additional demonstrations by Bose on the electrical conductivity of water, inspired Jurgen Georg von Kleist to inadvertently invent the *Leyden Jar* in 1745 (Priestley, 1767).

Various forms of these 'friction machines' have since been devised. Notable examples include the *electrophorus* - initially invented by Johan Carl Wilcke in 1762 (Wilcke, 1762) and later refined by Alessandro Volta in 1775 (Pancaldi, 2003), as well as the *Wimshurst machine* – developed in 1883 by

James Wimshurst (Pellissier, 1891), and the *van de Graaff generator* – developed by Robert J. van de Graaff in 1929 as a particle accelerator (Van De Graaff et al., 1933). Despite these progresses, very little research has previously investigated the mechanisms behind triboelectric charge transfer beyond identifying which material combinations tend to contribute a greater magnitude of charge.

The scientific field of tribology in itself is relatively novel, with the term ‘tribology’ first being coined in 1966 alongside the publication of the Jost report (Jost, 1966). The Jost report highlighted the significant relevance of research into lubrication, corrosion, and friction for maximising efficiency of industry as a whole in the United Kingdom at the time. The report estimated that tribology related costs accounted for between 1.1 and 1.4 % of the UK’s gross domestic product (GDP), and instigated a world-wide drive to develop a greater understanding.

1.3 The Triboelectric Series

What was evidently clear in research leading into the 18th century is that triboelectric charging primarily occurred between dissimilar materials, with the two contacting surfaces then electrostatically attracting one another once the triboelectric charges had been generated. These observations identified that triboelectric charging is the generation of equal and opposite electrostatic charge densities on the two contacting surfaces. It was observed that some material surfaces had a tendency to accumulate a negative charge against most counter-surfaces, whereas other materials developed positive charges. The magnitudes of such charge densities were also later shown to be dependent on the choice of contacting materials.

Early attempts to compare the triboelectric properties of material surfaces have resulted in various ‘triboelectric series’ being constructed, the first series being published by Johan Carl Wilcke as part of his magister degree dissertation (Wilcke, 1757). For these series, materials are arranged in the order of the relative polarity of the contact charge acquired each other, or against a control counter-surface. These materials range from those that produce the most positive charge polarity to those that produce the most negative polarity. These triboelectric series follow the convention that higher positioned materials in the series acquire a positive charge when contacted with a material at a lower position along the series, whereas the materials in the lower positions will acquire a negative charge when contacted with materials at a higher position. Because of this convention, triboelectric series have also been used to estimate the relative charge polarity of other material pairings within them or between different series (Diaz and Felix-Navarro, 2004). The findings of Shaw (Shaw, 1917) concluded that, with great care, it is possible to arrange materials into a replicable triboelectric series. This research did also however highlight the multitude of inconsistencies and contradictions in previous series.

Unfortunately, most triboelectric series remain only qualitative in terms of denoting the position of materials. They are based entirely on empirical findings, only relative to specific reference materials which differ between studies, and with many additional variables to consider in addition to the electro-chemical properties of an example surface (Zou et al., 2019). The propensity of triboelectric charging has since

been more accurately described as an interfacial property, rather than a characteristic used to describe an isolated surface. This implies that knowledge of how two different materials behave against a control counter-surface may not give an accurate prediction for how the two materials contact against each other. Because of this, specific surfaces may not have precise positions within a 'universal' triboelectric series, and such a series may not even be linear and one-dimensional in nature (Henniker, 1962). The series of findings of Shaw and Jex (Shaw and Jex, 1928b; Shaw and Jex, 1928a) were the first to state triboelectric charging as an interfacial phenomenon. Their findings highlighted the cyclic nature of some material positions and implied that triboelectric charging is a consequence of how the two contacting surfaces interact, more so than the properties of both surfaces individually.

Despite triboelectric charging being dependant on the electro-chemical compositions of both contacting surfaces in combination, certain structures have been identified as having affinities for certain polarities of charge (Lee, 1994). Before explaining these specific structures and explaining how they contribute to triboelectric charge transfer, a more fundamental understanding of the mechanisms behind the triboelectric effect is given.

1.4 Charge Transfer Mechanisms

Contact charging is generally classified into three categories according to the electrical properties of the contacting materials; i.e. conductor–conductor contacts, conductor–insulator contacts and insulator–insulator contacts (Matsusaka and Masuda, 2003; Matsusaka et al., 2010). These categorical definitions may also be extended regarding which phase(s) of matter the contacting materials are in; e.g. solid-liquid, solid-vapour, and liquid-vapour. During contact electrification, each contacting surface develops a charge of equal but opposing polarity for a given pairing; disregarding any external environmental interference. One surface will develop a positive charge density, with its counter-surface developing a negative charge density of equal magnitude.

The tribo-charging of conducting materials – such as metals – is usually unnoticeable, since having both materials in contact as conductors will cause the transferred electrons to immediately dissipate through the material upon the separation of contact. In the case of contacts where an insulator is involved, isolated charges are known to become trapped on the insulator surface(s) as part of a quasi-capacitance layer. It was initially hypothesised by the teachings of Alessandro Volta and later by Hermann von Helmholtz (Perucca, 1928) that the interface of two contacting surfaces could be treated as a form of capacitor, with a charge double-layer forming across the interface during contact, as would equal and opposite charges across a capacitor when an external voltage is applied. In the case of contact electrification, a contact potential is generated across the contact by the presence of this charge double-layer.

This Volta-Helmholtz hypothesis forms the basis for the qualitative understanding triboelectric charge transfer. Whilst this hypothesis holds true for the majority of triboelectric contacts, there are additional factors to consider regarding the exact nature of the charge carriers, in addition to the mechanisms that contribute to their transferral. The following section will discuss the possible theories for describing the

mechanisms for triboelectric charge exchange, in addition to the relevant material parameters that are inherently linked to them.

1.4.1 Electron Transfer

The electron is the first particle one would naturally assume to be a charge carrier when considering anything electric in nature. Its comparatively low rest mass of 9.1×10^{-31} kg allows for the relatively high mobility and penetration of its free particle through most media. Its unique interaction with protons – in addition to other positively charged subatomic particles such as muons – also forms the basis of atomic and molecular structure. Electrons have been experimentally observed as the primary triboelectric charge carrier between contacting solid surfaces (Murata and Kittaka, 1979; Wang and Wang, 2019), but the driving force behind why they are transferred across triboelectric interfaces is the subject of much discussion.

The mechanism of transferring electrons across triboelectric interfaces is mediated predominantly through quantum tunnelling (Willatzen and Wang, 2019). Quantum tunnelling is a phenomenon which allows for particles such as electrons to propagate through potential barriers rather than needing to overcome them with a certain amount of potential energy. This is useful in the presence of material interfaces, where a vacuum gap may exist between the potential wells of contacting atoms. For the cases of materials contacting intimately it is possible for electrons to simply transition from one atom to another due to their close proximity causing electron distributions to overlap, which ultimately lowers the potential barrier between them (Willatzen et al., 2020).

Individual transitions between electronic states are theorised to happen instantaneously, as is the proposed nature of quantum jumps. Any time dependent aspects of the triboelectric transference of electrons may arise from the changing availability of energy states involved in triboelectric transitions. A separate origin may arise from the development of real contact area across which triboelectric charge transfer may occur over time (Xu et al., 2020).

1.4.1.a Work Function

It was not until the findings of Richardson (Richardson, 1912) that the Volta-Helmholtz hypothesis was generally accepted as an intrinsically electronic phenomenon. This has later been reinforced by recent research conducted by (Wang and Wang, 2019) using atomic force microscopy in conjunction with Kelvin probe force microscopy to experimentally evaluate the nanoscale nature of contact electrification.

The findings of Shaw and Jex (Shaw and Jex, 1926) were the first to determine a material parameter for correlating with the triboelectric charging of conductive materials. It was discovered that metals would generate charges through contact electrification against filter paper, the magnitude of these produced charges being in correlation with their respective work functions. From this research it was established that the contact potential difference (V_{CPD}) generated between two contacting conductive surfaces in thermodynamic equilibrium is as expressed as below.

$$|V_{CPD}| = \frac{\phi_A - \phi_D}{q_e} \quad (1-1)$$

ϕ_A and ϕ_D are the work functions of the electron acceptor and donor surfaces respectively, and q_e is the elementary charge of an electron ($\sim 1.6 \times 10^{-19}$ C). Harper (Harper, 1951b; Harper, 1951a) was the first to eliminate previous inconsistencies in experimental results, reinforcing that the total charge transferred via contact electrification between metals can be calculated using the difference between their respective work functions and the topography of the contact. It was also first noted in these findings that charge would be transferred via contact electrification in an exponential fashion over time (t), as charge would accumulate on a traditional capacitor under a constant potential bias.

$$Q(t) = Q_{max} \left(1 - e^{-\frac{t}{\tau_0}} \right) \quad (1-2)$$

Q_{max} is the maximum charge collected, and τ_0 is a time constant that reflects the timescale over which charge accumulates. The definition of a material's work function arises from the fundamental nature of electrons being categorised as fermions. Fermions are a group of sub-atomic particles that constitute matter. As such they obey the Pauli exclusion principle (Pauli, 1925), which states that no two fermions may exhibit the same quantum numbers. Therefore, fermions cannot simultaneously occupy the same quantum state within a given quantum system, such as a single atom. In accordance with the first and second laws of thermodynamics, interacting particles share their energy and increase universal entropy (S) and disorder in order to collectively reach lower energy states whilst universally conserving energy. For example, an electron in a high energy excited state may release energy in the form of a photon (light) in order to relax into a lower unoccupied energy state.

A consequence of this is that all particles collectively endeavour to be in the lowest energy state that is achievable for the system. For closed quantum systems where the total energy is conserved throughout them, there is a minimum amount of energy that is possible for a quantum state to achieve, this particular state is known as the ground state. There may be multiple available quantum states that occupy the same energy level, for example multiple electron orbitals within an electron sub-shell, these states that occupy identical energies are known as degenerate states. The quantum states within a given system are presented as the solutions to the wavefunction (ψ) of the system. The wavefunction of a quantum system can be related to the probability density (ρ) of the system by taking the square of its absolute value.

$$|\psi(\vec{r}, t)|^2 = \rho(\vec{r}, t) \quad (1-3)$$

\vec{r} is the position of the particle within the quantum system, which can be represented in any form of spatial coordinate. Approximate time-independent solutions for an example atom such as Hydrogen can be calculated from a quantum mechanical approach using Schrödinger's equation in spherical coordinates as stated below.

$$E\psi(r, \theta, \varphi) = -\frac{\hbar^2}{2m^*} \nabla^2 \psi(r, \theta, \varphi) - V(r)\psi(r, \theta, \varphi) \quad (1-4)$$

E is the total energy of the system, both kinetic and potential. $\psi(r, \theta, \varphi)$ is the wavefunction of the system in spherical coordinates, which can be treated as a probability density function for the location of the electron. \hbar is the reduced Planck constant $\frac{h}{2\pi}$, also known as the Dirac constant with a value of 1.05×10^{-34} kg m² s⁻¹. m^* is the effective two-body reduced mass of the nucleus m_n and electron m_e as expressed in

(1-5). ∇^2 is the Laplace operator, which is used to retrieve the divergence of the gradient of a scalar function, in this case the wavefunction. $V(r)$ is the Coulomb potential experienced by the electron as expressed by Coulomb's law (1-6). The two terms on the right hand side of (1-4) represent the kinetic and potential energy of an electron within the system respectively.

$$m^* = \frac{m_e m_n}{m_e + m_n} \quad (1-5)$$

$$V(r) = \frac{N_p q_e^2}{4\pi\epsilon_0 r} \quad (1-6)$$

N_p is the atomic number of the atom in question, corresponding to the number of protons within the nucleus, and ϵ_0 is the permittivity of free space of $8.85 \times 10^{-12} \text{ C}^2 \text{ s}^2 \text{ kg}^{-1} \text{ m}^{-3}$. This specific form of Schrödinger equation is solvable through a separation of variables, and yields valid wavefunctions under the provision that certain parameters meet relevant criteria. Four parameters in particular arise from this particular solution, which are commonly known as the principle (n , not to be confused with the more general notation of number density n used in the remainder of this thesis), azimuthal (l), magnetic (m_l), and spin (m_s) quantum numbers. The principle quantum number is most strongly correlated to the total energy of a state, and may take any integer value above 0 i.e. $\{n \mid 0 < n, n \in \mathbb{Z}\}$. The azimuthal quantum number, which represents the quantised angular momentum of the state, can then take any integer value ranging from 0 to $n - 1$ i.e. $\{l \mid 0 \leq l < n, l \in \mathbb{Z}\}$. The magnetic quantum number, which represents the spatial orientation of the state, can then take any integer value ranging from $-l$ to l i.e. $\{m_l \mid -l \leq m_l \leq l, m_l \in \mathbb{Z}\}$. The spin quantum number differs between particles, with fermions taking half-integer values, and electrons specifically restricted to two arbitrary states of 'spin up' ($m_s = 1/2$) and 'spin down' ($m_s = -1/2$).

The possible combinations of these quantum numbers present the possible states that electrons can occupy around the nucleus. Since every state has a spin up and spin down equivalent, these spin-paired states are often grouped and commonly known as orbitals. Similarly, states that all possess the same principal quantum number are grouped into 'shells', and states within a particular shell that all possess the same azimuthal quantum number are grouped into 'subshells'. The lowest energy orbital is located in the closest electron shell to the nucleus, where the principle number is at its lowest value of 1. At this energy level both the azimuthal and magnetic numbers are restricted to a single value of 0, but the spin number remains able to take either up or down value. This means that the first electron shell only contains one subshell and one orbital, which in turn contains two spin-paired states. In the second shell the azimuthal and magnetic numbers are no longer restricted. This allows for the existence of one orbital that corresponds to $l = 0$, and three additional orbitals that correspond to $l = 1$. These two groups of orbitals are known as the sharp (s) and principle (p) subshells respectively, with additional types of subshell occurring in higher energy shells. The notation for a particular subshell is the principle number associated with it, followed by the letter representing its associated value of l . For example, the sharp orbital within the first electron shell would be represented as the '1s' orbital. It is also important to note that despite both the 2s and 2p subshells occupying the second electron shell, the 2s orbital is of a lower energy than the three 2p orbitals due to its lower angular momentum. The notation for specific orbitals reflects the

nature of their subshells, with an additional subscript included to denote their spatial orientation. Three good examples of this notation are the three 2p orbitals, which are denoted individually as $2p_x$, $2p_y$, and $2p_z$ according to their relative orientations along an arbitrary set of Cartesian axes.

Since electrons cannot occupy identical atomic orbitals, they instead occupy energy states of incrementing energy values, starting with the 1s orbital, as they become occupied in accordance with the Aufbau principle (Park and Stetten, 2001) and Madelung's Rule (Pan Wong, 1979). When considering orbitals and states within the same subshell, states with parallel spins are initially filled as to follow Hund's first rule (Kutzelnigg and Morgan, 1996). This implies that every orbital within a given subshell must be singularly occupied before any can become doubly occupied. There are a small number of elemental exceptions to these rules, one example being that of Platinum which has a single $6s^1$ electron in its outermost shell and a corresponding vacancy in its 5d subshell. This deviation from expected electron configurations only occurs within exceptionally massive elements where the mass of the nucleus causes electrons in the most fundamental orbitals to effectively travel at increasingly relativistic speeds.

The chemical and physical properties of elements are determined by their electron configuration, most notably the empty and occupied states within their outermost shell which are known as valence states (Gillespie and Robinson, 2007). As atoms are brought into proximity to one another, the potential wells generated by their nuclei begin to overlap. This causes the outermost electron orbitals of each atom to become shared between the two in the formation of co-valent bonds. Some of these new 'molecular' orbitals are lower in energy than their respective atomic counterparts. This arises due to the constructive interference of their constituent wavefunctions leading to the electron occupying them being most likely situated between the two atoms. These orbitals are known as bonding orbitals and are the mediators for covalent bonds. Some molecular bonds are higher in energy than their atomic counterparts due to the destructive interference of wavefunctions, and correlate to the electron being least likely situated between the two atoms. These orbitals are known as anti-bonding orbitals. There also exist non-bonding molecular orbitals, which are mostly identical to their atomic counterparts and are not involved in interatomic bonds. These non-bonding orbitals are usually low energy 'core' atomic orbitals, which are less likely to become perturbed by external influences.

The strength of a covalent bond is determined by the respective energies of the newly formed bonding and anti-bonding orbitals, which in turn determines the number of electrons that contribute to the covalent bond. In the extreme case of an ionic bond between two atoms, electrons are sheared from one atom and donated to the valence states of the other. This causes a strong Coulomb attraction between the two newly formed ions, as well as the formation of an electric dipole across the newly formed molecule. As more bonds are formed and larger structures are considered, these molecular orbitals often become more delocalised and their energies become further split. This occurs to the extent where it becomes favourable to consider electron energies in the form of continuous energy bands, rather than discrete levels. The width of an energy band at a given energy level is determined by the degeneracy of states, also referred to as the state density ($g(E)$). An example of the splitting of the valence states of carbon atoms as they are brought together to form a diamond crystal is given in Figure 1-1.

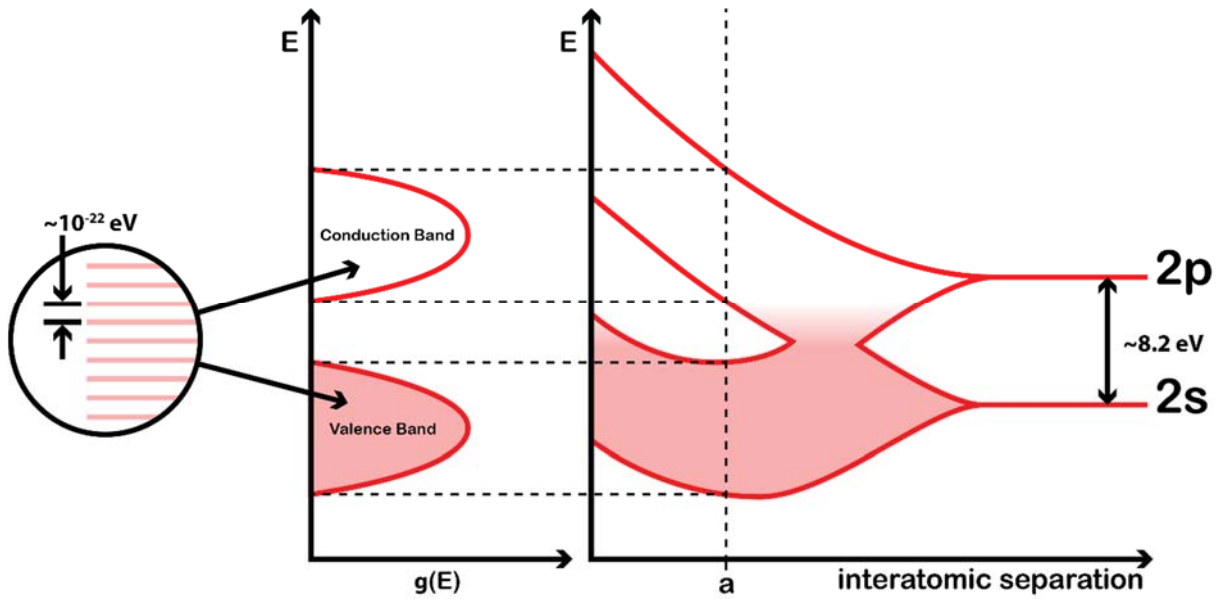


Figure 1-1 – Visual representation of the splitting of valence electron states for carbon atoms as they are brought into proximity to form a diamond crystal.

Due to the fermionic nature of electrons, these energy bands will fill up much like atomic orbitals, from the lowest energy states upwards in increasing energy. At the level of the highest occupied states it is important to take into account the influence of temperature on the behaviour of these electrons. At absolute zero temperature, all electron states are filled up to a given energy level, over which no states are occupied. At higher temperatures, electrons are given additional thermal energy and therefore are permitted to occupy higher states than they would at absolute zero. This also leaves some lower energy states unoccupied due to this movement of high energy electrons. This distribution of electron energies is described by Fermi-Dirac statistics, where the probability of a state being occupied at a given energy (E) and temperature (T) can be expressed as below.

$$f(E) = \frac{1}{e^{(E-\bar{\mu})/k_B T} + 1} \quad (1-7)$$

$\bar{\mu}$ is the Fermi level of the system, k_B is the Boltzmann constant of $1.38 \times 10^{-23} \text{ J K}^{-1}$, and T is the temperature of the system. The Fermi level is also commonly referred to as the 'electrochemical potential', 'total chemical potential' and 'Fermi potential'. It is also frequently confused with the concept of 'internal chemical potential' (μ_c , μ_{int}) which arises purely from the chemical environment of the particles in question such as temperature, density and enthalpy (H).

The internal chemical potential can be expressed using various thermodynamic equations depending on the circumstances being considered. For example, it can be expressed as the change in internal energy (U) of a system initially containing number (N) of particles through the addition or removal of a particle under constant entropy (S) and volume (V). It may also be expressed as the change in Gibb's free energy (G) upon the addition or removal of a particle under constant temperature (T) and pressure (P) or the change in enthalpy upon the addition or removal of a particle under constant entropy and pressure. The most relevant description, however, is the change in Helmholtz free energy (F) upon the addition or removal of a particle under constant temperature and volume. The Helmholtz free energy is a

thermodynamic potential used to measure the amount of useful work that can be obtained from a closed system at a constant temperature. Consequently, the Helmholtz free energy of a system in thermodynamic equilibrium is equal to zero.

$$\mu_{int} = \left(\frac{\partial U}{\partial N} \right)_{S,V} = \left(\frac{\partial G}{\partial N} \right)_{T,P} = \left(\frac{\partial H}{\partial N} \right)_{S,P} = \left(\frac{\partial F}{\partial N} \right)_{T,V} \quad (1-8)$$

The total chemical potential is expressed in terms of internal and external potentials as stated below in (1-9).

$$\bar{\mu} = \mu_{int} + \mu_{ext} \quad (1-9)$$

The external potential μ_{ext} is therefore dependent on external influences such as ambient electromagnetic or gravitational fields as depicted respectively below.

$$\mu_{ext} = -q_e V + m_e g h + \dots \quad (1-10)$$

The term mgh represents gravitational potential energy that an electron could lose by falling a height h through a vacuum under the influence of an arbitrary gravitational acceleration g . The term $-q_e V$ represents the electric potential energy the electron could lose by accelerating under the influence of an arbitrary electric potential V .

The Fermi level is generally defined as the energy required to add one electron to a given system or body. It represents the total free energy of the system per electron, and presents itself as a hypothetical energy level at which 50% of the available energy states would be occupied at thermodynamic equilibrium. For conductive materials, the Fermi level is situated within an energy band. The number of available states close to the Fermi level is partly what determines the electrical conductivity of such a material. The work function, most commonly denoted as ϕ , is a surface specific property of a material and is defined as the minimum thermodynamic work required to remove an electron from such a surface directly into a vacuum state immediately outside. The vacuum state is described as atomically distant from the surface but still close enough to not be influenced by any external electric fields.

$$\phi = E_{vac} - \bar{\mu} \quad (1-11)$$

$$E_{vac} = -q_e V \quad (1-12)$$

E_{vac} is the vacuum level used to denote the electric potential energy of the vacuum state, and V is the electric potential in the vacuum nearby the surface, also referred to as a Galvani potential due to it having no chemical contribution unlike the Fermi potential. Upon examination of these equations it is reasonable to conclude that the work function of a material is actually the internal chemical potential of the material relative to the vacuum, and the vacuum level is actually the electric component of the aforementioned external potential.

The term 'Fermi level' is also often confused – and used interchangeably – with 'Fermi energy'. The Fermi energy, often denoted as E_F , is more specifically described as the difference in energy between the highest and lowest occupied single-particle states in a system at absolute zero temperature. For conductive materials, this lowest state is often defined as the bottom of the conduction band, rather than

the absolute core electron ground state. A more detailed description of the different terminologies surrounding these forms of potential are given in Appendix B: The Terminologies of Potential.

1.4.1.b Fermi Gas Model

If electrons instead transferred across a contact interface through quantum tunnelling, then in static situations they can only be transferred between states of the same energy through resonant tunnelling (Lee, 1994). Once transferred across the interface, these electrons are then free to relax into lower energy states, provided they are unoccupied. The Fermi energy within a monatomic conductor of atomic mass number (M) and bulk mass density (ρ) can be calculated from first principles by first calculating the number density of electrons within the bulk of the material (n_e).

$$E_F = \frac{\hbar^2}{2m_e} (3\pi^2 n_e)^{\frac{2}{3}} \quad (1-13)$$

$$n_e = \frac{\rho N_{val}}{m_u M} \quad (1-14)$$

N_{val} is the number of valence electrons in the outermost atomic shell of the element the material is composed of. M is a dimensionless number but the atomic mass unit (u), also known as Daltons (Da), are used to convert this value into an actual value for atomic mass in kg. A single atomic mass unit represents the mass of a neutral Carbon-12 atom divided by 12. This value is assigned m_u and is equal to $1.66e^{-27}$ kg. For these calculations to hold true the electrons which contribute to conduction within the material are treated as a non-interacting gas, known as a Fermi gas. If the delocalised electrons in each metal are treated as a Fermi gas, the distribution of their energy states with regards to energy and volume can be represented by a density of states $g(E)$ in units of $m^{-3} eV^{-1}$.

$$g(E) = \frac{1}{2\pi^2} \left(\frac{2m_e}{\hbar^2} \right)^{3/2} \sqrt{E - E_0} \quad (1-15)$$

E_0 is the ground-state energy of the Fermi-gas system, the minimum amount of energy that any single electron in the system can possess. The total spatial density of states up to a given energy level E is the integral of this relationship with respect to energy.

$$n(E) = \frac{1}{3\pi^2} \left(\frac{2m_e}{\hbar^2} (E - E_0) \right)^{3/2} \quad (1-16)$$

E_{0_i} is the energy level at the bottom of the conduction band relative to the vacuum energy, which may be estimated by combining the Fermi level and work function of the metal in question.

$$-E_0 = \phi + E_F \quad (1-17)$$

Similarly to how the physical and chemical properties of an element is determined by the electronic structure of the outermost electron shell, the electrical properties of a bulk material are mostly determined by the location of the Fermi level relative to a material's electron band structure. When two conductive surfaces of differing work functions are brought into contact there is initially a discontinuity in Fermi level across the interface. It therefore becomes energetically favourable for electrons to reduce their free energy and travel from the high energy states of the surface with the lower work function into the counter-

surface where they are able to relax into lower energy states. This localised transport of electrons causes the build-up of the charge double-layer initially proposed by Volta. The Fermi levels of the two surfaces are locally perturbed where this charge transport occurs until thermodynamic equilibrium is achieved and the Fermi level is a constant value across the interface. The presence of the charge double-layer also shifts the electrostatic potential across the interface and creates a potential difference known as a Volta potential as shown in Figure 1-2. This Volta potential is also known as a contact potential difference (CPD) and can be expressed by Harper (Harper, 1951b) as a function of the difference in work function between the two contacting metals as shown in (1-1).

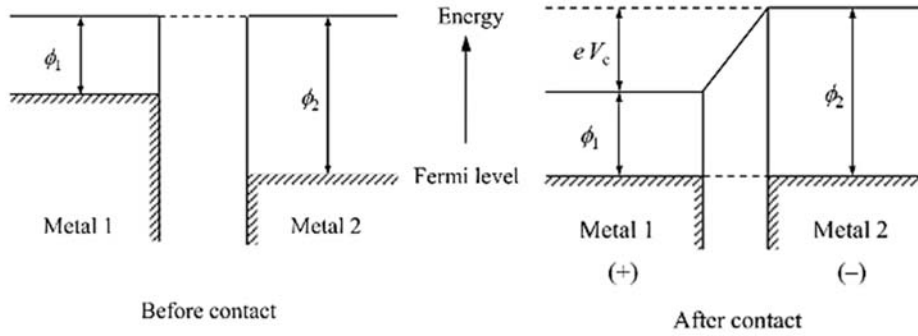


Figure 1-2 - Electron potential energy at a metal-metal contact as depicted by Matsusaka (Matsusaka and Masuda, 2003).

The equation (1-1) proposed by Harper is based on experimental observations and is dependent on two primary assumptions. These assumptions are that the state densities with respect to energy are constant, and that they are equal between both surfaces. Whilst these assumptions allow for good estimates of charge transfer to be made, the influence of state densities becomes increasingly important when considering semi-metals and non-metals. It is possible to derive an equation from first principles for estimating the total amount of charge transferred between two contacting metals via contact electrification. Firstly, only electrons within the conduction band of metals are considered, and are treated collectively as a Fermi gas in accordance with equations (1-15) and (1-16). The total carrier density (n) at a given energy in a surface is given by multiplying the state density at that energy by the probability that those particular states are filled.

$$n(E) = g(E)f(E) \quad (1-18)$$

Therefore the total spatial carrier density (n) within a material (i) is given by integrating this value over all possible energy values.

$$n_i = \int g_i(E)f_i(E) dE \quad (1-19)$$

And of course, the total number of electrons within the material is given by integrating this density across the entire volume V of material.

$$N_i = \int \int g_i(E)f_i(E) dE dV_i \quad (1-20)$$

Since the dimensions of this particular system are not currently being considered, it is favourable to use the terminology of densities for the time being. If the total number of electrons within a two surface system (denoted surfaces A and B) is conserved during contact electrification, the averaged spatial electron density will also remain constant and the following equation can then be derived.

$$\int g_A(E)f_A(E)dE + \int g_B(E)f_B(E)dE = \int g_A(E)f_A'(E)dE + \int g_B(E)f_B'(E)dE \quad (1-21)$$

$g_i(E)$ is the density of states per unit volume per unit energy, and $f_i'(E)$ and $f_i(E)$ are the perturbed and unperturbed Fermi-Dirac distributions respectively. The perturbed Fermi-Dirac distributions arise from the injection of charges causing the perturbations in Fermi level of each surface. This relationship can be simplified through the assumption that the Fermi level of a surface is approximately equal to the Fermi energy relative to the lowest energy state in the conduction band, rather than relative to any vacuum state. This implies that the process of contact electrification is occurring at or close to absolute zero temperature. The more accurate term for describing this variation of Fermi level is the 'internal chemical potential' or 'chemical potential' rather than 'electrochemical potential' in terms of the previously described terminology. At absolute zero temperature, the Fermi-Dirac distribution is simply a step function that transitions discontinuously from a value of 1 to 0 at the Fermi level. This allows for the relationship (1-21) to be altered from a combination of infinite integrals to finite integrals within set energy windows.

$$\int_0^{E_{FA}} g_A(E)dE + \int_0^{E_{FB}} g_B(E)dE = \int_0^{E_{FA}'} g_A(E)dE + \int_0^{E_{FB}'} g_B(E)dE \quad (1-22)$$

E_{Fi}' is the perturbed Fermi energy accounting for either a gain or loss of electrons. It can be expressed as the original Fermi energy of the material, perturbed by a value of ΔE_{Fi} .

$$E_{Fi}' = E_{Fi} + \Delta E_{Fi} \quad (1-23)$$

After triboelectric charge transfer has concluded, it is assumed that the Fermi levels of the two materials become aligned. Since the Fermi levels in this particular model are described as relative to the conduction band minimum, and equal to the Fermi energy, their values will not be equal. In order to better describe the nature of the perturbed state of the interface, a new parameter ϕ' is assigned as the final perturbed electrochemical potential for both surfaces relative to the original vacuum potential. This value can be calculated in terms of the work function of either surface and its respective perturbation in Fermi energy.

$$\phi' = \phi_i - \Delta E_{Fi} \quad (1-24)$$

Since the total electron density of a material can be calculated using equation (1-16), equation (1-22) can then be expressed in terms that can be either measured or estimated from first principles using the energy relationship given in equation (1-24).

$$\frac{3\pi^2}{m_u} \left(\frac{\hbar^2}{2m_e} \right)^{3/2} \left(\frac{\rho_A X_A}{A_A} + \frac{\rho_B X_B}{A_B} \right) = (\phi_A + E_{FA} - \phi')^{3/2} + (\phi_B + E_{FB} - \phi')^{3/2} \quad (1-25)$$

Since the unperturbed work function of each material can be measured using a variety of techniques (Eastment and Mee, 1973; Wojciechowski, 1997; Melitz et al., 2011) and values for all other constants

are attainable from first principles, this equation can then be solved for ϕ' using a binomial expansion. The new vacuum potential can then be calculated using the perturbations of both material fermi levels.

$$q_e V = \Delta E_{F_A} - \Delta E_{F_B} \quad (1-26)$$

The total number of electrons transferred ($n_{e\rightarrow}$) and the respective charge density of resulting excess charge on either surface (ρ_q) can also be calculated using parameters from either material.

$$\begin{aligned} n_{e\rightarrow} &= |n_A(E_{F_A}') - n_A(E_{F_A})| \\ &= |n_A(E_{F_A} + \phi_A - \phi') - n_A(E_{F_A})| \\ &= |n_B(E_{F_B} + \phi_B - \phi') - n_B(E_{F_B})| \end{aligned} \quad (1-27)$$

Figure 1-3 provides a visual representation of this particular model for electron transport, using Aluminium and Gold as example materials and their respective properties listed in Table 1.

Table 1 – Measured material parameters and calculated triboelectric interfacial properties of an Aluminium-Gold contact

	<i>Aluminium (Al₁₃)</i>	<i>Gold (Au₇₉)</i>
A (u)	26.98 ^a	196.97 ^a
X	3 (3s ² 3p ¹)	1 (6s ¹)
ρ (kg m ⁻³)	2710 ^b	19300 ^b
ϕ (eV)	4.08 ^c	5.10 ^c
n (m ⁻³)	1.63e ²⁹	5.90e ²⁸
E_F (eV)	11.73	5.54
E_0 (eV)	-15.81	-10.64
ΔE_F (eV)	-0.41	+0.61
ϕ' (eV)	4.49	
$n_{e\rightarrow}$ (m ⁻³)	9.7e ²⁷	
ρ_q (C m ⁻³)	1.55e ⁹	
$\langle d \rangle$ (μm) ^d	26	

^a relative atomic masses taken from (International Union of Pure and Applied Chemistry. Commission on Atomic Weights., 1976), ^b mass density values taken from (Cramer, 2005), ^c work function values taken from (Derry et al., 2015), ^d the average separation of transferred electrons within each surface is estimated by taking the inverse of the cube root of $n_{e\rightarrow}$.

The particular solution for ϕ' in equation (1-25) is only solvable graphically without an extensive derivation. Therefore, this equation can be reduced to that used by Harper by following the assumption that the electron state densities of both surfaces are identical and constant with respect to energy. If only

the latter part of these assumptions is made, the following equation is derived to estimate the perturbed work function and transferred charge.

$$\phi' = \frac{n_A \phi_A + n_B \phi_B}{n_A + n_B} \quad (1-28)$$

$$n_{e \rightarrow} = n_A(\phi_A - \phi') = n_B(\phi_B - \phi') \quad (1-29)$$

If the entire assumption is made then equations (1-28) and (1-29) are further simplified.

$$\phi' = \frac{\phi_A + \phi_B}{2} \quad (1-30)$$

$$n_{e \rightarrow} = n \left(\frac{\phi_A - \phi_B}{2} \right) \quad (1-31)$$

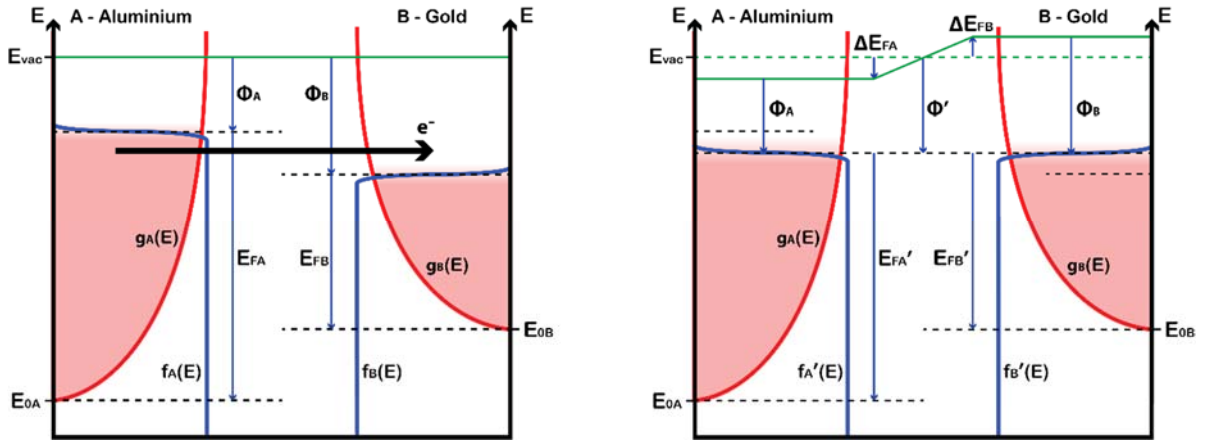


Figure 1-3 – Energy diagram for electron transport across an Aluminium-Gold contact. Denoting the electron state densities ($g_i(E)$, red lines), unperturbed and perturbed Fermi Dirac distributions ($f_i(E)$ and $f_i'(E)$ respectively, blue lines), vacuum state energies (E_{vac} , green line), conduction band ground state energies (E_{0i}), work functions (ϕ_i), Fermi energies (E_{Fi}) and Fermi energy / vacuum potential perturbations (ΔE_{Fi}) of the donor (D) and acceptor (A) surfaces, in addition to the final balanced electrochemical potential (ϕ') across the contact.

If the two contacting metals are otherwise electrically isolated, transferred charges are retained within their respective metals upon the separation of their surfaces, much like with Bose's prime conductor. During the process of separation, a number of electrons are able to back-tunnel across the gap between the surfaces as it becomes energetically favourable for them to do so. When the two surfaces reach a critical separation distance (C_0) this tunnelling ceases and the remaining excess charges are spread out across the metal surfaces to minimise their free energy. The amount of remaining charge upon separation (Q_s) is proposed as being equal to the product of the CPD and the capacitance between the two surfaces at the critical separation distance (Lu et al., 1975).

$$Q_s = C_0 V_{CPD} \quad (1-32)$$

This value of charge in principle also depends on the rate at which the two surfaces are being separated. However, this dependency is proven to be insignificant for practical purposes since the tunnelling resistance has been proven to increase at a considerably faster rate than at which the contact capacitance decreases (Young et al., 1971).

Experimental results by Harper also show less transferred charge in such contacts than what is predicted by this theory. The difference is hypothesised to be caused by factors such as surface roughness, impurities, oxidized layers and other tribological properties (Harper, 1951a; Matsusaka and Masuda, 2003) and will be further explained in section 1.5 Contributing Factors.

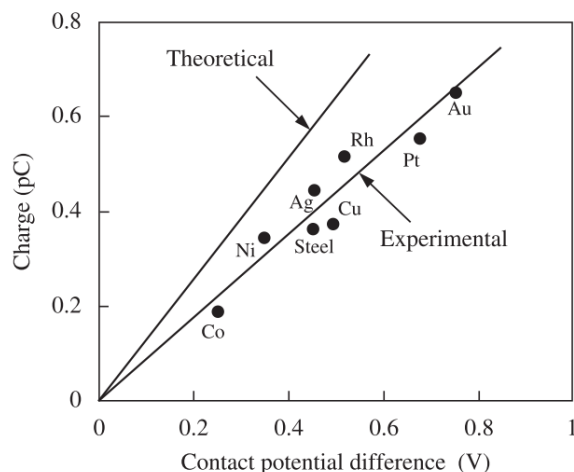


Figure 1-4 - Charge on a chromium sphere - 4mm in diameter - in contact with another sphere - 13mm in diameter - as a function of the CPD of chromium against each metal as stated and depicted by Harper (Harper, 1951a).

1.4.1.c Ultraviolet Photoelectron Spectroscopy

The work function of a surface can be measured experimentally in several ways. The most common method for measuring the work function of a surface is through ultraviolet photoelectron spectroscopy (UVPES / UPS) (Kim, 2019). Through this methodology, the surface is bombarded with ultraviolet photons of a specific energy in order to excite and liberate electrons from the highest occupied surface states. The resulting kinetic energy of these free electrons are measured during this process through the application of a varying voltage between the sample and a collector electrode and measuring the resulting current. The kinetic energies of the photoelectrons (E_K) are a function of the energy of incident light ($\hbar\omega$) and the energy barrier they must overcome in order to leave their surface (E_i).

$$E_K = \hbar\omega - E_i \quad (1-33)$$

As the external voltage is increased, electrons of increasing kinetic energy become turned away from the collector before reaching it and are returned to the sample surface. The electrons with the highest kinetic energy will have been liberated most easily from the sample surface. Therefore, the lowest voltage that can be applied where no current is detected between the sample and collector is known as the cut-off potential ($V_{cut-off}$). This potential represents the kinetic energy of electrons liberated from the highest possible occupied energy state in the sample surface. This state is often referred to as the highest occupied molecular orbital (HOMO) for molecules and larger molecular structures.

$$E_{K_{max}} = q_e V_{cut-off} \quad (1-34)$$

This energy value can then be correlated to the energy of the state it was first liberated from (E_{HOMO}) by subtracting it from the energy of the incident ultraviolet photons.

$$E_{HOMO} = \hbar\omega - q_e V_{cut-off} \quad (1-35)$$

E_i is the energy of an arbitrary state which an electron has been liberated from, relative to the vacuum, which E_{HOMO} takes the maximum value of. This methodology may also be implemented in a way that the frequency of the incident photons is adjusted rather than the bias voltage. This would make the resulting electron current in the absence of a voltage bias dependent on the total number of states that electrons are being liberated from, which in-turn would allow for the determination of state densities with respect to energy values. It is worth noting that the energy value of the highest occupied state relative to the vacuum state is not an accurate representative of the thermodynamic work function for materials which have their Fermi levels situated within an energy band gap, such as insulators and semi-conductors (Helander et al., 2010).

The ultraviolet photons used in UVPES have historically been generated through gas discharge lamps such as the deuterium arc lamp (Boehm et al., 2017), which is restricted to specific spectral line energies between 10.20 – 40.81 eV. UVPES has however recently seen a revival owing to the increasing availability of synchrotron light sources, capable of generating monochromatic ultraviolet photons for a wide range of energies (de Jong et al., 2006; Li et al., 2013). A similar principle can be used to analyse the kinetic energies of emitted electrons using a hemispherical electron energy analyser. This analyser creates a homogeneous electric field that propagates along a hemispherical path. Electrons enter this field and are deflected along this path. The extent to which they are deflected is dependent on their initial kinetic energies, therefore allowing for a wide range of energies to be directly measured (Tusche et al., 2019).

Ultraviolet photons normally are only able to penetrate ~10 nm into the sample surface, which makes them ideal for determining surface properties for triboelectric applications. A similar methodology known as X-ray photoelectron spectroscopy (XPS) is used to determine the nature of lower energy core electron states, as well as at higher surface penetration depths (Girardeaux and Pireaux, 2021).

UVPES has historically only been performed on conductive surfaces, due to the requirement of measuring an electron current between the sample and collector. This current also serves to replenish any states vacated by photoelectric emission. For insulating surfaces, a more complex approach is required. An electron emitter is often used to directly replenish any vacated states with incident electrons, rather than solely by the application of an external electric field (de Jong et al., 2006).

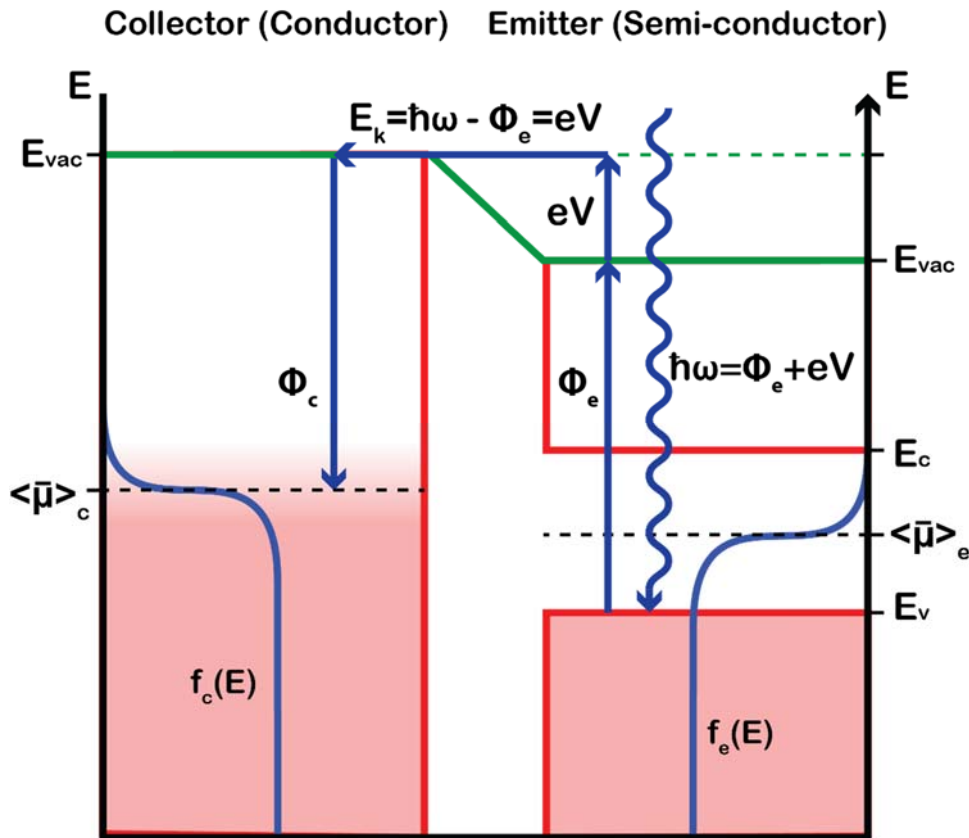


Figure 1-5 – Illustrating the mechanisms that underlie ultraviolet photoelectron spectroscopy, using a metal collector material and a semi-conductor emitter. Depicting an incident photon of energy $\hbar\omega$ equal to the work function of the emitter material (ϕ_e) plus the kinetic energy of the resulting emitted electron (E_k). The electric potential in the vacuum (eV , green line) is equal to the cut-off voltage (V) multiplied by the electron charge (e), which in turn is equal to the highest attainable kinetic energy for the emitted electrons.

1.4.1.d Thermionic Emission Spectroscopy

It is also possible to measure the energies of these states through a separate physical phenomenon known as thermionic emission. Thermionic emission is the phenomenon of thermal excitations providing electrons with enough energy to essentially 'evaporate' out of their surface states and into the surrounding vacuum. This form of thermal electron emission is also referred to as the Edison effect. Thermionic emission generally only occurs from materials in excess of 1000 K, where the average thermal energy ($k_B T$) of electrons is closer in value to that of the work function, and the Fermi-Dirac distribution allows for electron energies higher than the work function to be occupied. Therefore, this form of work function measurement is generally conducted for materials that can remain in their solid phase at these high temperatures. The work function of a material through thermionic emission is measured using an apparatus known as a thermionic diode. This device comprises of a heated emitter surface and a cooler collector surface, separated by a vacuum and subjected to an external electric field. As electrons are evaporated from the emitter surface, the electric field guides them across the vacuum into the collector surface and a current is observed between the collector and emitter. The measured electron current density can then be used to calculate the work function of the emitter surface using Richardson's Law as below (Racko et al., 1996).

$$J_E = -\lambda_R A_0 T_E^2 e^{-\phi_E/k_B T_E} \quad (1-36)$$

$|\vec{J}_E|$ is the magnitude of electric current density per unit area of the emitter surface in Am^{-2} , λ_R is the dimensionless material specific correction factor for the emitter, T_E is the temperature of the emitter in Kelvin, ϕ_E is the work function of the emitter in Joules, and A_0 is a universal constant often referred to as the 'Richardson constant', expressed below.

$$A_0 = \frac{4\pi m_e k_B^2 q_e}{h^3} \quad (1-37)$$

A reverse-bias electric, field similar to the field utilised in UVPES, can be applied to this apparatus as a way of instead measuring the work function of the collector surface. Since the energy barrier experienced by the free electrons is now dependent on the work function of the collector surface, rather than that of the emitter, equation (1-36) changes to a new form as stated below.

$$J_E = -A_0' T_E^2 e^{(\phi_C - q_e V_0)/k_B T_E} \quad (1-38)$$

A_0' becomes a Richardson-type constant that is dependent on the properties of both emitter and collector, ϕ_C is the work function of the collector, and V_0 is the applied voltage between the emitter and collector. This method for measuring work function is preferable, as it does not require the material being measured to be heated.

1.4.1.e Atomic Force Microscopy Methodologies

The atomic force microscope (AFM) is a flexible system that utilises a mechanical probe comprised of a nanoscale tip attached to a microscale cantilever to probe various sample properties on the nano- and picoscale. Atomic force microscopy is frequently used for the measurement of nanoscale electrostatic charges through electrostatic force microscopy (EFM). It is also implemented for the measurement of surface potentials and tip-sample contact potentials through Kelvin probe force microscopy (KPFM). KPFM is a technique used to measure the difference in work functions between contacting materials, rather than absolute values for work function for either material (Melitz et al., 2011).

This system provides a considerably higher spatial resolution for measurements that go beyond the diffraction limit for optical and electron-based measurement systems. The AFM can operate in one of three main modes; contact mode, intermediate (tapping) mode, and non-contact (lift) mode. In contact mode the AFM tip is in constant contact with the sample surface. The tip presses down on the sample surface and the tip cantilever is deflected upwards by the tip-sample repulsive force. This cantilever deflection is monitored and used to provide a feedback signal for re-adjusting the height at which the AFM probe is located above the sample. This feedback loop allows for the tip to exert a constant force onto the sample surface by retaining a constant level of cantilever deflection. In intermediate and non-contact AFM modes, the AFM tip is oscillated mechanically at its primary resonant frequency and at a particular amplitude set-point using a piezoelectric element. As the average tip-sample distance changes, the changes in tip-sample interaction cause differences in the oscillation amplitude (intermediate mode) and frequency (non-contact mode) of the tip.

These changes in amplitude and frequency – in a similar fashion to in contact mode – are used as feedback signals to maintain a constant tip-sample distance and to obtain the topography of the sample surface. Intermediate (tapping) mode and non-contact mode are often referred to as amplitude modulated (AM) and frequency modulated (FM) for certain AFM applications.

In intermediate mode and AM non-contact mode, the oscillation amplitude of the tip would increase with sample-tip distance as a result of the decrease in sample-tip interaction. Since the amplitude change is generally accepted as being dependant on the tip-sample interaction force, amplitude modulated (AM) measurements such as these represent the direct force between the tip and the sample (García and Pérez, 2002; Giessibl, 2003).

In FM non-contact mode, an increase in tip-sample separation would lead to a decrease in oscillation frequency. This change in frequency is dependent on the tip-sample force gradient when the cantilever restoring force associated with the tip oscillating energy is large in comparison to the tip-sample interaction force (Albrecht et al., 1991; Giessibl, 2003). This characteristic of frequency modulated (FM) measurements generally grant a higher spatial resolution than AM measurements, at the expense of having a lower sensitivity.

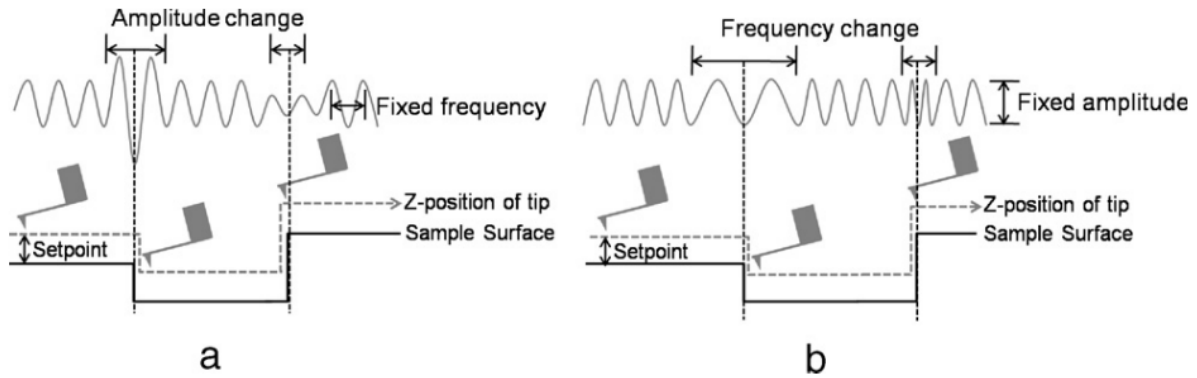


Figure 1-6 – Schematic description of amplitude modulated (a) and frequency modulated (b) non-contact mode AFM and their respective feedback systems for mapping topography and maintaining a constant sample-tip separation as depicted by (Melitz et al., 2011).

The spatial resolution and sensitivity of an AFM measurement is dependent on the quality factor (Q) of the cantilever being used. The quality factor is a measurement of the ‘sharpness’ of a cantilever’s resonant frequency peaks, which indicates the amount of energy lost through oscillation.

$$Q = \frac{f_0}{\Delta f} \quad (1-39)$$

Where f_0 is the resonant frequency of the cantilever and Δf is the full-width-half-maximum frequency bandwidth of the resonant peak. The Q factor of a cantilever is also dependant on the medium that the cantilever is oscillating in. For example, a cantilever operating within a vacuum would have a considerably higher Q factor than a cantilever operating in air; and even more so than one operating within a dense fluid (Giessibl, 2003). The minimum force (F_{min}) that can be detected by an AFM is determined by the resonant properties of the cantilever and the ambient thermal energy.

$$F_{min} = \sqrt{\frac{2k_s k_B T B \cdot \Delta f}{f_0^2 \langle z_{osc}^2 \rangle}} \quad (1-40)$$

Where k_s represents the spring constant of the cantilever in Nm^{-1} , $k_B T$ represents the ambient thermal energy for the measurement, B is specifically the measurement bandwidth in the context of this equation, f_0 is the resonant frequency of the AFM cantilever and Δf is the full-width-half-maximum frequency change for the resonant peak, and $\langle z_{osc}^2 \rangle$ is the mean-square amplitude of the driven cantilever vibration (Albrecht et al., 1991).

1.4.1.e.i Lateral Force Microscopy

Lateral force microscopy (LFM) is a form of AFM derived from contact mode. In addition to measuring the vertical distortion of the cantilever to map the topography of a sample, the lateral distortion of the cantilever is measured to determine surface friction characteristics when a tangential force is applied to the tip whilst in contact with the sample. LFM allows for an atomic force microscope to be used as a nanoscale tribometer, correlating surface topography and friction characteristics in two dimensions. This particular method of atomic force microscopy can theoretically be used to charge surfaces through nanoscale contact electrification, and as a result could potentially be used to correlate friction and triboelectric charge transfer when used in parallel with a methodology for measuring the deposited tribo-charges. LFM has previously been used with strong SiN AFM tips – with spring constants (k_s) of several hundred Nm^{-1} – to even wear down sample surfaces and deposit tribofilms onto surfaces when performed within certain additive containing fluids (Dorgham et al., 2019).

1.4.1.e.ii Electrostatic Force Microscopy

EFM and other electrical characterisation AFM methods require the use of a conductive AFM tip, and various types of conductive tip are commercially available. Most of these conductive tips are composed of or coated with Platinum; with a minimal amount of Iridium dopant to increase their hardness. Cheaper Cobalt-Chromium tips are available, and even diamond-coated Aluminium probes have been used for electrodynamic AFM applications (Sadewasser and Barth, 2012).

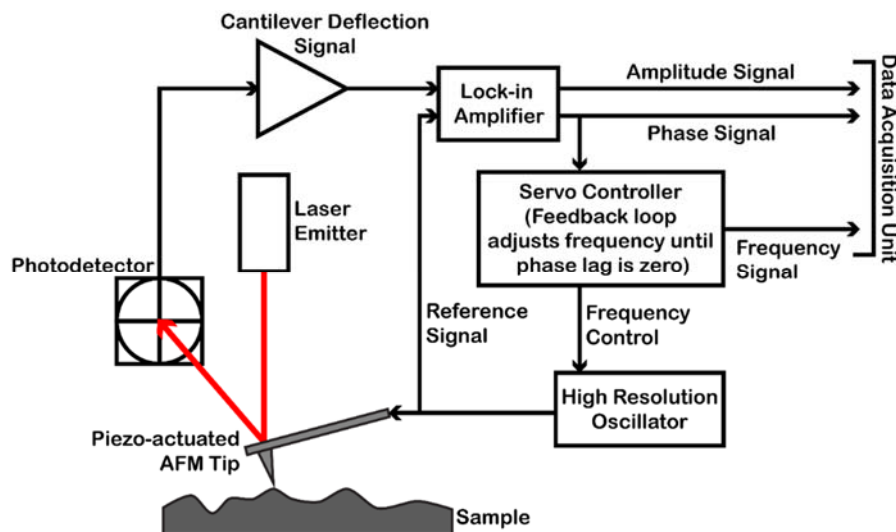


Figure 1-7 – Schematic diagram for an AFM system configured for EFM measurements.

EFM in specific is used to directly measure the force exerted on the AFM tip by the electric field emanating from the sample surface. The general procedure for EFM measurements involve using the conductive cantilever in non-contact mode (Qiu et al., 2008). Any difference in surface potential or presence of surface charges will change the resonant frequency of the AFM tip and resulting phase of the cantilever oscillation. These changes in phase are measured directly rather than through amplitude or frequency modulation. EFM measurements are primarily used to analyse samples with a low surface roughness and substantial changes in surface potential such as nanoscale electronics. The downside of EFM measurements is that topographical features have the potential to interfere with surface potential measurements.

Some AFM systems – such as the Bruker Dimension Icon – require a two-pass process for these measurements – often known as interleave scanning or ‘LiftMode’. This involves the AFM tip first being scanned across the surface of the sample in tapping mode to acquire topographical data. These data are then used to maintain a constant tip-sample distance whilst performing the electronic and magnetic portion of the measurement scan.

1.4.1.e.iii Kelvin Probe Force Microscopy

First devised in 1991 by Nonnenmacher et al. (Nonnenmacher et al., 1991), Kelvin Probe Force Microscopy (KPFM) has been used as a tool to map the surface potentials for a broad range of conducting and semi-conducting materials on the nanoscale. In principle it measures the contact potential difference (CPD) between the conductive AFM tip and the sample (Melitz et al., 2011). KPFM measurements work in an inverse sense to EFM. Instead of mechanically oscillating the conductive tip above the sample surface, an AC voltage (V_{AC}) is applied to the cantilever at its resonant frequency ($f_0 = \frac{\omega_0}{2\pi}$). The cantilever is treated as a reference electrode that forms a capacitor with the sample surface. The magnitude of the electric field forming between the tip and sample can be described as below.

$$|\vec{E}| = \frac{1}{2} C (V_{CPD} + V_{AC} \sin(\omega_0 t))^2 \quad (1-41)$$

where C is the effective capacitance between the sample and the tip. When a DC potential difference develops between the tip and the sample – arising from a difference in CPD or the presence of surface charges – the AC+DC offset voltage causes the cantilever to mechanically resonate with V_{AC} . The factor contributing to this resonant cantilever oscillation can be found by expanding the voltage terms of the electric field.

$$|\vec{E}_{\omega_0}| = \frac{1}{2} C \cdot V_{CPD} V_{AC} \sin(\omega_0 t) \quad (1-42)$$

This vibration is detected and nullified using a feedback loop to drive its own DC potential between the tip and sample. The total voltage acting between the tip and sample is therefore as shown below.

$$V = (V_{CPD} - V_{DC}) + V_{AC} \sin(\omega_0 t) \quad (1-43)$$

The resulting force acting on the cantilever can therefore be calculated.

$$F = \frac{1}{2} \frac{dC}{dz} V^2 \quad (1-44)$$

Where dC/dz describes how the effective capacitance changes with tip-sample separation (z). Expanding the voltage terms for this force yields the following equations.

$$F_{DC} = \frac{1}{2} \frac{dC}{dz} \left((V_{DC} - V_{CPD})^2 + \frac{1}{2} V_{AC}^2 \right) \quad (1-45)$$

$$F_{\omega_0} = \frac{dC}{dz} (V_{DC} - V_{CPD}) V_{AC} \sin(\omega_0 t) \quad (1-46)$$

$$F_{2\omega_0} = -\frac{1}{4} \frac{dC}{dz} V_{AC}^2 \cos(2\omega_0 t) \quad (1-47)$$

These three contributions to electrostatic force can be used for different purposes, the DC component is used for measuring topography, whereas the ω_0 component is used for CPD measurement and the $2\omega_0$ can be used for capacitance microscopy. A lock-in amplifier is used at ω_0 to detect any resonant cantilever oscillation, this oscillation is then nullified by adjusting V_{DC} . If V_{DC} is adjusted such that it becomes equal to the negative of V_{CPD} , then the only mechanical response of the cantilever will be oscillations at $2\omega_0$ in accordance with (1-47). Therefore the value for V_{CPD} can be directly measured through careful selection of V_{DC} value.

KPFM measurements can either be amplitude or frequency modulated. AM-KPFM measurements generally use interleave scanning whereas FM-KPFM measurements can use a single-pass technique. This technique uses non-contact mode AFM measurements at ω_0 to provide feedback and maintain a constant tip-sample distance. The AC voltage required for KPFM measurements is also applied, but instead it is either at a frequency near to ω_0 or at a separate resonant or harmonic frequency (ω_2) to the one used for mechanical oscillation.

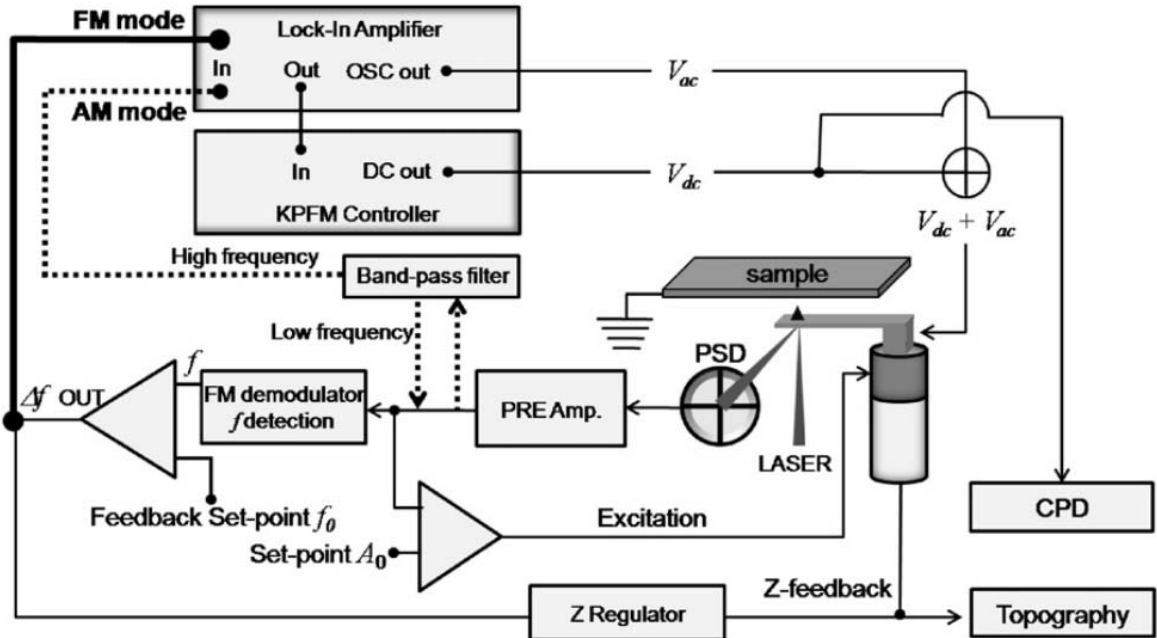


Figure 1-8 – Schematic diagram of an AFM system for both AM (bold line) and FM (dotted line) KPFM measurements. The lower section is an FM system for mapping topography and the upper section is the KPFM system for surface potential measurements (Melitz et al., 2011).

1.4.1.f Semi-metals, Semi-conductors, and Insulators

The phenomenon of triboelectric charge transfer between semi-conductors and insulators is notably more difficult to model than for conductive contacts. As previously mentioned, the conductivity of a material is partly determined by the electron state density at its Fermi level. For the case of semi-conductors and insulators, the Fermi level is situated directly between two energy bands, within a band gap, at a level where there are no available electron states. This feature loosely explains why electrons are unable to move freely through such materials under normal circumstances. The more accurate explanation is that electrons within a fully filled energy band have a net zero momentum (\vec{p}) under an applied electric field (\vec{E}), meaning they do not contribute to electron conduction. If electrons are to propagate through a material in response to an applied electric field, then there must be unoccupied states which these electrons can transition into in order to change their momentum. If no states are available, then the electrons simply remain in their original states. The highest energy band that has all of its available states occupied with electrons is known as the valence band. The energy band located directly above the valence band is referred to as the conduction band, and is where the Fermi level is situated in conductors. Since the conduction band is only partially filled in semi-metals and conductors, a non-zero net momentum is exhibited under the application of an applied electric field, and an electric current is therefore permitted.

Semi-metals are a similar class of materials to conductors with the important distinction that in semi-metals the Fermi level is usually situated at an overlap between two energy bands. Very few states are available at the Fermi level within a semi-metal due to this location, which often makes semi-metals poor electrical conductors. Semi-conductors are insulators where the Fermi level is situated within a narrow band gap. This allows for external influences such as thermal excitation and electric potentials to excite electrons from the valence band into the conduction band. A visual depiction of these differing electronic structures is given in Figure 1-9.

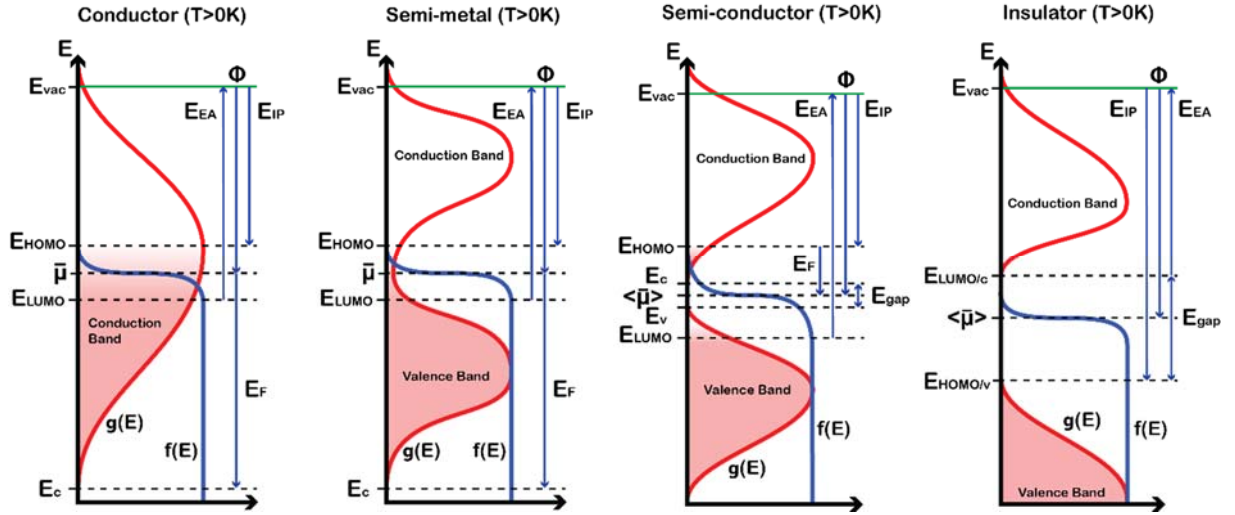


Figure 1-9 – Energy band diagrams for an example conductor, semi-metal, semi-conductor, and insulator at an arbitrary non-zero temperature. Denoting the vacuum energy (E_{vac}), state density ($g(E)$), Fermi-Dirac distribution ($f(E)$), Fermi level ($\langle\bar{\mu}\rangle$), Fermi energy (E_F), work function (Φ), ionisation potential (E_{IP}), electron affinity (E_{EA}), highest occupied molecular orbital (E_{HOMO}), lowest unoccupied molecular orbital (E_{LUMO}), conduction band bottom (E_c), valence band top (E_v), and band gap energy (E_{gap}). Note that the example semi-conductor purposefully exhibits an unusually small band-gap and in some situations may be considered a semi-metal, allowing for valence electrons to be thermally excited into the conduction band.

An important aspect of band structure is that the energies of states also have associated momenta. Example band structure diagrams for a semi-metal and two separate forms of semi-conductor are given in Figure 1-10. It is important to note that momentum in solid-state physics is usually expressed in terms of an angular wave-vector (\vec{k}) through the de Broglie relation.

$$\vec{p} = \hbar \vec{k} \quad (1-48)$$

This definition relates to the particle-wave duality of matter, and is treated as the spatial angular frequency of the plane wave wavefunction that represents the particle in three dimensions.

$$\psi(\vec{r}, t) = \psi_{max} \cos(\vec{k} \cdot \hat{r} + \omega t + \theta) \quad (1-49)$$

ψ_{max} is the amplitude of the plane wave, \hat{r} is the spatial unit vector which is usually expressed in Cartesian coordinates, ω is the temporal angular frequency, and θ in this context is defined as a phase offset. The implication of these momenta is that they must also be considered when investigating electron state transitions. Universal conservation of both energy and momentum must be obeyed as electrons transition between states of differing energies. The consequence of this and its application to triboelectrification is that as electrons are triboelectrically transferred across an interface into lower energy states, they must release this energy through some form of physical interaction. This is often manifested through coulomb interactions with the structure of the acceptor surface, creating quanta of physical vibration and thermal energy known as a phonon. If the electron is able to relax into its acceptor state without significantly changing momentum, it is possible for a photon to be created instead through a form of triboluminescence.

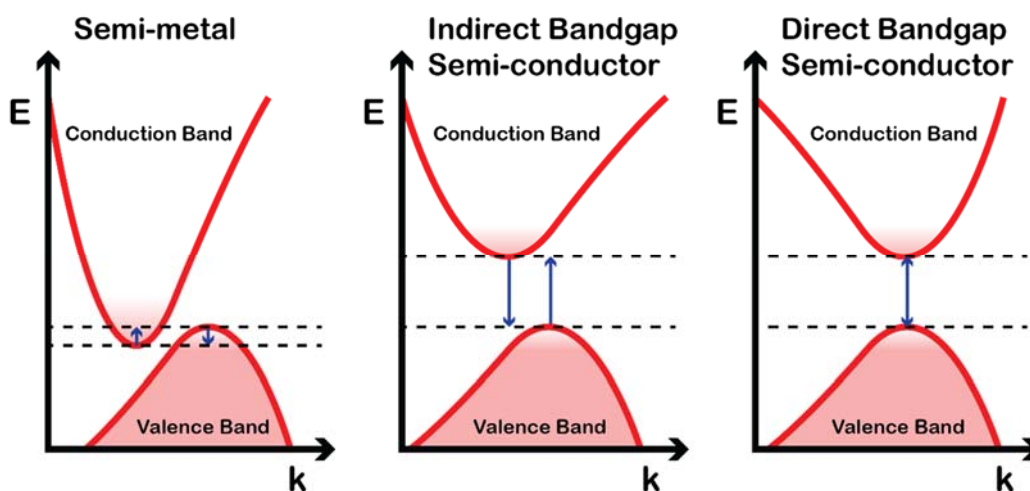


Figure 1-10 – Example energy band structures for a semi-metal, and indirect and direct bandgap semi-conductors plotted as wave-vector against energy.

1.4.1.g Electron Affinity and Electronegativity

Additional properties can be used to describe the electronic nature of materials that are related to their work function. These include electron affinity, electronegativity, and ionisation potential. These properties are all used to generally define how electrons interact with an atomic species or larger material structures. For example, how easy it is for a material to attract or expel free electrons. The work function of a material is closely related to electron affinity (E_{EA} , also referred to as χ), where the electron affinity of a specific atomic species is the change in energy of a neutral atom (X) when an electron (e^-) is added to the atom to form a negative ion (X^-) as depicted in the chemical equation below.



X is used here to denote an arbitrary atomic species. When generalised towards a material, the electron affinity is defined as the energy released when an electron is moved from a vacuum state just outside the surface to the lowest unoccupied state within the surface. The electron affinities of most alkaline earth metals, noble gases, and group 12 transition metals are yet to be measured empirically. The values of these electron affinities are often estimated as negative, implying that energy would be required to add an electron rather than having energy released by the process. The low electron affinities of alkaline earth metals, noble gases, and group 12 transition metals can be attributed to them possessing s, p, and d-type valence shells respectively that are fully occupied.

Electron affinity is also linked to another property known as electronegativity, which also often referred to as χ . Electronegativity is defined as the relative ability of an atom to attract electrons to itself within a chemical compound. The electronegativity of an atom within a given molecule is a dimensionless quantity and is normally measured along the notoriously arbitrary Pauling scale (Murphy et al., 2000). Electronegativity is often intuitively cited as being negatively correlated with electron affinity, as well as being closely linked to the ionisation potential (E_{IP}) of the particular atomic species in question. The ionisation potential, also referred to as the first ionisation energy, of an atomic species is the minimum energy required to remove the most loosely bound electron.

The Mulliken electronegativity scale is a more absolute method of determining the electronegativity of an atomic species through these more fundamental properties. The Mulliken electronegativity of an atomic species can be stated as the negative of its chemical potential, but is also historically expressed as the arithmetic mean of the electron affinity and ionisation potential. This infers that the electron states associated with the Mulliken electronegativity lie between the HOMO and LUMO states, which is a reasonable assumption when the electronic structures of semiconductors and insulators are considered.

$$\chi_{\text{mulliken}} = -\mu_{\text{mulliken}} = \frac{E_{EA} + E_{IP}}{2} \quad (1-51)$$

The electronegativity of an atom is not widely regarded as an effective measurement since it is not a fixed property that can be measured by a single experiment. The electronegativity of an atom can also be strongly influenced by its chemical environment and is therefore treated as more of an interfacial property rather than one of any specific isolated species. The electron affinity of a given material can be expressed in terms of energy levels as the difference between the previously aforementioned vacuum state and the bottom of its conductance band (E_c), described below.

$$E_{EA} = E_{vac} - E_c \quad (1-52)$$

There are several shortcomings to the use of work function in modelling triboelectric charge transfer. The most prominent reason being its relative difficulty to accurately measure for semi-conducting and insulating materials. Since the Fermi level for these materials is situated within an energy band gap, it represents a purely theoretical state with no physical representation other than through the thermodynamic Fermi potential. The work function in reality is also not a concept that can be generalised to being a material property. There are various additional factors that affect the work function of a given chemical environment, which are further explained in 1.5 Contributing Factors.

In previous works (Matsusaka et al., 2010) the charge transfer across insulator–metal contacts is explained by a simulated variation of the metal-to-metal electron transfer. This assigns an ‘effective’ work function (ϕ_I^*) to the insulator or semi-conductor surface. The amount of the transferred charge is determined so as to equalize the energy levels of the two materials, as with conductive contacts. Combining equations (1-1) and (1-32) whilst using this definition of the effective work function yields the following equation for total charge transferred.

$$Q_s = -C_0 \frac{(\phi_I^* - \phi_M)}{q_e} \quad (1-53)$$

ϕ_I^* is the effective work function of insulator and ϕ_M is the work function of metal, both measured in units of Joules. The effective capacitance C_0 is also dependent on the characteristics of the insulator as described by (Matsusaka et al., 2010). Dekker (Dekker, 1960) developed a similar expression to calculate surface charge density (σ) through the integration of Poisson’s equation.

$$\sigma = 1.77 \cdot 10^{-9} \epsilon_I \left(\frac{\phi_I^* - \phi_M}{E_{EA}} \right) \quad (1-54)$$

Where σ is the surface charge density in Cm^{-2} , ϵ_I is the dielectric constant for the insulator and E_{EA} is the electron affinity of the insulator in eV.

The effective work functions of materials have historically been assigned in literature as being in the direct centre of the energy band gap, as this is the ideal case for intrinsic semi-conductors. Unfortunately this is not the reality for most insulators and semi-conductors. In fact, this concept has been long understood in the field of semi-conductor physics. As well as classifying semi-conductors by the momentum orientation of their energy bands it is common practice to chemically alter the structure of semi-conductors as a way of changing their electronic structure and fermi potentials.

The most commonly used material for semi-conductor applications is silicon (Si), a tetravalent crystalline metalloid with a high melting point of 1687 K. The bulk electronic structure of purely crystalline silicon (c-Si) differs from that of amorphous hydrogenated silicon (a-Si:H) in that it possesses a larger energy band gap (Jarolimek et al., 2017). The electronic structure of silicon can further be tailored by the addition of different atomic species to the bulk material.

The addition of pentavalent species such as phosphorus (P), arsenic (As), and antimony (Sb), contributes additional electrons to the system and therefore raises the Fermi level closer to the bottom of the conductance band, creating an n-type semi-conductor. The addition of trivalent species conversely introduces unoccupied orbitals known as 'holes' to the system and lowers the Fermi level closer to the valence band. These dopants usually occur in relatively low concentrations, with 'light' doping being generally classified at around one dopant atom for every 100 million silicon atoms, and 'heavy' doping being described as one dopant atom for every ten thousand silicon atoms.

In an n-type semi-conductor, the introduction of the pentavalent n-type dopant creates a series of occupied valence states close to lowest energy conduction states. At zero temperature these electrons are still part of a filled valence band and therefore do not contribute to conduction. However, at higher temperatures these electrons are now able to be thermally excited into the conductance band and propagate through the material before relaxing back into these valence states. The introduction of these high-energy electrons also raises the Fermi level of the material closer to the conduction band.

Similarly for p-type semi-conductors, the trivalent nature of the dopant means the removal of otherwise available valance states. In the wake of this, a series of unoccupied conduction states are introduced close to the highest energy valence states. Once thermal excitations are introduced, electrons are able to occupy these states and leave behind empty valance states. These vacant states can be treated as positively charged particles known as 'holes' that behave in a similar way to electrons in the conductance band, although exhibiting a different effective mass to them. This removal of valance states and subsequent introduction of low energy unoccupied conduction states lowers the Fermi level of the semi-conductor material. The magnitude of change in the Fermi level of a semi-conductor as a result of carrier injection and doping can be expressed as below.

$$\Delta\bar{\mu} = k_B T \cdot \log\left(\frac{n_{A/D}}{n_i}\right) \quad (1-55)$$

$n_{A/D}$ is the dopant carrier spatial concentration, where A and D represent 'acceptor' p-type hole states and donator n-type excess electron states respectively. n_i is the intrinsic charge carrier spatial

concentration for the un-doped semi-conductor. Typical energy band diagrams for example intrinsic, n-type, and p-type semi-conductors are given in Figure 1-11.

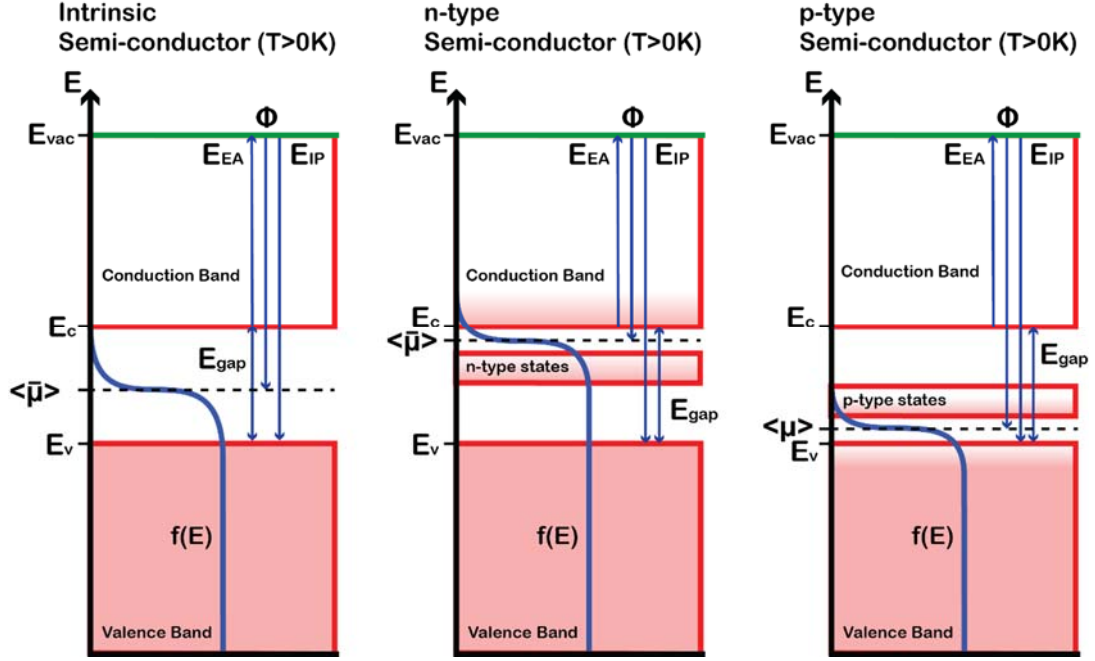


Figure 1-11 – Energy band diagrams for example intrinsic, n-type, and p-type semi-conductors. Denoting the vacuum energy (E_{vac}), Fermi-Dirac distribution ($f(E)$), Fermi level ($\langle \bar{\mu} \rangle$), work function (Φ), ionisation potential (E_{IP}), electron affinity (E_{EA}), conduction band bottom (E_c), valence band top (E_v), and band gap energy (E_{gap}).

When an electron from the valence band of a material is excited into the conduction band a hole is also generated in the form of the vacated valence state. This process is known as electron-hole pair generation and is a constantly reoccurring phenomenon within semi-conductors. These electron-hole pairs then recombine after a time and release the energy of the electron in the form of either a phonon or a photon. Electrons and holes are able to propagate through a semi-conductor material with differing ability, often represented by their respective mobilities (μ_i) and effective masses (m_i^*). The mobility of a charged particle is defined as its ability to move through a medium in response to the application of a driving electric field (\vec{E}), and is represented by the following equation.

$$\langle \vec{v}_d \rangle = \mu_i \vec{E} \quad (1-56)$$

$\langle \vec{v}_d \rangle$ is known as the drift velocity of the particle. It is defined statistically as the average velocity of a collection of particles as they are subjected to separate interactions and collisions.

$$\langle \vec{v}_d \rangle = \frac{\vec{J}}{n_i q_i} \quad (1-57)$$

J is the measured current density travelling through a given cross sectional area of the material. n_i is the three dimensional charge carrier spatial density, which may be calculated for metals using (1-14), and q_i is the electric charge of the carrier in question. These mobilities are related to the effective masses of the charged particles through the nature of the collisions they encounter whilst travelling through a medium.

The acceleration (\vec{a}) that a charged particle experiences in the presence of an electric field is defined as below.

$$\vec{a} = \frac{q_i \vec{E}}{m_i^*} \quad (1-58)$$

As these charged particles propagate through a material they are subjected to collisions. The mean free time (τ_c) that these particles experience between collisions is useful for defining their drift velocity.

$$\langle \vec{v}_d \rangle = \vec{a} \tau_c \quad (1-59)$$

This results in the following alternative definition for carrier mobility.

$$\mu_i = \frac{|q_i| \tau_c}{m_i^*} \quad (1-60)$$

The absolute value of charge is given in order for both electrons and holes to possess positive mobilities. Electrons and holes may normally exhibit effective masses between a factor of 0.1 and 10 times the rest mass of an electron ($m_e = 9.11 \times 10^{-31}$ kg). The interactions between semi-conductors of differing chemical compositions forms the basis of modern computing (Brennan, 2005). With two examples of such applications to the computing and electronics industry being the Zener and the Schottky diodes. Zener diodes are created using the interface between a p-type and an n-type semi-conductor, also known as a p-n junction. Such an interface is usually formed by inhomogeneously doping a single crystal of silicon such that there are two distinct regions of differing electronic structure. This method is preferred to the adhesion of two separate semiconducting bodies, due to the tendency of electrons to be reflected by surfaces and grain boundaries (Feldman et al., 2010).

At the interface, the internal chemical potential is different for electrons on differing sides. Electrons within the n-type silicon region would exhibit a higher internal potential than those on the p-type side, since the n-type side would exhibit a lower work function. As a direct result of this, a discontinuity in electrochemical potential and Fermi level is initially observed across the interface. Since electrochemical potential always strives to be equal everywhere as a means to reach thermodynamic equilibrium, electrons from the n-type region migrate across to fill the vacant states of the p-type region near the interface. This creates what is known as a depletion region across the interface, which normally penetrates between 0.1 – 10 μm into either region (Poole and Darwazeh, 2016). A charge imbalance and resulting ‘built-in’ electric potential (V_{b-in}) then exists across this depletion layer due to this movement of electrons. The magnitude of this potential can be calculated using the intrinsic charge carrier concentrations and the concentrations of both n-type and p-type dopant carriers.

$$V_{b-in} = k_B T \cdot \log \left(\frac{n_A n_D}{n_i^2} \right) \quad (1-61)$$

n_A is the carrier concentration of holes within the p-type region, and n_D is the concentration of excess electrons in the n-type region. The charge double-layer formation and resulting potential is remarkably similar to the quasi-capacitance and CPD across a triboelectric interface of two contact metals, and it plays an important role in modelling the triboelectric behaviour of semi-conductors. Across the depletion

layer of a p-n junction, the band energies of both regions deform in a parabolic fashion and become continuously joined as shown in Figure 1-12.

Zener diodes operate based on a principle known as the Zener effect. Because of the electric potential that forms naturally across a p-n junction, a directional preference for electron transport emerges with a non-ohmic dependence on external voltage. When a forward bias is applied (i.e. a positive voltage ‘anode’ is applied to the p-type region, and vice versa) this applied voltage counteracts the intrinsic V_{b-in} and allows for electrons to migrate from the conduction band of the n-type region into the conduction band of the p-type region more easily. Under a reverse bias, a more significant potential must be applied in order for it to be energetically favourable for electrons in the p-type region to migrate to the n-type conduction band. At and beyond this breakdown voltage the current characteristics of the reverse-biased diode resemble the non-ohmic qualities of the forward-biased diode.

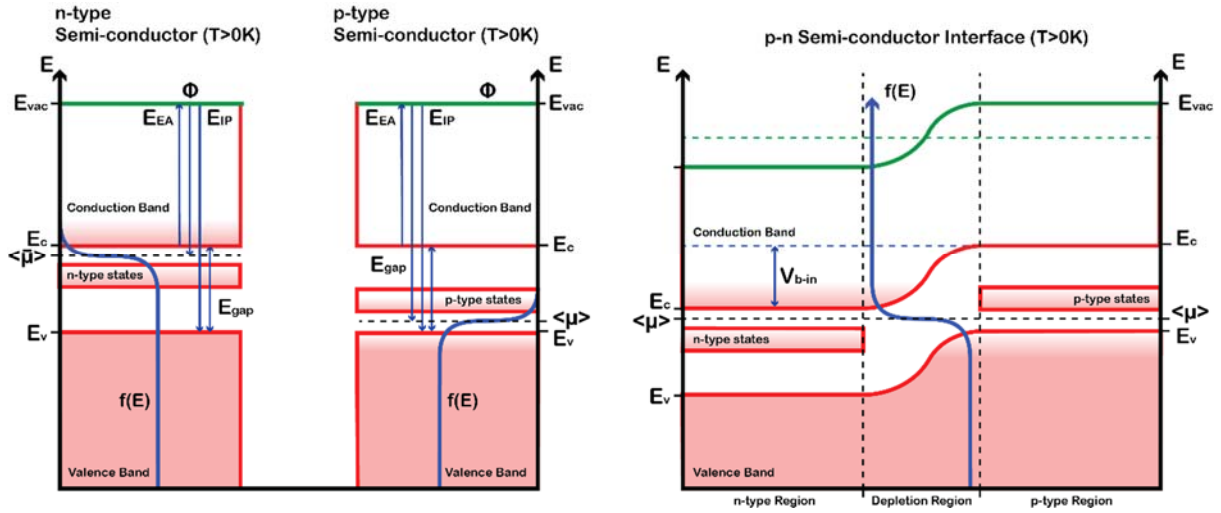


Figure 1-12 – Energy band diagrams for separate n-type and p-type semi-conductors (left), and a p-n junction diode (right). Denoting the built-in potential (V_{b-in}), vacuum energy (E_{vac}), Fermi-Dirac distribution ($f(E)$), Fermi level ($\langle \mu \rangle$), work function (Φ), ionisation potential (E_{IP}), electron affinity (E_{EA}), conduction band bottom (E_c), valence band top (E_v), and band gap energy (E_{gap}).

Schottky diodes operate in a similar fashion to Zener diodes, with the main physical distinction being that the interface is between a metal and a semi-conductor, rather than two distinct semi-conductors. In the vast majority of cases the conductive metal is used in conjunction with an n-type semi-conductor. Schottky diodes behave very similarly to Zener diodes in terms of electronic characteristics under both forward and reverse biases. The built-in potential for a Schottky diode can be estimated using the Schottky-Mott rule (Park et al., 2021).

$$V_{b-in} = \phi_M - \chi_{SC} \quad (1-62)$$

ϕ_M is the work function of the metal, and χ_{SC} is the electron affinity of the semi-conductor. A energy band diagram of an example Schottky diode interface is given in Figure 1-13. The assumption is made that the contact between the metal and semi-conductor is intimate – with no presence of any interstitial layer such as an oxide film – with no inter-diffusion of the two materials and no impurities.

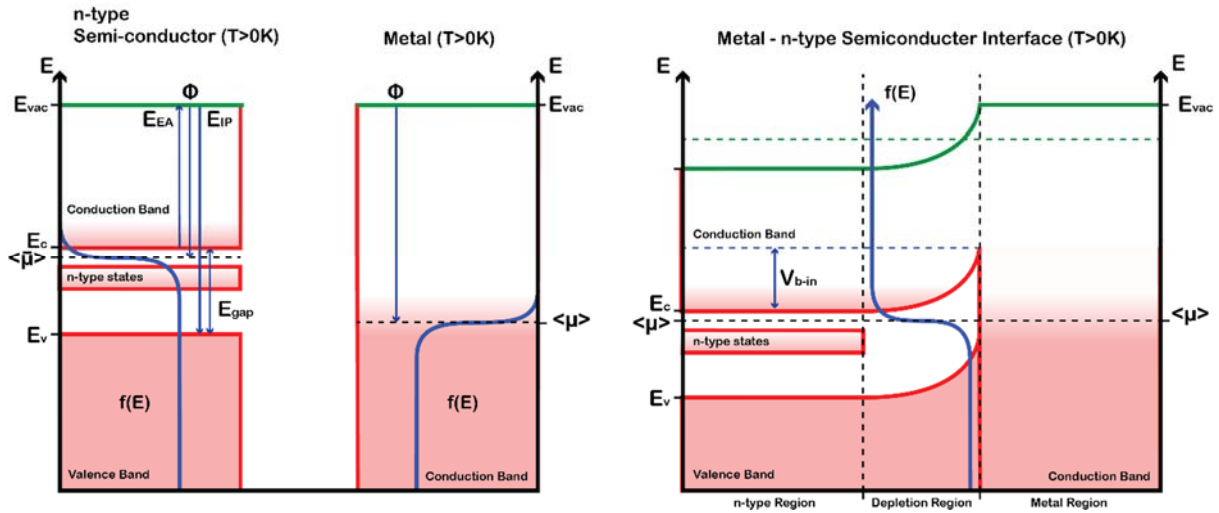


Figure 1-13 – Example energy band diagrams for an n-type semi-conductor and a metal (left), and a Schottky diode (right). Denoting the built-in potential (V_{b-in}), vacuum energy (E_{vac}), Fermi-Dirac distribution ($f(E)$), Fermi level ($\langle \mu \rangle$), work function (Φ), ionisation potential (E_{IP}), electron affinity (E_{EA}), conduction band bottom (E_c), valence band top (E_v), and band gap energy (E_{gap}).

These band theory models provide useful estimations for predicting the electronic behaviour of most materials. Although there are many complicating factors to include when discussing the nature of triboelectric contacts. A limitation of band theory as a method for determining the triboelectric properties of materials is that it is used to model 'single electron states' that describe the behaviour of electrons within a periodical structure. Examples of such structures include metallic monatomic lattices, as well as other crystalline structures such as ionic lattices; or in more complex scenarios, highly oriented polymer chains. This means that only Coulomb interactions between the electron and surrounding nucleons are considered, whereas in reality there are many electron-electron interactions that arise from charge injection and ejection. Additionally, the assumption is made that the overall material structure is static and unmoving. This assumption breaks down when considering that thermal and acoustic phonons are constantly propagating through materials. These phonon interactions cause time-dependent nanoscale deformations that in-turn affect the potentials that electrons experience. Band theory also breaks down in the presence of discontinuities and inhomogeneous structures. Examples of discontinuities are impurities, crystal grain boundaries, atomic dislocations, and surfaces. Examples of inhomogeneity would be residual stresses within the material, as well as gradients in chemical composition imposed by doping and surface treatments.

Another implication of the limitations of band theory is that the Schottky-Mott rule (Park et al., 2021) – whilst correctly predicting the phenomenon of energy band bending within semi-conductor interfaces – fails to agree with experimental measurements of actual Schottky barrier heights (Hasegawa, 1999). The reason for this is a phenomenon known as Fermi level pinning. Fermi level pinning is defined as the locking of the Fermi level for a material relative to its band structure, regardless of the presence of doping or a material interface. This effect is most prominent in Gallium Arsenide (GaAs) semi-conductors (Pashley et al., 1993).

1.4.1.h Surface State Model

As previously stated, the electronic structure of a material at the surface tends to differ from that which is within the bulk (Vick, 1953). This change in structure can be better described through describing the nature of electron wavefunctions that result from the spatial termination of an otherwise perfectly periodic potential. Solving the time independent Schrödinger equation for an electron travelling within an infinitely periodic potential yields an equation for a plane wave modulated by a periodic function, as per Bloch's theorem (1929) of a 'nearly free' electron (Bloch, 1929).

$$\psi(\vec{r}) = e^{i\vec{k}\cdot\vec{r}} U(\vec{r}) \quad (1-63)$$

\vec{r} is the position vector of the particle, i is the imaginary unit of value $\sqrt{-1}$, \vec{k} is the momentum vector of the particle, and $U(\vec{r})$ is a periodic function that represents the potential introduced by a repeating structure. Due to this periodic nature, the different possible wavefunctions of this system are represented in a way such that any repeated values of \vec{k} are omitted. This leads to the definition of a unit cell known as the first Brillouin zone, and represents the smallest cell over which the possible states of a particle can be represented in reciprocal space without redundancy. At values of \vec{k} that exceed the first Brillouin zone, the system can still be treated as being in an equivalent state within it, with a momentum of $\vec{k} - \vec{K}$, where \vec{K} is a reciprocal lattice vector.

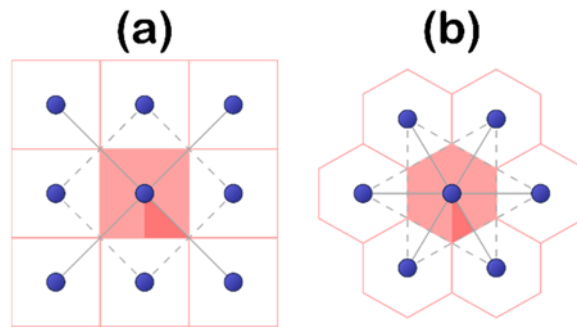


Figure 1-14 - Depicting example Brillouin zones (light red) and irreducible Brillouin zones (dark red) for example 2D square (a) and hexagonal (b) lattices.

Bloch's theorem is incredibly useful for describing the quantum behaviour of electrons within a lattice structure. It however breaks down in the presence of any deviations from perfect periodicity such as defects and terminations. At the surface of a material states can no longer be effectively described by Bloch's theorem and new states arise depending on the nature of the surface. The wavefunctions of bulk states are shown to exponentially decay into the vacuum, and localised surface states are also introduced that decay into both the vacuum and bulk. These surface states are known to possess energy values that lie within energy band gaps of semiconducting bulk materials. However, as a direct result of their mathematical definition they are given imaginary momenta and therefore exponentially decay into the bulk. Surface states can be categorised as either being intrinsic or extrinsic, with intrinsic states originating solely from the termination of the material to the vacuum. The potential represented by the termination of a material at the surface has traditionally been represented by a step function. It is more accurate instead to use a decaying function as a way of representing the Coulomb potential presented by the outermost atomic nuclei. There are two types of intrinsic state that emerge at the surface of materials.

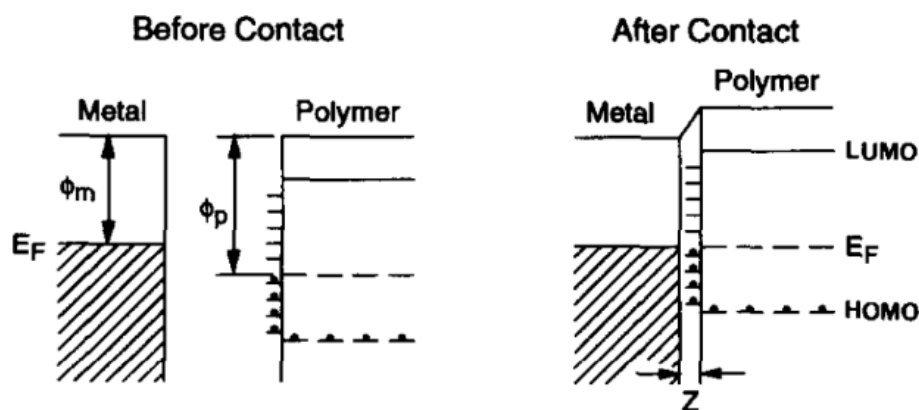


Figure 1-15 – Surface states model for metal-polymer contact charging as shown by Lee (Lee, 1994). ϕ_m and ϕ_p are the work function of the metal and the effective work function of the polymer respectively, LUMO is known as the lowest unoccupied molecular orbital, and HOMO is known as the highest occupied molecular orbital.

The first form of state is known as a Shockley state. These states arise from the solving of Schrödinger's equation using the aforementioned Coulomb potential, and are responsible for describing the surface states of both metals and narrow band-gap semi-conductors. These states physically originate purely from the geometry of the terminated material (Yan et al., 2015). The second form of state is known as a Tamm state. These states arise from a separate 'tight-binding' model. The wavefunctions in this model are expressed as linear combinations of their respective atomic orbitals (LCAOs), and therefore represent more localised atomic and molecular orbitals at the surface of a material. Some of these molecular orbitals are usually responsible for chemical bonding within the bulk, but at the surface they are exposed as 'dangling' bonds and exhibit energies significantly different to what they would within the bulk (Shen et al., 1998). In addition to these intrinsic states, extrinsic factors such as the development of an oxide layer or introduction of a counter-surface contribute further complications to the electronic structure of surfaces.

In early surface-state models, polymers were treated in a similar fashion to semiconductors in terms of their electronic properties (Lee, 1994). Cowley and Sze (Cowley and Sze, 1965) devised an expression to aid in calculating the surface charge density for a metal – n-type semiconductor interface, based on this assumption and that the charge exchange between the surfaces takes place at a gap separation distance (z_0) of $\leq 4\text{Å}$ ($4\text{e}^{-10}\text{ m}$) at equilibrium.

$$\sigma = eg_E \left(\frac{\phi_M - \phi_{SC}}{\left(1 + \frac{q_e^2 z_0 g_E}{\epsilon_{SC}}\right)} \right) \quad (1-64)$$

Where ϕ_M and ϕ_{SC} are the work functions of the metal and semiconductor respectively measured in eV, ϵ_{SC} is the permittivity – or dielectric constant – of the semiconductor, and g_E being the density of states in $\text{cm}^{-2}\text{eV}^{-1}$ stated as a constant here, rather than as a function of energy. On the basis of this equation it was proposed to divide semiconductors into two categories; ionic and covalent (Lee, 1994). Examples of ionic semi-conductors are given as oxides such as silicon oxide (SiO_2) and alumina (Al_2O_3); whereas covalent semi-conductors are given as either monatomic materials such as silicon and germanium (Ge), or materials that consist of less polar bonds such as gallium arsenide, zinc sulphide (ZnS) and aluminium

nitride (AlN). This classification may be deemed inappropriate due to the aforementioned surface characteristics of some semiconductors, however it is useful to note the importance of intermolecular separation (z_0) on surface charge density. It is theorised that for ionic semiconductors – which inherently have low state densities – the charge density is independent of z_0 , unlike with covalent semiconductors – with a high density of states – where charge exchange is affected by several types of molecular interactions (Lee, 1994).

Historically the triboelectric transfer of charge between surfaces is treated as a similar mechanism to that which occurs between bulk materials, with the specific inclusion of surface states for the energy level distributions of both materials involved. The charge transfer expectedly causes a change in the fermi-level for each insulator by values stated in literature as Δ_1 and Δ_2 respectively until they are both equivalent (Matsusaka et al., 2010), with a resulting electric potential difference also being produced between the two surfaces of $E_F z_0$.

$$\phi_1 + \Delta_1 + eE_F z_0 = \phi_2 + \Delta_2 \quad (1-65)$$

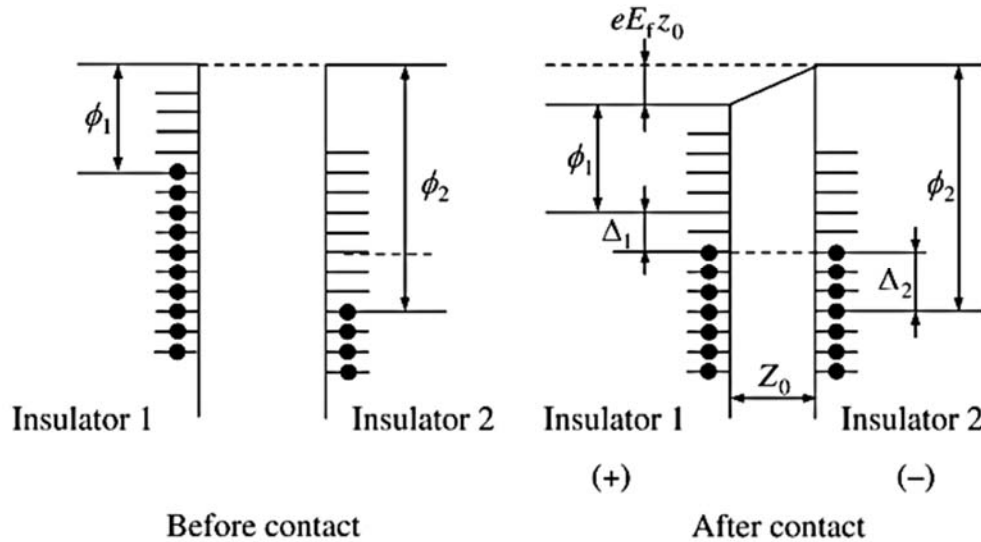


Figure 1-16 – Energy level diagram for insulator-insulator contact as depicted by Matsusaka (Matsusaka et al., 2010). The horizontal dashed depict set surface states for each insulator and the large dots indicate which states are filled.

The charge exchange itself is also not an equilibrium process. Observations have been made that report triboelectric charge exchange instead being a multi-step process. These observations state that extrinsic interfacial states are formed upon establishing contact. Charge exchange then occurs across these states. Upon separation of the contacting surfaces, these states are eliminated, allowing electrons and holes to be subsequently transferred to the surface states of the materials involved (Yu and Watson, 1989; Lee, 1994). One particularly useful way of describing the existence of these interfacial states is by treating them as chemical bonds that briefly form between the two surfaces.

1.4.1.i Surface Energy and Surface Tension

Firstly, atoms located on the surface of materials are generally situated in higher energy states than atoms that are found deep within the bulk of that same material. This is primarily due to the fact that surfaces are discontinuities in an otherwise cohesive material structure, and are therefore intrinsically energetically unfavourable due to giving the system a higher Gibb's free energy. This is the physical explanation as to why liquids form droplets which often conjoin and take a spherical shape in the absence of gravity, as to minimize their ratio of surface area to volume (Birdi, 2021).

Materials and substances exhibit this tendency to minimize surface area to different degrees, depending on their composition. This is most easily observed in liquids, where the surface of a body of mercury (Hg) generally tends to form a convex meniscus within a given container, whereas a body of water (H_2O) would form a concave meniscus within an identical container as depicted in Figure 1-17.



Figure 1-17 – Photograph of example menisci within a glass test tube for mercury (left) and water (right).

This can also be observed in solid-liquid interfaces, where droplets of a sample liquid may form more prominently on a Teflon surface than on a glass surface, with a larger contact angle (θ_c) as shown in Figure 1-18. This tendency for liquids and solids to form surfaces more readily is categorised as a physical quantity known as surface energy (usually denoted as σ but is often referred to as γ in terms of surface tension and interfacial energies – as well as in this thesis in order to avoid confusion with mechanical stress), also referred to as the interfacial free energy or surface tension specifically for liquids. The surface energy is defined as the excess energy at the surface of a material in comparison to within the bulk.

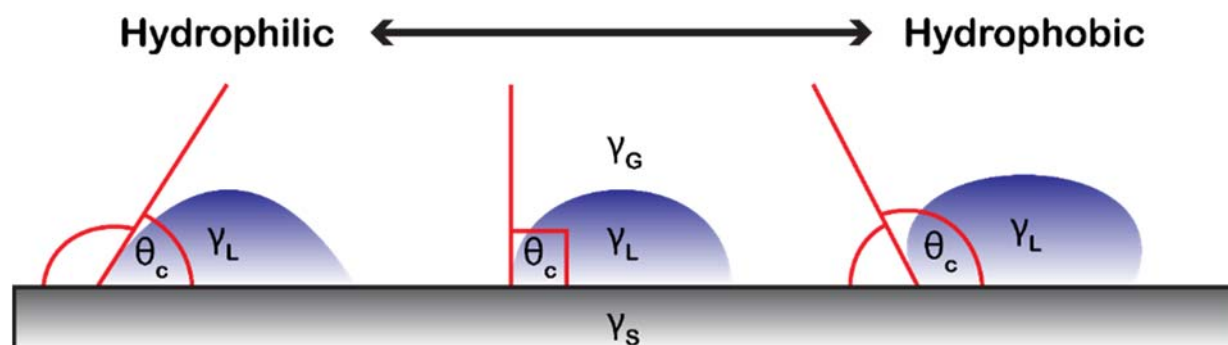


Figure 1-18 – Sessile drop method for the measurement of contact angle between three sample liquids and substrate.

A term often used in relation with surface tension is that of vapour pressure. Vapour pressure is defined as the pressure exerted by a vapour in thermodynamic equilibrium with its condensed phases at a given temperature in a closed system. In more general terms it is described as the tendency for a substance to evaporate or sublime. Substances with low vapour pressures generally exhibit high surface energies and low boiling points. The surface tension of liquids is usually measured using a force tensiometer and a technique known as the Du Noüy ring method (Ebnesajjad, 2011). In this method, a thin platinum ring is brought into contact with the liquid surface and gradually pulled away as shown in Figure 1-19. The resistive force exerted by the liquid on the ring is then measured using an electrobalance. A platinum ring has historically been chosen due to its relatively low chemical reactivity and surface energy for a metal.

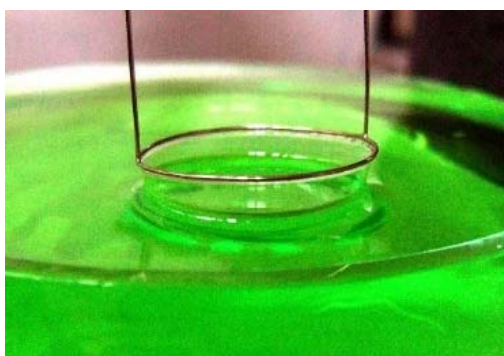


Figure 1-19 – Du Noüy ring method for measuring the surface tension of a sample liquid.

This measured force (F) is then correlated to the surface tension of the liquid through the following equation.

$$\gamma_L = \frac{F + F_b - m_o g}{4\pi R} \quad (1-66)$$

F_b is the buoyancy force imparted onto the ring, m_o is the mass of the ring, g is gravitational acceleration, and R is the averaged outer and inner radii of the ring. This equation is assuming that the thickness of the ring is considerably smaller than its radius. The most common methodology for measuring the surface energy of a solid substrate is the Sessile drop technique as shown in Figure 1-18. This technique involves placing a droplet of a liquid onto the surface being analysed and measuring the contact angle of the solid-liquid-gas interface. The contact angle is measured visually using an apparatus known as a contact angle goniometer. This device illuminates the droplet from behind and uses dedicated image analysis software to accurately measure the contact angle. The specific volume of the drop does not need to be known, as the contact angle is largely independent of volume provided that the drop is small enough. The typical volume of droplet used in these measurements is between 1 and 10 μL . The surface tension of the liquid drop is required in order for the surface energy of the solid to be calculated. The contact angle of a solid-liquid interface is dependent on the surface texture and roughness of the solid substrate. As increasing surface roughnesses have largely been known to enhance the liqueophobic/philic properties of surfaces (Bhushan, 2012). In turn it also possible for localised changes in surface energy to arise depending on the surface curvature, which has previously been used to explain the bi-polar and spatially varying triboelectric charging of particulates of differing sizes (Baytekin et al., 2011). The influence of surface topography on contact angle is represented in the Wenzel equation as stated below.

$$\frac{\cos \theta_m}{\cos \theta_Y} = \frac{A_n}{A_r} \quad (1-67)$$

θ_m is the measured contact angle, θ_Y is the Young's contact angle one would expect to observe with a perfectly flat substrate, and A_n is the nominal surface area as is projected onto a 2-dimensional plane without accounting for 3-dimensional roughness. A_r is the total real surface area of the sample, across the projected A_n . The Young equation describes how contact angle can be used to determine the interfacial energies involved in the contact.

$$\gamma_{SG} - \gamma_{SL} - \gamma_{LG} \cos \theta_c = 0 \quad (1-68)$$

γ_{SG} is the solid-gas interfacial energy, γ_{SL} is the solid-liquid interfacial energy, and γ_{LG} is the liquid-gas interfacial energy.

There are several methods of determining the surface energy of a substrate from sessile drop contact angle measurements. The Zisman theory (Zisman, 1964) defines the surface energy of the substrate to be equal to that of a liquid capable of fully wetting the surface to give a contact angle of 0° . Even if such a liquid doesn't exist, it is possible to use multiple liquids of varying surface tensions to measure multiple contact angles. The intercept at 0° of the resulting Zisman plot of θ versus σ_L will give a value of surface tension that would be of a hypothetical liquid capable of wetting the entire substrate surface.

The disadvantage of using the Zisman technique for calculating surface energy is that it treats it as a single parameter, and not the combination of different factors like it is. In fact, surface tension and energy is the summation of multiple forms of physical interaction at the surface of a material known as van der Waals forces. Van der Waals forces are distant-dependant intermolecular Coulomb interactions that are comparatively weaker than the formation of covalent and ionic bonds. These forces manifest in three separate forms of interaction; London dispersion forces, Debye forces, and Keesom forces.

Keesom forces are Coulomb interactions between two or more permanent dipoles. The dipoles are normally formed through ionic or polar covalent bonds between dissimilar atomic species. Examples of such an intrinsic dipole include the previously mentioned C-F covalent bond, as well as the ionic bond that forms between hydrogen (H) and chlorine (Cl) to form hydrochloric acid (HCl). Keesom forces are heavily temperature dependant since thermal excitation can cause the rotation and misalignment of such dipoles and therefore reduce the Keesom interactions between them. The strongest examples of Keesom interactions are that of hydrogen bonds, which are responsible for the relatively high surface tension of water. Since hydrogen and oxygen form polar covalent bonds, water molecules (H_2O) have a strong resulting electric dipole. As water begins to cool and solidify, these hydrogen bonds align and create a crystalline structure, which contributes to why snowflakes have their iconic shapes (Libbrecht, 2012).

Debye forces are interactions between these intrinsic dipoles and any induced dipoles that are formed from the Coulomb attraction or repulsion of molecular electron densities. One example of a Debye force could be that which occurs between an Argon (Ar) with a polar molecule of hydrochloric acid. The electron density around the Argon nucleus becomes perturbed in response to the presence of the permanent dipole of the HCl molecule, either being attracted to the positive hydrogen proton or repelled by the

electron density surrounding the chlorine atom. This perturbation of electrons surrounding the argon nucleus can generate a momentary dipole across the argon atom, which then interacts with the permanent HCl dipole.

London dispersion forces are entirely propagated between induced dipoles in the absence of any intrinsic dipole moment. These induced dipoles are generally instigated by random fluctuations in the electron densities surrounding atoms and molecules, and then further propagated by interactions between these random dipoles. Surface energy is therefore generally as a summation of two terms as shown below, due to the nature of these three types of van der Waals interaction.

$$\gamma_i = \gamma_i^P + \gamma_i^D \quad (1-69)$$

γ_i is the total surface energy of the substance i in question, γ_i^P is the polar component and is generally thought of as the contribution of the Keesom and Debye forces, and γ_i^D is the dispersive contribution of the London force. The most prominently implemented technique for determining the individual components of surface energy is the Owens, Wendt, Rabel, and Kaelble (OWRK) method (Owens and Wendt, 1969; Kaelble, 2008). In this method, two sample liquids with known polar and dispersive components are used to determine the polar and dispersive components of the substrate surface energy through the following equation.

$$\gamma_{SL} = \gamma_S + \gamma_L - 2 \left(\sqrt{\gamma_S^D \gamma_L^D} + \sqrt{\gamma_S^P \gamma_L^P} \right) \quad (1-70)$$

Combining this with the definition of γ_{SL} as given by Young's equation (1-2) ultimately yields to the following linear equation in the familiar form of $y = m \cdot x + c$.

$$\frac{\gamma_L(1 + \cos \theta_c)}{2\sqrt{\gamma_L^D}} = \sqrt{\gamma_S^P} \cdot \sqrt{\frac{\gamma_L^P}{\gamma_L^D}} + \sqrt{\gamma_S^D} \quad (1-71)$$

The values of γ_S^P and γ_S^D can then be solved graphically using the known parameters of the sample liquids and measured contact angles. The polar and dispersive components of an unknown liquid can be measured by first measuring the total surface tension using the Du Noüy ring method. The dispersive component can then be measured through the Sessile drop method on a sample substrate which is known to only interact via London dispersive forces, and therefore does not have a polar component to surface energy. An example of such surface is Teflon, which is explained in more detail in the experimental analysis of the triboelectric properties of Teflon in 3.2.3.c.i Influence of Polymer Composition.

The surface energies and their relative components may provide a simple and cost-effective methodology for determining the electronic and triboelectric properties of material interfaces, without the need for any of the comparatively expensive aforementioned analysis techniques for determining work function. Recent research conducted by (Zhang et al., 2022) has used solid-liquid triboelectrification as a method for detecting the true contact area between solid-liquid interfaces.

1.4.1.j Molecular Ion State Model

Whilst being a reliable tool for estimating the charges transferred within triboelectric contacts, surface states models have additional flaws that need addressing. Firstly, the charge states for polymers have entirely different microscopic origins for those of most semiconductors. The high density of states that occur within polymer surfaces indicate a highly non-linear dependence of charge exchange on energy. Since the physicochemical structure of surface states are difficult to strictly define, Fabish and Duke (Fabish and Duke, 1977) proposed the molecular-ion-state model and highlighted the importance of localised molecular orbital states. Despite the inclusion of 'ion' in the name of the model, this is actually an electron transfer model (Matsusaka et al., 2010).

Initially proposed to describe the triboelectric charging behaviour of polymers, their theory uses 'molecular-ion' states to describe the relevant acceptor and donor states for the triboelectric charging of polymers. The driving force is still described as the difference in electrochemical potentials between the two surfaces, and the existence of states that occur within what is normally an energy and gap still holds true in this model. The defining difference between the molecular-ion state model and surface-state models is that these states are theorised to originate from the localisation of molecular orbitals, rather than from the surface structural termination. Another important distinction between this model and others is that the assumption is made that the states are non-communicative, meaning that triboelectrically transferred electrons remain in their injected states rather than relax into ones situated at lower energies.

Molecular-ion states are defined as representing those of free molecular ions in solution, rather than bound ions that we observed previously as unoccupied valence orbitals of inorganic semi-conductors. When an electron is injected into a molecular structure, its presence induces changes in atomic positioning and the spatial distribution of electron densities. These changes in turn cause changes in electronic structure known as 'relaxations' as the rest of the molecule 'relaxes' into a more energetically favourable state as a molecular ion. The primary reasoning for this definition of localised states is the distinction between polymeric materials and crystalline structures. Fabish and Duke noted that dangling bonds are less prominent on polymeric surfaces, since chemical bonds are rarely broken in their formation as opposed to crystal surfaces. Therefore the origin of these triboelectric states must lie within the intermolecular and intramolecular structures. They proposed that the chemical and morphological structures within several μm of the surface govern the ability of a polymer to accept and donate electrons through localised molecular orbital states, in contrast to surface-state theory which is restricted to the nanoscale.

Fabish and Duke theorised that these molecular-ion acceptor (cation) and donor (anion) states can be described by neighbouring Gaussian peaks in state densities with respect to energy. These distributions are shown as being centred on the solid-state cation and anion energy values E_{cation} and E_{anion} . These energy values, as well as the Gaussian band-widths and state-density peaks are experimentally determined using methods such as photoelectron spectroscopy (UVPES). The energy of this distribution centroid ($\langle E \rangle$) is said to be crucial for understanding whether the polymeric material will donate or accept

electrons across a contact interface. Their theory presents an equation to govern charge transfer which is stated as follows.

$$J_{1 \rightarrow 2} = \frac{4\pi e}{\hbar} \int |\mathbf{M}_{1 \rightarrow 2}|^2 g_1 g_2 \left(f_1(E)(1 - f_2(E)) - f_2(E)(1 - f_1(E)) \right) dE \quad (1-72)$$

$J_{A \rightarrow B}$ is the current density across the interface between materials A and B , and $\mathbf{M}_{A \rightarrow B}$ is a matrix element that describes the nature of the transition. Two equations to predict triboelectric charge transfer in static contact are derived from this statement. Both are described as functions of acceptor and donor surface state distributions and Fermi-Dirac distributions. The equation devised to describe triboelectric charge transfer between insulators is as stated below.

$$Q_{1 \leftrightarrow 2} = \int_{\langle E \rangle_1}^{\langle E \rangle_2} \min[g_{D2}(E), g_{A1}(E)] f_2(E) (1 - f_1(E)) dE \\ - \int_{\langle E \rangle_1}^{\langle E \rangle_2} \min[g_{D1}(E), g_{A2}(E)] f_1(E) (1 - f_2(E)) dE \quad (1-73)$$

$\langle E_i \rangle$ is the distribution centroid energy between the two Gaussian acceptor and donor state distributions for material i , which can also effectively be treated as the Fermi level. $g_{Di}(E)$ and $g_{Ai}(E)$ are the donor and acceptor state densities for material i .

In the case of contacts involving both a conductor and an insulator, the direction of electron transfer is entirely dependent on whether the fermi-level of the conducting material is aligned with an acceptor or a donor state for the insulator. In most cases such as this the fermi-level is aligned with an acceptor state, meaning electrons are transferred from the conductor across to the insulator. In this model, electrons can only tunnel into the polymer if their energy is within a narrow range – a so-called ‘window’ (ΔE) – around the Fermi level of the metal. The density of the charge acquired from the metal of a given Fermi level E_F is therefore supposed to be the density of the insulator states at energy E_F . The general equation for the charge transfer ($Q_{I \rightarrow M}$) is expressed as below.

$$Q_{I \leftrightarrow M} = \int_{E_F}^{E_F + \Delta E} g_M(E) f_M(E) dE - \int_{E_F - \Delta E}^{E_F} g_I(E) (1 - f_M(E)) dE \quad (1-74)$$

ΔE is the window for charge transfer, $g_M(E)$ and $g_I(E)$ are the density of the metal and insulator states respectively, $f_M(E)$ is the probability of the electron states within the metal being occupied, and consequentially $1 - f(E)$ is the probability that these states are unoccupied.

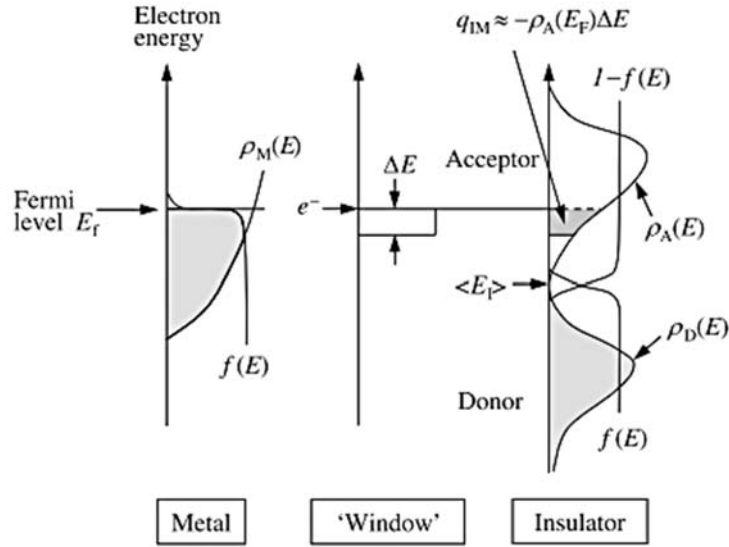


Figure 1-20 – Molecular ion state model for a metal-insulator contact. Specifically for the injection of electrons into the acceptor states of the insulator as depicted (Matsusaka et al., 2010). Depicting the electron state densities (referred to as $\rho_i(E)$ by Fabish and Duke, using A and D to denote acceptor and donor states for the insulator, but traditional notation defines these as $g_i(E)$ instead), Fermi-Dirac distributions $f_i(E)$, electron state energy distribution centroids ($\langle E_i \rangle$) of the metal-donor (M) and insulating-acceptor (I) surfaces.

As shown in Figure 1-20, for $f_I(E_F) = 0$ the charge transferred is approximately $-g_A(E_F)\Delta E$. An illustration of the states for an insulator-insulator contact are shown in Figure 1-21 where the donor states of one insulator align in energy with the acceptor states of the other insulator between the energy distribution centroids $\langle E_1 \rangle$ and $\langle E_2 \rangle$. The charge transfer is obtained by summing up the number of aligned donor-acceptor charge states. The general equation is stated below.

$$Q_{1 \rightarrow 2} = \int_{\langle E_1 \rangle}^{\langle E_2 \rangle} \min[g_{D2}(E), g_{A1}(E)] f_2(E) (1 - f_1(E)) dE \quad (1-75)$$

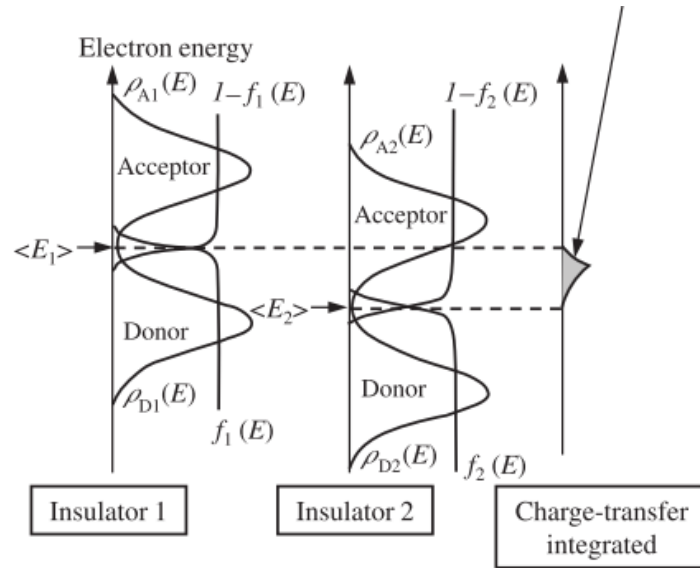


Figure 1-21 – Molecular ion state model for an insulator-insulator contact as shown in (Matsusaka et al., 2010). Depicting the electron state densities (referred to as $\rho_i(E)$ by Fabish and Duke, using A and D to denote acceptor and donor states for the insulators) but traditional notation defines these as $g_i(E)$ instead), Fermi-Dirac distributions $f_i(E)$, electron state energy distribution centroids ($\langle E_i \rangle$) of the two insulating surfaces (1 and 2).

The direction of charge transfer and resulting polarity on the insulator surfaces after contact are dependent on the values of the two centroid energies. The complexity of localised states is difficult to model without a detailed approach. More recently, density functional theory (DFT) has been implemented to more effectively determine the specific energy distributions of localised and interfacial states (Nan et al., 2022).

1.4.1.k Electron-Phonon Interactions

Upon considering the role of friction in triboelectric charging, the majority opinion initially remained in favour of Volta's hypothesis. Volta hypothesised that the sole contribution of sliding friction in triboelectric charging was merely to generate more points of contact when accounting for the microscale roughnesses of surfaces. Despite this consensus, the influence of friction on triboelectric charging was noted by Richards (Richards, 1920; Richards, 1923), whose findings concluded that electrification by light contact, heavy pressure, and impact, must be fundamentally different.

Whilst contact electrification in a static environment has received much attention, not much attention has been given to triboelectric charge transfer in more dynamic environments. Pan and Zhang devised a dynamic model for charge transfer during frictional contact. This model takes into account the function of phonons and their interactions with electrons during the transfer process by focusing on a quantum physical approach (Pan and Zhang, 2017).

Since triboelectric charge transfer is dynamic and somewhat affected by frictional heat, systems under sliding motion are inherently easier to reach thermodynamic equilibrium (or pseudo-equilibrium) than those in the case of static contact charging (Lee, 1994). This model agrees once again with the hypothesis that triboelectric charge transfer is driven by imbalances in electrochemical potential as they attempt to equalise. It introduces a 'quasi-Fermi level' to insulating surfaces which resembles the distribution centroid $\langle E \rangle$ in the molecular-ion state model and is analogous to the Fermi-level of metals and semi-conductors.

The primary contribution of this model is introducing the role of phonons to triboelectric charge transport. As previously mentioned, a phonon is defined as a quasiparticle that represents quantised kinetic vibrations of an elastic arrangement, and manifest as heat and sound depending on their frequencies and wavevectors. Phonons are similar to photons in the sense that they are treated as bosons. Bosons are the subclass of particles that mediate forces between matter, and fundamentally differ from fermions that constitute matter. Unlike fermions, bosons obey Bose-Einstein statistics instead of Fermi-Dirac statistics. This distribution ($b(E)$ as opposed to $f(E)$) implies that bosons such as phonons and photons can condense into identical states and become indistinguishable, and is expressed below.

$$b(E) = \frac{1}{e^{(E-\bar{\mu})/k_B T} - 1} \quad (1-76)$$

The thermodynamic properties of a solid are known to be directly related to its phononic structure. The phononic properties of simple and repeating structures such as crystals are most easily described. Atoms

within a crystalline lattice structure are treated as quantum harmonic oscillators under a harmonic potential that is analogous to Hooke's Law.

$$F_s(x) = k_s x \quad (1-77)$$

F_s is the force required to extend a spring with a linear spring constant k_s by the distance Δx . For single covalent bonds, this spring constant value is estimated to range between 100 and 1000 Nm^{-1} (Huber and Herzberg, 1979). Integrating this linear dependency of force over distance, a quadratic equation for potential energy (E_s) is derived.

$$E_s(x) = \int F_s(x) dx = \int k_s x dx = \frac{1}{2} k_s x^2 \quad (1-78)$$

Substituting this potential into the Schrödinger equation yields the following result.

$$E\psi(x) = -\frac{\hbar^2}{2m^*} \frac{\partial^2 \psi(x)}{\partial x^2} - \frac{1}{2} k_s x^2 \psi(x) \quad (1-79)$$

Solving this version of the Schrödinger equation for E gives a range of possible energy values.

$$E_n = \left(n + \frac{1}{2}\right) \hbar \sqrt{\frac{k_s}{m^*}} \quad (1-80)$$

n can take the value of any non-negative integer, with $n = 0$ representing the lowest energy 'ground' state of the system. This implies the discretisation of energy states for these vibrations, meaning that they can only oscillate as specific frequencies and require a specific amount of energy to transition between states. This quantisation is where phonons originate, taking the form of these discrete vibrational state excitations. An interesting quality of phonons as quasiparticles is that they are shown to exhibit a negative effective mass. This is exhibited in how both acoustic and thermal phonons tend to travel faster through denser materials (Compton and Duncan, 2015). The phonon state densities for each material describe the material's thermal properties, with high frequency phonons contributing to the specific heat capacity and low frequency phonons contributing to thermal conductivity (Jena, 2022).

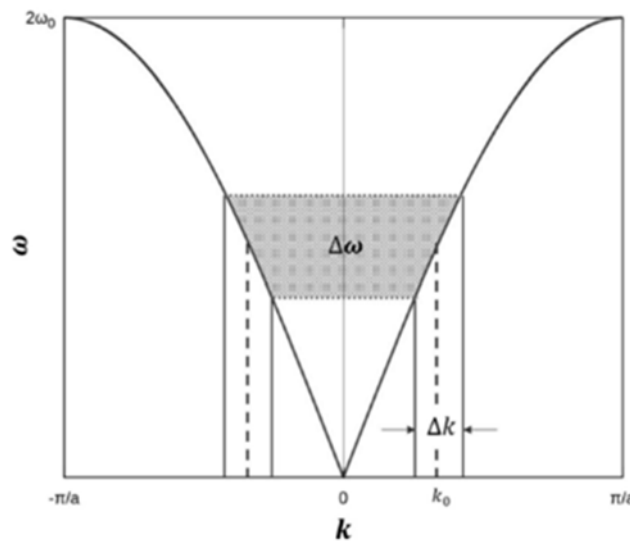


Figure 1-22 – Changes in phonon energy corresponding from changes in vibrational modes from frictional contact as shown by Pan & Zhang (Pan and Zhang, 2017).

As free electrons propagate through a material, the electromagnetic forces they exert onto the surrounding structures generate phonons in the form of a lattice response. This lattice deformation in turn alters the states of bound electrons within the lattice. These electron-phonon interactions play a pivotal role in the electronic properties of materials. Most notably, these interactions explain how the electrical conductivities of metals decrease with increasing temperature due to increasing phonon interactions. Electron-phonon interactions are also necessary for superconductivity to exist as a phenomenon. Within a superconducting material electrons form Cooper pairs by interacting through a phonon. This effectively makes the electron pair behave as though it is a boson and allows for both electrons to pass through the material with zero resistance (Bardeen et al., 1957). Phonons and photons can also directly interact with one another through the electromagnetic excitation of dipole moments (Böer and Pohl, 2017).

It has long been understood that friction is a reliable mechanism for generating both thermal and acoustic phonon wavelets through frictional heating and stick-slip behaviour (Dransfeld and Li-Jie, 1995). Therefore it is reasonable to assume that friction mechanisms can directly affect the behaviour of surface electrons through phonon interactions. The theory introduced by Pan and Zhang (Pan and Zhang, 2017) postulates that the phonons generated by friction would be capable of providing surface-state electrons with enough energy to overcome a potential barrier presented by a material interface.

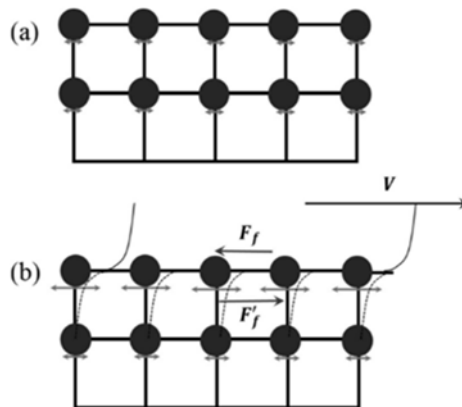


Figure 1-23 – Lattice deformation and vibration mode change when two surfaces are in frictional contact as depicted by Pan & Zhang (Pan and Zhang, 2017). (a) represents the equilibrium vibration modes whereas (b) represents the friction-induced lattice vibration modes.

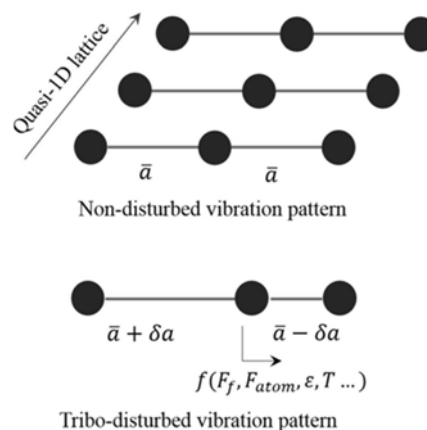


Figure 1-24 – Changes in lattice spacing resulting from frictional contact as shown by Pan & Zhang (Pan and Zhang, 2017).

This hypothesis fails to address the highest attainable phonon energy that can contribute in triboelectric charge transfer. Substituting typical bond strength and atomic mass values into equation (1-80) yields phonon energy increments in the range of meV. These energy values mirror the typical thermal energies expected at room temperature ($k_B T_{\sim 300K}$). The highest energy phonon available within a lattice structure would be one with the shortest wavelength. The wavelength of phonons is restricted by the lattice spacing, since any phonon with a wavelength shorter than four times this value would resemble a phonon of longer wavelength due to Nyquist-Shannon sampling theory. For example, the energy of a phonon propagating at the measured speed of sound through a bulk of a metal, at a wavelength that is twice the lattice spacing constant would yield a similar energy through the Planck-Einstein relation. Despite these low predicted energies, it is still possible for electron-phonon interactions to diversify the energy spectra of surface electrons. This in-turn opens up more avenues for direct transitions between electronic states of differing energies and momenta and enhances triboelectric charge transfer. The energy needed for an electron within a material to transfer across a triboelectric contact is usually very specific, therefore phonons induced by friction – having a wide range of energies – will be more likely to interact and donate the correct amount of energy needed. The bosonic nature of phonons also allows for any number of them to occupy a given state.

Another postulation of this theory is that the lattice deformation induced by friction and strain diversified the energy spectra of phonons within a material (Sow et al., 2012). This mechanism would also therefore enhance triboelectric charge transfer by providing an even wider variety of possible triboelectric interfacial transitions. One additional hypothesis raised as a result of this postulation is that materials with more amorphous and irregular structures such as polymers may exhibit a greater tendency to triboelectrically charge with counter materials than materials with a regular crystalline structure. Whilst this hypothesis does hold some degree of truth, further experimental validation is required to fully understand the implications of phononic structure.

1.4.1.I Mechano-ions and radicals

The role of molecular-ions have briefly been explored in the molecular-ion state theory, although more recent research has further elaborated on the chemical alteration of physical structures resulting from friction and wear. Sagakuchi et al. (Sakaguchi et al., 1990) initially proposed that the mechanical failure of polymeric materials create mechano-radicals, mechano-cations, and mechano-anions. Radicals are known as electrically neutral molecules that exhibit unpaired valence electrons, and are therefore highly reactive. Cations and anions are molecular ions that respectively have an excess of either negative or positive charge, and also react readily with species as a way to regain charge neutrality. In order to observe the formation of these radicals and ions, the fracturing of polymers were undertaken in the presence of electrophilic tetracyanoethylene (TCNE, $C_2(CN)_4$) without any electromagnetic or ambient interference. The electronic states of the resulting molecules were analysed in order to investigate the movement of electrons upon material fracture. The four nitrile functional groups present in TCNE exhibit low energy π^* orbitals, which are anti-bonding orbitals that correspond to the π bonds on either side of the primary σ bond of the carbon-nitrogen triple bond ($C\equiv N$). These orbitals, in conjunction with the low-

energy carbon-carbon (C–C) double bond at the centre of the molecule lead to the creation of very low energy molecular orbital states with excess electrons can occupy without breaking apart the molecule. It was found that mechano-radicals formed upon the homolytic scission of the polymeric C–C bonds as depicted below.



$\begin{matrix} (A - A) \\ poly \end{matrix}$ represents two single-bonded elemental species A , and A° represents the un-bonded electrically neutral equivalent mechano-radical of A . The heterolytic scission of the same C–C bonds was observed to form both mechano-anions and mechano-cations through the unequal redistribution of electrons.



A^+ represents the positively charged anion with a recently vacated valence state, and A^- represents the negatively charged cation with an excess valence electron. The formation and breaking of physical and chemical bonds are phenomena that occur regularly within tribological contacts (Burgo et al., 2012).

The formation of these varied and unstable electronic structures during friction and wear has been theorised to contribute to triboelectric transfer through the significant alteration of resulting electronic structures (Sakaguchi et al., 2014).

1.4.1.m Flexoelectricity

Recent research by (Mizzi et al., 2019)(Mizzi and Marks, 2022) has concluded that the flexoelectric effect plays a significant driving role in triboelectric charge transfer. The flexoelectric effect is the generation of an electric potential across a strain gradient within a material. This draws a parallel to the piezoelectric effect, in which potential differences arise across a body of a material when it is subjected to strain. Piezoelectricity only occurs within specific materials, which normally contain inherent dipole moments, whereas flexoelectricity has the potential to occur within any material.

Mizzi and Marks describe the presence of strain gradients across a surface, and penetrating into a surface, through contact deformation generating localised perturbations in electric potential. These localised potential differences are theorised to be significant in lowering the potential barriers that electrons must overcome in order to participate in triboelectric charge transfer. Not only has this been exhibited for the application of a purely normal force, but the introduction of tangential forces and shear strains are also theorised to further enhance this effect.

These perturbations have also have been cited as an explanation for the triboelectric charging of identical surfaces in contact, and the bi-polar charging of particulates. The comprehensive equation used by Mizzi and Marks (Mizzi and Marks, 2022) describes the change in energy of an electronic band feature largely as a function of the change in average Coulomb potential arising from strain gradients via the bulk flexoelectric effect (ΔV_{FxE}).

$$\Delta(E_i(\vec{r}) - E_{vac}(\vec{r})) = \Delta V_{FxE}(\vec{r}) + (\varphi + D_i)\epsilon(\vec{r}) \quad (1-83)$$

$E_i(\vec{r})$ is the energy of the band feature i as a function of position \vec{r} , and $E_{vac}(\vec{r})$ is the vacuum energy as a function of position. The second and third terms (φ and D_i) shown in (1-83) are largely shown to cancel each other out, but are described respectively as the shift in average Coulomb potential \bar{V} with respect to the vacuum E_{vac} under strain ϵ , and the local change in energy of a band feature E_i , relative to the average Coulomb potential $\langle V \rangle$ under strain ϵ .

$$\varphi = \frac{d(q_e \langle V \rangle - E_{vac})}{d\epsilon} \quad (1-84)$$

$$D_i = \frac{d(E_i - q_e \langle V \rangle)}{d\epsilon} \quad (1-85)$$

$\Delta V_{FxE}(\vec{r})$ is expressed in (1-87) as a function of the flexoelectric polarisation \bar{P}_{FxE} .

$$\Delta V_{FxE}(\vec{r}) = q_e(V(\vec{r}) - V_0) \quad (1-86)$$

$V(\vec{r})$ is the average Coulomb potential at point r , referenced to V_0 , which is the average Coulomb potential sufficiently far from the contact point.

$$\Delta V_{FxE}(\vec{r}) = \frac{1}{4\pi\epsilon} \int \frac{\bar{P}_{FxE}(\vec{r}') \cdot (\vec{r} - \vec{r}')}{|\vec{r} - \vec{r}'|^3} d\Omega' \quad (1-87)$$

$\bar{P}_{FxE}(\vec{r}')$ is the flexoelectric polarisation at point r' which can be expressed as a function of the local strain gradient at point r' .

$$\bar{P}_{FxE}(\vec{r}') = \mu_{ijkl} \frac{\partial \epsilon_{jk}}{\partial x_l} \quad (1-88)$$

$\bar{P}_{FxE}(\vec{r}')$ is the flexoelectric polarisation at point \vec{r}' , μ_{ijkl} is a fourth-rank polar tensor describing flexoelectric coupling, and $\frac{\partial \epsilon_{jk}}{\partial x_l}$ is the strain gradient. If the material being considered is isotropic, then cubic symmetry can reduce the non-trivial components of this tensor.

$$\mu_{ijkl} = \mu(\delta_{ij}\delta_{kl} + \delta_{ik}\delta_{jl} + \delta_{il}\delta_{jk}) \quad (1-89)$$

δ_{ij} is the Kronecker delta, which is a discrete function equal to unity when $i = j$ and zero when $i \neq j$ as shown below.

$$\delta_{ij} = \begin{cases} 1 & \text{if } i = j \\ 0 & \text{if } i \neq j \end{cases} \quad (1-90)$$

The electric field component in the z direction resulting from flexoelectricity can then be expressed as a function of the relevant strain gradients that are geometrically allowed. The flexoelectric tensor can then be expressed instead as a scalar. This constant is then multiplied by the electric permittivity of the material ϵ in order to relate the flexoelectric polarisation to a value of electric field. The electric field component perpendicular to the contacting surface can therefore be expressed as below through a coupling constant defined as the flexocoupling voltage (V_f).

$$\vec{E}_{FxE_Z}(x, y, z) = -V_f \frac{\partial \epsilon(x, y, z)}{\partial z} = -V_f(3\partial \epsilon_{zzz} + 2\partial \epsilon_{zxx} + \partial \epsilon_{xxz} + 2\partial \epsilon_{zyy} + \partial \epsilon_{yyz}) \quad (1-91)$$

$$\partial \epsilon_{jkl} = \frac{\partial \epsilon_{jk}}{\partial x_l} \quad (1-92)$$

The strain gradients can be calculated from a thorough analysis of the stress fields that are present within the material. These normalised stress fields are calculated by (Mizzi et al., 2019) using Hertzian analysis (Hertz, 1882) and are expressed below in cylindrical coordinates (r, θ, z) . These stress fields are calculated for an idealised rigid sphere on an elastic flat half-space. These surfaces are assumed to be homogeneous and isotropic, and deformations are assumed to be perfectly elastic in accordance with Hooke's law.

$$\frac{\sigma_{rr}}{\langle P \rangle} = \frac{3}{2} \left(\frac{(1-2\nu)a^2}{3r^2} \left(1 - \left(\frac{z}{\sqrt{u}} \right)^3 \right) + \frac{ua^2}{u^2 + a^2z^2} \left(\frac{z}{\sqrt{u}} \right)^3 + \frac{z}{\sqrt{u}} \left(u \left(\frac{1-\nu}{a^2 + u} \right) + (1+\nu) \frac{\sqrt{u}}{a} \arctan \left(\frac{a}{\sqrt{u}} \right) \right) \right) \quad (1-93)$$

$$\frac{\sigma_{\theta\theta}}{\langle P \rangle} = \frac{3}{2} \left(\frac{(1-2\nu)a^2}{3r^2} \left(1 - \left(\frac{z}{\sqrt{u}} \right)^3 \right) + \frac{z}{\sqrt{u}} \left(2\nu + \frac{u(1-\nu)}{a^2 + u} + \frac{(1+\nu)\sqrt{u}}{a} \arctan \left(\frac{a}{\sqrt{u}} \right) \right) \right) \quad (1-94)$$

$$\frac{\sigma_{zz}}{\langle P \rangle} = \frac{3}{2} \left(\frac{ua^2}{u^2 + a^2z^2} \left(\frac{z}{\sqrt{u}} \right)^3 \right) \quad (1-95)$$

$$\frac{\sigma_{rz}}{\langle P \rangle} = -\frac{3}{2} \left(\frac{rz^2}{u^2 + a^2z^2} \right) \left(\frac{a^2\sqrt{u}}{a^2 + u} \right) \quad (1-96)$$

ν is the Poisson's ratio of the material, and u is a spatial parameter defined as below.

$$u = \frac{1}{2} \left((r^2 + z^2 + a^2) + \sqrt{(r^2 + z^2 - a^2)^2 + 4a^2z^2} \right) \quad (1-97)$$

$\langle P \rangle$ is the average pressure exerted across the circular Hertzian contact, with a radius a and under the applied load F_a .

$$\langle P \rangle = \frac{F_a}{\pi a^2} \quad (1-98)$$

a itself can be expressed as a function of applied load, elastic modulus of the elastic half-space (Y) – also often referred to as Young's modulus, and the radius of the spherical indenter (R).

$$a = \sqrt[3]{\frac{3F_a R}{4Y} (1 - \nu^2)} \quad (1-99)$$

These stress fields are then related to strains through the use of the isotropic Hooke's law in cylindrical coordinates.

$$\epsilon_{rr} = \frac{1}{E} (\sigma_{rr} - \nu(\sigma_{\theta\theta} + \sigma_{zz})) \quad (1-100)$$

$$\epsilon_{\theta\theta} = \frac{1}{E} (\sigma_{\theta\theta} - \nu(\sigma_{rr} + \sigma_{zz})) \quad (1-101)$$

$$\epsilon_{zz} = \frac{1}{E} (\sigma_{zz} - \nu(\sigma_{\theta\theta} + \sigma_{rr})) \quad (1-102)$$

$$\epsilon_{rz} = \frac{2(1+\nu)}{E} \sigma_{rz} \quad (1-103)$$

These strain fields are then converted into Cartesian coordinates (x, y, z) using the relevant transformation matrix ($\mathbf{T}_{r,\theta,z \rightarrow x,y,z}$).

$$\mathbf{T}_{r,\theta,z \rightarrow x,y,z} = \begin{pmatrix} \cos\theta & -\sin\theta & 0 \\ \sin\theta & \cos\theta & 0 \\ 0 & 0 & 1 \end{pmatrix} \quad (1-104)$$

The resulting strain fields were then differentiated in order to find the relevant strain gradients to be substituted into (1-91). The strain field is then averaged across the deformation volume, defined as a^3 .

$$\left\langle \frac{\partial \epsilon}{\partial z} \right\rangle = \frac{1}{a^3} \iiint \frac{\partial \epsilon}{\partial z} dV \quad (1-105)$$

The flexoelectric perturbation in surface potential can then be calculated as the integral of the flexoelectric field \vec{E}_{FxEZ} from the surface to infinity.

$$V_{FxE}(x, y) = - \int \vec{E}_{FxEZ}(x, y, z) dz \quad (1-106)$$

This value for surface potential perturbation has been graphically determined to be proportional to applied load, contact curvature, and equivalent elastic modulus for the case of indentation as expressed below.

$$V_{FxE}(x, y) \propto -V_f^3 \sqrt{\frac{F_a}{(1 - \nu^2)R^2Y}} \quad (1-107)$$

This has also been expanded to include adhesion in the case of pulling away from contact, which is often the case for charge separation.

$$V_{FxE}(x, y) \propto V_f^3 \sqrt{\frac{\gamma}{(1 - \nu^2)RY}} \quad (1-108)$$

γ is defined as the surface energy per unit area as previously described in 1.4.1.i Surface Energy and Surface Tension.

1.4.2 Ion Transfer

A conflicting theory in the early stages of triboelectric research questioned the driving force behind triboelectric charge transfer, and hypothesised that the nature of contact potentials produced via contact electrification were instead electrolytic potentials (Knoblauch, 1902). This implied that triboelectric charging was a result of chemical reactions occurring within the contact, rather than the product of a purely physical and electronic phenomenon that occurs without the breaking and formation of chemical bonds. In the early 1960s, ion transfer was originally considered as the dominant charging mechanism involving insulators (Lee, 1994). It was considered that mobile ions have the ability to transfer upon contact with another material because of their counter-ions being either attached to polymers or otherwise are part of a larger molecule which is considered to have less mobility for such transfer (Williams, 2012).

Despite recent studies concluding that electron transport plays the dominant role in triboelectric charge transfer between solid surfaces (Xu et al., 2018), the transference of larger charged masses such as ions remains plausible in certain situations. Whilst triboelectric charge transfer can often be treated as a purely electronic phenomenon for solid-on-solid interfaces, the influence of surface chemistry cannot be

overlooked in the context of a more generalised approach. Surface chemistry has a dominating influence on triboelectric charge transfer in ionic environments. An example of such can be as simple as an ion-containing liquid droplet coming into contact with a solid substrate (Nie et al., 2020), or as complex as the galvanic corrosion of two differing metal surfaces in the presence of an electrolyte (Lax et al., 2020) (Cheung et al., 2022). It has been observed that the sign of the charge exchanged was always consistent with the transfer of mobile ion species (Williams, 2012). For example, substances with cationic functional groups have a positive charging property, while ones with anionic groups have a negative charging property (Matsusaka et al., 2010). Most recent research into the ion transfer process has been in the development of electro-photographic printer technologies and the implementation of ionic charge control agents (CCAs) in toners (Williams, 2012).

Experimental approaches have recently been made to observe ion transfer through scanning probe microscopy (Saurenbach et al., 1992) and secondary ion mass spectrometry (Mizes et al., 1990). Nie et al. (Nie et al., 2020) investigated the contact electrification of various liquids against a Teflon substrate. Their findings concluded that contact electrification occurs even between Teflon and oil in the complete absence of mobile ions, highlighting electron transport as the only possible mechanism for such a contact. Their observations of various aqueous solutions against the Teflon substrate provided strong evidence that ion transport remains as a competing mechanism where mobile ions are present within the fluid. Aqueous solutions of copper sulphate (CuSO_4), sodium chloride (NaCl), hydrochloric acid (HCl), and sodium hydroxide (NaOH) were all found to contribute to contact electrification through the transport and screening of their mobile ions. Their ionic concentrations were shown to have a direct influence on triboelectric charging, either competing with or amplifying the charges generated via electron transport. Figure 1-25 was taken from their article as a visual depiction of their proposed mechanisms for electron and ion transport.

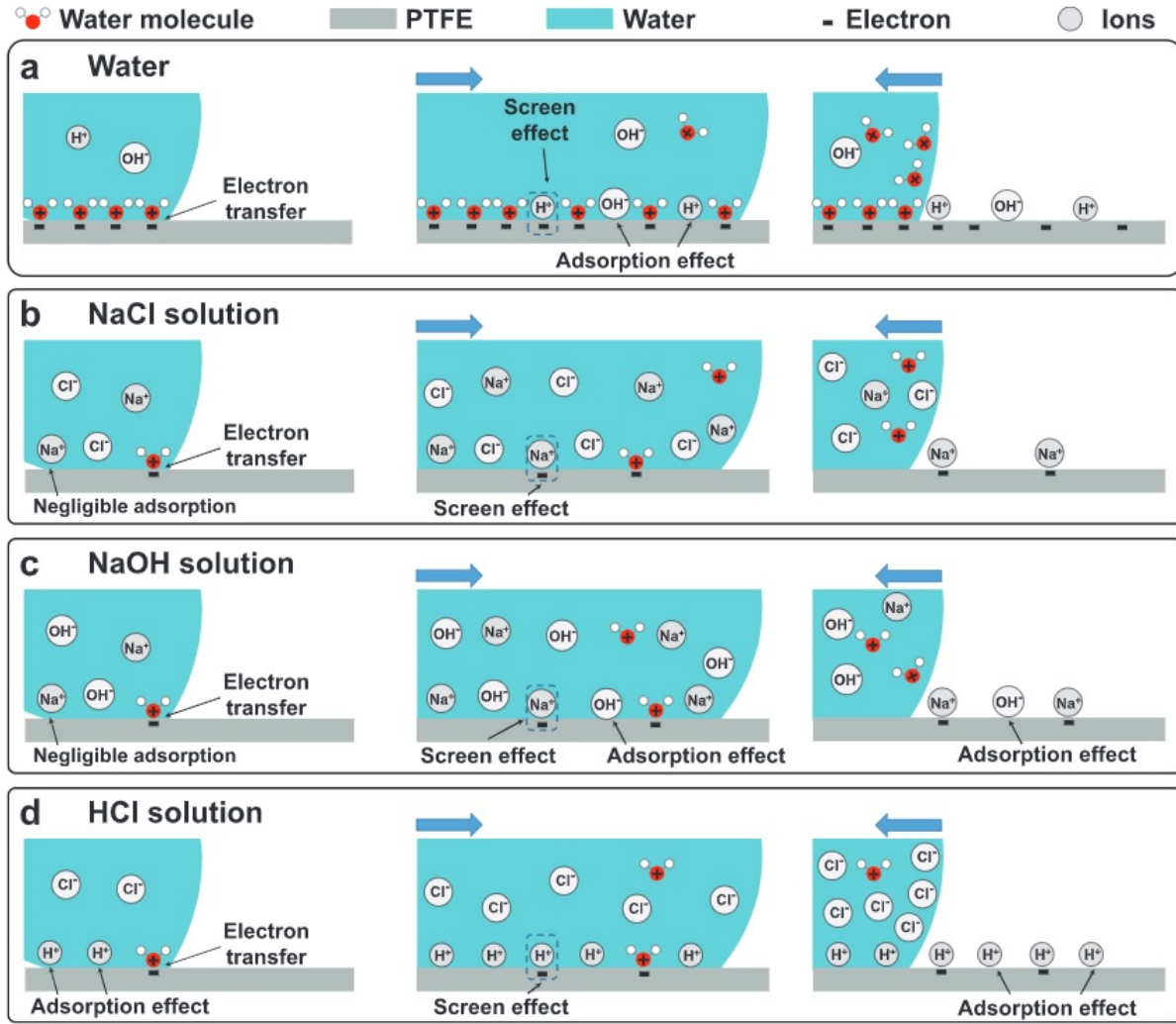


Figure 1-25 – Visual depictions of charge transfer mechanisms for contact electrification between Teflon and water (a), a sodium chloride solution in water (b), a sodium hydroxide solution in water (c), and hydrochloric acid (d) as depicted by (Nie et al., 2020).

The model proposed in conjunction with these findings suggests that electron transfer initially competes with the adsorption of mobile ions onto the substrate surface. For the case of water and Teflon, electrons are transferred from the oxygen atom in H₂O and donated to the carbon backbone of the PTFE polymer. This causes the electrostatic attraction of the positively charged water molecule to the negatively charged Teflon surface. This negative charge on the Teflon surface also attracts positively charged hydrogen ions (H⁺) in the solution. Therefore the model is summarised with an initial stage of electron transport and ion adsorption, followed by the resulting electrostatic attraction of additional mobile ions.

This dual mechanism for describing contact electrification has also been mathematically modelled by (Lee, 1994), where the interaction energy between two molecules engaging in triboelectric charge transfer is expressed as the summation of an electron transfer term and an ionic attraction term.

$$\Delta E_{INT} = -\frac{Q_N Q_E}{\epsilon_0 r} + \frac{2(C_N C_E \beta)^2}{E_{HOMO} - E_{LUMO}} \quad (1-109)$$

Q_N and Q_E are the total charges of the nucleophile and electrophile respectively and r is their separation distance. The second term assumes that only two 'frontier' molecular orbitals are involved in charge

transfer, the highest occupied state of the nucleophile, represented by the wavefunction ψ_N , and the lowest unoccupied state of the electrophile (ψ_E). A transfer state $\psi_{N \rightarrow E}$ is assumed as the linear combination of atomic orbitals (LCAO), where the atomic orbitals are actually the two previously mentioned molecular orbitals which are assumed to be localised to a single atom within the molecule.

$$\psi_{N \rightarrow E} = C_N \psi_N + C_E \psi_E \quad (1-110)$$

C_N and C_E are the relevant coefficients for the LCAO combination of the two atomic orbitals. β is the resonance integral constant, describing the resonance between the two orbitals as expressed below in Dirac notation.

$$\beta = \langle \psi_N | \hat{H} | \psi_E \rangle \quad (1-111)$$

\hat{H} is the Hamiltonian operator, which yields eigenvalues for the energy of a system when applied to a wavefunction (ψ). Despite electron transfer playing the dominant role in most forms of contact electrification, the influence of ion transport has revealed triboelectric charging to be the driving force behind corrosion mechanisms. Galvanic corrosion in specific is described as the degradation of one metal placed in electrical contact with another in the presence of an electrolyte. Galvanic corrosion is known to occur between dissimilar metals, most notable between an anodic electron donator and a cathodic electron acceptor. The anodic material is shown to degrade significantly over time due to electrochemical oxidation whereas the cathodic material remains relatively inert. The relative 'inertness' of metals is displayed in the Galvanic series, with this property of inertness directly correlating to work function. The Galvanic cell is a device that was initially utilised by Galvani and Volta (Popov, 2015) to harness Galvanic corrosion for the storage of electrochemical energy. Galvanic cells utilise the occurrence of reduction and oxidation reactions to generate an electrical current between two differing electrodes.

1.4.3 Material Transfer

When polymers come into contact with other materials, their chain-like molecular structure allows for a transfer layer of said polymer to develop on the counter-surface. Material can also be transferred as a result of more significant wear processes involving brittle materials (Matsusaka and Masuda, 2003; Matsusaka et al., 2010). Research using rubbing and sliding polymer contacts suggests that material transfer occurs to a large extent on the first contact and to a much smaller extent on subsequent contacts. Because of this behaviour it was concluded that material transfer was not the primary mechanism of contact electrification (Williams, 2012). Unfortunately there is currently no theoretical model for equilibrium charge transfer through such a substantial mass transfer mechanism (Matsusaka et al., 2010). It has previously been demonstrated that the pressing together and separation of two films of different compositions can result in both material and charge transfer, although both of which of a different kind than previously reported.

It has long been thought that, in contact charging, each surface charges uniformly positive or negative, with charge density represented by only one in ten thousand surface molecules or less. It has more recently been that each surface supports both positive and negative charges distributed in irregular mosaic patterns (Baytekin et al., 2011). The net charge of one sign on both surfaces is shown as a direct

consequence of transfer of material from one surface to another. Kelvin probe force microscopy (KPFM), used to image the surface potentials, revealed irregular patterns or mosaics of randomly distributed positive and negative patches on both surfaces, and this is accompanied by changes in the surface compositions and transfer of material between the surfaces (Baytekin et al., 2011). Other propositions for the cause for these charge mosaics is the influence of surface geometry and strain distributions across a contact interface (Baytekin et al., 2011).

1.5 Contributing Factors

Contact electrification is a complicated process where the development of triboelectric charges on contacting surfaces are sensitive to material composition and contact parameters, as well as external environmental conditions such as humidity and ambient temperature (Diaz and Felix-Navarro, 2004). This following section will describe the factors that are known to influence triboelectric charging.

1.5.1 Surface Composition

As previously described in theories describing the triboelectric effect, triboelectric charge transfer is strongly dependent on surface composition. Not only does the electronic and chemical structure of surfaces determine their triboelectric behaviours, but it also determines their mechanical properties and resulting tribological behaviours. When selecting a material to be used in a triboelectric contact, it is of paramount importance to carefully tailor its electrical properties. As discussed earlier, electro-negativity and electro-positivity is the key to generating the largest surface charge densities through triboelectric charge transfer. The difference in Fermi level between two contacting materials determines the total thermodynamic drive for triboelectric charge transfer, whilst the electronic and phononic state distributions localised to their respective surfaces determine the total amount of charge that can be transferred. This generally means engineering two separate materials to act as an optimised pairing. Usually these materials are contrasting in structure, which is reflected in their electronic state distributions. Specific material combinations can also be used to generate preferable interfacial phenomena. This could manifest in the tailoring of polymer structures with specific donor and acceptor pendant groups to ensure an efficient use of surface area.

Results demonstrate that the triboelectric charging of solids is related to the molecular structure of the material surface, and subsequently to the molecular orbital energy levels of the isolated molecules (Lee, 1994). The chemical structure of these materials play the primary role in how well they can accept or donate electrons across a contact. This can firstly be tailored through the introduction of specific elemental species. Electronegative materials generally have an elemental composition rich with atoms that have a high electron affinity such as halides. The most common materials with this form of structure are polymers with a high content of halides such as Vinyl (polyvinylchloride, PVC); but most notably with Teflon, polyvinylidene fluoride (PVDF) and fluorinated ethylene propylene (FEP) (Diaz and Felix-Navarro, 2004; Xie et al., 2014). In addition, some polymeric organosilicon compounds such as polydimethylsiloxane (PDMS) have exhibited electronegative behaviour (Xia et al., 2017; Tcho et al., 2017). Metallic MXenes

with halide surface functional groups have also been proposed as a conductive family of materials for triboelectric contacts (Jiang et al., 2018; Dong et al., 2018).

Beyond choice for atomic species, the chemical bonding structure of a material also strongly determine its electronic and mechanical properties. In terms of electronegative materials, a structure is required which produces many low energy unoccupied electron orbitals which can subsequently be filled. Low energy orbitals usually arise from strong chemical bonds and coherent molecular structures. One example of such a molecular structure is that of the previously mentioned electrophilic tetracyanoethylene (TCNE). Carbon-nitrogen triple bonds have an incredibly high bond dissociation energy of 9.23 eV (Luo, 2002), which shows that electrons participating in such bonds are in low energy states. This is similarly exhibited for the carbon-fluorine (C–F) bond, having the highest dissociation energy for a single covalent bond at 4.70 eV, and the carbon-oxygen double bond (C=O) with a bond dissociation energy of 7.72 eV. These bonds also exhibit a high dipole moment, caused by the drawing of electrons away from the carbon atom and towards the corresponding electrophilic atom. This implies that the unoccupied low energy states associated with these bonds are located closer to the carbon atom.

Little research has been taken into electropositive materials, which is counterintuitive as these materials act as a source for electrons during triboelectric transfer. Metals have mostly been used as electro-positive conducting electrodes, despite their inability to place high in any empirical triboelectric series (Diaz and Felix-Navarro, 2004; Ding et al., 2018). Metals are inherently dense and tightly bonded, resulting in favourably high mechanical moduli and surface energies. Recent work has reported the use of polyethylene oxide (PEO) as a highly effective electro-positive material, more so than the initially-used Nylon 6-6 (Ding et al., 2018). Polyvinyl-2-pyridine (PV2P) has also been tested as highly electro-positive insulating material (Diaz and Felix-Navarro, 2004). The underlying physical reasons behind these results have however not been investigated sufficiently.

The origin of electron donor tendencies in polymers such as Nylon and Delrin may arise in hydrogen bonding between individual polymer chains. Hydrogen bonds are a form of Keesom interaction which occur between hydrogen atoms and other electrophilic atoms in a medium. Normally hydrogen atoms have very little electron density surrounding them when they are involved in chemical bonds with other elements, since its single 1s electron is involved in covalent bonding. A result of this is that the positively charged hydrogen nucleus is more exposed to its surroundings, and is subject to electrostatic attraction from nearby electron densities. Simultaneously, nearby electrons will feel the electric potential exerted by the hydrogen nucleus and their orbitals become distorted into higher energy arrangements. It is possible that these electrons are donated to counter surfaces during triboelectrification as a result of their higher energy states. The polymer structure of Nylon is composed of multiple amide groups, which involve a hydrogen atom covalently bonded to an electrophilic nitrogen atom. These groups also contain a ketone group within themselves, which consists of an electrophilic oxygen atom double-bonded to the carbon polymer chain. In Nylon these amide groups align and form inter-chain hydrogen bonds (Garcia and Starkweather, 1985).

If we are to assume that triboelectric charge transfer occurs primarily through the transfer of excited electrons after interacting with phonons within a donor material (Pan and Zhang, 2017), a wide-spectrum of available phonon energies will be needed; i.e. a highly irregular material structure. It is because of this that polymers are a prime candidate for triboelectric contacts. If the material in a triboelectric contact has too regular a structure, the phonon energy window arising from lattice deformations may be too uniform and too small to transfer a wide range of electrons. The inclusion of mechanical moduli such as elastic modulus (Y^*) is most certainly an important aspect to consider when deriving relationships involving mechanical contact. The importance of tribological factors is further highlighted when considering the use of viscoelastic materials such as polymers; materials very popular triboelectric interfaces. Indeed, the contributions of tangential stresses and shear strains during friction are also in need of further investigation.

1.5.2 Contact Force and Surface Roughness

Before describing the current theories that describe the influence of contact force and surface roughness on triboelectric charging, an overview of topographical parameters is given and referred back to throughout this thesis.

The easiest parameters to calculate for a given surface are the maximum peak height (S_p) and maximum valley depth (S_v) which are simply treated as the maximum and minimum height values for a given heightmap. These are often given in reference to the arithmetic mean height value of the surface. The difference between these two values give the total height range of the surface (S_z).

The most common parameter that tribologists refer to when discussing the roughness of a surface is the arithmetic mean roughness S_a . This parameter describes the average deviation in height from its mean value z_0 across the surface being considered. The value for z_0 is simply treated as the arithmetic mean of all the height values being considered, which can be treated as either a finite sum in the case of typical height map data or as an integral of a 2D function that described the surface.

$$z_0 = \frac{1}{A_n} \iint z(x, y) dx dy \quad (1-112)$$

Therefore S_a can be defined as the mean of this deviation from the mean height value.

$$S_a = \frac{1}{A_n} \iint |z(x, y) - z_0| dx dy \quad (1-113)$$

A similar parameter that is also used to describe the deviation in height of a given surface is the root mean square (rms) roughness (S_q), which is expressed below.

$$S_q = \sqrt{\frac{1}{A_n} \iint |z(x, y) - z_0|^2 dx dy} \quad (1-114)$$

Whilst S_p , S_v , S_z , S_a and S_q all describe the magnitude of surface roughnesses, they do little to describe the distribution of these heights and the nature of asperities. Two additional parameters are often used to describe these factors, known as the surface skewness (S_{sk}) and kurtosis (S_{sk}). The skewness of a surface describes where the surface distribution lies relative to the mean value. A positive skewness

implies that the majority of a surface is 'skewed' below the mean plane, with its surface topography dominated by asperities. A surface with a negative skewness is therefore dominated by valleys and pits.

$$S_{sk} = \frac{1}{A_n S_q^3} \iint |z(x, y) - z_0|^3 dx dy \quad (1-115)$$

The kurtosis of a surface describes the 'sharpness' of asperities. A kurtosis value between zero and three describes a platykurtic distribution and broad asperities, whereas a kurtosis value higher than three implies a leptokurtic distribution and sharper asperities. A kurtosis value of 3 exactly implies a normal mesokurtic height distribution. An exceedingly high kurtosis value for a surface scan may also imply the presence of anomalous values, causing an unusually sharp peak or pit across one datum of a height map.

$$S_{ku} = \frac{1}{A_n S_q^4} \iint |z(x, y) - z_0|^4 dx dy \quad (1-116)$$

Another useful roughness parameter for determining the spatial and height distribution of asperities is the arithmetic mean slope $S_{\Delta a}$. This is calculated by averaging the gradient of a given surface.

$$S_{\Delta a} = \frac{1}{A_n} \iint \Delta z(x, y) dx dy = \frac{1}{A_n} \iint \left(\frac{\partial z(x, y)}{\partial x} + \frac{\partial z(x, y)}{\partial y} \right) dx dy \quad (1-117)$$

A useful visual description of surface skewness and kurtosis is given by (Zeng et al., 2018), which is displayed below as Figure 1-26.

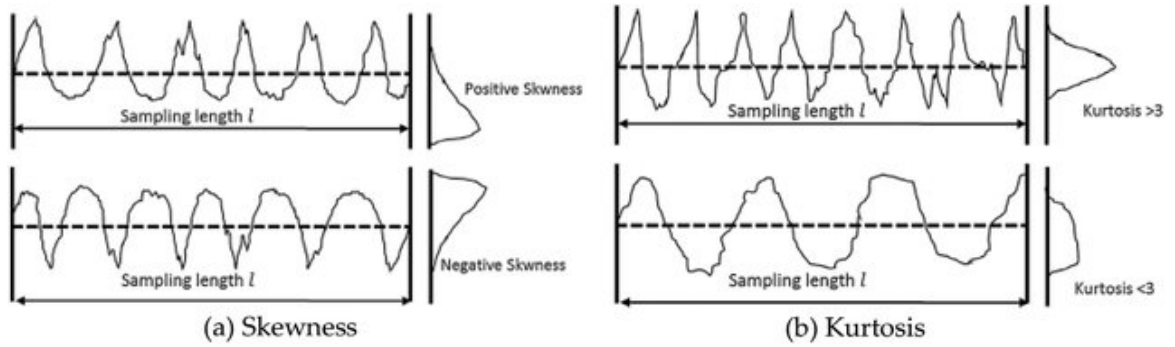


Figure 1-26 – A visual depiction of surface skewness R_{sk} and kurtosis R_{ku} , as given by (Zeng et al., 2018). The left side of the four example plots are direct height maps, whereas histograms of their height distributions are placed to the right of each plot.

Further research using specific TENG orientations and differing material properties have revealed that contact force is proportional to transferred charge (Seol et al., 2017a; Vasandani et al., 2017). This is explained by how increasing the contact force (F_z) of a contact generally increases the real area contact (A_r) by deforming surface asperities into a more conforming shape; as well as by increasing the number of asperities in contact. A semi-empirical relationship has been derived by Vasandani et al. (Vasandani et al., 2017) to describe this dependence on charge transfer (Q).

$$Q = \frac{(\phi_2 - \phi_1) A_r \epsilon_0}{3 q_e z_0} \quad (1-118)$$

The statistical contact model of Bush et al (Bush et al., 1975) is used to estimate the real area of contact, where the contact is treated as fully elastic, and contacting asperities are treated as identical paraboloids in Hertzian contact.

$$A_r = \frac{F_z}{Y^*} \sqrt{\frac{\pi}{\langle R_{\Delta q} \rangle}} \quad (1-119)$$

Y^* is the equivalent elastic modulus of the contact, as a function of the Young's moduli (Y_i) and Poisson's ratios (ν_i) of the respective contacting surfaces.

$$Y^* = \frac{Y_A Y_D}{Y_D(1 - \nu_A^2) + Y_A(1 - \nu_D^2)} \quad (1-120)$$

$\langle S_{\Delta q} \rangle$ is the composite root-mean-square slope of the two contacting surfaces (Ω), each with their respective height maps as a function of position $z(x, y)$. $\langle S_{\Delta q} \rangle$ is calculated simply by averaging the $S_{\Delta q}$ of both surfaces, with the value of $S_{\Delta q}$ for a given surface being described by (Vasandani et al., 2017) as stated below.

$$S_{\Delta q} = m_2 = \frac{1}{N} \sum_{n=1}^N \left(\frac{dz(x)}{dx} \right)_n^2 \quad (1-121)$$

Whereas the more mathematically robust, widely used alternative for calculating the RMS slope of a given surface is $S_{\Delta q}$, defined by Li et al. (Li et al., 2000) as stated below.

$$S_{\Delta q} = \sqrt{\frac{1}{A_n} \iint |\Delta z(x, y)|^2 dx dy} = \sqrt{\frac{1}{A_n} \iint \left(\left(\frac{\partial z(x, y)}{\partial x} \right)^2 + \left(\frac{\partial z(x, y)}{\partial y} \right)^2 \right) dx dy} \quad (1-122)$$

A_n is the nominal area of contact between the two surfaces. Equation (1-119) is further refined by (Xu et al., 2020) through the utilisation of Persson's contact theory to more accurately predict the real area of contact.

$$A_r = A_n \operatorname{erf} \left(\frac{F_z}{A_n Y^*} \sqrt{\frac{1}{\langle S_{\Delta q} \rangle}} \right) \quad (1-123)$$

A flaw in this relationship between contact force and triboelectric charge transfer is that it assumes that surface charge density (σ) is dependent on the applied force only through this evolution of real contact area. The assumption is made here that the surface charge density is independent of contact pressure, where in-fact more recent models (Mizzi and Marks, 2022) have proposed that localised pressure distributions and their resulting strains have a significant influence on charge transport.

The surface structure of a triboelectric material has also the potential to be modified to increase the real surface area of the contact; in turn increasing the transferred charge (Thomas III et al., 2009; Tcho et al., 2017; Vasandani et al., 2017). Polydimethylsiloxane (PDMS) surfaces have been nano-textured through different methods to explore the effects of surface nanostructures in triboelectric charge transfer (Vasandani et al., 2017; Tcho et al., 2017).

Altering the surface roughness (Vasandani et al., 2017) as well as the nano-texturing of surfaces to create dome and pillar-like nanostructures (Tcho et al., 2017) has been used to explore the durability and

efficiency of triboelectric surfaces. Hysteretic behaviour has also been observed in textured PDMS and Teflon triboelectric contacts in terms of surface charge retainment and dissipation (Seol et al., 2017a). As previously mentioned, surface topography also influences the wetting behaviour of substrates by enhancing any liqueophobic/philic behaviours that are inherent of the surface's chemical structure (Bhushan, 2012).

1.5.3 Temperature

The temperature within a triboelectric contact plays a significant role in contact and frictional electrification; both through its influence on material mechanical properties and the thermodynamic processes that drive charge transfer. Temperature has a significant influence on the thermodynamic properties of electrons within a material. At absolute zero temperature, the Fermi-Dirac distribution of electron energies is simply a step function, where the highest energy state that an electron can occupy is strictly defined as the Fermi energy. It is only at zero temperature that the Fermi energy and Fermi level are identical. As thermal energy is introduced to a system of electrons, the Fermi-Dirac distribution smoothens out as electrons are subjected to random thermal excitations. At temperatures above absolute zero the Fermi energy of a system is no longer clearly defined due to the now probabilistic nature of state occupation.

The introduction of thermal energy implies that electrons exist with energies in excess of the Fermi level, as well as vacated states now existing below it. This has been shown to enhance triboelectric charge transfer between conducting materials through the use of temperature controlled AFM measurements of nanoscale contact electrification (Wang and Wang, 2019). As previously stated, the role of quantised thermal vibrations known as phonons and their interactions with electrons influence triboelectric charging by providing a wider spectra of energy states for electrons to transition between. It has been theorised that the introduction of thermal energy through frictional heating enhances triboelectric charging of surfaces through thermoelectric effects (Z. Zhang et al., 2021).

Wen et al. (Wen et al., 2014) highlighted the importance of thermal fluctuations in the role of thermodynamic phenomena. Since additional thermal energy is available to both surfaces at higher temperatures, it is theorised that the possibility for electrons to tunnel back across the material interface is increased; reducing the efficiency of charge transfer rather than enhancing it. Tests were conducted at temperatures ranging from -198°C up to 227°C on perfluoroalkoxy alkane (PFA) on aluminium contacts (Wen et al., 2014). It was observed that the triboelectric charge generated between the surfaces has a complex relationship with temperature; rising steadily up with temperature up to an optimum value, then dropping drastically as depicted in Figure 1-27 below.

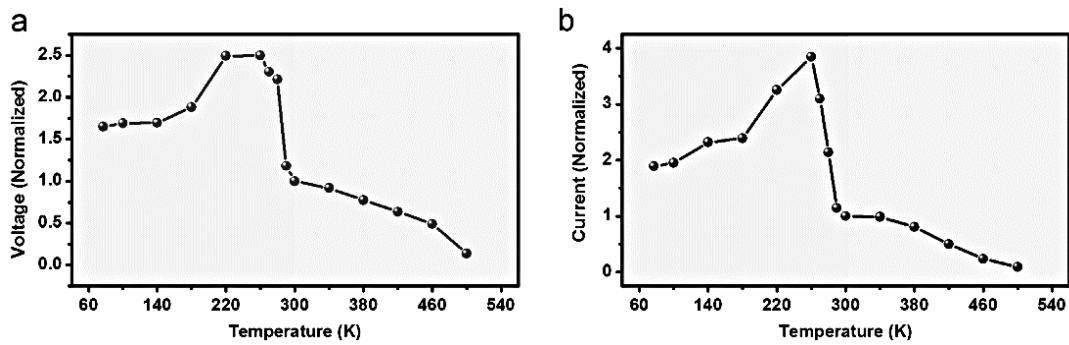


Figure 1-27 – Temperature dependence on output Voltage and Current of an Aluminium-PFA (50mm x 50mm apparent contact area, PFA film thickness not stated but constant) oscillating triboelectric contact, attached to a 5M Ω load resistance as depicted by (Wen et al., 2014).

Material pairings with differing thermal and electrical conductivities can amplify or inhibit these thermal fluctuations. Since aluminium is an electrical conductor and PFA is an insulator, this is most probably the explanation for the observations of Wen et al (Wen et al., 2014). Due to this competition between multiple processes, it becomes evident that the role of surface topography plays a much more significant role at low temperatures.

In terms of mechanical properties, it is widely known that the elastic modulus (E) of most materials decreases with increasing temperature (Zakarian et al., 2019). This decrease in E causes an increase in real contact area (A_r) as the topographies of the materials in contact more easily conform to each other. In addition to this, a reduction in the mechanical moduli of contacting materials due to temperature increase can lead to increased rates of material wear (Briscoe and Sinha, 2002; Tewari et al., 2014).

1.5.4 Ambient Medium

Another important factor that influences the transference of triboelectric charge across an interface is the ambient medium in which the interface exists. It has long been observed that electrostatically charged surfaces gradually return to an electrically neutral state over time when exposed to an ambient medium such as air. The cause of this loss of surface charge is the occurrence of charge exchange interactions between the charged surface and particles in the air, in addition to the thermionic emission of surface electrons in exceptionally high energy states. As a result, electrostatically charged surfaces retain these surface tribo charges for a significantly longer amount of time when placed within a vacuum. This retainment of charge within a vacuum causes several implications for tribological applications in space (Francis, 1982).

In the presence of an ambient medium, the composition of said medium also influences the retainment of triboelectric charges, as well as the mechanisms for charge exchange. The presence of water molecules in the form of humidity is known to significantly affect the charging characteristics of contacting surfaces. Studies have been conducted into quantising the effects of relative humidity and ambient pressure on the performance of triboelectric applications. It was found that a 20% increase in generated charge occurred as a result in lowering the ambient relative humidity from 90% to 10%. It was also shown

that the generated charge was reduced as the ambient pressure was reduced from atmospheric levels to 50Torr whilst the relative humidity was close to 0% (Nguyen and Yang, 2013). (Lax et al., 2020)

Increasing relative humidity and water presence has been shown to decrease the resistivity and dielectric breakdown strength of air (Nguyen et al., 2015) which may lead to counterproductive discharging within a triboelectric contact. It is also theorised that a layer of water at the interface can dissipate generated charges and increase surface conductivity. (Nguyen and Yang, 2013) As well as, in some cases, the adsorption and absorption of water molecules into the contacting surface structures. Nylon is a material known to readily absorb water by creating hydrogen bonds with the amide groups that compose its polymer structure (Hoshina et al., 2020). This relationship between charge transfer and humidity has been observed by Nguyen et al. (Nguyen et al., 2015) where TENG set-ups displayed a lower contact potential difference with water being present within the contact. A lower CPD was also observed after dropping small amounts of water onto hydrophilic contact materials such as Nylon 6 (PA6); this affect was considerably lessened with hydrophobic materials such as Teflon.

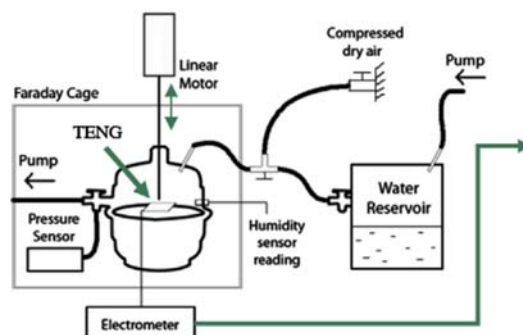


Figure 1-28 – Experimental setup used by Nguyen & Yang (Nguyen and Yang, 2013) to investigate the effects of humidity and ambient pressure on PDMS-AI contact-separation mode triboelectric nanogenerators (TENGs).

Oxide and contaminant films, as well as the relative environmental humidity, have been shown to reduce contact electrification between certain contacts (Nguyen and Yang, 2013; Nguyen et al., 2015; Seol et al., 2017b). Oxide layers and contaminant films alter the surface chemistry of triboelectric contacts, and in most cases this reduces the amount of transferred charge.

1.5.5 Friction

Despite the comprehensive models implemented to describe contact electrification, the specific role of tribological factors such as friction, material wear, and surface fatigue have largely been overlooked until recently. The aim of this research is to investigate the role of sliding friction on triboelectric charging between polymers under a matrix of controlled tribological parameters. The resulting semi-analytical model and accompanying equations describe the role of phonon-electron interactions in the expedition of triboelectric charging, as well as complimenting existing research on the modification of saturation charge densities through flexoelectric perturbations in surface potential (Mizzi and Marks, 2022). Tribology in itself is the study of interfacial interactions. It mostly encompasses interactions of the mechanical nature but often expands into surface chemistry and physics, in addition to being applied to countless applications within industry and medicine.

The importance of surface stresses and deformation has already been highlighted by (Mizzi and Marks, 2022) through the generation of flexoelectric perturbations in surface potential. The influence of friction-generated phonon-electron interactions has also been explored by (Pan and Zhang, 2017). The following chapters will provide experimental data to aid in validating these theories, as well as providing additional insight into how tribological processes may affect triboelectric charging within potential applications.

1.6 Applications of the Triboelectric Effect

1.6.1 Implications

Triboelectric charge transfer and resulting electrostatic charge build-up can have unwanted impacts in many engineering applications. In the processing and transport of pharmaceutical powders, triboelectric charging occurs between individual particulates and causes the electrostatic ‘clumping’ and resultant blockages in powder handling systems (Šupuk et al., 2012). This is a similar mechanism to how dust grains within sand storms and dust clouds resulting from volcanic eruptions accumulate charge, which is subsequently dissipated in the form of lightning (Gu et al., 2013). In electronics, electrostatic discharge from the recombination of triboelectrically separated charges between clothing and skin can cause the failure of sensitive electronic components (Cilveli et al., 2020).

Triboelectric charges may also be generated within flowing fluids, as well as upon surfaces across which fluids flow. For example, in fuel transport systems, triboelectric charges are generated between the fuel molecules and vessel walls, as well as within the fuel itself as it flows through the system. Therefore, fuel transport systems are effectively grounded in order to quickly dissipate such charges before they are able to accumulate to the point where a discharge may cause fuel ignition (Kiss et al., 2005). Similarly, in aerospace applications, great care is taken to mitigate the accumulation of triboelectric charges on the fuselages of aircraft from interactions with air, ice, and water particles in-flight (Zarrebini et al., 2013).

1.6.2 Benefits

This electrostatic charge accumulation can instead be beneficial in some applications; most notably in harnessing the relative movement of triboelectric charges for energy recycling and sensing technologies (Zhu et al., 2013; Wang, 2017a; Chen and Wang, 2017). It has also been speculated for use in a wide variety of potential self-powered devices (Wang et al., 2015). For such applications it is important to maximise the transferred charge density between the contacting surfaces, rather than current applications where great effort is taken to inhibit the build-up of electrostatic charge. Maximizing the spatial density of triboelectrically generated charges allows for the most effective generation of electrical power through electrostatic induction (Wang, 2017a). This section provides a brief overview of the main applications of triboelectric charge transfer to industry and everyday life; as well as any challenges that remain to be overcome.

1.6.2 Triboluminescence

First observed by Picard in 1675, and noted in the observations of Hawksbee (Hawksbee, 1709), triboluminescence is a phenomenon often described as a by-product of triboelectric charge transfer. It occurs upon the separation of media between which triboelectric charges are separated and trapped, which is not limited to solid interfaces. It is a form of mechanoluminescence where a material emits photons when subjected to some form of mechanical disturbance.

It is theorised that, as triboelectrically charged surfaces are separated, the trap states which the transferred electrons inhabit increase in energy upon exposure to the ambient medium (Wang and Wang, 2019). This increase continues as the charges further separate, until it becomes energetically favourable for these electrons to discharge and travel through the ambient medium back to their original donor surface. This electrostatic discharge (ESD) causes the ionisation of particles within the conducting medium, which in turn emits observable photons (Keithley, 1999), as well as audible phonons through the rapid thermal expansion of the conducting medium. The most prominent example of such ESD is that of lightning where triboelectric charges accumulate between water droplets and ice crystals – different phases of the same substance – and are subsequently conducted through the air to the ground across large distances (Dash and Wettlaufer, 2011). This form of triboluminescence is known as gas discharge triboluminescence. Triboluminescence may also refer to the coronal discharge of materials that generate a substantially high enough surface potential to ionise the surrounding air and produce a photon-emitting electrically-conductive plasma, similarly to gas discharge. Coronal discharge is observed within van de Graaff generators (Van De Graaff et al., 1933). As charges accumulate between the two insulating rollers and collector belt, the resulting high voltages ionise the surrounding air. This ionisation in the presence of an electric field draws a current from the nearby conductive combs. It is important to note that the characteristic ‘sparking’ that is traditionally observed with the use of a van de Graaff generator is gas discharge arising from the dielectric breakdown across the space between the two *prime conductor* charge-storing spheres as a significantly high voltage is generated.

Through this understanding, it may appear reasonable to assume that triboluminescence may not occur within a vacuum environment. The absence of a conductive medium, such as air, would make it considerably harder for the trapped electrons to arc back towards their donor surface. If the trapped electrons do manage to tunnel back to their donor surface, similarly to electron transfer within a cathode-ray tube, no photons will be emitted since the electrons do not interact with the vacuum whilst they travel through it. Contrary to this assumption, the emission of 30 keV x-ray photons has been observed from the peeling of adhesive tapes and the separation of mica in a vacuum environment (Camara et al., 2008). This separate form of triboluminescence is not gas discharge triboluminescence. These x-rays are instead Bremsstrahlung photons, generated from the recombination of previously tribo-separated high energy electrons within the donor surface rather than through any interactions with an ambient medium. These triboelectrically generated high energy photons have already been conceptualised as an affordable alternative for medical x-ray generation in the same publication. Triboluminescence has also been linked

to other forms of mechanoluminescence, citing friction as an instigating force for effects such as thermoluminescence and fractoluminescence in crystalline materials (Walton, 1977).

1.6.3 Triboelectric Nanogenerators

The most prominent beneficial application of the triboelectric effect in engineering is that of the triboelectric nanogenerator (TENG). Initially devised in 2012 TENGs are devices that use isolated electrical charges – produced through triboelectric charge transfer – to drive a current through an external circuit using electrostatic induction (Chen and Wang, 2017). Much of the electrical properties of these devices have previously been investigated (Niu, 2015) but research into optimising the tribological aspects of TENGs have only been undertaken in a small sample of materials; as well as using one specific orientation of device for each specific application (Vasandani et al., 2017; Tcho et al., 2017; Ding et al., 2018). The past decade has witnessed a remarkable progress in the development of TENG applications through their potential use as power sources and as self-powered sensors (Chen and Wang, 2017).

The triboelectric nanogenerator has been viewed as a fundamentally novel technology (Luo and Wang, 2020). However, it may be more accurate to describe it as the revival of technologies such as the previously mentioned ‘friction machines’ of the 18th century. With considerable scientific progress in the understanding of electricity and the nature of matter as a whole, research conducted in the 20th century and the consequent miniaturisation of electronic technologies has opened up a new field for the triboelectric effect to be applied to. TENGs have been cited as the most promising technology to revive the field of vibration and waste mechanical energy harvesting, as well as self-powered sensing. This especially for low-frequency oscillations such as human motion, automobile, machine, and acoustic vibrations (Chen and Wang, 2017). TENGs have the potential to be used for a wide variety of applications. These applications can be categorised into two main areas; self-powered devices and self-powered sensing (Wang, 2017a; Chen and Wang, 2017). Wang (Wang et al., 2017) has also suggested the possibility for harnessing the mechanical energy of water waves to drive macro-scale TENGs.

TENGs are highly efficient at harnessing low frequency oscillating sources of mechanical energy. They generally are a low cost, low weight and low density solution for powering small devices. Their disadvantages are that they have a high electrical impedance and require more complex power management circuits due to their high-impedance, high-voltage, and low-current pulse-like power output (Mitcheson et al., 2008; Xi et al., 2017; Yang et al., 2018). The voltage and current output characteristics of TENG devices can be altered somewhat by changing the impedance characteristics of the external circuit. It has previously been shown that the output power of a TENG can be maximised through optimising the impedance of a purely resistive external circuit to around 0.1 GΩ (Niu, 2015).

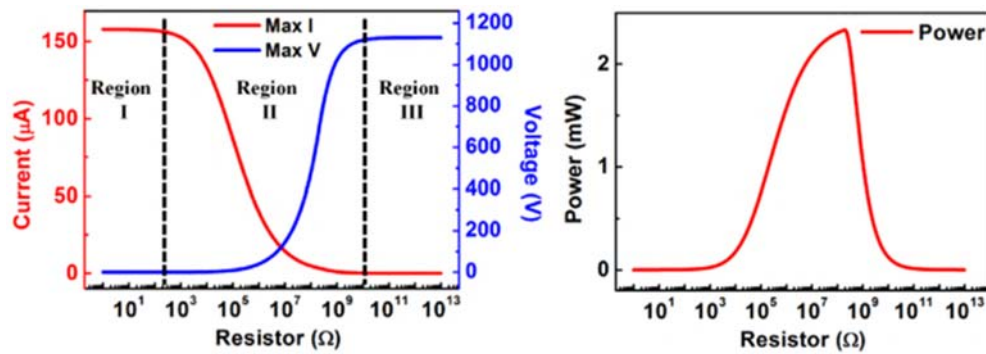


Figure 1-29 – Peak current and voltage output (left) and power output (right) for generic TENG applications with varying external resistances as calculated using finite element analysis (FEA) techniques (Niu, 2015).

Each mode and orientation of TENG is capable of harnessing different forms of mechanical and tribological contact; from impact forces that arise when walking (Hou et al., 2013) when placed inside the sole of a shoe, to sliding friction between layers of clothes (Ha et al., 2015). Since TENGs are based on frictional and contact electrification, their very nature requires materials to be put in contact with each other; raising the question of material wear and the longevity of these devices after extensive use. (Chen and Wang, 2017).

Another speculated application for TENG devices is in the recently conceived field of tribotronics. Tribotronics involves research into the application of TENG devices within nanoscale electronics. The most prominent development within this field is the creation of a triboelectric transistor (Xi et al., 2018). A triboelectric transistor operates in a similar fashion to a traditional semi-conducting transistor which allows for current to pass through it when a given gate voltage is applied. Triboelectric transistors differ from traditional transistors in the sense that the gate potential is provided by triboelectric charge transfer between contacting elements. This has the potential to be useful for microelectromechanical (MEM) applications.

The capabilities of TENGs are described in various literature and their applications are summarised in several literature reviews (Wang, 2017a; Wang et al., 2017; Chen and Wang, 2017). They have been demonstrated to have an instantaneous conversion efficiency of up to approximately 70% with a total energy conversion efficiency of up to 85% (Chen and Wang, 2017). An extremely wide working bandwidth of up to 127Hz has also been achieved for low-frequency (<150Hz) vibration energy harvesting (Chen and Wang, 2017).

TENGs are generally no larger than several centimetres in surface area and less than a centimetre in thickness, with contacting larger ranging in thickness from several microns up to several millimetres. The inclusion of the prefix 'nano' originates from the original inventor of the TENG – professor Zhong Lin Wang – and his initial investigations into using zinc oxide nanowires for use in piezoelectric nanogenerators. It is also implied that the inclusion of this term is also related to the miniaturisability and high volumetric power output of TENG devices, quoted in the range of 1-100 mWcm⁻² (Wang, 2017b). The typical output of a TENG is a pulsed current, with the exact shape of the pulse dependant on the

geometry and form of contact being utilised. This form of output characteristic is difficult to convert into useful alternating current or direct current forms, although research has suggested several configurations of power management system to circumvent this challenge (Yang et al., 2018). The high impedance nature of TENG devices also present a similar challenge in that a typical output exhibits high voltage pulse amplitudes (ranging from 1V – 1kV) and low current amplitudes (ranging from 10 nA to 1 μ A) that are also time dependant over the lifetime of the device.


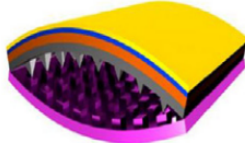
	Electromagnetic generator	Triboelectric nanogenerator
		
Mechanism	<ul style="list-style-type: none"> ● Electromagnetic induction; ● Resistive free electron conduction driven by Lorentz force 	<ul style="list-style-type: none"> ● Contact electrification and electrostatic induction; ● Capacitive displacement current arising from time-dependent electrostatic induction and slight motion of bonded electrostatic charges
Pros	<ul style="list-style-type: none"> ● High current, low voltage; ● High efficiency at high frequency; ● High durability, long life 	<ul style="list-style-type: none"> ● High voltage, low current; ● High efficiency at low frequency; ● Low cost, low density, low weight; ● Multiple working modes; ● Diverse choice of materials; ● Diverse use of fields; ● Broad use as sensors
Cons	<ul style="list-style-type: none"> ● Low impedance; ● Heavy, high density; ● High cost 	<ul style="list-style-type: none"> ● High impedance; ● Low durability

Figure 1-30 – Comparison of TENG technology with the electromagnetic (EM) generator, highlighting the advantages and disadvantages of both with regards to applications.

1.6.3.a Device Geometries

Triboelectric nanogenerators operate through coupling the principles of triboelectric charge transfer and electrostatic induction. Therefore a typical TENG device must consist of a mechanical contact that undergoes some form of cyclic motion. This contact generally involves two contacting surfaces. A higher number of contacting surfaces are possible within a TENG device, although this can then generally be treated as a composition of multiple triboelectric contacts. The nature of the contacting surfaces can be either solid or liquid, and examples of both are given in literature where solid-solid TENG devices are more common (Wang et al., 2017).

As two insulating solid surfaces are brought into contact, triboelectric charge transfer occurs between them, and electrostatic charges of equal magnitude and opposing polarities become trapped on either side of the contact. For the case of a solid-liquid triboelectric interface, charges are trapped on the solid insulating surface, whereas they remain more mobile within a non-conducting liquid medium due to the free-flowing convective nature of its molecular structure.

The presence of water is theorised to play an important role in charge transfer since water has been proven to be highly electro-positive due to the polar structure of water molecules (Burgo et al., 2016). This characteristic may be used advantageously, and may even lead to the use of water as a conductive electrode or triboelectric layer in possible hydro-triboelectric nanogenerator applications (Kim et al., 2018; Lee and Hwang, 2018).

The triboelectric contacts within solid-solid TENGs are normally plate-on-plate in nature. The highly conformal geometry of these contacts arises from the need to generate large amounts of electrostatic charge for practical applications. The relative motion of the two surfaces – whether it be in contact or out of contact – creates a time-dependant electric field between these charges as they separate and recombine. The remaining component for a TENG device is a means to measure or harness this electric field to the fullest extent.

For most forms of TENG device construction, the contacting triboelectric layers are thin relative to the dimensions of the contact, and are backed with a conductive material (Niu, 2015). As trapped electrostatic charges develop on each contacting surface, the electric field produced by these charges interacts with free electrons within the conductive layers, polarising them and creating what are known as ‘*mirror*’ charges. These conductive layers are therefore used as electrodes, and their purpose is to provide mobile charges that can be induced by the movement of trapped charges within the TENG contact itself. For some cases of TENG device a contacting layer can also be conductive, provided that the counter-surface remains able to retain triboelectric charges when not in contact. For most TENG devices, there are two electrodes which are attached to and represent polarised charges on either side of the contact. Geometries of TENG exist where three or more electrodes are used in various methods to optimise electronic output (Xie et al., 2014), but two electrodes are used in this study for the sake of simplicity. The specific device geometry used for this study is further explained in 2.1.1 The F-TENG Contact.

The possible geometries of TENG devices are effectively limitless, since all that is needed is a method to generate and detect electrostatic charges developed through triboelectric charge transfer. Four prominent orientations were proposed in early publications on the development of TENGs; vertical contact separation, lateral sliding, single-electrode, and freestanding triboelectric layer. The example given for a contact separation TENG is given in Figure 1-31bii, the example given for a laterally sliding TENG is given in Figure 1-32bii, the example given for a single electrode TENG is given in Figure 1-31ai, and the example given for a freestanding triboelectric layer TENG is given in Figure 1-32ci. These configurations are initially described in the literature as being four modes of classification for triboelectric nanogenerators, despite there being significant overlap between them in terms of possible device geometries (Wang, 2017b).

Firstly, the nature of the contact can take many forms. Either the contacting surfaces could be brought into and out of contact through separation that is perpendicular to the plane of the contact as shown in Figure 1-31 – which is defined as ‘*vertical contact separation*’ in the literature – or the surfaces can remain in contact but slide across each other parallel to the plane of the contact as shown in Figure 1-32 – defined

as '*lateral sliding*'. Other forms of contact are also possible, such as some combination of the previous two forms, rolling contacts, or a solid-liquid interface.

The overall electrode configuration relative to the contact can also take several forms. For example, a single electrode may be used to represent a single side of the contact as shown in Figure 1-31a, Figure 1-32a and Figure 1-34a. This electrode is connected to electrical ground through the external circuit rather than a second electrode being used. This configuration is referred to as '*single electrode*' mode. With the use of two electrodes, there are two primary ways in which they can be utilised. They can be directly attached to either side of a single TENG contact, and the external circuit measures the flow of current and potential difference between them as shown in Figure 1-31b and Figure 1-32b, or a separate freestanding triboelectric layer is introduced in between the two electrodes as shown in Figure 1-31c, Figure 1-32c, Figure 1-33 and Figure 1-34b. The introduction of a freestanding triboelectric layer allows the TENG device to be treated similarly to a combination of two single-electrode outputs, where a separate contact occurs in proximity of either electrode. The nature of this freestanding layer can also differ, either being composed of an insulating or conductive solid, or even a free-flowing liquid medium as shown in Figure 1-34b.

Finally, the nature of each electrode can also be a field used to classify the nature of a TENG device. Either electrodes can be 'exposed' to the contact and used as a contacting layer as previously mentioned and depicted in Figure 1-31i and Figure 1-32i, or they can be coated with an insulating triboelectric layer in a configuration known as '*attached electrode*' in literature and depicted in Figure 1-31ii-iii, Figure 1-32ii-iii, Figure 1-33 and Figure 1-34. Due to the variety of possible configurations, a more effective form of classification than the existing four modes would be to determine the type of TENG device based on three primary factors. The first factor being the nature of the contact (i.e. contact-separation, lateral sliding, rolling, solid-liquid etc.), the second being the configuration of the electrodes relative to the contact (i.e. single electrode, dual electrode, freestanding triboelectric layer), and the third being the nature of the individual electrodes (i.e. attached electrode, exposed electrode). This classification matrix is more effectively depicted in Figure 1-31 and Figure 1-32 where previously mentioned configurations of TENG device are depicted and arranged into their respective classifications.

Contact Separation TENGs	a) Single Electrode	b) Dual Electrode	c) Freestanding Triboelectric Layer
i) Conductor-Insulator Exposed Electrode			
ii) Conductor-Insulator Attached Electrode			
iii) Insulator-Insulator Attached Electrode			

Figure 1-31 – Example configurations of contact separation TENG devices. Depicting the *conductive electrodes*, and respective *electronegative* and *electropositive* triboelectric insulating layers. The white box represents an arbitrary load circuit.

Lateral Sliding TENGs	a) Single Electrode	b) Dual Electrode	c) Freestanding Triboelectric Layer
i) Conductor-Insulator Exposed Electrode			
ii) Conductor-Insulator Attached Electrode			
iii) Insulator-Insulator Attached Electrode			

Figure 1-32 – Example configurations of laterally sliding TENG devices. Depicting the *conductive electrodes*, and respective *electronegative* and *electropositive* triboelectric insulating layers. The white box represents an arbitrary load circuit.

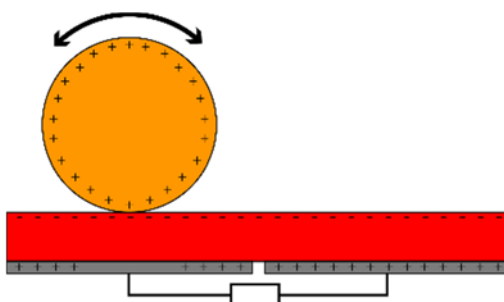


Figure 1-33 – Example configuration for a laterally rolling TENG device. Depicting the *conductive electrodes*, and respective *electronegative* and *electropositive* triboelectric insulating layers. The white box represents an arbitrary load circuit.

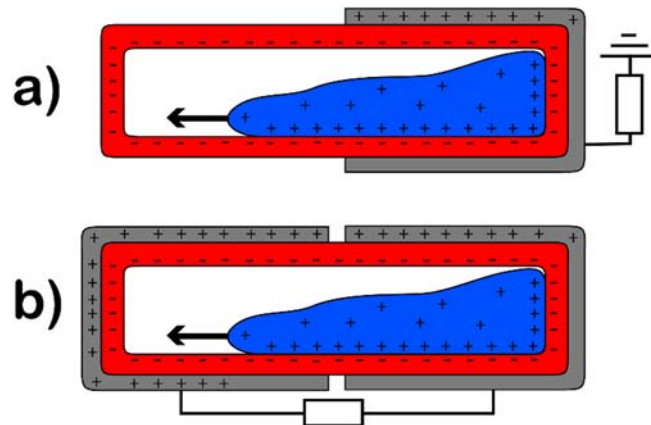


Figure 1-34 – Example configurations for a solid-liquid single electrode (a) and freestanding triboelectric body (b) TENG device. Depicting the *conductive electrodes*, *electronegative* triboelectric insulating layers and *charge-carrying liquid*. The white box represents an arbitrary load circuit.

1.6.3.b Electrical Properties

Triboelectric charge transfer between the contacting surfaces within a TENG generates trapped electrostatic charges on their respective surfaces. These surfaces are also connected through an external circuit, and their relative movement induces a current through said circuit as a result of electrostatic induction (Niu, 2015). The nature of the electronic output of a TENG device is dependent on several factors. The device geometry and the nature of mechanical contact, alongside the electrical properties of the external circuit, determine output characteristics such as electrical voltage and current. The following section will describe the electronic outputs of example TENG device configurations in compliance with the development of different existing models. Since an important aspect of what makes a TENG function is the generation of electrostatic charges, the interface across which these charges are generated exhibit capacitive behaviour. This allows for the charge-retainment element of the TENG contact to be approximated as a series of variable capacitors used in conjunction with a variable voltage source as shown in Figure 1-35.

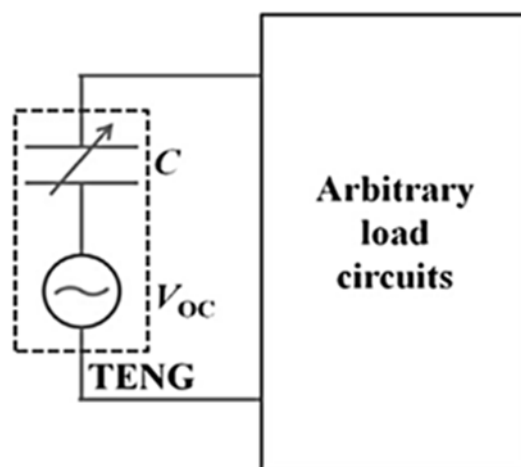


Figure 1-35 – First-order lumped-parameter equivalent circuit model of a typical triboelectric nanogenerator as shown by Niu (Niu, 2015).

The output power of a TENG can be optimised by modifying the resistance of the external circuit through which the induced charge flows between the conductive electrodes. In open-circuit (OC) mode, the resistance across the external circuit is infinite. For the case of a dual electrode TENG when both surfaces are contacting, the voltage across the external circuit is equivalent to zero as the electric fields of the trapped charges on each surface effectively screen each other. As the surfaces become separated, this screening effect is lessened with increasing separation distance and the voltage across the external circuit increases. Both cases are also dependant on the thickness of the triboelectric layers and the orientation of the electrodes, since the trapped charges within the TENG contact may not be equal in magnitude to the mirror charges they polarise within the electrodes due to the limited penetration of their resulting electric field. The voltage across an open circuit (V_{oc}) directly corresponds to the location of charges (Q) across it, as such as across a variable capacitor of capacitance (C) where no direct current is permitted to flow.

$$V_{oc}(t) = \frac{Q(t)}{C(t)} \quad (1-124)$$

The theory presented by Niu (Niu, 2015) treats the contact-separation TENG contact as an infinite plate capacitor, where the charges (Q) stored on it are the trapped charges (Q_T) on each insulating surface.

$$Q = Q_T = \sigma_T A \quad (1-125)$$

σ_T is the spatial charge density of the trapped charges on each surface, and A is the area of contact between the two surfaces. The dual electrode vertical contact separation configuration of TENG is the earliest experimentally demonstrated and usually agreed on as simplest form of TENG to model (Fan et al., 2012; Niu, Wang, et al., 2013), where the distance between the two triboelectric contacts is the variable that changes the effective capacitance between them (Niu, Wang, et al., 2013).

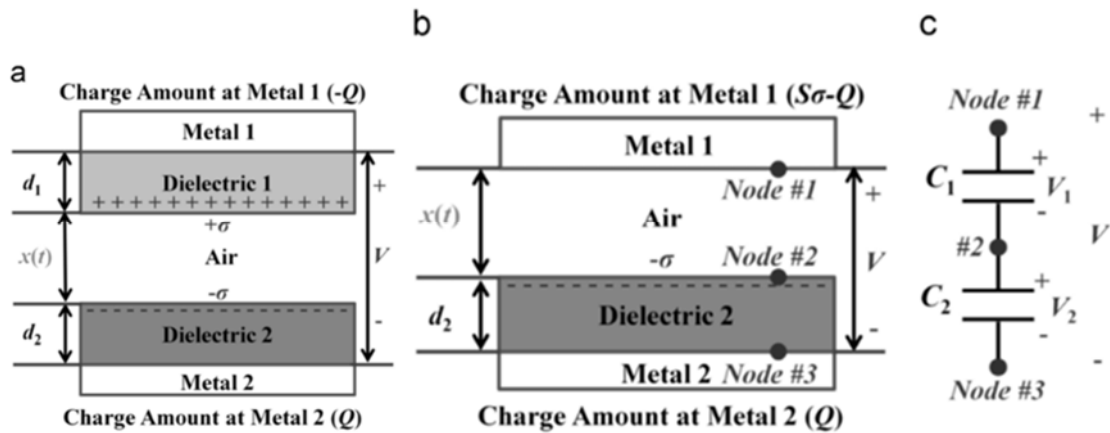


Figure 1-36 – Schematics for a double attached electrode contact-separation mode TENG (a) and an attached electrode contact-separation mode TENG (b) alongside a brief circuit section showing how the different sections of the device correlate to effective capacitances.

For the case of both electrodes being coated with an insulating layer to form the triboelectric contact, the internal contact capacitance between the trapped charges (C_c) on these insulating surfaces can therefore be expressed as below.

$$C_c(t) = \frac{\varepsilon_c A}{z(t)} \quad (1-126)$$

ε_c is the electric permittivity of the ambient medium between the trapped charges – often treated as a vacuum, and $z(t)$ is the separation distance between the trapped charges as a function of time. These equations are then combined in order to derive an equation for the open circuit voltage of the TENG device.

$$V_{OC}(t) = \frac{\sigma_T z(t)}{\varepsilon_c} \quad (1-127)$$

Laterally sliding mode TENGs (referred to as S-TENGs from hereon) have triboelectric layers that slide over each other, reducing the cross-sectional area of the contact to lower the contact capacitance (Wang et al., 2013; Yang et al., 2013; Niu, Liu, et al., 2013) instead of through manipulating the separation distance.

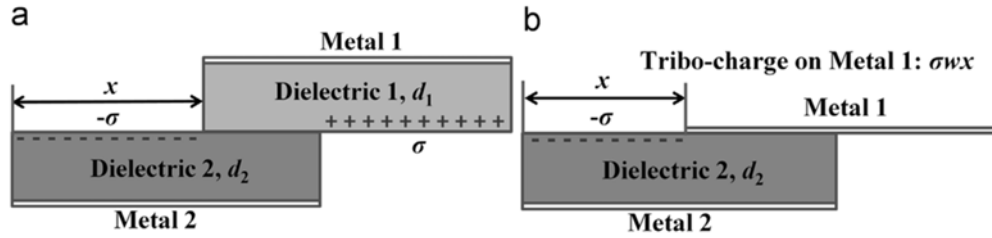


Figure 1-37 – Schematics for a double attached electrode linear in-plane sliding mode TENG (a) and an attached electrode S-TENG (b) as shown by Niu & Wang (Niu, 2015).

Therefore the change in contact capacitance arises from the change in cross-sectional area of contact for sliding TENG devices, rather than through the change in separation distance. Therefore equation (1-127) can be rewritten as below.

$$V_{OC}(t) = \frac{\sigma_T z_0}{\varepsilon_c} \left(\frac{L_x}{L_x - x(t)} \right) \quad (1-128)$$

z_0 is the separation of the trapped charges whilst they are in contact – normally assumed to be in the order of atomic separation, L_x is the length of the contact in the direction of lateral sliding (x), and $x(t)$ is the lateral between the two contacting surfaces – equal to zero when they are fully in contact and L_x as they slide out of contact. An obvious flaw in this equation is the prediction of an infinite open-circuit voltage for the case of the surfaces sliding out of contact with no overlapping contact area.

In short-circuit (SC) mode a current is permitted to flow through the external circuit as a way of balancing out the electric fields being generated at each electrode. The voltage response for the case of zero resistance (V_{SC}) is purely ohmic and corresponds to the current flowing through the external circuit in accordance with Ohm's law (Keithley, 1999).

$$V_{SC} = IR = R \frac{dQ_{SC}(t)}{dt} \quad (1-129)$$

Under short-circuit conditions, the mirror charges within each electrode (Q_{SC}) fully screen the electrical potential generated by the trapped tribo-charges. Therefore, the following equation is derived for TENGs under short-circuit conditions by Niu.

$$0 = V_{OC}(t) - \frac{Q_{SC}(t)}{C_{total}} \quad (1-130)$$

$C_{total}(x)$ is the total capacitance between the two electrodes, rather than between the surfaces of the contacting materials. It can be expressed as a function of C_c and the dielectric thicknesses of the insulating layers.

$$C_{total} = A(t)\epsilon_0 \left(\frac{1}{z(t)} + \frac{\epsilon_{r1}}{z_1} + \frac{\epsilon_{r2}}{z_2} \right) \quad (1-131)$$

ϵ_{ri} is the relative permittivity of material i , and z_i is the thickness of the respective layer. Thus, the fundamental relationship between Q_{SC} , C_{total} , and V_{OC} is expressed below.

$$Q_{SC}(x) = C_{total}(x)V_{OC}(x) \quad (1-132)$$

These two open-circuit and short circuit operating modes are depicted visually in Figure 1-38 for a vertical contact separation TENG.

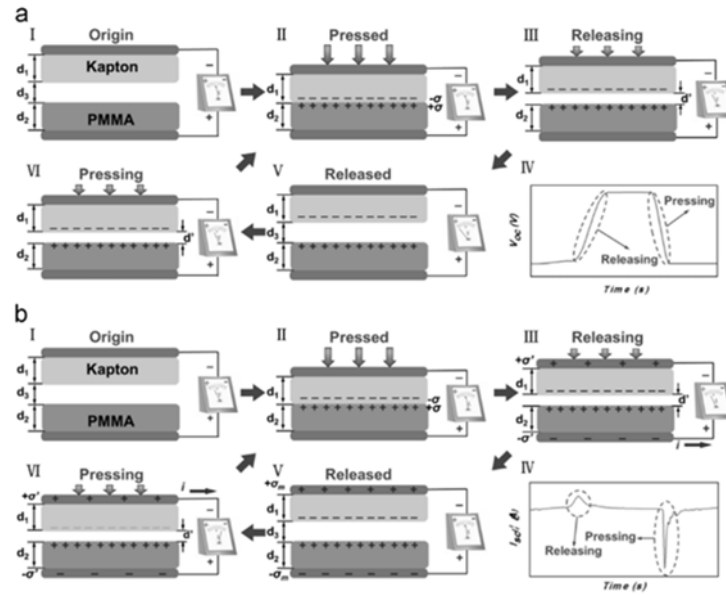


Figure 1-38 – Illustrating how a contact-separation mode TENG operates in open circuit (a) and short circuit (b) mode as shown by Vasandani et al. (Zhu et al., 2015).

If the impedance of the external circuit is non-zero and finite the electrical potential difference between the two electrodes of TENG consists of two parts. The first part is derived from the trapped triboelectric charges upon the insulating surfaces, and their contribution to the voltage is $V_{OC}(x)$. The second part being contributed by the movement of free charges within the electrodes to screen the electric field caused by the trapped charges, represented by $\frac{Q_R(t)}{C_{total}(t)}$. For the case of the external circuit consisting purely of a resistive load, this potential difference is expressed as below.

$$V_R(t) = R \frac{dQ_R(t)}{dt} = V_{OC}(t) - \frac{Q_R(t)}{C_{total}(t)} \quad (1-133)$$

This relationship is conventionally named as the V–Q–x relationship, with variables instead being expressed as a function of position, rather than time. This is stated as the governing equation of any TENG, and aids in explaining their inherent capacitive behaviour.

As well as the two previous two types of C-TENG, there can also be single-electrode and freestanding triboelectric layer C-TENGs that will be further explained in this literature. Niu & Wang (Niu, 2015) describe a single electrode TENG device using a reference electrode to act as electrical ground whilst having an effective capacitance between the primary electrode and hence the rest of the device.

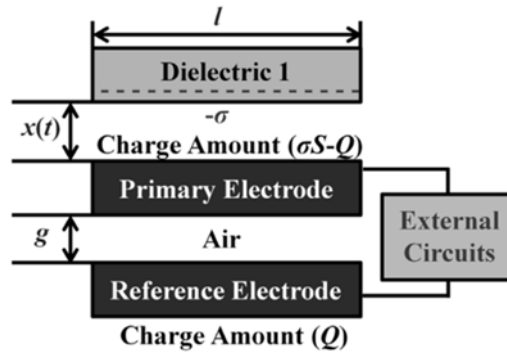


Figure 1-39 – A contact-separation mode single electrode TENG (C-SE-TENG) as described by Niu & Wang (Niu, 2015).

Freestanding triboelectric layer TENGs involve a third body that oscillates contact between the two electrodes attached to the external circuit. This layer can either be conductive or an insulator. A conductive freestanding layer would be required to be electrically isolated and oscillating contact between two insulating surfaces, whereas an insulating freestanding layer could oscillate contact between insulating or conductive surfaces (S. Wang et al., 2014; Niu et al., 2015).

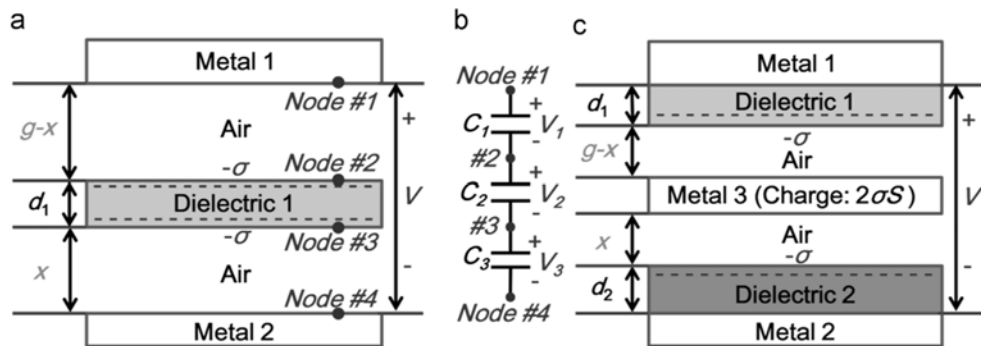


Figure 1-40 – Schematics for a contact-separation mode conducting F-TENG (a) and a dielectric C-F-TENG (c) as shown by Niu & Wang (Niu, 2015) with partial circuit diagram describing their capacitive behaviour (b).

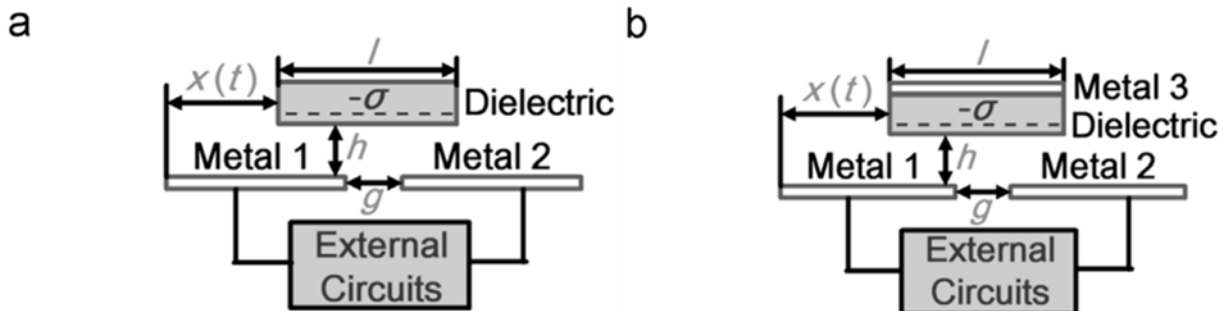


Figure 1-41 – Schematics for a linear in-plane sliding mode dielectric F-TENG (a) and a metal-coated S-F-TENG (c) as shown by (Niu et al., 2015).

The open-circuit voltages, short-circuit charges and subsequent V-Q-x behaviours of F-TENGs can be calculated by combining the capacitances of the different contact elements and electrodes as with previous dual electrode TENG orientations.

(Dharmasena et al., 2017) correctly highlighted that the assumption of contacting surfaces and their respective electrodes being infinite plates would mean that the electric field outside of the contact would be zero regardless of separation distance. Therefore, the fact that these surfaces and electrodes are finite in size is crucial to effectively modelling the electrical output of TENG devices. They instead proposed a model based on a distance dependant electric field (DDEF) which accounts for the finite geometry of the TENG device. This model is based on the following equation for electric field variation (\vec{E}_z) above the midpoint of a uniformly charged finite rectangular surface with dimensions L_x and L_y and spatial charge density σ .

$$\vec{E}_z(z) = \frac{\sigma}{\pi\epsilon_c} \arctan \left(\frac{L_x}{2z \sqrt{4 \left(\frac{z}{L_y}\right)^2 + \left(\frac{L_x}{L_y}\right)^2 + 1}} \right) = \frac{\sigma}{\pi\epsilon_c} \mathcal{F}(z) \quad (1-134)$$

z is the distance from the midpoint at which the electric field is being measured. Using this equation, it is then possible to evaluate the superposition of electric fields from multiple finite plates aligned along the z axis.

$$\vec{E}_{Total}(z) = \frac{1}{\pi\epsilon_i} \sum_i \sigma_i \mathcal{F}(z_i) \quad (1-135)$$

z_i is the location of the i^{th} plate along the z axis, and σ_i being the respective spatial charge density. This relationship can be further modified using the following relationship for describing how an electric field is permitted through differing media.

$$\epsilon_1 \vec{E}_1 = \epsilon_2 \vec{E}_2 \quad (1-136)$$

The assumption is also made that both plates have equal magnitudes of spatial charge density (σ_T) and surface dimensions (L) for simplicity, but the model is not limited to these assumptions and can be applied to contacts beyond this particular scope. The open circuit voltage of a dual electrode attached electrode TENG device can therefore be calculated as the electric potential at either electrode (V_i) solely in the presence of the trapped charges on their respective insulating surface (i.e. at an infinite separation of surfaces one can treat the opposing trapped charges as non-existent).

$$V_{OC} = V_i = \frac{\sigma_T}{\pi\epsilon_i} \int_{z_i}^{z_i+z_0} \mathcal{F}(z) dz \quad (1-137)$$

This integral is redefined as below.

$$\int_0^{z_i} \mathcal{F}(z) dz = [\mathcal{M}(z)]_{z_i}^{z_i+z_0} \quad (1-138)$$

The integrated function $\mathcal{M}(z)$ can then be evaluated as stated below.

$$\mathcal{M}(z) = z \arctan\left(\frac{L}{2z\sqrt{\frac{4z^2}{L} + 2}}\right) - \frac{L}{2} \log\left(\frac{\sqrt{\frac{4z^2}{L} + 2} + 1}{\sqrt{\frac{4z^2}{L} + 2} - 1}\right) \quad (1-139)$$

The short circuit current output for such a device can be calculated through the re-inclusion of both contacting surfaces, as well as the free charges ($-\sigma_U$) within the external circuit. The electric potential at each electrode can then be expressed as a function of the electric fields produced by both bound and mobile charges.

$$V_{ij} = \frac{\sigma_T}{\pi\epsilon_i} \int_{z_i}^{z_i+z_0} \mathcal{F}(z) dz - \frac{\sigma_U}{\pi\epsilon_i} \int_0^{z_i+z_j+z_0} \mathcal{F}(z) dz \quad (1-140)$$

z_j is the thickness of the opposing insulating layer. Equating the potentials of both electrodes yields the following equation for σ_U .

$$\sigma_U = \frac{\sigma_T \left(\frac{1}{\epsilon_1} \int_{z_1}^{z_1+z_0} \mathcal{F}(z) dz + \frac{1}{\epsilon_2} \int_{z_2}^{z_2+z_0} \mathcal{F}(z) dz \right)}{\left(\frac{1}{\epsilon_1} + \frac{1}{\epsilon_2} \right) \int_0^{z_1+z_2+z_0} \mathcal{F}(z) dz} \quad (1-141)$$

$$\therefore \sigma_U = \frac{\sigma_T \left(\frac{1}{\epsilon_1} [\mathcal{M}(z)]_{z_1}^{z_1+z_0} + \frac{1}{\epsilon_2} [\mathcal{M}(z)]_{z_2}^{z_2+z_0} \right)}{\left(\frac{1}{\epsilon_1} + \frac{1}{\epsilon_2} \right) [\mathcal{M}(z)]_0^{z_1+z_2+z_0}} \quad (1-142)$$

The short circuit current (\vec{I}_{SC}) can therefore be expressed as stated below.

$$\vec{I}_{SC} = A \vec{J}_{SC} = L^2 \frac{d\sigma_U(z)}{dz} \frac{dz(t)}{dt} \quad (1-143)$$

\vec{J}_{SC} is defined as the short-circuit current density. The output power and finite resistance characteristics of such a TENG device are also explained by this model using Ohm's law and solving the resulting first order ordinary linear equation.

$$V_1 - V_2 = L^2 R \frac{d\sigma_U(t)}{dt} \quad (1-144)$$

(Xu et al., 2020), in addition to including the reduction in real area of contact resulting from rough surfaces, simplified this expression by treating the aligned layers as circular with a device radius of a , rather than square or rectangular. This simplification yields a new definition of the function $\mathcal{F}(z)$.

$$\mathcal{F}(z) = \frac{\pi}{2} \left(1 - \frac{z}{\sqrt{a^2 + z^2}} \right) \quad (1-145)$$

The permittivity of the ambient medium is also accounted for in this model, giving a new definition for open circuit electric potential.

$$V_{OC} = \frac{\sigma_T}{\pi} \left(\frac{2}{\epsilon_0} \int_0^{z(t)} \mathcal{F}(z) dz + \frac{1}{\epsilon_1} \left(\int_{z(t)}^{z(t)+z_1} \mathcal{F}(z) dz - \int_0^{z_1} \mathcal{F}(z) dz \right) + \frac{1}{\epsilon_2} \left(\int_{z(t)}^{z(t)+z_2} \mathcal{F}(z) dz - \int_0^{z_2} \mathcal{F}(z) dz \right) \right) \quad (1-146)$$

Whilst this model is an accurate representation of vertical contact-separation TENG devices, models are yet to effectively model TENG devices that involve separate forms of motion that are not perpendicular

to the plane of contact. The geometries of these devices are inherently difficult to mathematically model, since the relevant dimensions cannot be condensed to what is effectively a one-dimensional model as presented. Despite these mathematical limitations, provided that a function for electric field exists for a given geometry through Gauss' law, this model is able to predict the electric output for a wide variety of TENG configurations.

Considering the sheer volume of research conducted on the development of TENG applications since their inception, it is safe to assume that this technology has the potential to aid in increasingly varied aspects of industry and daily life if the correct approach is taken. The prominent concern that arises from reviewing the literature surrounding these devices is that their longevity is rarely brought into question. Since the very nature of TENGs involve the mechanical contact of materials, it is reasonable to assume that tribological processes will have a significant effect on their operating efficiency and durability. This study examines on a macroscale the effects of such processes specifically on laterally sliding TENG applications.

Chapter 2 – The Freestanding TENG Apparatus

Whilst a great deal of effort has been put into optimising the electrical properties of TENG devices, very little research has been taken into the engineering and tribological optimisation of the triboelectric contacts themselves. The fundamentals of contact electrification have also been the subject of much research and discussion in the past decade, but little has been investigated about the dynamic effects of friction and wear on triboelectric charge transfer; in addition to how this translates into the average lifetime of TENG devices (Jason A. Wiles et al., 2003; Zhang et al., 2018).

This initial research chapter entails the production of a cost-effective preliminary test apparatus, capable of replicating the operation of macroscale laterally sliding TENG devices. The influence of surface composition and texture on triboelectric charging is also investigated for several configurations of polymer-on-metal sliding freestanding layer TENG using this apparatus. The results of these tests are also correlated with additional compositional analyses, such as contact angle measurements, as a means of determining a cost-effective methodology for predicting the triboelectric properties of materials for industry. The combination of this TENG contact and measurement circuit allows for the quantitative investigation of the current and voltage output of a sliding freestanding layer TENG set-up. This configuration uses the feedback ammeter to convert the current output of the TENG into a measurable voltage, whereas the voltage output of the TENG can be measured directly by attaching the TENG to the data acquisition unit. Through the implementation of this freestanding test apparatus, a clear difference can be distinguished in output current and contact charge accumulation as different insulating and conductive materials are used. A relationship between the rms slope ($S_{\Delta q}$) of contacting surfaces and their respective charging rates via triboelectrification is also demonstrated. This following chapter uses data collected

2.1 Methodology

The tribological tests involving the use of this apparatus have been conducted as a preliminary method for investigating the roles of surface chemical composition and roughness parameters in triboelectric charge transfer. The apparatus itself consists of a supporting structure that can accommodate the necessary components for the TENG configuration being investigated, and an electronic circuit capable of measuring the relevant output properties for measurement. The structure allows for the interchanging of materials and sample geometries for a given configuration. This in turn allows for the investigation of differing surface characteristics on triboelectric charging, in addition to the influence of device geometrical parameters – such as electrode size and spacing – on electronic output. The measurement circuit consists of an in-house built feedback ammeter and National Instruments myDAQ data acquisition unit. The feedback ammeter being able to measure the expected low current output of the TENG device.

2.1.1 The F-TENG Contact

The tribological contact is configured to replicate the mechanical properties of a typical sliding TENG application within the freestanding apparatus. Freestanding triboelectric layer TENG devices (as depicted

in Figure 1-32c, abbreviated to F-TENG) involve the movement of a separate freestanding triboelectric layer that is separate to the two electrodes. This device geometry only requires electrical connection to one side of the contact, albeit at different ends of the stroke, unlike attached-electrode TENGs. This orientation allows for the two electrodes to remain stationary to each other, which in turn provides a more secure attachment to the measurement circuit and a greater flexibility in terms of available sample geometries.

The output of TENG devices that involve two electrodes are also generally easier to model and have higher output characteristics than single electrode devices with identical contacts. This device geometry is symmetric around the centre of reciprocating sample movement unlike single-electrode and attached-electrode TENG designs. This mitigates any changes in contact pressure resulting from sample deflection across the stroke. Another advantage of using a laterally sliding F-TENG configuration is that mechanical contact is sustained throughout the entire cycle of operation for the device – with the exception of the lateral spacing of the electrodes if they are also used as triboelectric contact surfaces. The introduction of an insulating layer between the freestanding element and electrodes will allow for contact to be fully maintained between the two insulating surfaces across the stroke, regardless of the electrode lateral spacing. This is dissimilar to single or dual electrode sliding TENGs where the triboelectric surfaces are generally slid into and out of contact with each other, especially considering the cases where an electrode is exposed to the contact.

The combination of these characteristics allow for F-TENG devices to be accommodated within a reciprocating tribometer environment with more ease than single and dual electrode TENGs. The exact chosen configuration for this preliminary study is that of a polymer-on-metal laterally sliding freestanding triboelectric layer TENG (SF-TENG). This particular configuration of F-TENG is composed of an insulating polymer block that slides in a reciprocating fashion across the surface of two conductive electrodes as shown in Figure 2-1.

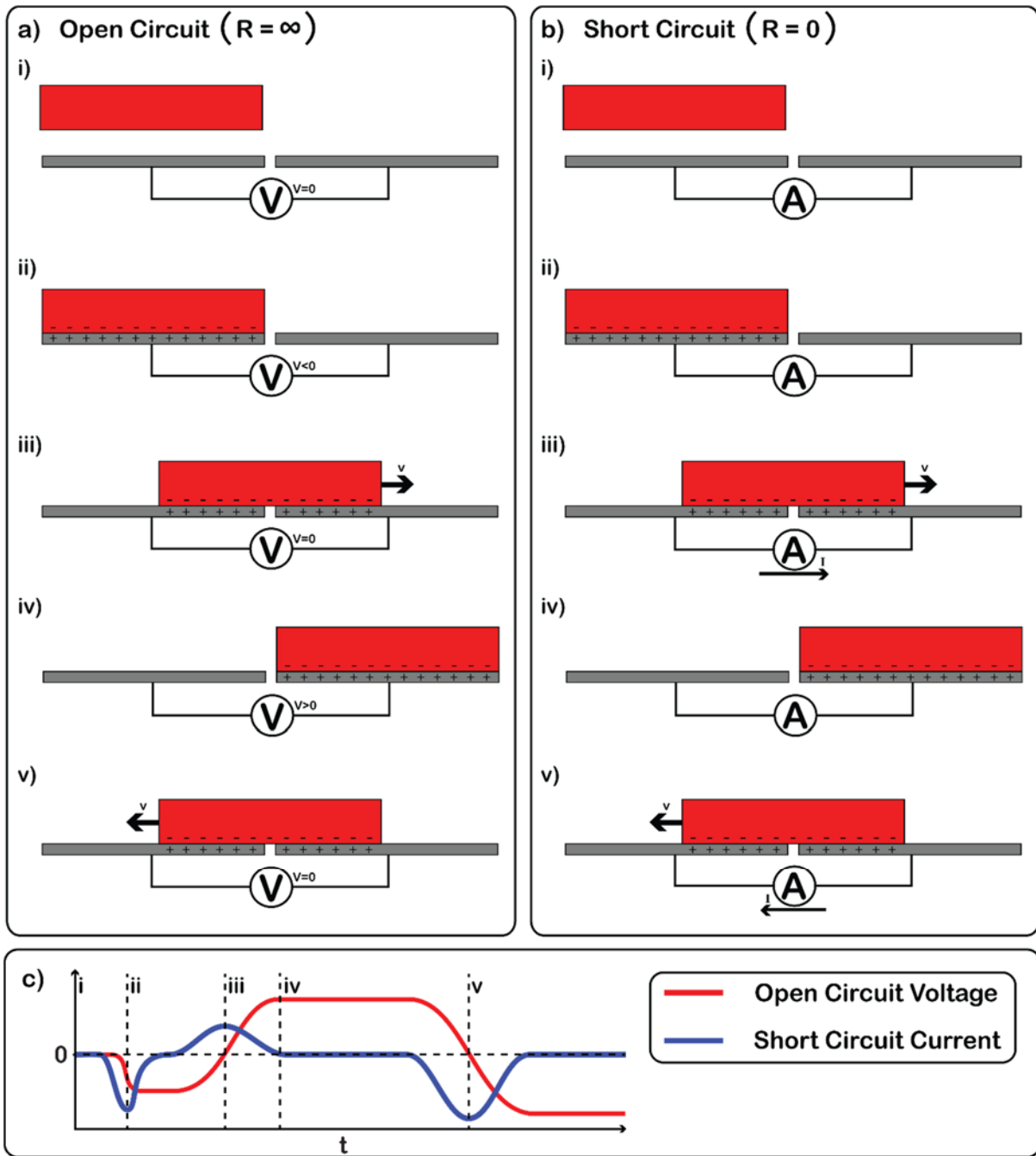


Figure 2-1 – Side-on diagram of a polymer-on-metal laterally-sliding freestanding-triboelectric-layer triboelectric nanogenerator (F-TENG) at subsequent stages of operation (i) before contact, (ii) first contact, (iii) mid-first-stroke, (iv) end-stroke, (v) and mid-stroke. The positions of trapped and mobile charges are given for open circuit (a) and short circuit (b) configuration, and the respective electronic outputs (c). Depicting the output voltage (red) and current (blue) for both (c). The red block represents an electronegative material, whereas the grey blocks denote an electropositive conductor.

The conductive electrodes serve a dual purpose as triboelectric layers in this particular configuration. This allows for the total charge on the insulating surface to approximately equate to the charge passing through the measurement circuit in short-circuit measurement mode. To avoid any complications in the modelling of this device, the two lower samples for each test are composed of the same conductive material. The electrodes are placed next to each other in-plane with a separating gap of in order to direct any induced

current between them through the measurement circuit. The conductive electrodes are normally equal to the insulating layer in terms of surface dimensions. The reasoning behind maximizing the surface area is based on the hypothesis that the surface charges accumulated within a triboelectric contact reach a certain spatial saturation density; past which they cannot further accumulate. Therefore, in order to maximize the total accumulated charge – and as a result, induce a larger output current – the total contact area has been maximized. The lateral spacing between the two electrodes is also minimised in order to maximize the contact time throughout the reciprocal motion of the device. The total stroke length of the reciprocating motion is also set as the length of the polymer block – equal to the length of the electrodes – on the direction of motion (i.e. the x direction) as to optimise the electric output.

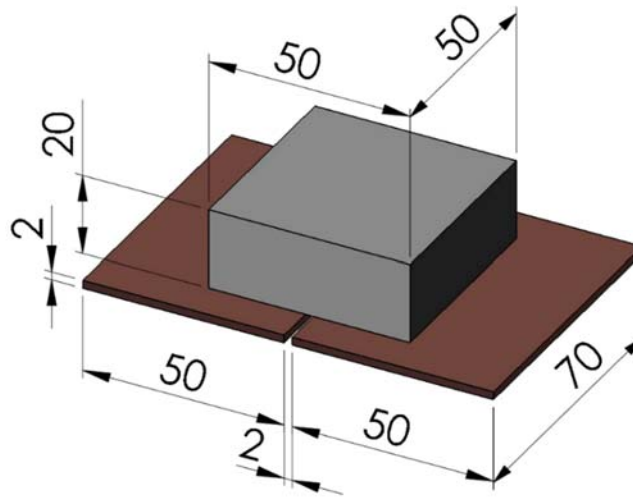


Figure 2-2 – Sample dimensions and configuration for the F-TENG apparatus.

This structural support was printed using a PolyJet™ 3D printing system by StrataSys and is composed of Vero PureWhite™ polymer. The support geometry consists of a base with two shallow (1mm deep in the z direction) recesses for housing the conductive electrodes, and two vertical clamps to both hold the electrodes in place in addition to guiding the movement of the polymer block over their surfaces in the x direction. It is designed in a way that accommodates varying electrode thicknesses, lengths, and lateral spacing. The contact geometry for the majority of previously tested TENG devices is plate-on-plate, with contact sizes in the order of several cm^2 (Chen and Wang, 2017). This is to provide a large enough contact area for an accurately measureable amount of charge to be generated for most conventional material pairings, in the order or several tens of nanocoulomb.

The specific geometry of the F-TENG apparatus consists of two 70 x 50 x 2 mm conductive plates secured in place alongside each other – separated by a 1 mm gap of air – along their 70 mm edges by the supporting structure. These conductive plates are secured to the base of the apparatus via the vertical clamps which cover the top and bottom 50 x 10 mm sides of each electrode. This results in the two 50 x 50 mm electrode surfaces exposed, separated by a 50 mm x 1 mm air gap. This lower part of the apparatus remains stationary whereas the insulating upper plate reciprocates laterally across the surfaces of the two lower electrodes.

The width of the polymer block is kept at 50 mm, which is equal to the separation of the two vertical clamps in the y direction. This allows for the motion of the polymer block to be guided by these clamps, preventing any deviation in the y direction. The polymer block also has a length of 50 mm, which is equal to the dimensions of the electrodes in the x direction. A visual representation of the supporting structure is given in Figure 2-4 alongside schematic representations in Figure 2-3, alongside an exposed view of how the electrodes fit within the structure, and a photograph of the assembled configuration.

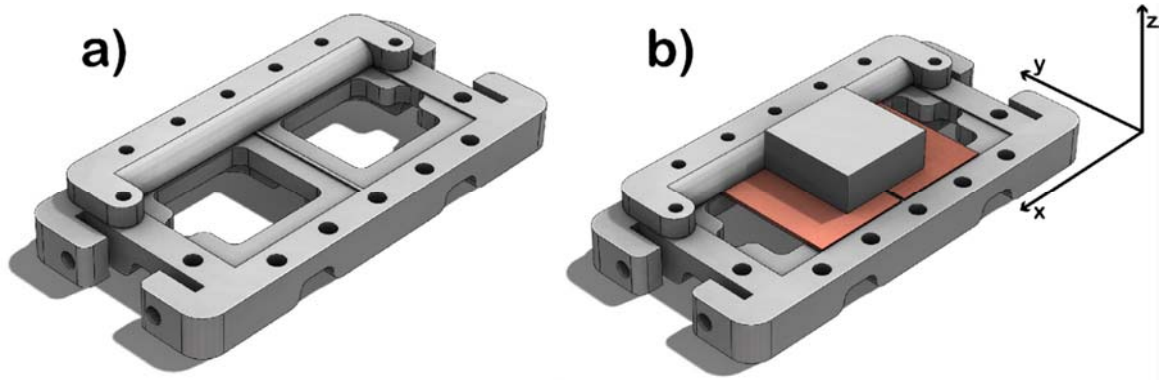


Figure 2-3 – Schematic representation of the F-TENG supporting structure without samples (a), and with samples (b), one upper clamp is removed here to show the lower sample holder and demonstrate how the lower samples sit within the supporting structure.

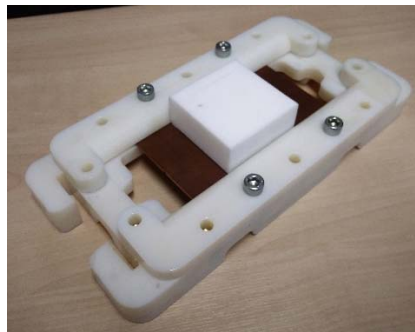


Figure 2-4 – Photograph of the F-TENG supporting structure.

For initial measurements, the polymer block was slid in a reciprocating motion across the two electrodes using hand motion. This particular method of motion comes with several disadvantages, the first being inconsistencies in both oscillating frequency and velocity profile for the polymer block being moved. Since the induced current is directly proportional to the relative motion of the block and electrodes, any discrepancy in hand motion can lead to differences in any TENG output characteristics. After initial testing a belt driven linear actuator powered by a step motor was implemented as a way to automate and more consistently control the movement of the block. An Arduino control program was written to give the polymer block a square wave velocity profile with adjustable reciprocating frequency and stroke length. A visual representation of this updated configuration is given in Figure 2-5. Another disadvantage of using handheld motion is the lack of measurement or consistency in the applied load to the contact. Not only does the hand exert an inconsistent load to the contact, but differences in the mass densities of the freestanding polymers – as listed in Table 2 – will also generate inconsistencies in applied load between tests.

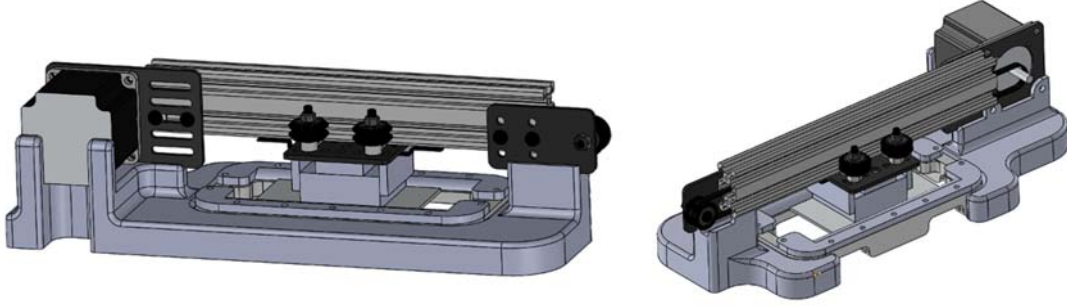


Figure 2-5 – Solidworks model for the updated freestanding rig apparatus, following the addition of a belt driven linear actuator.

2.1.2 Electronic Measurements

As explained previously, triboelectric charges accumulate within the polymer-metal contact. The charge density developing on the insulating polymer surface is isolated to the surface within trap states, whereas the charges on the electrode surface are locally retained at the surface by the Coulomb attraction of the trapped charges on the polymer counter surface. As the polymer block is reciprocated across the surfaces of the two electrodes, the relative movement of these trapped charges on the polymer surface will induce a similar movement of mobile charges.

If a voltmeter (theoretically, each with an infinite internal resistance) is connected to each of the two lower samples, both connected via a common ground, an oscillating ‘open-circuit’ voltage (V_{OC}) would be measured as the difference between the two voltmeter readings (Zhang et al., 2020; W. Zhang et al., 2021). This V_{OC} would correlate with the relative position of the upper and lower samples. Physically the potential difference between the two lower samples would reach a maximum when the upper sample reaches either end of its stroke, when the polymer block fully encompasses the surface area of a single electrode, as a result of the distance dependent electric field (DDEF) produced by the trapped tribocharges on the insulator surface (Dharmasena et al., 2017). This open circuit voltage would also equal zero when the polymer block is equally contacting both electrodes. If a low resistance is instead between the two electrodes, then the induced current is able to flow freely across this resistance in an ohmic fashion.

The magnitude of this induced current will be dependent on the speed of relative motion, the resistive properties of the external circuit, and the charge densities deposited on the contacting surfaces through triboelectrification. If the assumption is made that the total mobile charge stored at the surface of each electrode Q_{U_i} is the negative of the amount of trapped charge on the polymer surface directly in contact with it Q_{T_i} , then a simple equation can be derived to estimate the short circuit current output of the TENG device. The total mobile charge stored on a given electrode is then treated as a function of the total contact area ($A_i(t)$) with the polymer sample.

$$Q_{U_i}(x) = -\sigma_T A_i(t) = -\sigma_T L_y l_{x_i}(t) \quad (2-1)$$

L_y is the width of the device, and $l_{x_i}(t)$ is the total overlapping length of the polymer and electrode i in the x direction, which changes as the polymer block is reciprocated. When the polymer block is at the

end of its stroke and is fully encompassing the surface area of an electrode, the total mobile charge at the surface of that electrode should be equal to $-\sigma_T L_y L_x$, where L_x is the full length of both the polymer block and electrode in the x direction.

The existence of the lateral spacing g complicates this calculation by adding an area at either end of the stroke where the charge only changes on one electrode as a result of movement. A reasonable assumption can however be made that $g \ll L_x$ which allows for the current flowing through the external circuit to be equated to the physical movement of trapped charges. If $x(t)$ corresponds to the position of the polymer block relative to the centre of the electrode lateral spacing (i.e. at $x = 0$ the block will be equally contacting both electrodes) then $l_{xi} = \frac{L_x}{2} \pm x(t)$ depending on which electrode is being considered. This then shows that the short circuit current is directly proportional to the relative velocity profile of the polymer block and electrodes.

$$I_{sc}(t) = \frac{dQ_{U_i}(l_{xi})}{dl_{xi}} \frac{dl_{xi}(x)}{dx} \frac{dx(t)}{dt} = -\sigma_T L_y v_x(t) \quad (2-2)$$

$v_x(t)$ is the time derivative of position along the x axis, also corresponding to the velocity of the polymer block in the x direction. Since this short circuit current can be measured it is then possible to use this measurement to estimate the total triboelectric charge density on the polymer surface.

In terms of current measurement there are two main methods used in electronic applications; the shunt ammeter method and the feedback ammeter method. The shunt ammeter method is most widely used in typical digital multimeter applications. A shunt ammeter uses a shunt resistor as an ohmic low-resistance path for current to pass through, the voltage across this resistor is measured and is directly proportional to the current passing through it. Shunt ammeters generally use low-resistance shunts in order to minimize the potential difference across it; known as the voltage burden. If the shunt resistance is significantly higher than the resistances in the circuit being tested this can cause considerable errors in low-current measurements for that particular circuit. The feedback ammeter method can be implemented to circumvent the large errors that arise from low-current shunt ammeter measurements. These ammeters use an active transimpedance amplifier (TIA) to convert the low current into a measurable voltage.

2.1.2.a Feedback Ammeter Design

In order to effectively and reliably measure the output of a TENG device. A low current feedback ammeter was developed alongside the University of Leeds School of Mechanical Engineering Electronic Services department in order to measure currents from the micro- to nano-ampere scale. These measurements are achieved without the issue of a burden voltage as previously explained through the use of a transimpedance amplifier (TIA, also referred to as an operational amplifier or op-amp) and its high-gain properties, rather than through typical shunt resistance methods. A diagram for a basic TIA circuit is given in Figure 2-6.

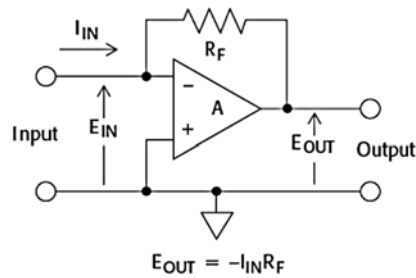


Figure 2-6: Circuit diagram for a generic feedback ammeter.

Current is measured by a feedback ammeter through comparing the input (V_{in}) and output (V_{out}) voltages of the TIA. Any change in output voltage of an idealised TIA corresponds to a small change in the input current as stated by the equation below.

$$V_{out} = -I_{in}R_F \quad (2-3)$$

Therefore the sensitivity of a feedback ammeter can be easily adjusted by changing the resistance of the feedback resistor (R_F). This can be done through the use of a variable resistor. However it is more commonly seen that an array of resistors and switches in parallel is used, since variable resistors lack a wide range of operational resistances. An example circuit diagram of this implementation is given in Figure 2-7, and a photograph of the resistor and switch array used in our feedback ammeter is given in Figure 2-8.

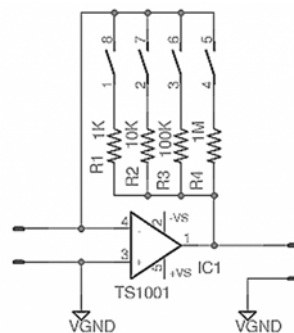


Figure 2-7 – Circuit diagram for a feedback ammeter with selectable sensitivity.

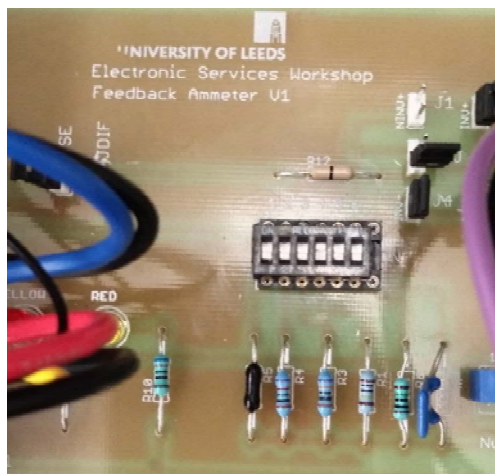


Figure 2-8 – Image of a circuit board section from the manufactured low current amplifier, showing the multiple resistive ranges of the device with multiple resistors in parallel.

The feedback ammeter for the F-TENG apparatus utilised resistors ranging from 1 k Ω to 100 M Ω . The highest impedance feedback resistor of 100 M Ω allowed for the scaling of a 10 nA input current to a 1 V output voltage, decreasing in orders of magnitude of sensitivity with each resistor down to a ratio 1 mA to 1 V with the 1 k Ω resistor. The limitation of the myDAQ data acquisition unit is that it cannot record voltages above 10 V, meaning that the feedback resistor must be carefully chosen in order to collect output current data at high resolutions without exceeding this value. The circuit schematic for the feedback ammeter incorporated into the F-TENG apparatus is given in Figure 2-9, with a photograph of the feedback ammeter internals given in Figure 2-10.

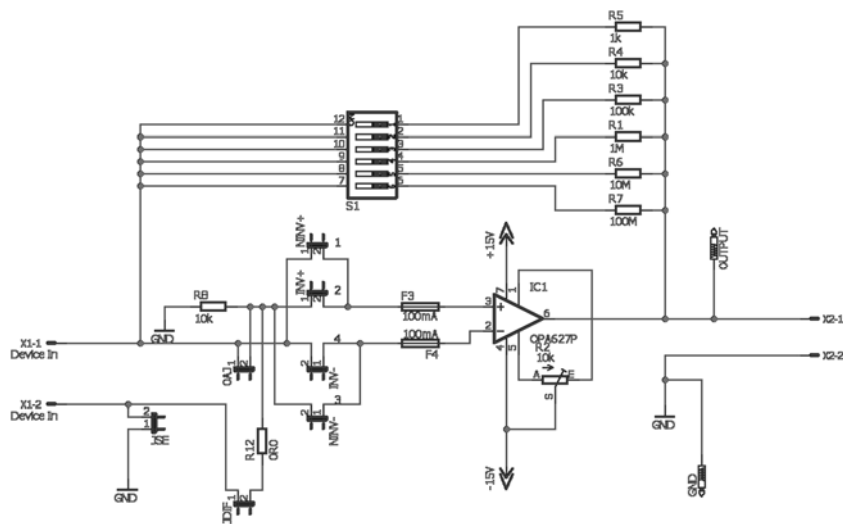


Figure 2-9 – Final Circuit diagram for the low current feedback ammeter, excluding external circuits.

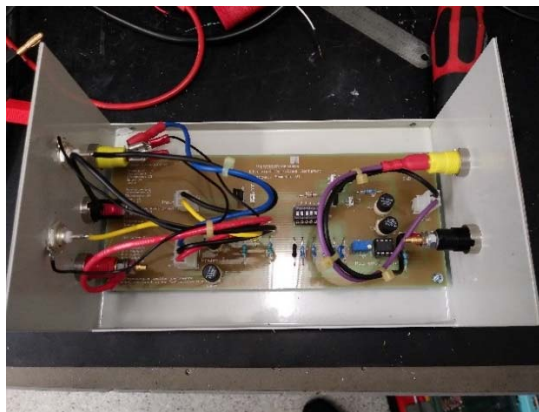


Figure 2-10 – Image of the low current feedback amplifier, manufactured by the Electronic Services Workshop at the University of Leeds School of Mechanical Engineering.

The feedback ammeter is connected to a triple-output GPC-3030D power supply unit from GW Instek to provide a 30V supply voltage to the operational amplifier and to provide a virtual ground at 15V during measurements. The electrodes of the TENG set-up were connected to the measurement circuit via two Bayonet Neill–Concelman (BNC) cables into the differential input of the ammeter. The positive terminals of the BNC cables were attached to the TENG electrodes via a conductive aluminium tape, whilst the two negative terminals were grounded to aid in shielding the current from external influences.

A DPO2012 digital phosphor oscilloscope from Tektronix was initially used to measure the output of the feedback ammeter in real-time as an initial validation for use of the F-TENG apparatus. The oscilloscope was connected to both the output of the ammeter and the virtual ground through a BNC cable to measure the potential difference between the two over time. The oscilloscope was also directly connected differentially to each electrode of the F-TENG device as a way to measure the open circuit voltage in addition to verifying that the output was not an artefact of the feedback ammeter power supply.

After these initial proof-of-concept measurements, the myDAQ unit was incorporated for the purpose of recording the output current of the F-TENG device during testing. A simply 50 Hz notch filter was also incorporated to the feedback ammeter input as a way to mitigate the influence of external electrical interference from surrounding power conduits and lighting fixtures. The circuitry for this notch filter is given in Figure 2-11.

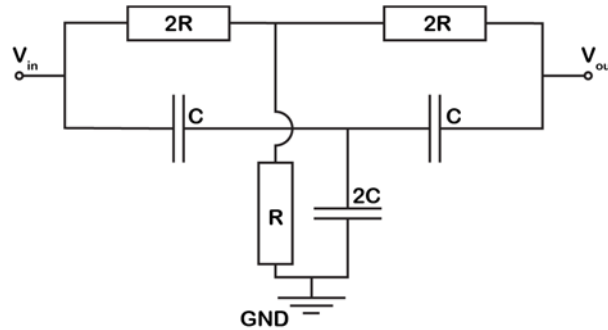


Figure 2-11 – Circuit diagram of the 50Hz notch filter implemented within the F-TENG apparatus. $R = 160 \, \Omega$, and $C = 10 \, \mu\text{F}$.

The notch frequency of such a filter is calculated using the resistances and capacitances of the constituting components.

$$f_N = \frac{1}{4\pi RC} \quad (2-4)$$

The Q factor for this basic notch filter is fixed at 0.25 in the order of -12dB. This is calculated by the following equation.

$$Q = \frac{\Delta f}{f_N} \quad (2-5)$$

Δf is the bandwidth of the notch filter, which is 12.5 Hz. The schematic diagrams for both F-TENG measurement configurations are given in Figure 2-12.

2.1.2.b Measurement Circuit

The measurement circuit for the freestanding TENG apparatus consists of a single feedback ammeter used to measure the output current under negligible resistances, which in turn is used to estimate the total triboelectric charge density within the F-TENG contact. The output of the feedback ammeter is directed initially directed into an oscilloscope for proof-of-concept measurements, then a National Instruments myDAQ USB data acquisition unit is implemented for the purposes of data collection. A Kiethley 6517B electrometer replaces the feedback ammeter for later tests owing to its increased resolution, as outlined in 2.1.5 Testing procedure.

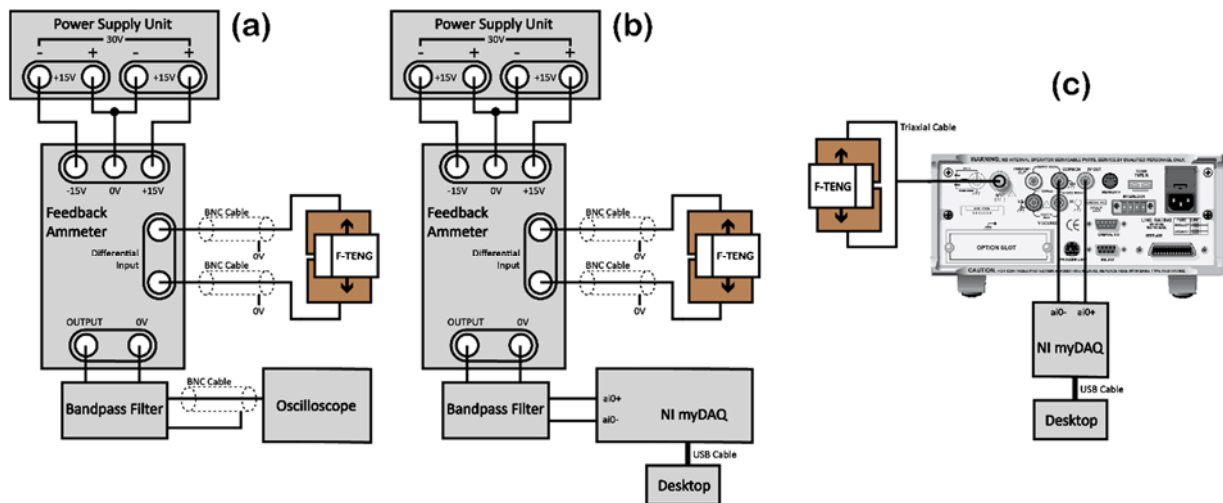


Figure 2-12 – F-TENG measurement circuit configurations for a) the initial feedback ammeter and oscilloscope series of tests, b) the feedback ammeter and myDAQ series, and c) the electrometer and myDAQ configuration series.

If a sufficient balance between output current and voltage is struck through calculation of an optimal resistance value, the output power of the TENG device can be maximized (Niu, 2015). The introduction of more complex methods of impedance such as capacitors and inductors would have a similar effect on the device output, dependent on the frequency of the physical reciprocation.

2.1.3 Data Processing

When taking sensitive current measurements across a device that exhibits a high effective capacitance such as a TENG device, it is important to identify the different contributing factors to electrical interference. The initial output from the device was first analysed with the polymer block being absent in order to identify any sources of noise that may interfere with measurements being taken. Throughout the duration of initial tests it was evident that the main contributors to this interference were unshielded overhead lighting fixtures and mains power lines around the testing facility, both oscillating at 50 Hz.

The movement of any surfaces or bodies that may hold an electrostatic charge within the vicinity of the F-TENG device can also interfere with the measured device output. For example, a person walking past the TENG whilst wearing a wool jumper or Nylon shirt was shown to induce a small current between the electrodes, depending on the direction, distance, and speed of movement of the charges. This noise evaluation highlights the importance of using effectively electrically shielded equipment to obtain accurate results for low-current measurements. The electrical interference from a stepper motor was speculated to contribute significantly to the device output, especially if the electrical signal being emitted by the step motor is correspondent to the relative motion of the block; having the potential to introduce large systematic errors. This interference was however found to be negligible in comparison to the output current of the TENG. The current output of the F-TENG was recorded which was written into a tab delimited .txt format through the use of the myDAQ device. An in-house MATLAB program was then composed to further remove background electrical interference from the raw data and analyse the resulting cleaned data.

Background data was identified through Fourier transform analysis and removed using selective virtual notch filters. Background samples predictably found residual interference at 50 Hz as well as at various harmonic frequencies being emitted from the mains power lines within the testing room. Notch filters were applied at 50, 100, 150 and 200Hz in order to remove this background interference. The effectiveness of this technique is shown in Figure 2-13, Figure 2-14, and Figure 2-15.

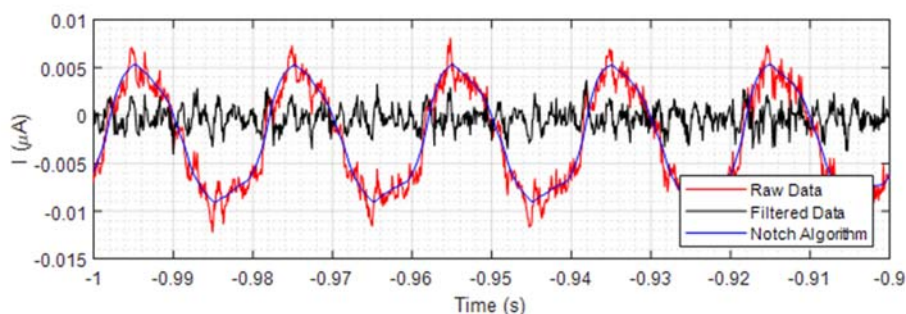


Figure 2-13 – Raw induced background current (red) over time, alongside fitted data produced by the four-stage notch filter (blue) and the final filtered data (black).

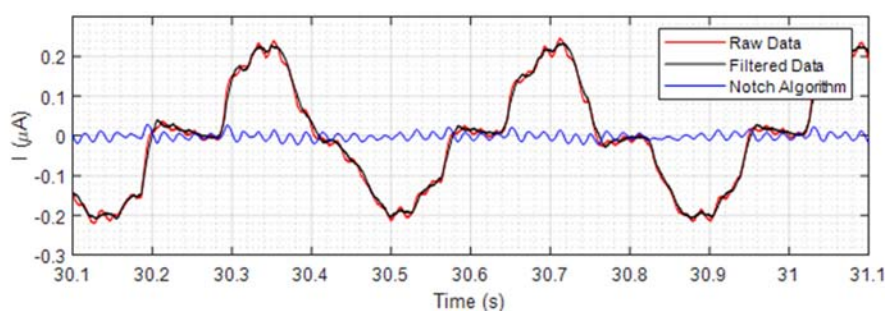


Figure 2-14 – Raw induced current (red) over several oscillations during an example test, alongside fitted data produced by the four-stage notch filter (blue) and filtered data (black) to show how the filter discerns between the signal and background noise.

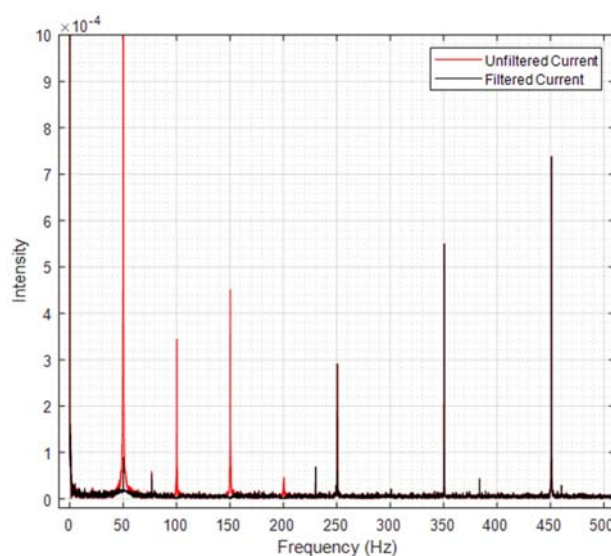


Figure 2-15 – Fourier transform of a generic initial 10 s of background raw current (red) induced by external interference; illustrating significant interference at 50 Hz and its even harmonic frequencies. These data were processed through a four-stage notch filter to remove interference at 50Hz and its first three harmonics (black).

Due to the hand-held nature of the polymer block movement during initial tests, a threshold trigger was included within the MATLAB code to identify the start and end of each stroke in order to account for inconsistencies in oscillation frequency, as well as to compare how certain output properties change per oscillation across the duration of each test. The exact waveform for the oscillatory output for the F-TENG is dependent on several factors, including device geometry and spatial charge distribution in the direction of sliding motion. Because of this characteristic, the current waveform can change considerably between and across the duration of identical tests due to the spatial evolution of contact charge densities. The maximum output current per half-oscillation was plotted across testing duration, but the sporadicity in current waveform was predicted to affect similar perturbations in peak current per oscillation. Therefore, a more consistent value to measure as an accurate representation of the processes occurring within the contact would be a value that removes this influence. Integrating the current trace over time across every half-oscillation provides a value of charge that can be treated as approximately equivalent to the total trapped charges (Q_{Tn}) on the polymer surface during the n^{th} half-oscillation in accordance with (2-1). The contact charge can then be evaluated by integrating the current output for each half-oscillation over time.

$$Q_{Tn} = [-Q_U(t)]_{t_n}^{t_{n+1}} = \int_{t_n}^{t_{n+1}} I_{SC}(t) dt \quad (2-6)$$

The short circuit current ($I_{SC}(t)$) can be described as the time derivative of the movement of mobile charges ($Q_U(t)$) as they pass through an arbitrary aperture (e.g. the cross-section of a wire). This allows charge to be calculated as an integral of current between two points in time. These two points (t_n, t_{n+1}) being the start and finish of each respective half-oscillation. This integration method is visually represented by Figure 2-54. Because of this relation, the value for integrated current is a more consistent method for analysing the charge accumulation characteristics within the TENG contact. This method is also less sensitive to discrepancies in block velocity profile, since the integrated area for each pulse should be independent of the velocity of the block. This is however based on the assumption that sliding speed has a negligible effect on triboelectric charge transfer, and that the current is purely induced by the movement of the block rather than the generation of any new charges within the contact. A comparison between peak current output and integrated contact charge for an example test is given in Figure 2-55.

2.1.4 Sample Preparation

Four different metals were used as material choices for the lower samples in order to compare their triboelectric potentials and correlate to their respective work functions. The four metals used were copper (Cu, CAS 7440-50-8), an Aluminium-Scandium alloy (Al wt.98% , Sc 2 wt.%, CAS 113413-85-7), a mild steel (AISI 4340, EN24, 1.5% Ni, 1% Cr, 0.2% Mo), and a Stainless Steel (AISI 316L, UNS S31603, 17.5% Cr, 11.5% Ni, 1.5% Mn, 2.5% Mo). The work functions of aluminium and stainless steel are given as 4.26 eV (Eastment and Mee, 1973) and 4.30 eV (Barrett et al., 2014) respectively, which are both comparatively lower than most metals. The mechanical properties of the four metals differ substantially, where steels have a higher density and higher mechanical moduli than copper and aluminium (Peckner and Bernstein, 1977). The mechanical properties of all materials used in this study are given in Table 2. Both stainless steels and aluminium alloys are known to develop oxide layers on their surfaces by reacting with oxygen within the ambient air. This oxidation mechanism is known to protect the underlying metal

from corrosion by creating a relatively unreactive coating. The presence of these oxide layers are already shown to change the chemical properties of their underlying surfaces. Therefore it is reasonable to assume that the electronic surface states of both aluminium and stainless steel are altered considerably from those of the bulk by the presence of their respective oxide layers.

Three different polymers were also chosen for the upper sample block composition in order to provide a more comprehensive matrix for investigating the influence of chemical composition on triboelectric charging. The three polymers chosen were Polytetrafluoroethylene (PTFE, Teflon, $(C_2F_4)_n$), Poly(hexamethylene adipamide) (PA66, Nylon 6-6, $(C_6O_2)_m(C_6(NH)_2)_n$), and Polyoxymethylene (POM, Delrin/Actetal, $(COH_2)_n$), and were supplied by Industrial Plastic Supplies Ltd. (IPS). The molecular structures of these polymers are given in Figure 2-16, with existing functional groups highlighted. Delrin, Nylon 6-6 (shortened to Nylon in this thesis), and Teflon are also used extensively in engineering applications for their different mechanical properties.

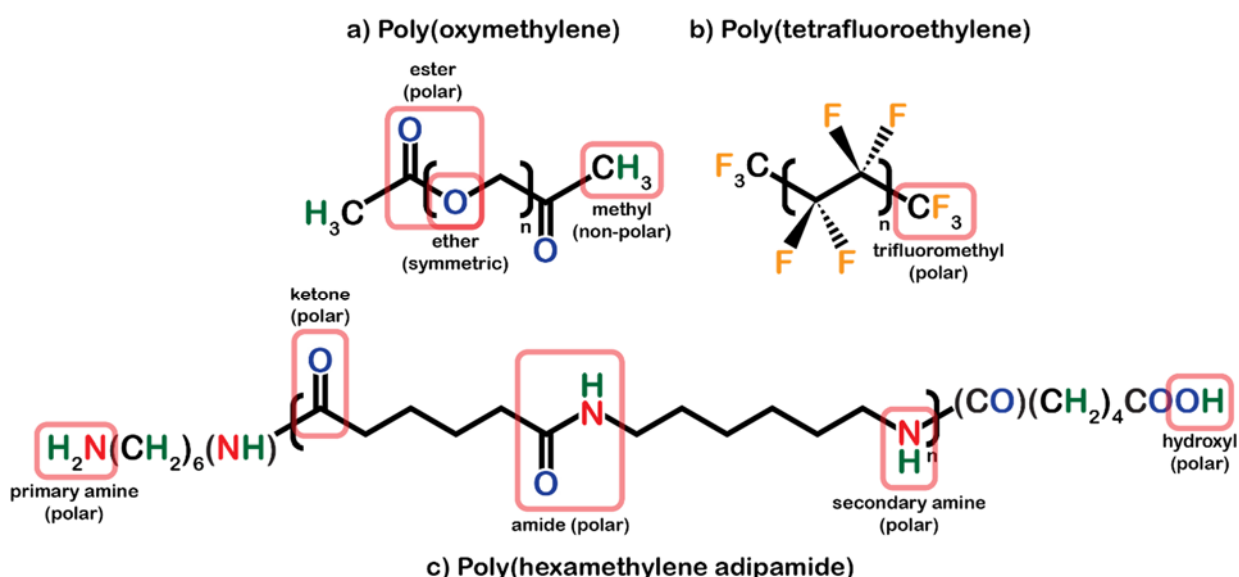


Figure 2-16 – Molecular diagrams of a) Delrin, b) Teflon, and c) Nylon 6-6; with functional groups highlighted. Delrin is intentionally terminated differently to how one would expect – by its manufacturer DuPont – in order to prevent breakdown of the polymer into trioxane ($C_3H_6O_3$). Nylon may also be terminated differently to how it is depicted in this diagram due to the presence of terminal hydroxyl and amine groups.

Teflon exhibits a very low surface energy and is widely known as a material with a strong tendency to accept electrons from physical contact with most other media (Chen et al., 2020). This electronegative behaviour is historically attributed to the molecular structure of PTFE, which is displayed in Figure 2-17.

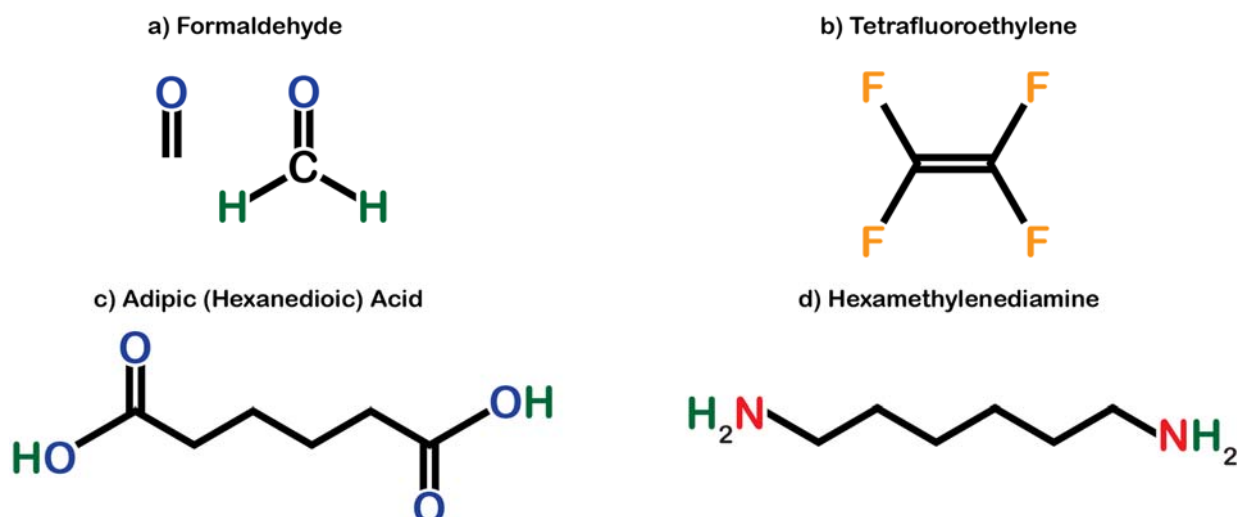


Figure 2-17 – Molecular diagrams for the monomers of a) Delrin, and b) Teflon, and the two monomers of Nylon 6-6 (c and d). Formaldehyde is depicted in both its reduced form and with the carbon and hydrogen atoms shown in order to better display its structure.

PTFE polymer chains consist of a carbon backbone saturated with fluorine atoms in place of the usual hydrogen atoms found in polyethylene. Fluorine is the most chemically reactive and electronegative of all the elements owing to a single vacant 2p orbital in its outer electron shell. Because of this, Fluorine atoms form highly polarised covalent bonds as it draws the shared electron mass closer to its own nucleus. In the context of PTFE, the binding energies of the backbone C1s electrons are increased from 285 eV typically exhibited of C-C bonds to 291 eV and 292 eV by the presence of C-F and C-F₂ bonds respectively, as shown by previous XPS studies (Girardeaux and Pireaux, 2021). The unique molecular structure of PTFE ultimately allows for many low-energy electron molecular orbitals, explaining its relatively high effective work function of 5.75 eV as recorded by previous studies (Seki et al., 1990).

The fluorine pendant atoms that surround the PTFE carbon backbone act as a shield of low energy electrons that generally prevent the PTFE molecules from forming chemical bonds or otherwise interacting with other molecules. The collective repulsion between the fluorine pendant atoms along a PTFE polymer chain pull it taught, making them appear more rod-like and harder to deform. These PTFE rods have a helical structure, meaning no electric dipole exists across them despite the presence of highly polar C-F bonds. The surface energy of Teflon is resultantly low, with no polar component. This rod-like structure also allows for individual PTFE polymer chains to stack in a highly compacted manner. This close packing of polymer chains gives bulk Teflon a highly dense and crystalline structure. This close proximity of neighbouring PTFE molecules is also the reason why Teflon remains feasible as a solid state of matter, despite no apparent intermolecular bonds or interactions. At these separation distances and with such a high degree of conformity in a crystalline structure, London dispersive forces act as intermolecular bonds and allows Teflon to maintain its structure. Whilst London dispersive forces keep PTFE chains closely packed perpendicularly to their lengths, they remain able to easily slide parallel to each other. This causes Teflon to generally exhibit a low durability in tribological contacts, with PTFE molecules being delaminated from the bulk with relative ease.

These PTFE wear particles however have a tendency to adhere themselves to counter-surfaces and form a low friction transfer layer within the contact. The combination of these unique properties explain why Teflon sees extensive use as a solid lubricant (Benabdallah, 2003) and as a surface coating for hydro/oleo-phobic applications (Pang et al., 2021).

Both Delrin and Nylon have previously been demonstrated to have a high surface energy, making them both strongly electropositive materials which prefer to donate electrons to counter-materials (Diaz and Felix-Navarro, 2004). Very little research has been conducted into the electronic structure of Nylon, with the few quoted values for its effective work function being similar to that of Aluminium, close to 4.3 eV (Arridge, 1967; Zhang et al., 2019). Nylon has however been cited as a material with a strong tendency to donate electrons upon contact with other media. This indicates that the effective work function for Nylon may be closer to the lower quoted values. Nylon polymer chains are constructed from two alternating monomers; hexamethylenediamine ($\text{H}_2\text{N}(\text{CH}_2)_6\text{NH}_2$) and hexanedioic acid ($(\text{CH}_2)_4(\text{COOH})_2$). These monomers become connected via amide bonds in the polymerisation process. The presence of these N-H and C=O bonds also increase the binding energies of the backbone C1s electrons, but not to the extent of the C-F₂ and terminating C-F₃ bonds present in Teflon. The carbonyl oxygen atoms and amide hydrogen atoms present in the polymer chains are known to form hydrogen bonds, which create inter-chain crosslinks mediated by these bonds. These bonds have previously been thought to be responsible for the high mechanical moduli exhibited by Nylon, however further research has disproved this, attributing these moduli primarily to its solid-state morphology instead (Schroeder and Cooper, 2008). The relatively low binding energy of these hydrogen bonds may explain the supposed low effective work function of Nylon, but this remains to be confirmed. Nylon is often used in applications where a polymer with high mechanical strength and thermal and chemical stability is required (Kohan, 1986).

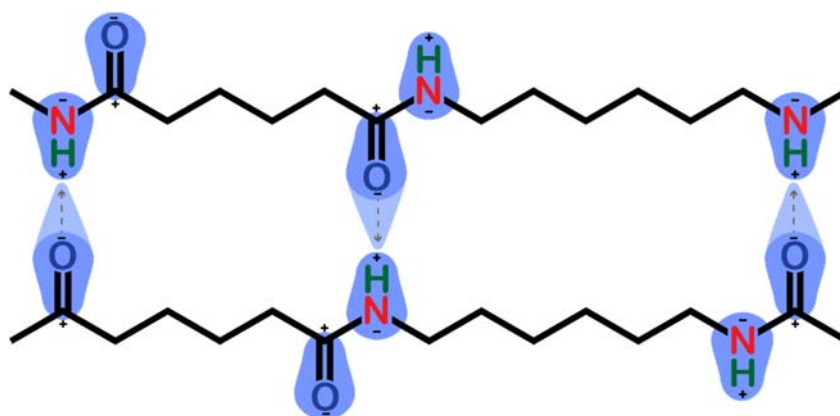


Figure 2-18 – Depicting the intermolecular hydrogen bonds in Nylon 6-6. The blue regions approximate the skewed distribution of electron densities.

The main polymer structure of Delrin is composed of alternating oxygen and carbon atoms in a zig-zig structure. Each carbon atom is also bonded to two hydrogen atoms as is seen for backbone carbon in polyethylene (PE, $(\text{C}_2\text{H}_4)_n$). The resulting POM structure exhibits a dipole moment between the oxygen and hydrogen atoms in its structure. This provides a case for hydrogen bonds to exist within the bulk of

Delrin. This would explain its high mechanical moduli, in addition to why Delrin is shown to exhibit similar triboelectric surface characteristics to Nylon.

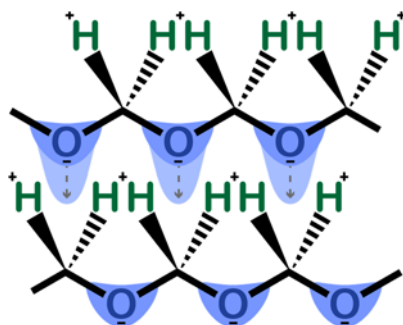


Figure 2-19 – Depicting the hypothetical hydrogen bonds in Delrin. The blue regions approximate the skewed distribution of electron densities.

Table 2 – Mechanical properties for all sample materials used in F-TENG testing.

<i>Material</i>	<i>Elastic Modulus (GPa)</i>	<i>Shear Modulus (GPa)</i>	<i>Hardness (Rockwell)</i>	<i>Poisson's Ratio</i>	<i>Mass Density (kg m⁻³)</i>	<i>Work Function (eV)</i>
Aluminium	68 ^b	25 ^b	29 (B) ^b	0.36 ^b	2710 ^b	4.23 - 4.32 (Derry et al., 2015)
Copper	110 ^b	46 ^b	51 (B) ^b	0.34 ^b	8960 ^b	4.56 – 4.90 (Derry et al., 2015)
Mild Steel	210 ^b	80 ^b	70 (B) ^b	0.30 ^b	7850 ^b	-
Stainless Steel	193 ^b	77 ^b	79 (B) ^b	0.27 ^b	8000 ^b	4.92 - 5.06 (Barrett et al., 2014)
Delrin	3.15 ^a	0.915 ^a	93 (R) ^a	0.37 ^a	1410 ^a	-
Nylon	1.85 ^a	1.15 ^a	115 (R) ^a	0.42 ^a	1140 ^a	4.20 (Arridge, 1967)
Teflon	0.575 ^a	0.23 ^a	54 (R) ^a	0.41 ^a	2200 ^a	5.75 (Trigwell et al., 2003)

^a mechanical properties provided by the distributor, Industrial Plastic Supplies Ltd., ^b (ASM Handbook Committee, 1990)

The surface topographies of the untextured samples were examined using an NPFLEX white light interferometer from Bruker Systems. These surfaces were examined under a range of magnifications to gauge the surface hierarchical topography on a range of length scales. Several surface roughness

parameters were measured using the NPFLEX's accompanying Vision64 software such as the mean arithmetic height roughness (S_a), surface skewness (S_{sk}), and Kurtosis (S_{ku}), with an in-house MATLAB program being composed to create normal maps for each surface in addition to surface slope magnitude and direction. These maps were utilised by this program to calculate additional surface parameters such as the mean arithmetic slope $S_{\Delta a}$, and rms slope $S_{\Delta q}$, in addition to calculating the real surface area of the sample surface relative to the projected surface area for correcting contact angle measurements in accordance with the Wenzel equation (1-67). The topographical parameters of the untextured samples are given in Table 3. Surface height maps, gradient magnitude and direction maps are also provided in Figure 2-20 to Figure 2-29.

Table 3 – Surface topographies of untextured samples.

<i>Material</i>	S_a (nm)	S_q (nm)	$S_{\Delta a}$	$S_{\Delta q}$	S_{sk}	S_{ku}
Aluminium	147	179	0.018	0.024	-0.63	3.44
Copper	34	50	0.007	0.011	1.47	16.9
Mild Steel	549	646	0.029	0.040	-0.25	2.18
Stainless Steel	249	328	0.025	0.037	0.55	7.91
Delrin	456	606	0.018	0.025	-1.57	5.61
Nylon	306	394	0.018	0.024	-0.20	4.17
Teflon	104	164	0.019	0.029	-3.88	29.3

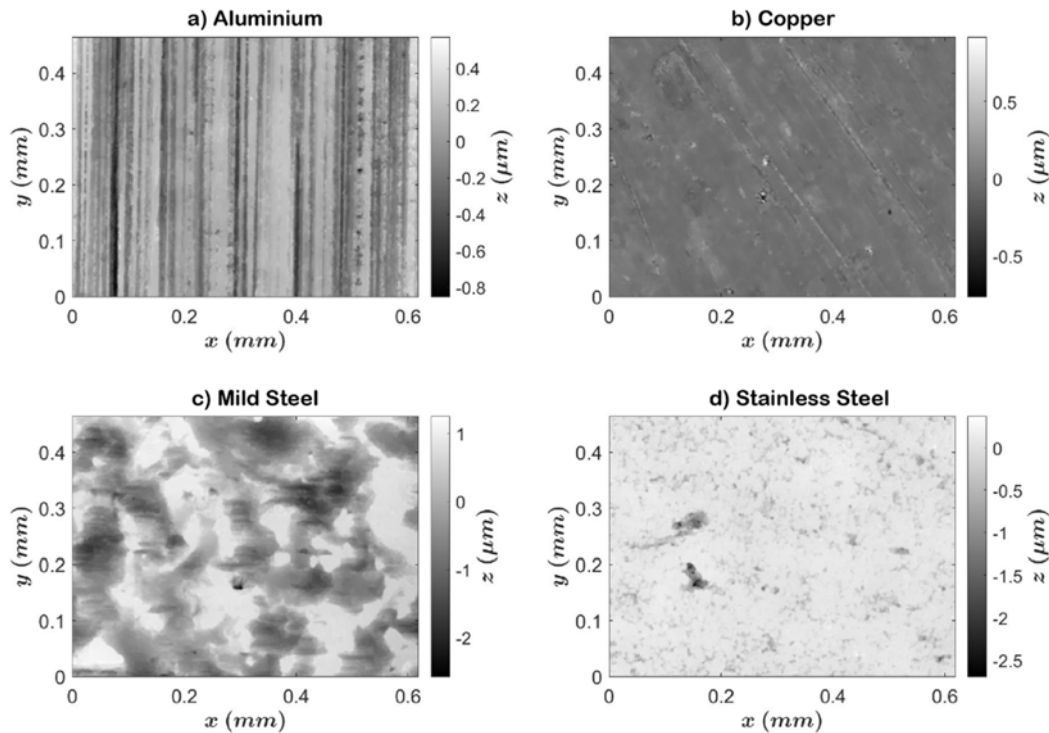


Figure 2-20 – Surface height maps for the untextured metal surfaces.

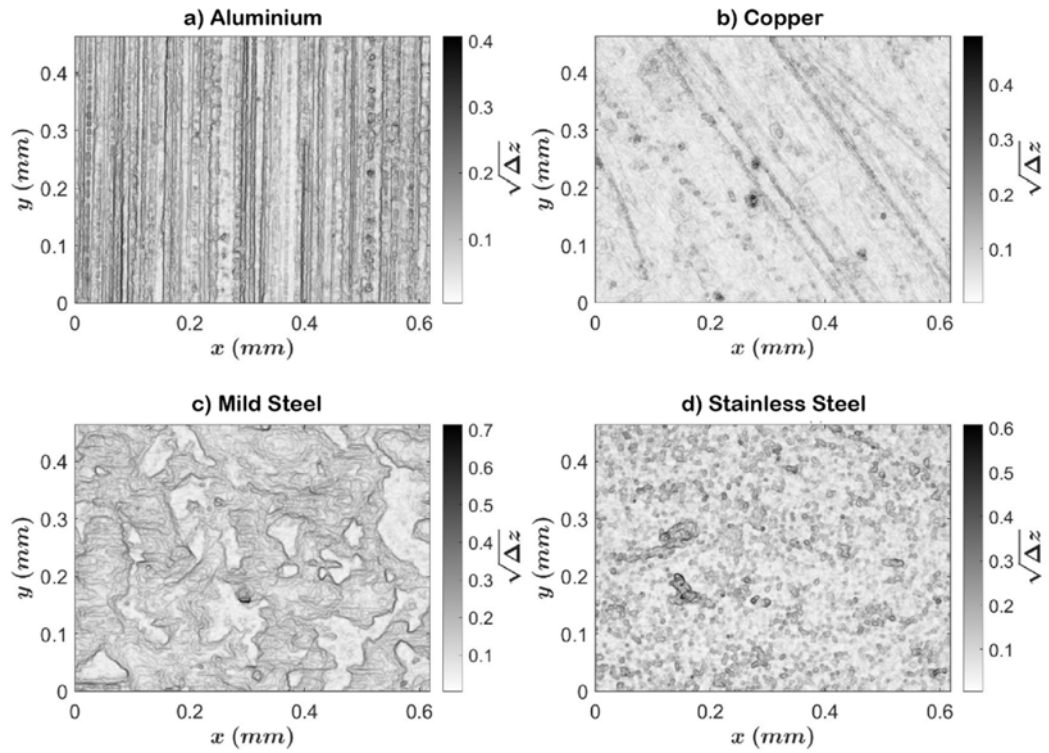


Figure 2-21 – Surface gradient maps for the untextured metal surfaces.

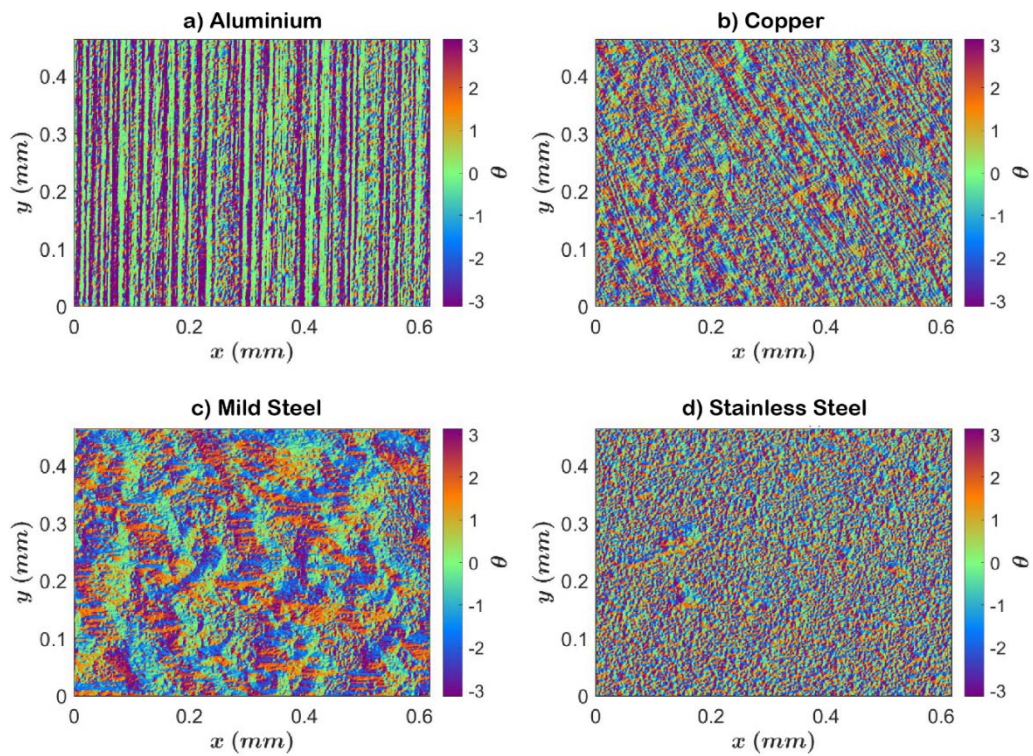


Figure 2-22 – Surface gradient direction maps for the untextured metal surfaces.

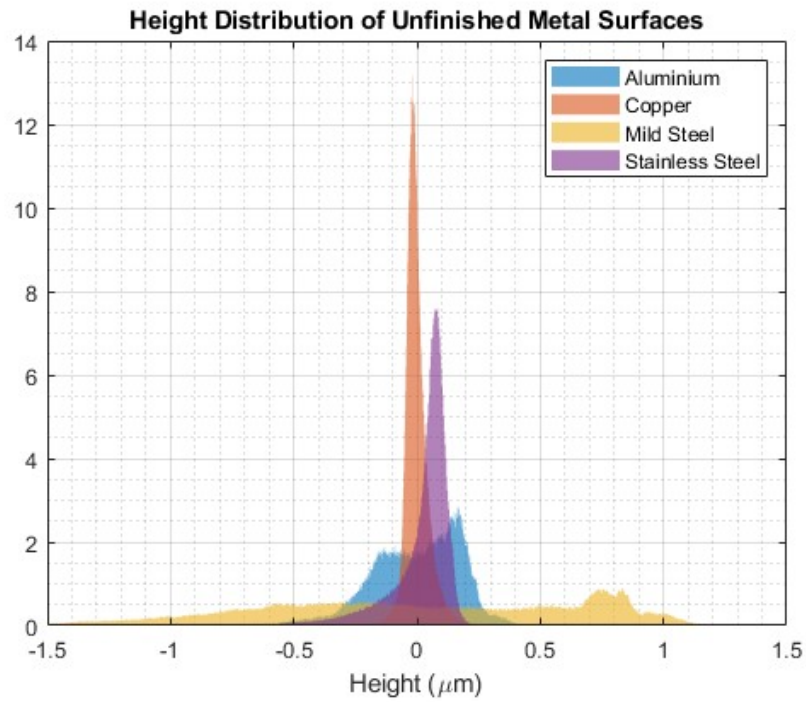


Figure 2-23 – Surface height histogram for the untextured metal surfaces.

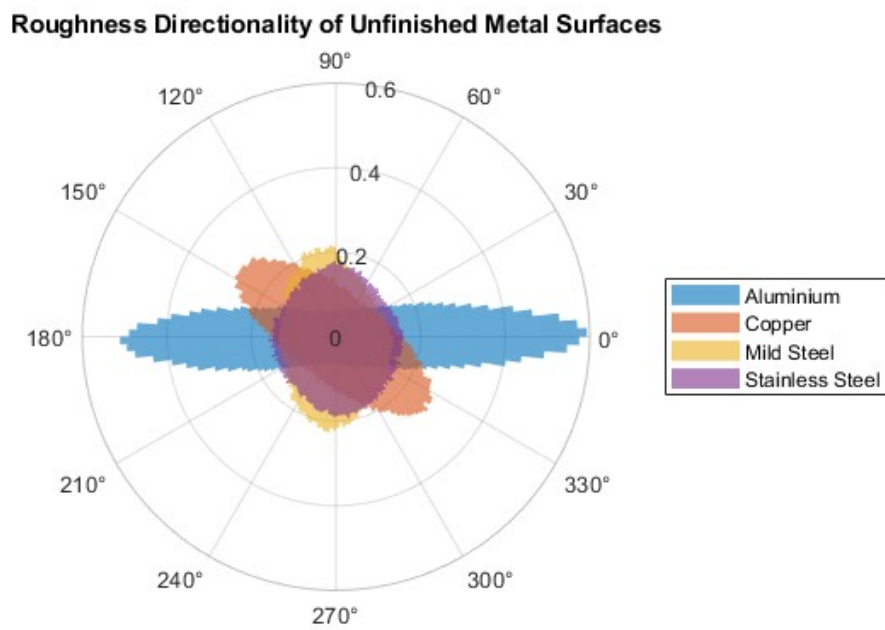


Figure 2-24 – Surface gradient direction polar histogram for the untextured metal surfaces.

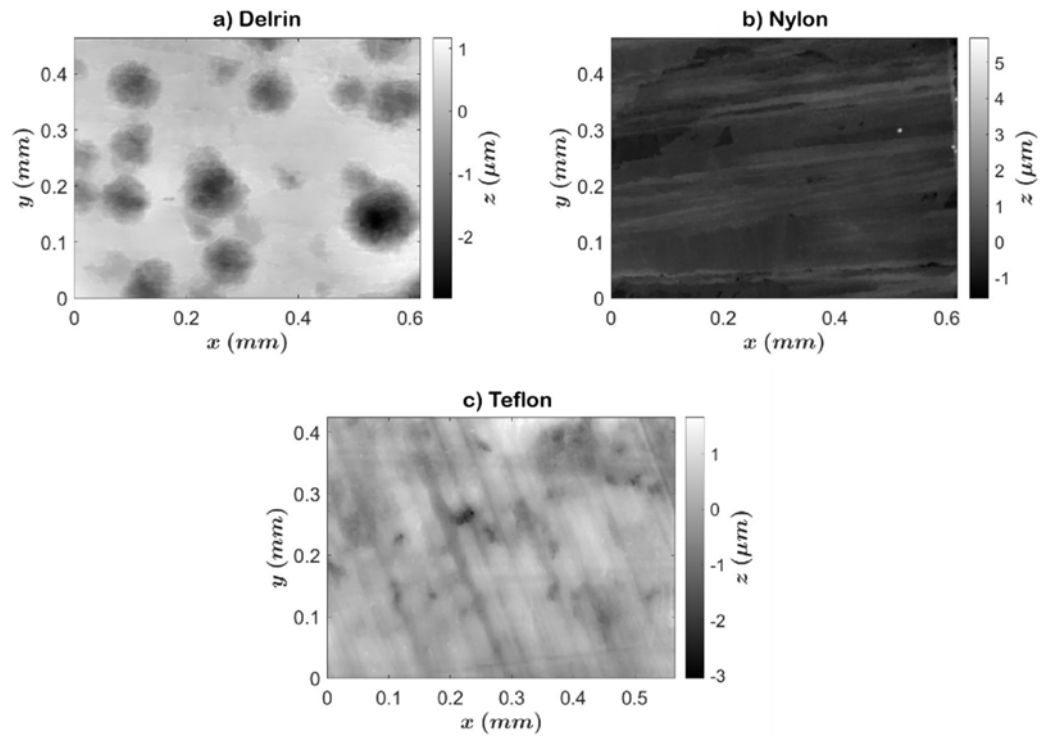


Figure 2-25 – Surface height maps for the untextured polymer surfaces.

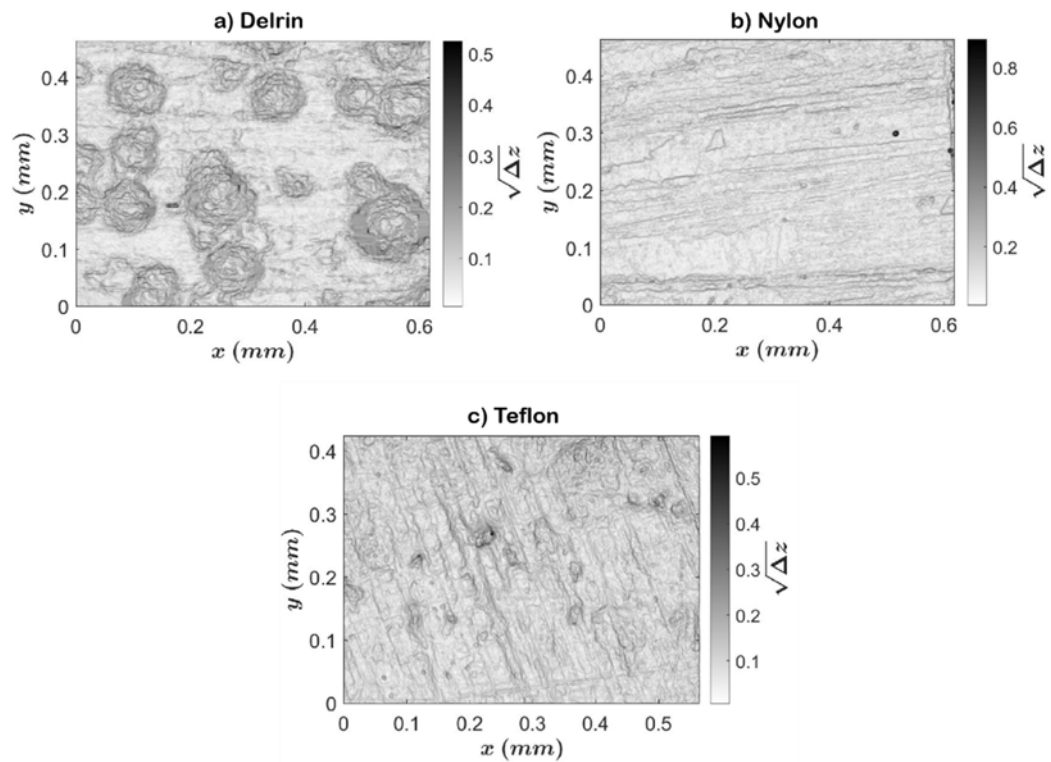


Figure 2-26 – Surface gradient maps for the untextured metal surfaces.

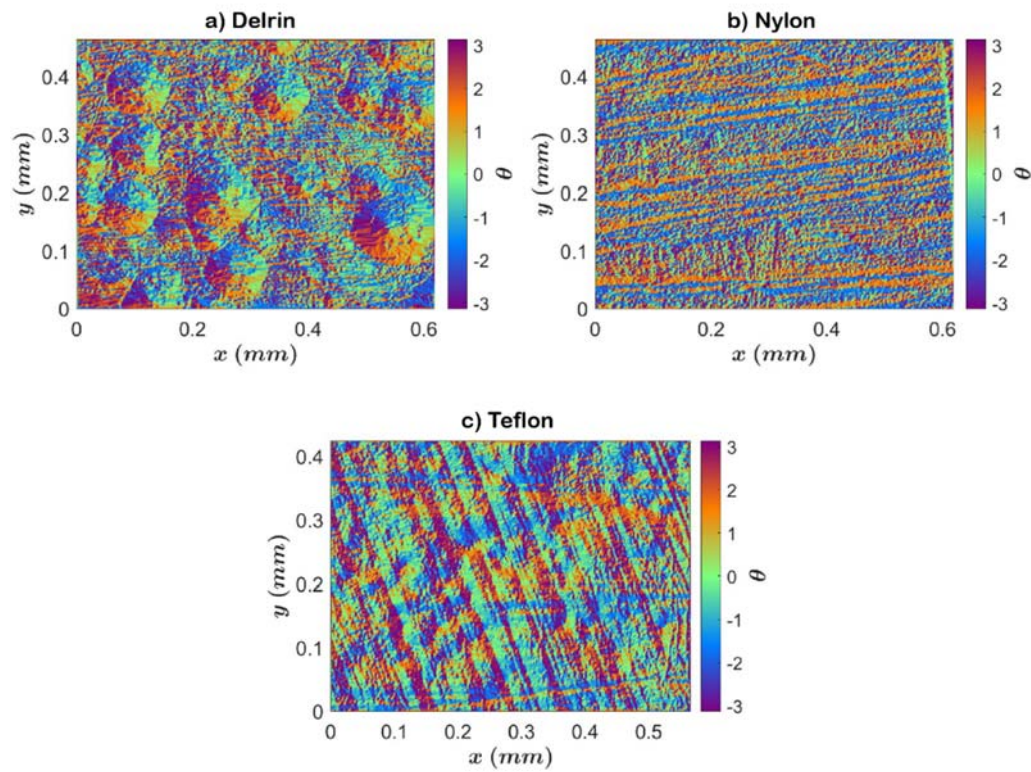


Figure 2-27 – Surface gradient direction maps for the untextured metal surfaces.

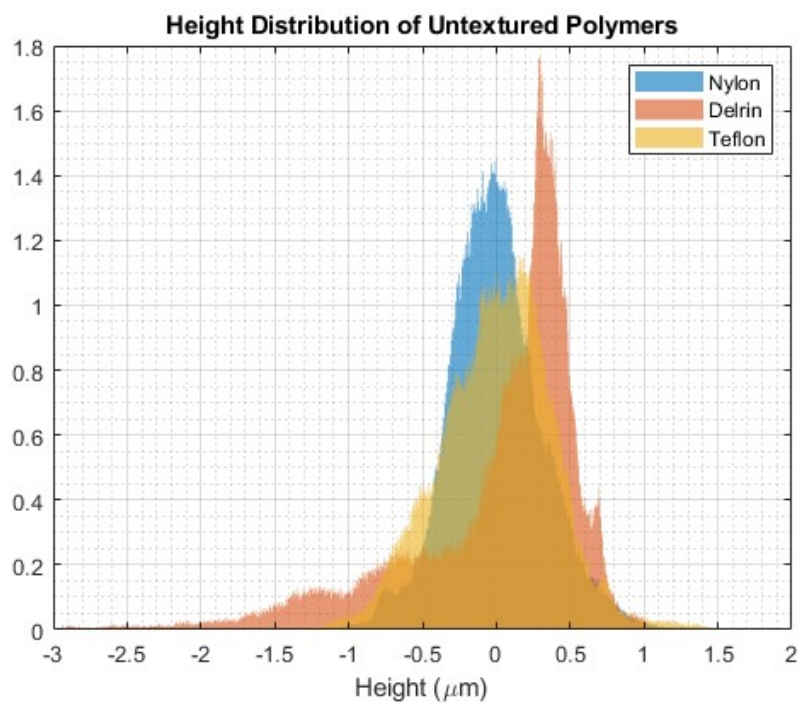


Figure 59

Figure 2-28 – Surface height histogram for the untextured metal surfaces.

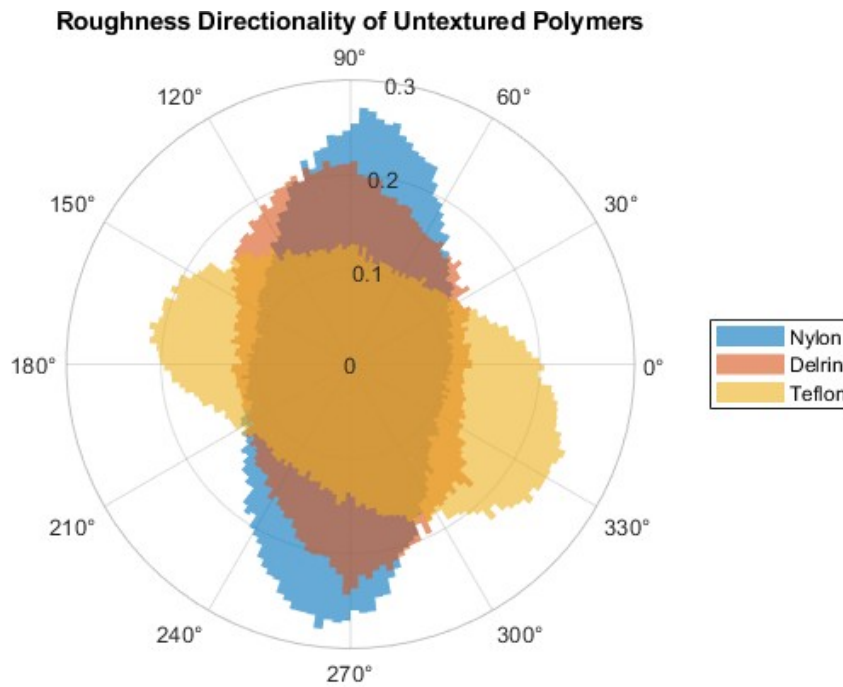


Figure 2-29 – Surface gradient direction polar histogram for the untextured metal surfaces.

The topographies of the untextured polymer samples were found to vary drastically between each polymer composition. This was also the case for the electrode surfaces, as the surfaces of the steel samples exhibited a significantly higher roughness than the copper and aluminium samples. All samples remained untextured during the initial series of tests as a way to briefly investigate the effects of differing surface textures. The samples were then intentionally textured via identical methods as a way to eliminate surface texture as a factor in the second series of tests onwards. All metal and polymer samples were polished using a LaboPol-60 and LaboForce-100 combined grinding and polishing apparatus from Struers, a non-woven nap-free polishing pad, and a diamond suspension in order to attain a consistent low surface roughness across all electrodes. The topographies of the electrode surfaces were flattened as much as possible in order to eliminate the electrode topography as an influencing factor.

The polymer blocks were also subjected to an additional grinding process using the same apparatus and silicon carbide (SiC) grinding pads in order to approximate a uniform surface across the different polymer surfaces. SiC grinding pads of differing grit values from 120 up to 1200 were used on the polymer samples as a method for investigating the contribution of differing surface roughness parameters, real contact area, and the distribution of contact pressures to triboelectric charging. The post-processing surface roughness parameters of both the conductive and insulating samples were measured using the NPFLEX and are shown in Table 10. Surface height maps, gradient magnitude and direction maps for the polished metal and polymer surfaces are provided in Figure 2-30 to Figure 2-34, and Figure 2-35 to Figure 2-36 respectively.

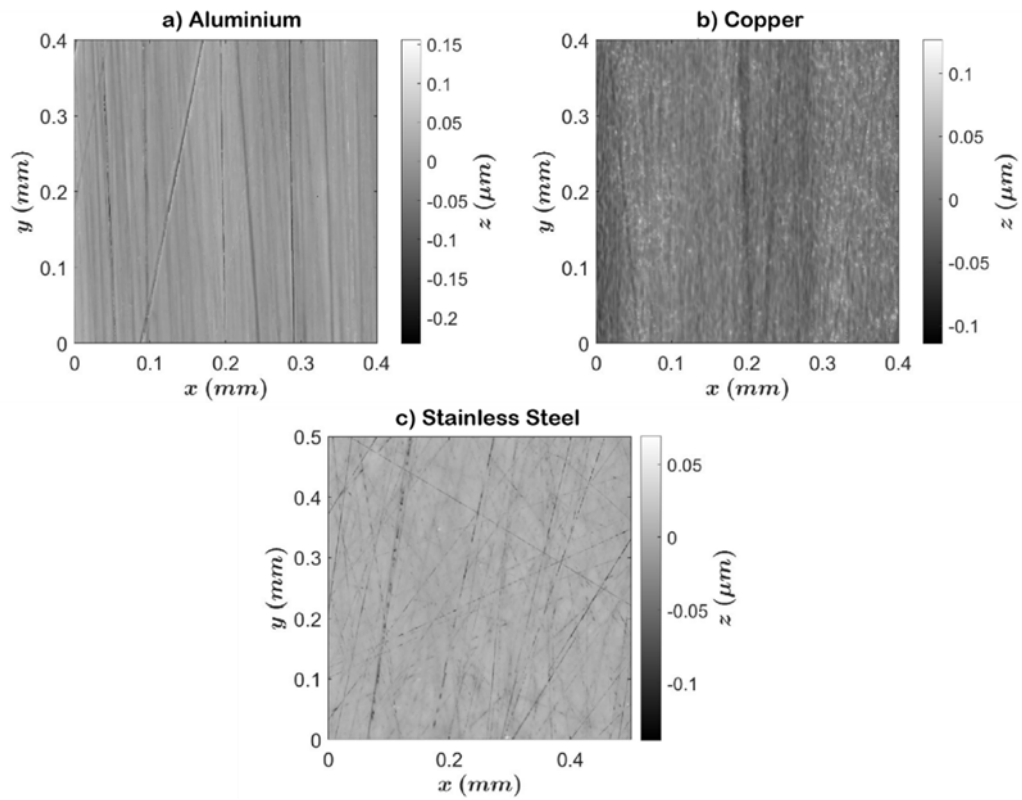


Figure 2-30 – Surface height maps for the polished metal surfaces.

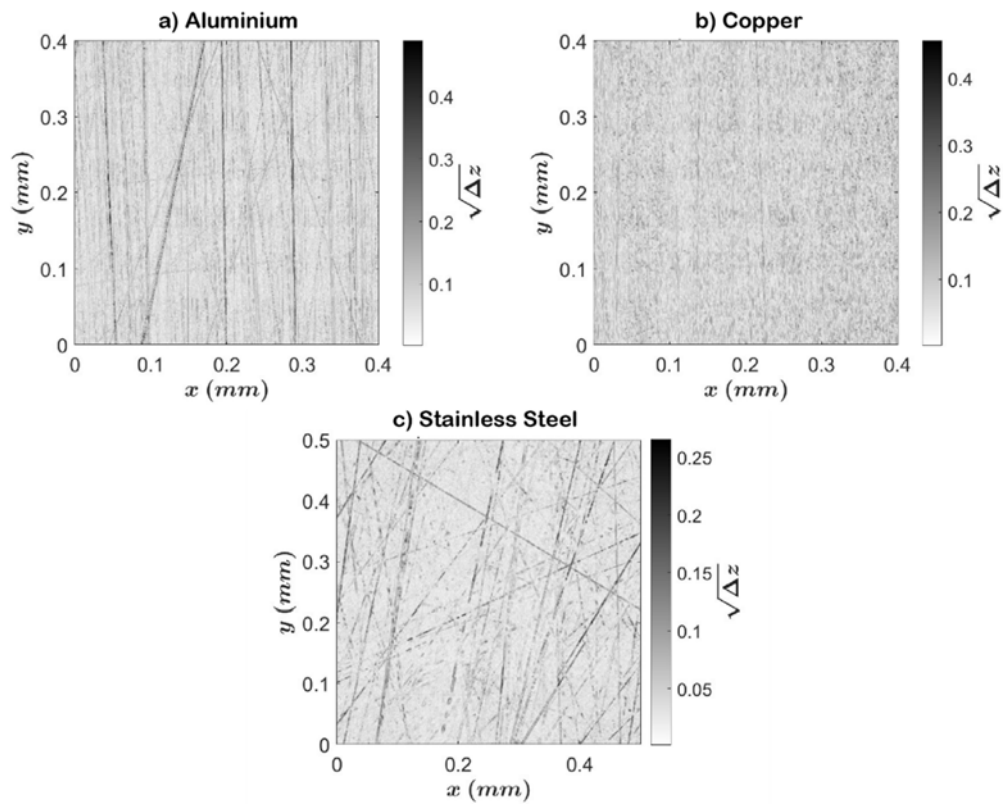


Figure 2-31 – Surface gradient maps for the polished metal surfaces.

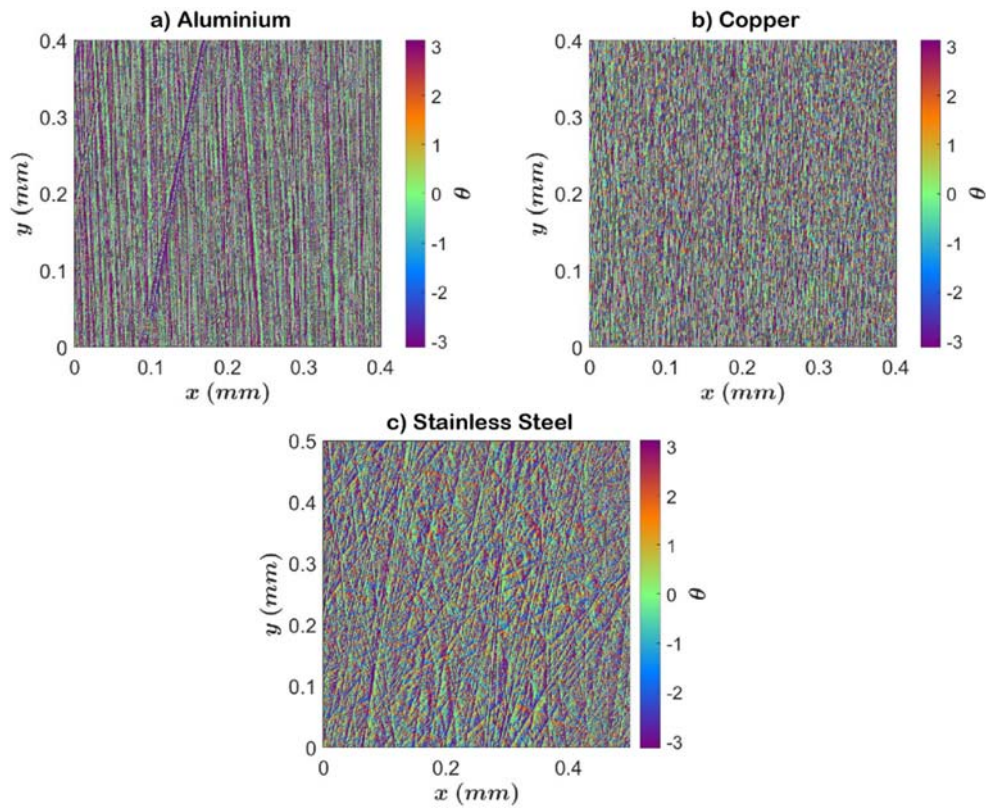


Figure 2-32 – Surface gradient direction maps for the polished metal surfaces.

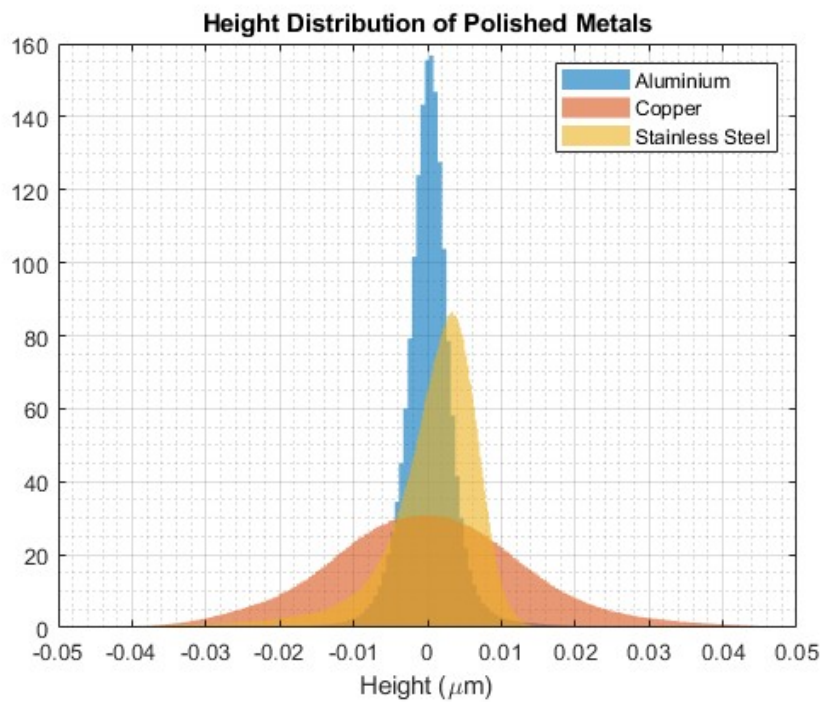


Figure 2-33 – Surface height histogram for the polished metal surfaces.

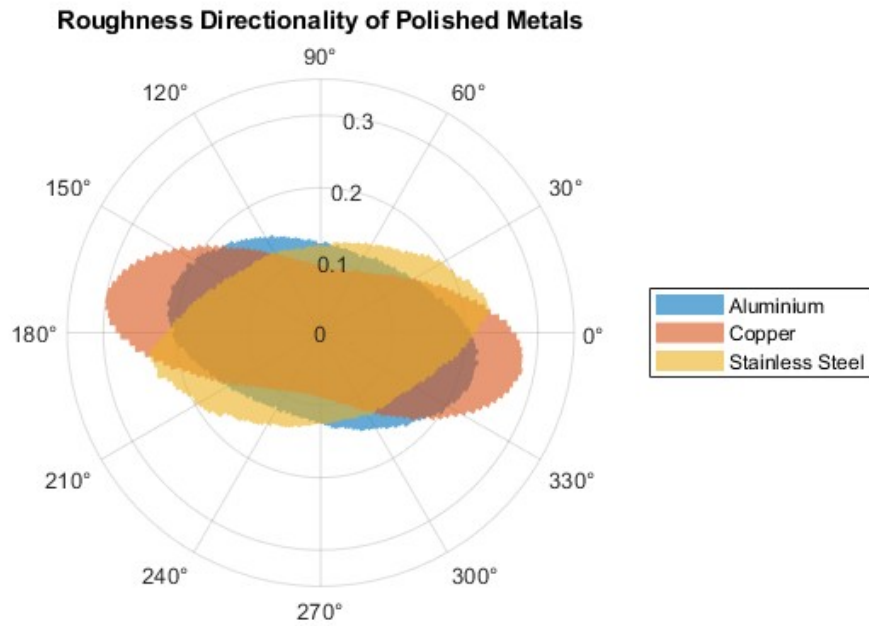


Figure 2-34 – Surface gradient direction polar histogram for the polished metal surfaces.

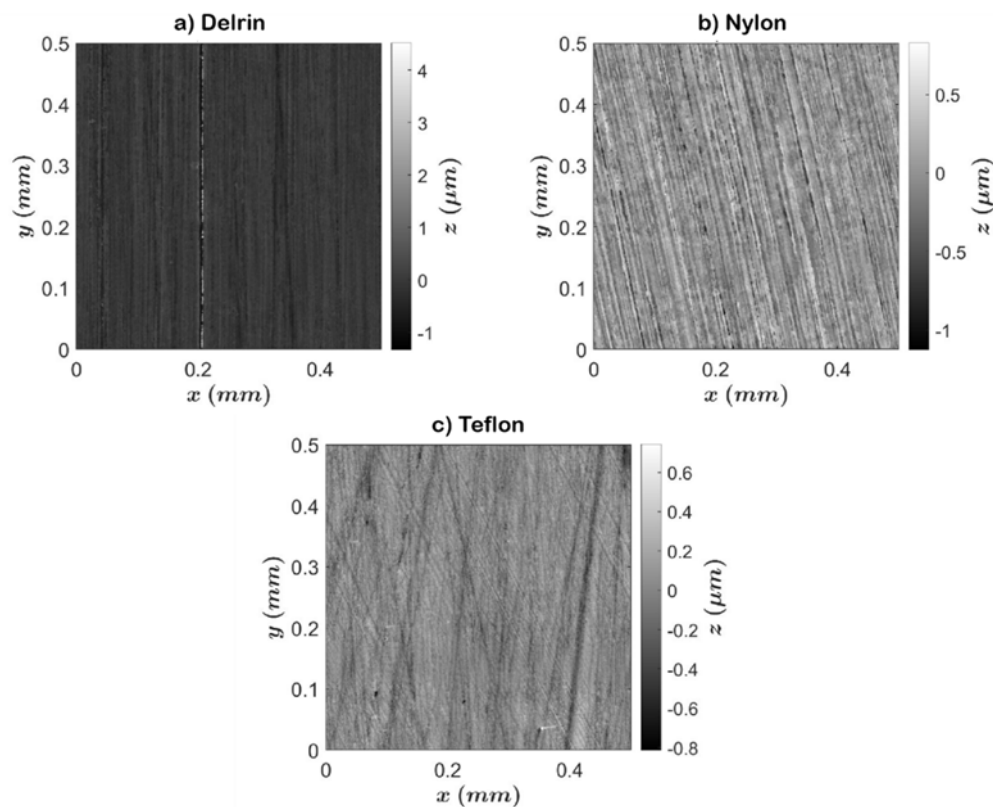


Figure 2-35 – Surface height maps for the polished polymer surfaces.

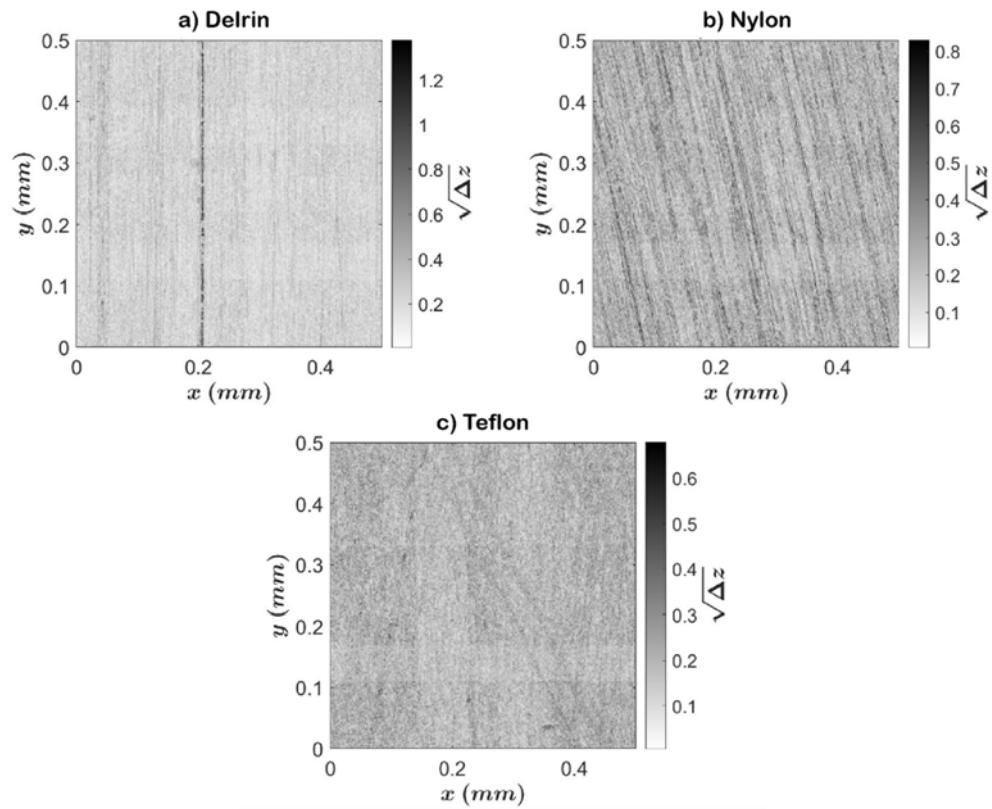


Figure 2-36 – Surface gradient maps for the polished polymer surfaces.

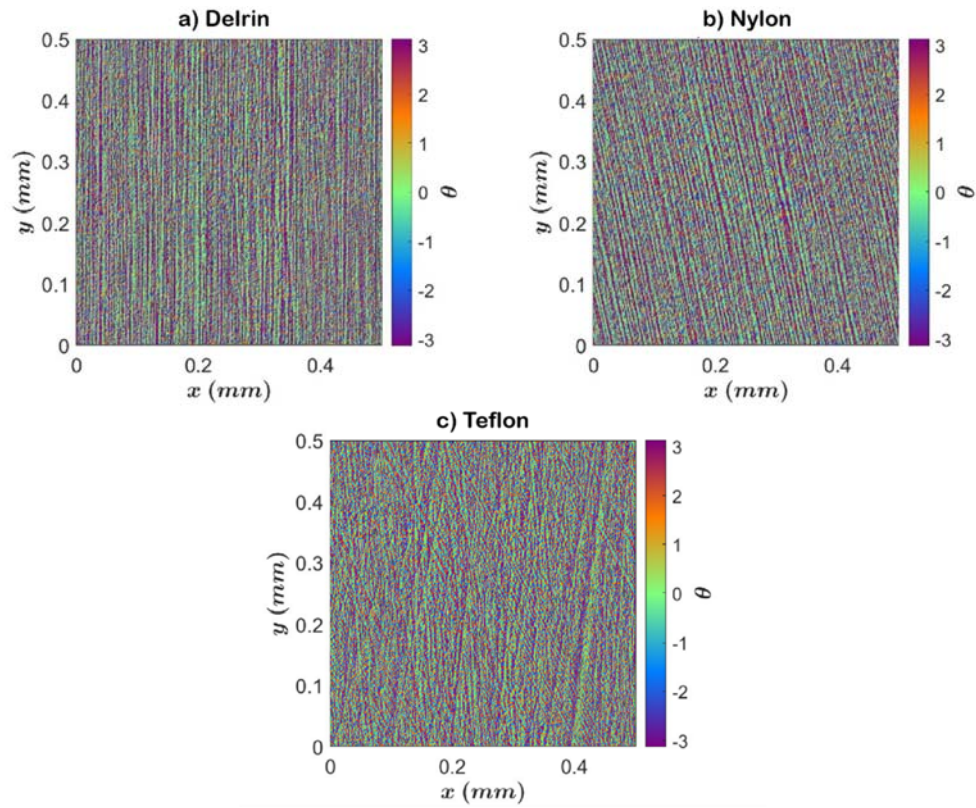


Figure 2-37 – Surface gradient direction maps for the polished polymer surfaces.

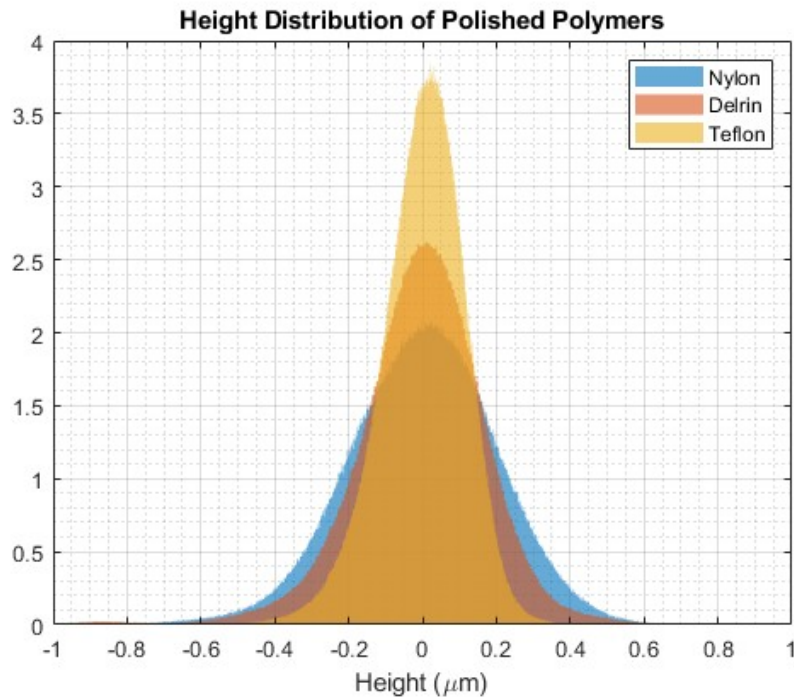


Figure 2-38 – Surface height histogram for the polished polymer surfaces.

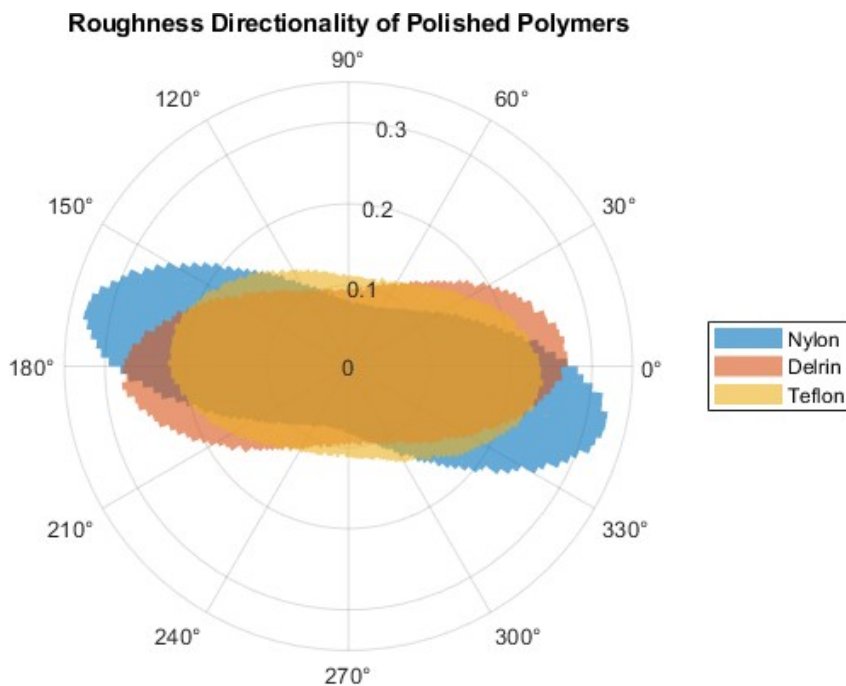


Figure 2-39 – Surface gradient direction polar histogram for the polished polymer surfaces.

Before any form of triboelectric analysis is performed, all samples were submerged in an ultrasonic bath of non-polar heptane for 20 minutes and then placed in an oven at 60 °C for an hour in order to remove any surface contaminants or residual electrostatic charges, without inducing a glassy transition within any of the three polymers. Teflon is known to have beta transitions at 19 °C and 31 °C however, corresponding to a slight unravelling of the helical PTFE polymer rod (C. Wang et al., 2014).

2.1.5 Testing procedure

Once the composition and surface properties of each sample material were determined using the aforementioned techniques, their triboelectric properties were investigated using the F-TENG apparatus. This initial methodology involves three main series of tests.

2.1.5.a Feedback Ammeter and Oscilloscope Configuration

The first series of tests served as an initial proof of concept for the F-TENG apparatus, and used the feedback ammeter and oscilloscope to measure the maximum current output for the hand-held motion of the polymer block. All three polymer materials were used for this series in addition to all four electrode materials. The samples for this series were cleaned but remained untextured. These tests involved bringing the polymer block into contact with an electrode such that their projected surface areas fully overlapped, and then immediately oscillating the block using hand motion. The polymer block was reciprocated by hand, assisted by the use of a metronome operating at 150 bpm in order to help approximate a reciprocating frequency of 2.5 Hz. The polymer block was reciprocated for 30 s and then removed from the contact. The resulting current trace was recorded by the oscilloscope and a maximum current value was measured from it. To aid in minimising the effect of the disparity in reciprocating frequency caused by hand motion, five measurements were made with each material pairing. The standard deviation of these multiple measurements was used as a margin of error. In order to prevent any possible contact electrification prior to the test start, the insulating layer was not put into stationary contact with the electrodes before the oscillations began. If static triboelectrification was to occur before the test start, the resulting data would not be a reliable representation of how contact charge initially accumulates in a sliding contact environment. The measurement circuit configuration for these tests is given in Figure 2-12a.

2.1.5.b Feedback Ammeter and myDAQ Configuration

The second series of tests involved the use of the feedback ammeter and myDAQ unit to record the output current data of the F-TENG during testing. This series of tests involved the same procedure as the first with the exception of removing stainless steel as an electrode material owing to its redundancies in similarity with the mild steel samples and data from the first series of testing. The in-house MATLAB code was also utilised to calculate the integrated charge values for each forward and reverse stroke during the test. The MATLAB code was also able to determine the exact inconsistencies in reciprocating hand motion, showing the actual frequency of motion to be 2.7 ± 0.3 Hz rather than 2.5 Hz. Background measurements were taken for 10 s with the feedback ammeter attached to the F-TENG apparatus before beginning every test in order to evaluate the influence of external electrical interference from lighting fixtures and power supplies during each individual test. These background measurements were taken as previously described in the same environment as the tests themselves, only with both electrodes exposed to air within the lower sample holder, instead of one or both being in contact with the insulating upper layer. The measurement circuit configuration for these tests is given in Figure 2-12b.

An additional test was conducted within this series in order to further investigate the electronic output of the F-TENG device. A 10 M Ω resistor was placed in series with the F-TENG device and feedback ammeter. The secondary input channel for the myDAQ unit was also connected to the external circuit such that it would measure the potential difference across this resistor. The measurement circuit configuration for this measurement is given in Figure 2-40.

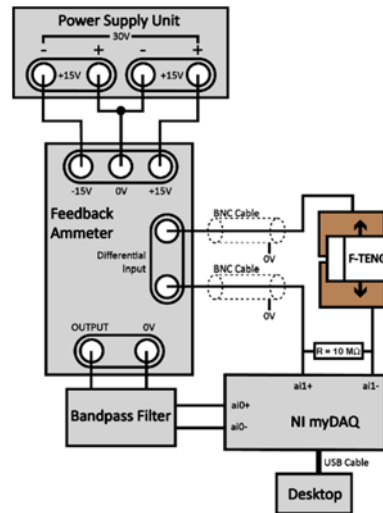


Figure 2-40 – F-TENG measurement circuit for finite resistive load voltage and current output configuration.

2.1.5.c Belt Driven Actuation and Electrometer Configuration

The third series of tests included the use of the belt driven actuator to actuate the polymer block. The reciprocating motion of the polymer block was held at a constant 2.5 Hz with a square-wave velocity profile. Once the background noise had been sampled at the start of each test within this series, the polymer block being tested was placed within the upper sample holder and held out of contact directly above one electrode such that their projected surface areas completely overlapped. The block was then brought into contact and the Arduino code was initiated to cause the stepper motor to oscillate the polymer block. These arrangements for actuation remained unable to measure the applied load to the TENG contact during testing. The applied load was minimised for both the hand-held and belt-driven F-TENG tests. For the series of tests involving the belt driven actuator, the polymer was not fastened to the upper sample holder, instead being pushed back and forth by it, and was free to move vertically. The hand-held nature of the initial series of tests however could not guarantee the minimisation of applied load. Therefore a small discrepancy in applied normal load will arise from the differing mass densities of the polymers.

The feedback ammeter was replaced by a 6517B/E electrometer from Keithley instruments in order to provide resolution and more accurate current output data. The Keithley 6517B is capable of measuring currents with as high a resolution as 10 aA at its most sensitive setting. This measurement circuit configuration is given in Figure 2-12.

The selection of materials for this third series of tests involved all three polymers, although only the copper and aluminium electrode materials were used due to the relatively low current output generated by the mild and stainless steel samples. The samples for this series were textured using the aforementioned

grinding and polishing techniques. The polymer surfaces were ground to varying degrees of roughness whilst the metal electrodes were polished to a mirror finish. All combinations of the polished polymer and metal surfaces were tested in this series as to gauge the triboelectric properties of each interface whilst minimising the influence of contact geometry. The relevant surface topographic parameters for these polished polymer and metal samples are given in Table 10. The Nylon samples were also ground using 120, 600, 800, and 1200 grit SiC pads and tested against the polished electrodes in order to gauge the influence of contact geometry for a specific material pairing. The topographic parameters of these Nylon surfaces are given in Table 8, with surface height maps, and gradient maps given in Figure 2-68.

2.2 Results & Discussion

2.2.1 Current Measurements

2.2.1.a Feedback Ammeter and Oscilloscope Configuration

The first iteration of the F-TENG apparatus tests – using the oscilloscope to record current data – were able to record a change in potential difference between the feedback ammeter output and the virtual ground as the polymer block was moved between the two electrodes. As the polymer block was reciprocated, a pulsed waveform was produced through the oscilloscope. The oscilloscope firmware was able to determine the peak and trough output voltages from the feedback ammeter. The ammeter was set to give 1 V of potential difference for every 100 nA of input current, allowing for the indirect determination of the induced current.

The induced current was shown to correlate with the velocity of the polymer block as it was reciprocated between the two electrode surfaces. The polarity and magnitude of the induced current corresponded to the relative direction and speed of the polymer block relative to the two electrodes. This was observed for higher frequencies of oscillating motion, as well as for pulsed movements conducted at higher velocities. These characteristics support the notion that this output current is indeed electrostatically induced by the relative motion of static charges on the polymer surface with respect to the conductive electrodes. An example trace recorded by the oscilloscope is given in Figure 2-41.

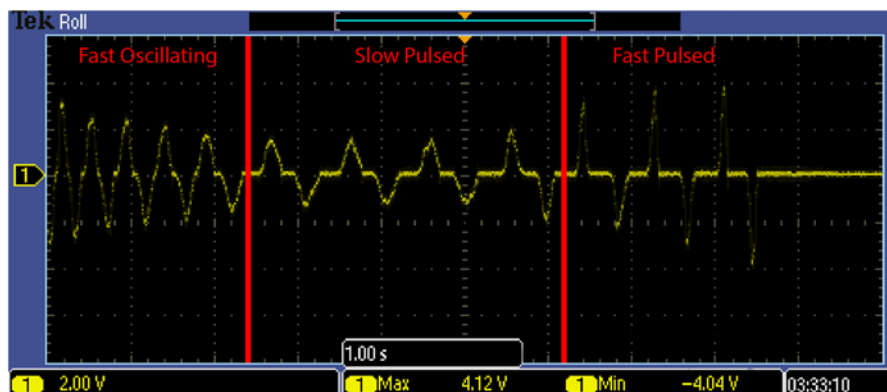


Figure 2-41 – Induced voltage output of the low current feedback ammeter for an example material pairing (Nylon on Copper). The initial pattern is the result of oscillating motion from electrode to electrode, the second is slow pulsed movement from electrode to electrode, and the third is a result of faster pulsed movement.

Not only was this induced current observed, but a difference in output characteristics was observed between each material pairing. This indicated that the magnitude of static charge distribution on the polymer surface was dependant on the surface properties of both the polymer and the conductive electrode. The maximum induced current recorded by the oscilloscope for each material pairing is given in Table 4.

Table 4 – Maximum induced current magnitudes from oscillating the polymer block by hand.

<i>Electrode Material</i>	<i>Polymer Material</i>	<i>I_{max} (nA)</i>
Copper	Nylon	270 ± 63
	Delrin	521 ± 30
	Teflon	-170 ± 14 ^a
Aluminium	Nylon	134 ± 30
	Delrin	368 ± 62
	Teflon	-132 ± 20 ^a
Mild Steel	Nylon	64 ± 8
	Delrin	226 ± 80
	Teflon	-88 ± 3 ^a
Stainless Steel	Nylon	56 ± 8
	Delrin	68 ± 12
	Teflon	-74 ± 4 ^a

^a The Teflon surfaces were shown to develop a negative polarity of surface charge.

Upon first inspection of the results there are some clear areas where the surface composition of the contacting materials correlate with the maximum induced current. However, before examining the data in further detail it is imperative to evaluate the accuracy and reliability of the results. Firstly, taking into consideration that the polymer block was moved by hand across the electrodes for the initial series of tests, there will be a large disparity in the velocity profile of the block. Since the induced current is directly proportional to the velocity of the block – and it is difficult to quantise the margin of error arising from this without direct and thorough visual examination – these data must be approached with the understanding that this disparity may be carried over into these initial results. When considering the different material pairings, the results are mostly in agreement with the semi-quantitative triboelectric series developed by Diaz & Felix-Navarro (Diaz and Felix-Navarro, 2004). Delrin is shown to induce the largest current against all electrode materials and produces the largest current when specifically paired with copper. This result is expected as Delrin is noted as the most electropositive of the selected polymers (Diaz and Felix-

Navarro, 2004). The higher work function of copper in comparison with aluminium and both steels indicates that it has a greater tendency for accepting electrons from an electron donor counter-surface such as Delrin. The Nylon surfaces follow a similar trend to Delrin, since Nylon has also been credited in literature as a material with a strong tendency for donating electrons.

Nylon has seen a more extensive use in triboelectric applications, but Delrin has seen less consideration despite these results. The Teflon surfaces exhibited a unique trait amongst the three chosen polymers in that the induced current was shown to directly correspond to the direction of motion of the polymer block. From this observation it is reasonable to deduce that the flow of conventional current towards the location of the polymer block corresponds to the movement of mobile electrons being repulsed by its presence. Thereby the Teflon surfaces were shown to accumulate tribo-charge densities that were negative in polarity, corresponding to the presence of excess electrons. This is largely in agreement with previous literature unanimously agreeing that Teflon exhibits electronegative triboelectric behaviour. This behaviour is depicted in Figure 2-44 as recorded by the myDAQ unit in the second series of tests. The magnitude of the currents induced by the Teflon block were however substantially smaller than those expected for all paired electrode materials during this first series of tests. The Teflon samples also induced a larger current with copper than with aluminium, which is contradictive to where the two metals are placed within the triboelectric series in terms of their work functions (Diaz and Felix-Navarro, 2004). Both mild steel and stainless steel pairings exhibited similar behaviours, both groups of pairings induced smaller currents than the copper and aluminium pairing groups. These low output currents are likely caused by the higher surface roughnesses of the steel electrodes limiting the real contact area against the polymer counter surfaces during sliding.

It was also shown that, despite the relatively low applied load and short duration of these tests, evidence of material wear appeared on the contacting surfaces after testing. The main observed examples of material wear for these tests were the small presence of polymer wear debris deposited onto the mild and stainless steel electrode surfaces, most notably close to the separating gap between them. This indicates that the edges of the electrodes were the main cause for the removal of material from the polymer blocks. The cause for this wear is likely to be the higher hardness of the steel electrodes relative to the polymer counter surfaces as well as those of the copper and aluminium electrodes. This mechanism of material wear may also explain to a slight degree the reduced electric output characteristics due to the removal of charged material from the polymer surface. Metallic wear debris was also observed as embedded into the surfaces of the Nylon blocks when tested against aluminium, indicating that material wear is occurring for both surfaces in contact despite the disparity of mechanical moduli between two surfaces. Nylon is however the hardest of the three polymers being tested, and aluminium is the softest of the four metals which may explain why this wear behaviour only occurs for this particular material combination. The transfer of materials within the contact as a result of material wear may either contribute towards or inhibit charge transfer, as previously mentioned. For these short duration tests it is difficult to determine the exact influence of material wear mechanisms on triboelectric charging, which is why a key advantage of

the final developed UMT-TENG testing apparatus is capable of significantly longer duration automated tests.

2.2.1.b Feedback Ammeter and myDAQ Configuration

With the addition of the myDAQ data acquisition unit, a much more in-depth analysis of the F-TENG contact became available. A more accurate insight into the output current characteristics of the F-TENG set-up was given through analysis of these data. The current plotted with respect to time gave a distinct alternating pulse-like pattern as shown in the oscilloscope data. The waveform produced by the oscillatory motion of the polymer block is also shown to vary across the duration of some individual tests as they progressed, as shown in Figure 2-42. Alongside this it became clear that the shape of each oscillatory pulse varied between tests. Example current traces for each material pairing are given in Figure 2-43 and Figure 2-44.

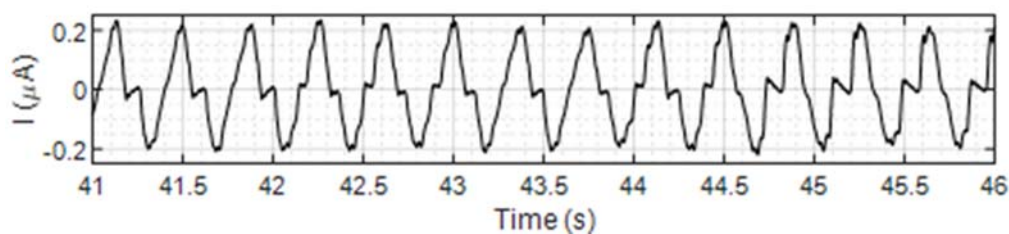


Figure 2-42 – An example of how current waveform can change across the duration of a typical F-TENG test.

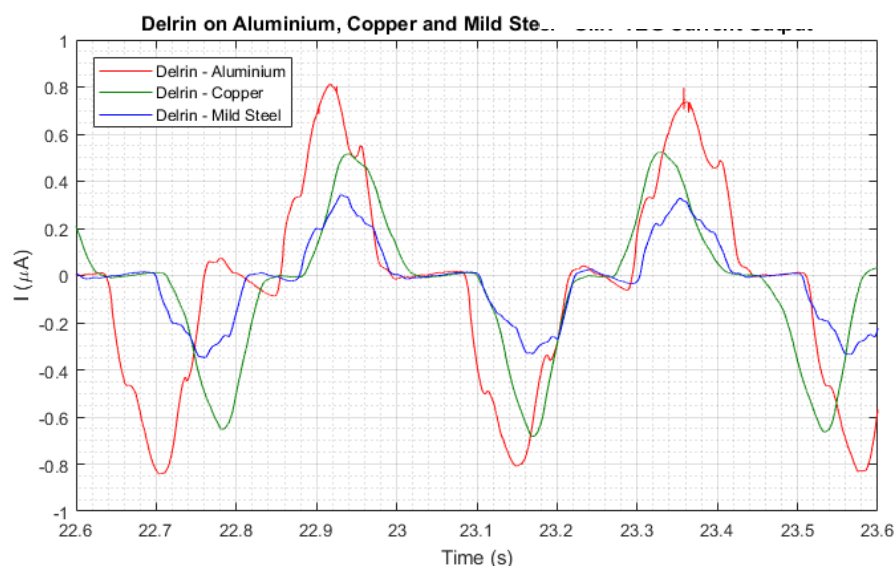


Figure 2-43 – Example plots for induced current over time for the Delrin block reciprocating over aluminium (red), copper (green) and stainless steel (blue) electrodes.

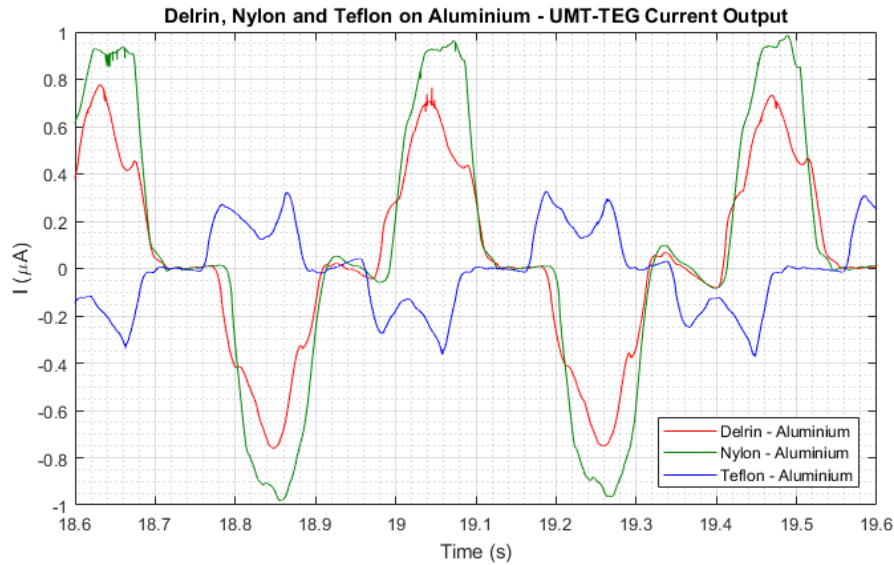


Figure 2-44 – Example plots for induced current over time for the Delrin (red), Nylon (green) and Teflon (blue) blocks reciprocating over aluminium electrodes.

Three-dimensional line-plots and two-dimensional colour-scaled images were produced by stacking side-by-side the pulses induced by each forward and reverse stroke respectively throughout each test. The previously discussed changes in waveform can be seen more clearly in Figure 2-45 and Figure 2-46 where an overlying pattern in is present across the duration of the test. Whilst an overlying pattern in waveform is seen for all F-TENG tests, these overlying patterns developed and changed progressively across the duration of each individual test. In addition to this, each test exhibited different overlying patterns.

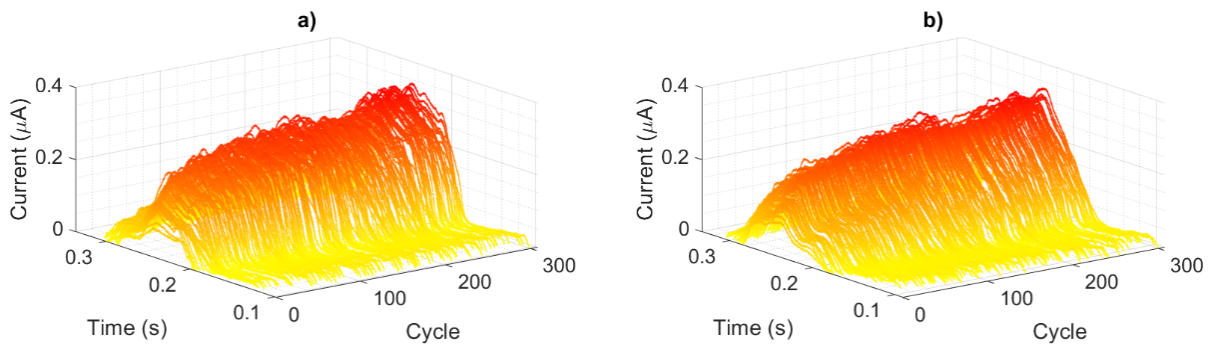


Figure 2-45 – 3D colour-scaled line-plot depicting output current over time for each forward (a) and reverse stroke (b) of a Delrin on Aluminium F-TENG contact over the duration of the test (cycles); Depicting the changes in current waveform as the test progressed.

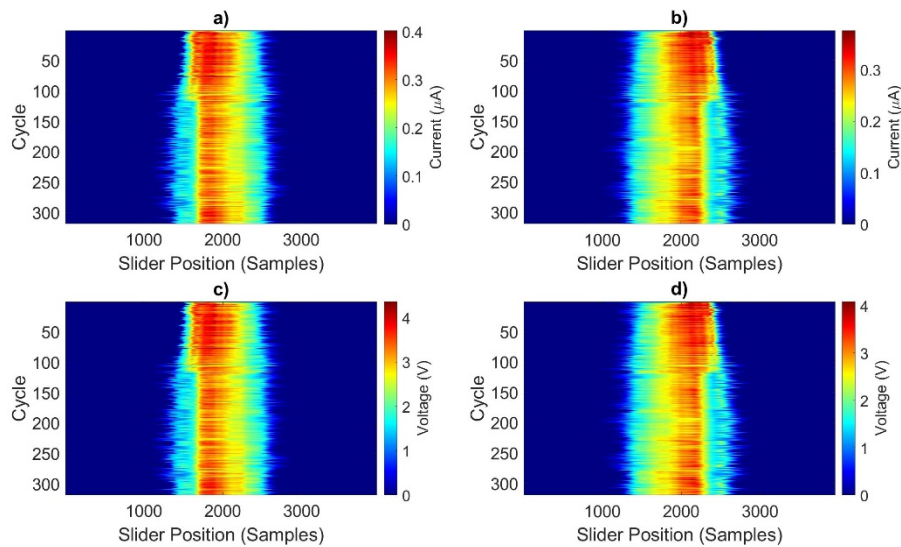


Figure 2-46 – 2D colour scaled images depicting output current (a & b) and voltage (c & d) over time (measured in samples at 1 kHz, directly corresponding to 1 ms) for each forward (a & c) and reverse (b & d) stroke of a Teflon on Copper F-TENG contact over the duration of the test (cycles); depicting the changes in current and voltage waveform as the test progressed.

More abrupt changes in waveform and overall amplitude occurred during a number of tests, which persisted for up to dozens of oscillations during testing. These changes in waveform often coincide with changes in the maximum recorded current and voltage values for their respective oscillations. This change in shape for the pulse-like output of the F-TENG set-up could have numerous origins. Changes in the velocity profile for the polymer block will affect this shape since the induced current is directly proportional to the velocity of the block. Geometrical factors – such as the lateral gap between the two electrodes and whether the block travels beyond the edges of the electrode with too large a stroke length – may also be the cause of these changes in pulse shape. These factors were eliminated however, through the introduction of the belt driven actuator to the apparatus providing consistency in sample motion.

Another possible cause for this disparity in current waveform is the reality that the accumulation of triboelectric charge within each contact cannot be assumed to develop uniformly. The plate-on-plate nature for these triboelectric contacts arise from the need to maximise the electric output for measurement purposes. Plate-on-plate contacts are however notoriously difficult to achieve perfect surface conformation for. The rough nature of real surfaces cause a small fraction of the nominal contact area to actually be in contact for most tribological applications. For the case of the polished polymers, the application of any non-uniform load to the polymer samples during the grinding and polishing process causes a minute curvature of the polymer surface, which in turn causes a reduction in effective contact area when these surfaces are placed against harder counter surfaces. Even if perfect surface conformity is achieved for a plate-on-plate contact, the presence of the sample edges cause localised increases in contact pressure under a uniform applied load. These combined implications highlight the difficulty in controlling the spatial uniformity of triboelectric charge accumulation within the F-TENG apparatus.

The peak current from each oscillation is plotted over time to provide a clearer insight into how the current output changes over the duration of each test. It was shown that the overall amplitude of the current output increased each cycle across the duration of each test. This increase in current output amplitude is assumed to be independent of the velocity of the polymer block upon inspection, and therefore must be a result of changes in electrostatic charge within the F-TENG contact. These changes in current output amplitude are in fact caused by the accumulation of triboelectric charge within the contact, rather than through any discrepancy in block velocity as the oscillation frequency was shown to remain constant upon examination of the data. Plots of per stroke peak induced current output over time for all material combinations during the second series of tests are given in Figure 2-47, Figure 2-48, Figure 2-49, Figure 2-50, Figure 2-51, and Figure 2-52.

The reason behind this gradual accumulation of charge is a subject of debate in triboelectric research. Since electronic transfer is mediated by quantum jumps and tunnelling between states, it is assumed that the triboelectric transfer of each individual electron is instantaneous. Since the maximum charge density is not immediately reached by triboelectric contacts, there must be an additional factor that spreads this transference of charge across time. A likely cause of this time dependence is the introduction of new surface sites for triboelectric charge transfer either upon repeated contacts or through lateral sliding motion. This would mean that the rate at which charge is transferred is directly dependant on the cumulative development of real contact area against the insulating surface, rather than any time constant that describes quantum transitions. Another explanation for this time dependency is that new energy state transitions are made available over time during contact, either by time-dependant flexoelectric perturbations in surface potentials, or by frictional excitation and electron phonon interactions.

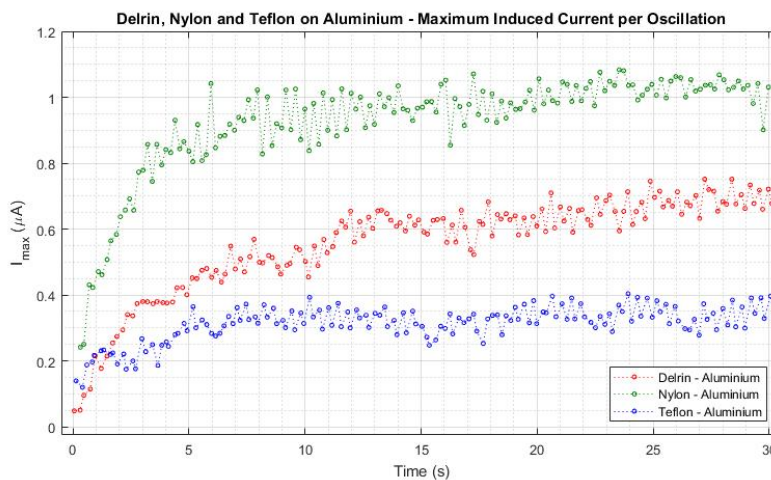


Figure 2-47 – Peak induced current over time for 50x50mm Delrin (red), Nylon (green) and Teflon (blue) on aluminium contacts sliding with a stroke length of 50mm and a frequency of 2.5 Hz. Electrodes were spaced 1mm apart laterally.

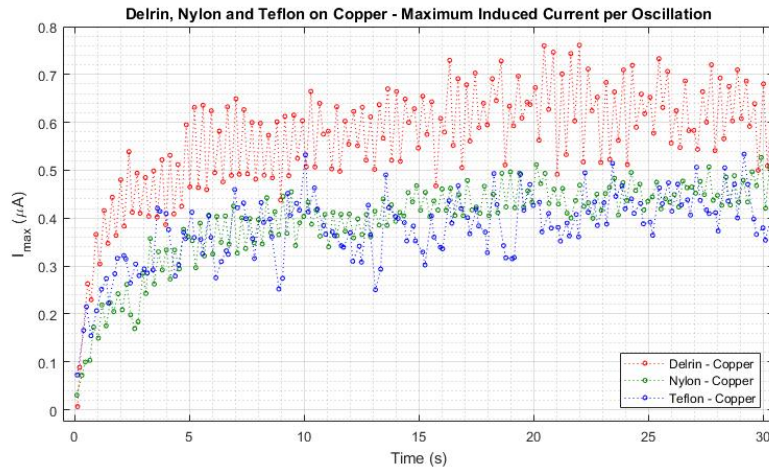


Figure 2-48 – Peak induced current over time for 50x50mm Delrin (red), Nylon (green) and Teflon (blue) on copper contacts sliding with a stroke length of 50mm and a frequency of 2.5Hz. Electrodes were spaced 1mm apart laterally.

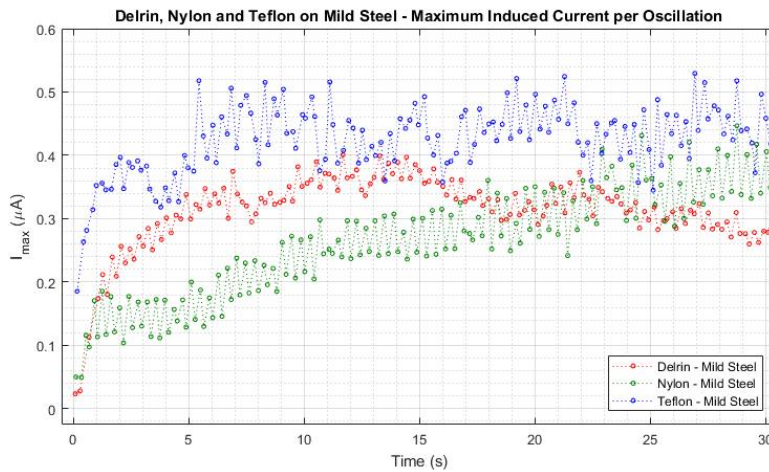


Figure 2-49 – Peak induced current over time for 50x50mm Delrin (red), Nylon (green) and Teflon (blue) on mild steel contacts sliding with a stroke length of 50mm and a frequency of 2.5Hz. Electrodes were spaced 1mm apart laterally.

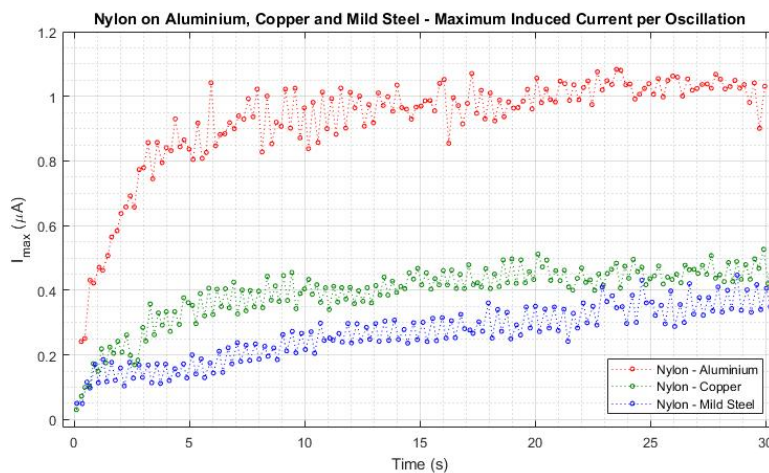


Figure 2-50 – Peak induced current over time for 50x50mm Nylon on aluminium (red), copper (green) and mild steel (blue) contacts sliding with a stroke length of 50mm and a frequency of 2.5Hz. Electrodes were spaced 1mm apart laterally.

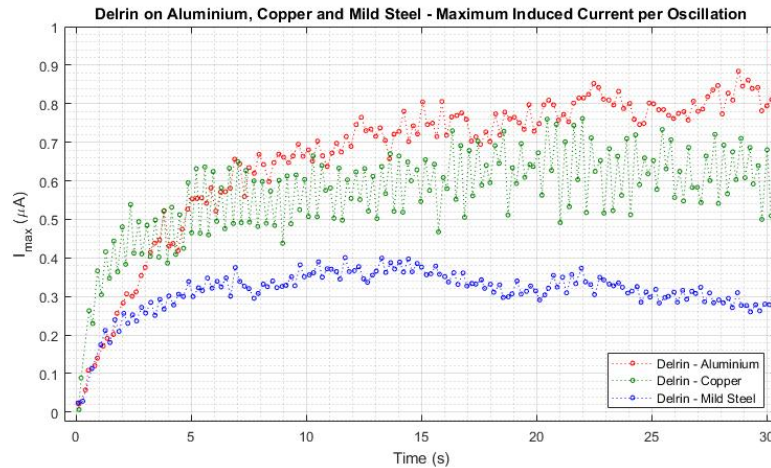


Figure 2-51 – Peak induced current over time for 50x50mm Delrin on aluminium (red), copper (green) and mild steel (blue) contacts sliding with a stroke length of 50mm and a frequency of 2.5Hz. Electrodes were spaced 1mm apart laterally.

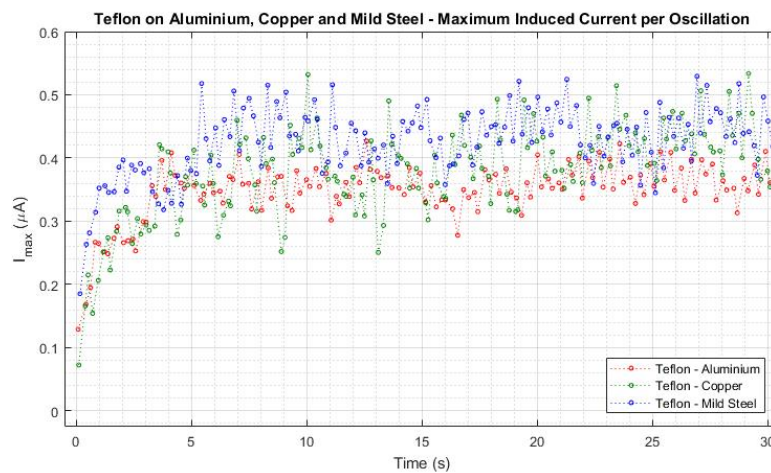


Figure 2-52 – Peak induced current over time for 50x50mm Teflon on aluminium (red), copper (green) and mild steel (blue) contacts sliding with a stroke length of 50mm and a frequency of 2.5Hz. Electrodes were spaced 1mm apart laterally.

It becomes evident that the current output from TENGs of different material pairings also develops at differing rates in addition to reaching different maximum values. The highest current output of 1 μA was produced by the Nylon-Aluminium interface. The current output for this test rapidly rose during the first 6 seconds of testing before stabilising at the peak measured value. The contact that generated the lowest output current of 0.26 μA by the end of the 30 second test was the Delrin-Mild Steel contact. This test in particular displayed a diminishing current output towards the end of the test.

The resulting current output of the F-TENG apparatus under a 10 $\text{M}\Omega$ resistive external load was similar to that of the short circuit output. The current waveform remained in-phase with the velocity profile of the block, although the magnitude of the current waveform was reduced by a small fraction as shown in Figure 2-53. The secondary data acquisition channel for the myDAQ acted as a voltmeter for this test. An almost identically oscillating voltage was recorded on this channel, with a frequency correlating to that of the physical motion of the block as shown in Figure 2-53. In fact, this voltage output corresponded directly

to the current output in accordance with Ohm's Law (1-129) with the exception that it was reversed due to the configuration of the myDAQ attachment to the circuit. An open-circuit case was also imposed for an additional test, however the magnitude of the resulting voltage output of the F-TENG device then exceeded the recording capabilities of the myDAQ unit, rendering the current data for said test also unreliable.

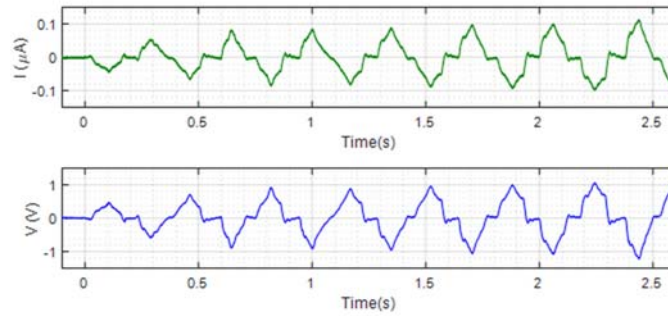


Figure 2-53 – Output current (green, top) and voltage (blue, bottom) for 50 x 50 mm Nylon on Copper F-TENG contact reciprocating at $2.7 (\pm 0.3)$ Hz for 2.5 s with a stroke length of 50 mm and a 1 mm lateral electrode spacing.

2.2.2 Triboelectric Charge Measurements

2.2.2.a Hand Held Actuation and Feedback Ammeter

Upon initial comparison of this contact charge accumulation alongside the maximum output current per oscillation, it becomes clear that this time-integrated value is more reliable for providing information on what is electronically happening within each TENG contact. The method for measuring the time-integrated value of triboelectric contact charge (Q) is now more clearly depicted in Figure 2-54. The calculated values for charge yielded smaller deviations in value from stroke to stroke throughout test durations, as depicted in Figure 2-55. This higher consistency arises from the time-integrated property of the measurement, as it mitigates the large errors introduced with inconsistencies in oscillating frequency and velocity profile of the moving block.

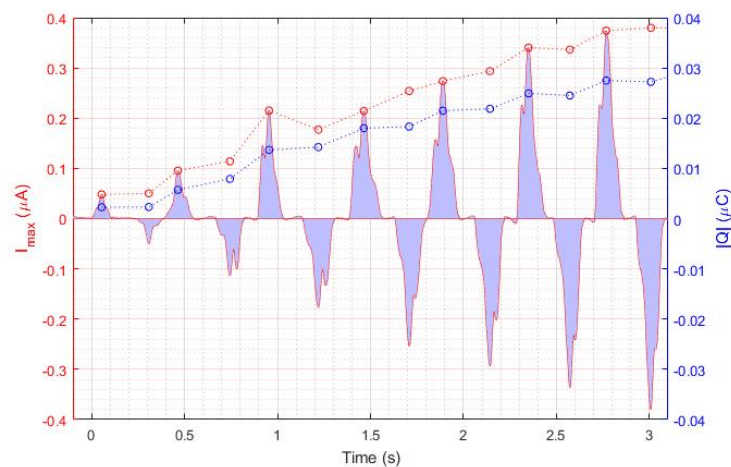


Figure 2-54 – Comparison for output current (solid red), peak output current (dotted red) and contact charge (blue) over time for 50x50mm Delrin and aluminium contact reciprocating at 2.5Hz with a stroke length of 50mm and electrodes spaced 1mm apart laterally at the middle of the stroke.

Upon examination of the integrated charge data it is clear that there is significantly less variation in contact charge than in peak induced current as hypothesised. Each material pairing displays a distinct accumulation of charge over time. This time-dependent relationship could either be described by a power law, logarithmic, or exponential function, but longer tests are needed to provide enough data for a full analysis. This function is likely to be exponential in nature as to represent a similar charging behaviour to that of a traditional capacitor. This is also in agreement with the capacitive term in the first order lumped parameter equivalent circuit described by Niu (Niu, 2015).

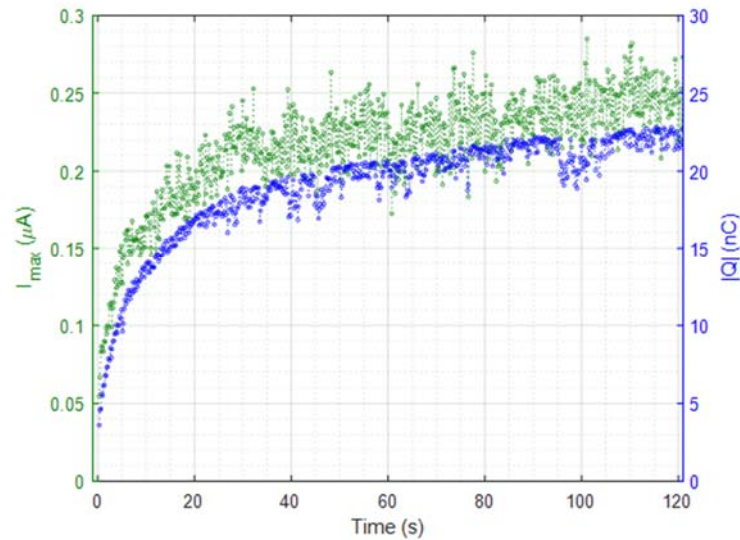


Figure 2-55 – Maximum output current per half-oscillation (green, left), and contact charge per stroke (blue, right) for a generic F-TENG contact.

The contact charge data for each material pairing were plotted against time across the test duration and are presented from Figure 2-56 up to Figure 2-61. A clear pattern is seen in the integrated charge values, showing the contact charge accumulating across the duration of every test. The charging rate for all material pairings also slows as the contact charge density approaches a particular saturation value.

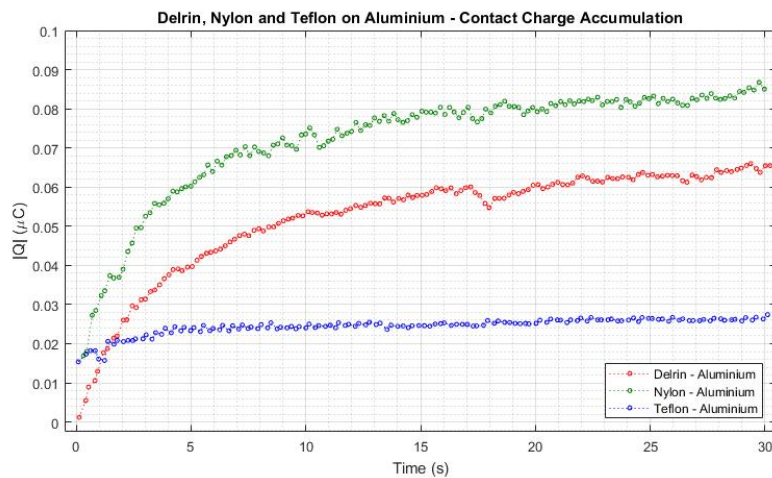


Figure 2-56 – Integrated contact charge over time for 50x50mm Delrin (red), Nylon (green) and Teflon (blue) on aluminium contacts sliding with a stroke length of 50mm and a frequency of 2.5Hz. Electrodes were spaced 1mm apart laterally.

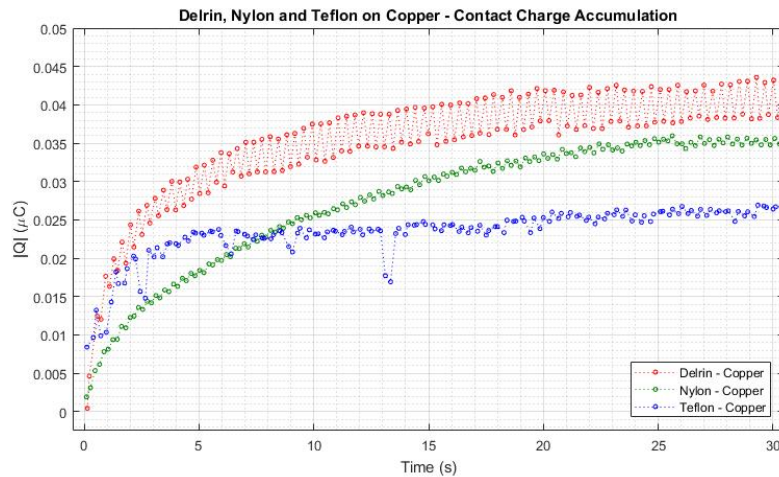


Figure 2-57 – Integrated contact charge over time for 50x50mm Delrin (**red**), Nylon (**green**) and Teflon (**blue**) on copper contacts sliding with a stroke length of 50mm and a frequency of 2.5Hz. Electrodes were spaced 1mm apart laterally.

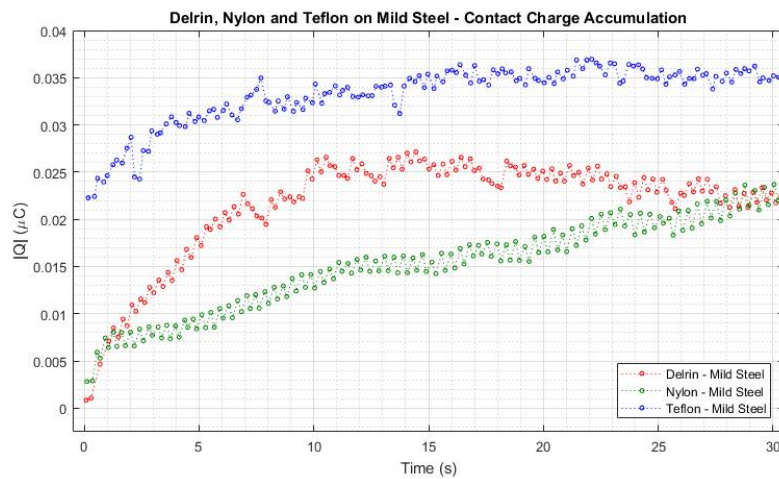


Figure 2-58 – Integrated contact charge over time for 50x50mm Delrin (**red**), Nylon (**green**) and Teflon (**blue**) on mild steel contacts sliding with a stroke length of 50mm and a frequency of 2.5Hz. Electrodes were spaced 1mm apart laterally.

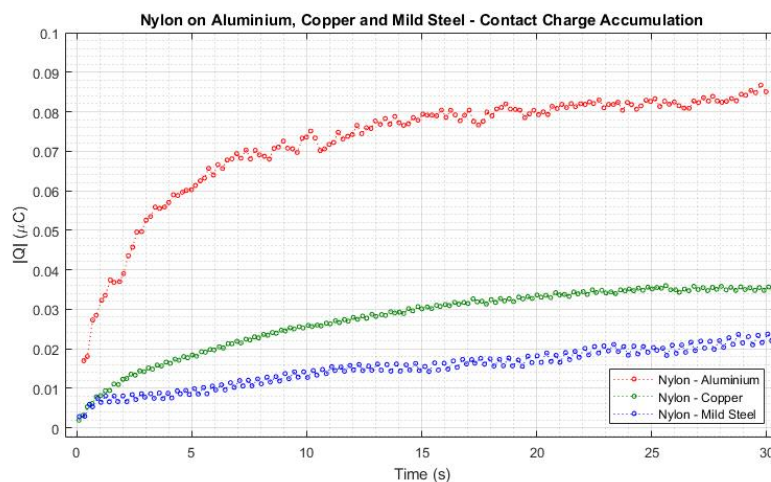


Figure 2-59 – Integrated contact charge over time for 50x50mm Nylon on aluminium (**red**), copper (**green**) and mild steel (**blue**) contacts sliding with a stroke length of 50mm and a frequency of 2.5Hz. Electrodes were spaced 1mm apart laterally.

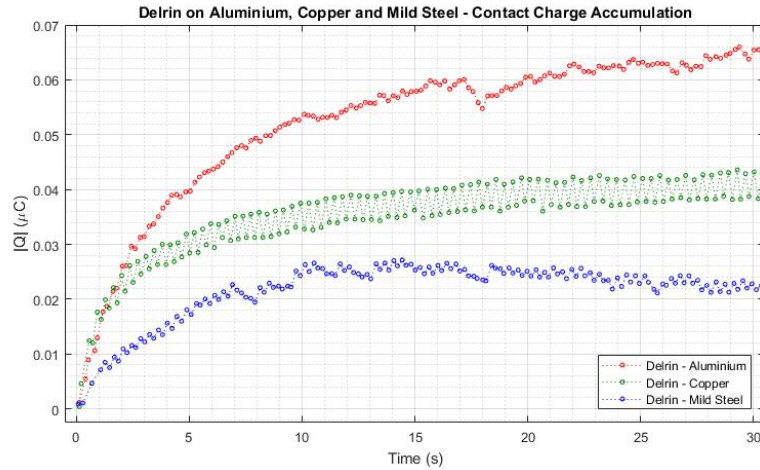


Figure 2-60 – Integrated contact charge over time for Delrin on aluminium (red), copper (green) and mild steel (blue) contacts sliding with a stroke length of 50mm and a frequency of 2.5Hz. Electrodes were spaced 1mm apart laterally.

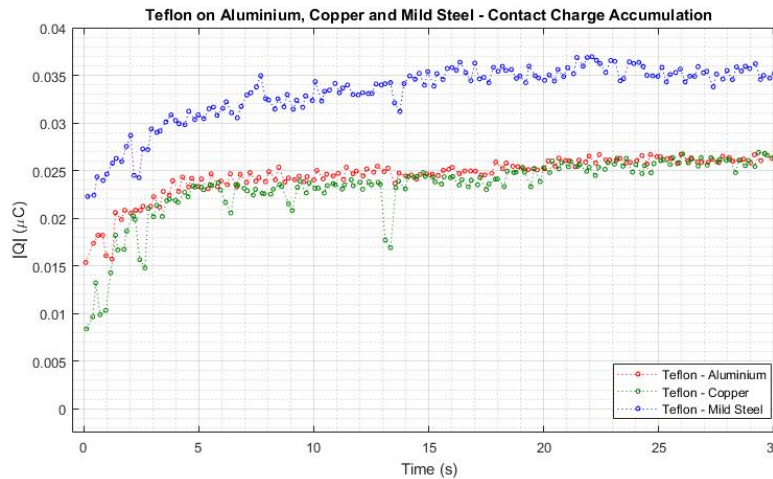


Figure 2-61 – Integrated contact charge over time for Teflon on aluminium (red), copper (green) and mild steel (blue) contacts sliding with a stroke length of 50mm and a frequency of 2.5Hz. Electrodes were spaced 1mm apart laterally.

The physical reason behind this behaviour is that as the surface charge density increases, the electric potential from the presence of these charge densities counteracts the chemical potential between the two differing surfaces, making the net electrochemical potential across the contact zero and preventing further charge transfer. This accumulation of triboelectric charge within the contact appears similar to charge accumulating on either side of a linear capacitor as an external voltage is applied to it. The relationship between charge (Q) over time (t) for a linear capacitor with a capacitance of C being charged by a supply voltage (V_0) across a circuit with a load resistance of R is described in a similar fashion to Harper's original equation for time dependency (1-2).

$$Q(t) = CV_0 \left(1 - e^{-\frac{t}{RC}} \right) \quad (2-7)$$

The in-house MATLAB program was adapted to fit this particular function to the charge accumulation data for each test. Two arbitrary constants (a and b) were assigned to the values of CV_0 and RC respectively. CV_0 represents the maximum charge (Q_{max}) contained by such a capacitor, whereas RC

represents a time constant (τ) that describes the rate of charge accumulation. An additional constant c was included to account for any potential offsets in the starting time (t_i) for the start of each test, giving the following *fittype* in MATLAB.

$$Q(t) = a(1 - e^{-b(t+c)}) \quad (2-8)$$

The charge accumulation trends shown in the majority of tests using the F-TENG apparatus showed exponential accumulation as one would find in a linear capacitor. An example of this exponential fitting for a text is shown in Figure 2-62.

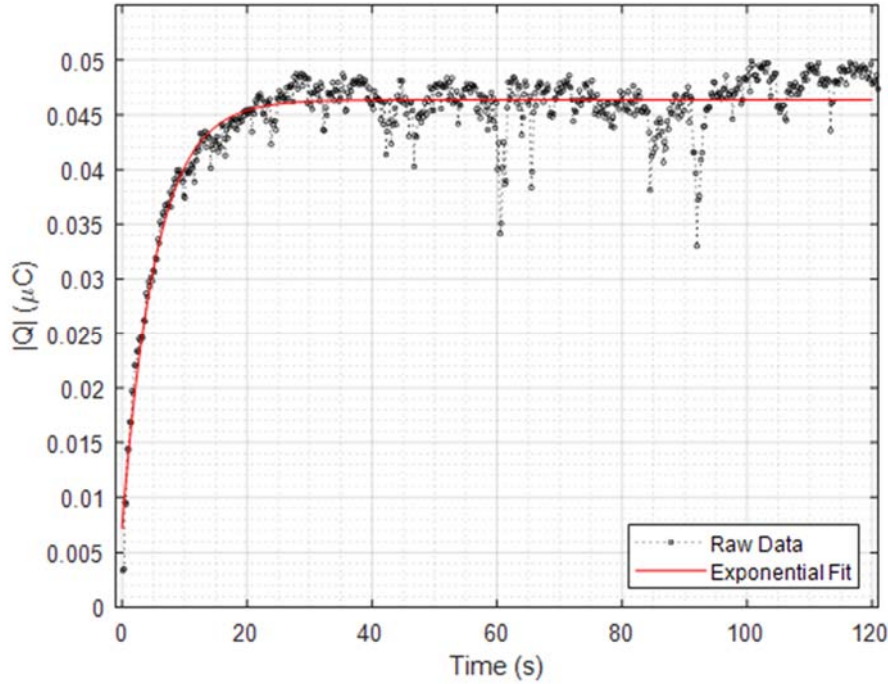


Figure 2-62 – Contact charge per half-oscillation (black) fitted against an exponential (red) charging function for a generic F-TENG contact, exhibiting a more exponential charging pattern with an R^2 value of 87.89. The coefficients for the exponential function are as follows: $a = 0.04637 \pm 0.0019$, $b = 0.1849 \pm 0.011$, $c = 0.9141 \pm 0.2591$.

There are points during a number of tests where the integrated value for contact charge drops sharply – either over the course of one half-oscillation or several – and then steadily rises back up over the course of the following seconds as shown in Figure 2-63. Changes in values calculated using time-dependent integrations such as contact charge coincide with changes in current waveform, however some changes in waveform do occur without any changes in contact charge. Figure 2-64a is a 2D representation of how the current waveform changes across the same charge accumulation depicted in Figure 2-64b. An abrupt change in waveform is observed after approximately 117 oscillations during this particular test, coinciding with a drop in contact charge.

These more abrupt changes may be an indication of dielectric breakdown across the F-TENG contact. Dielectric breakdown in this situation would be caused by it becoming energetically favourable for some transferred electrons to tunnel back to their original material surface as a result of the charge density on the surface they had previously transferred to being close to complete saturation (Zhai et al., 2018). These

abrupt drops in contact charge often accompany changes in the way that current is induced across the stroke of the sliding contact, making the pulse-shape – or effectively waveform – of the alternating current pattern produced by the T-FENG sliding contact another interesting characteristic to examine.

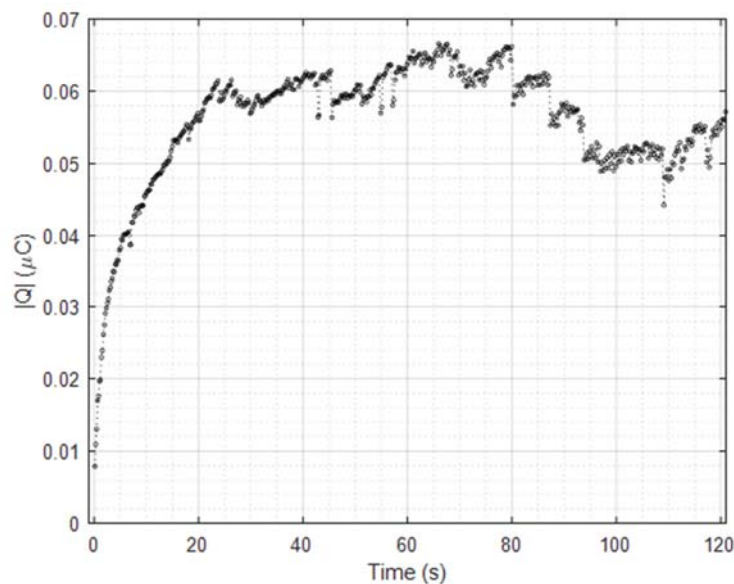


Figure 2-63 – An extreme-case example of how contact charge can abruptly drop and attempt to rise back up several times during F-TENG testing. The material combination used for this specific test was Nylon on Copper.

One important observation in a portion of the tests, and one that is most prominent during the Delrin-Copper contact testing, is that there is some deviation in both peak induced current and induced charge dependant on the direction of movement. This phenomenon could be caused by errors in the stroke not being centred directly above the gap between the two electrodes. This would also lead to a change in pulse shape due to the geometrical change in device orientation. This discrepancy could also be caused electrically, either by a poor electrical connection to one of the two electrodes or an internal resistance within the feedback ammeter causing a bias to one specific electrode.

These changes in waveform could have a number of causes due to the nature of testing. Changes in velocity profile of the block can lead to a change in how the current is induced across each stroke as previously explained. Another cause could be geometric changes within the F-TENG apparatus. It is more likely however that these changes are directly resulting from the changes in trapped charge distribution on the polymer surface. This can manifest in several ways. The sliding nature of the contact can introduce new sites for triboelectric charge transfer to the contact along the length of the stroke. This is Volta's original explanation for why triboelectric charging within sliding contacts experimentally show higher charge densities than static contacts. This however does not explain the change in waveform across the span of multiple oscillations.

Another explanation is that the deformation of the contact geometry over time introduces new sites for charge transfer over time as surface profiles become more truncated and conformal. Similarly, the presence of material wear can delaminate and remove surface material from the contact. This can subsequently remove trapped charges associated with the wear debris from the contact and expose new

sites for charge transfer. Another possibility is that this wear debris becomes somehow re-entrained into the contact. If this wear debris becomes adhered to the counter surface, this prevents further charge transfer from occurring within the site of the adhesion due to the lack of chemical potential across the site.

Another explanation for more abrupt reductions in triboelectric charge density could be electrostatic discharge through dielectric breakdown across the contact. If a suitable trapped charge density is reached locally somewhere on either surface, it may become energetically favourable for those charges to recombine with states in the original donor surface through the mechanism previously described for driving triboluminescence. The driving force behind why it may become energetically favourable for this to happen may originate from flexoelectric increases in surface potential that result from local stains and deformations. The nucleation and propagation of surface cracks and fractures may also contribute to significant increases in surface potentials.

In the particular case described by Figure 2-64, the sudden drop in integrated contact charge coinciding with a change in waveform is likely caused by a localised dielectric breakdown within the F-TENG contact. A sudden transference of charge between the polymer and metal surfaces, contained within a small area of the overall contact, would explain the sudden change in only a small portion of the overall current waveform which then in turn lowers the integrated contact charge. Repeat tests, using samples that are identical in terms of composition and surface topography, for each material pairing reveal that these phenomena of localised breakdown has the potential to occur for every polymer-metal material pairing. These phenomena only occur during tests when the contact charge exceeds a particular threshold value; which changes for every material pairing. For the case of the Teflon on copper contact described in Figure 2-64, the value for this charge magnitude is shown to be approximately 28.7 nC. However, it cannot be assumed that the triboelectric charge density is uniform across the F-TENG contact, since the topographies of the contacting surfaces are not perfectly flat and conforming. Therefore, a multitude of factors must be included in the determination of whether localised charge breakdown occurs within a contact or not; including the topographies of the interactive surfaces, and the surface spatial density of electron acceptor/donor sites on any interacting dielectric surface.

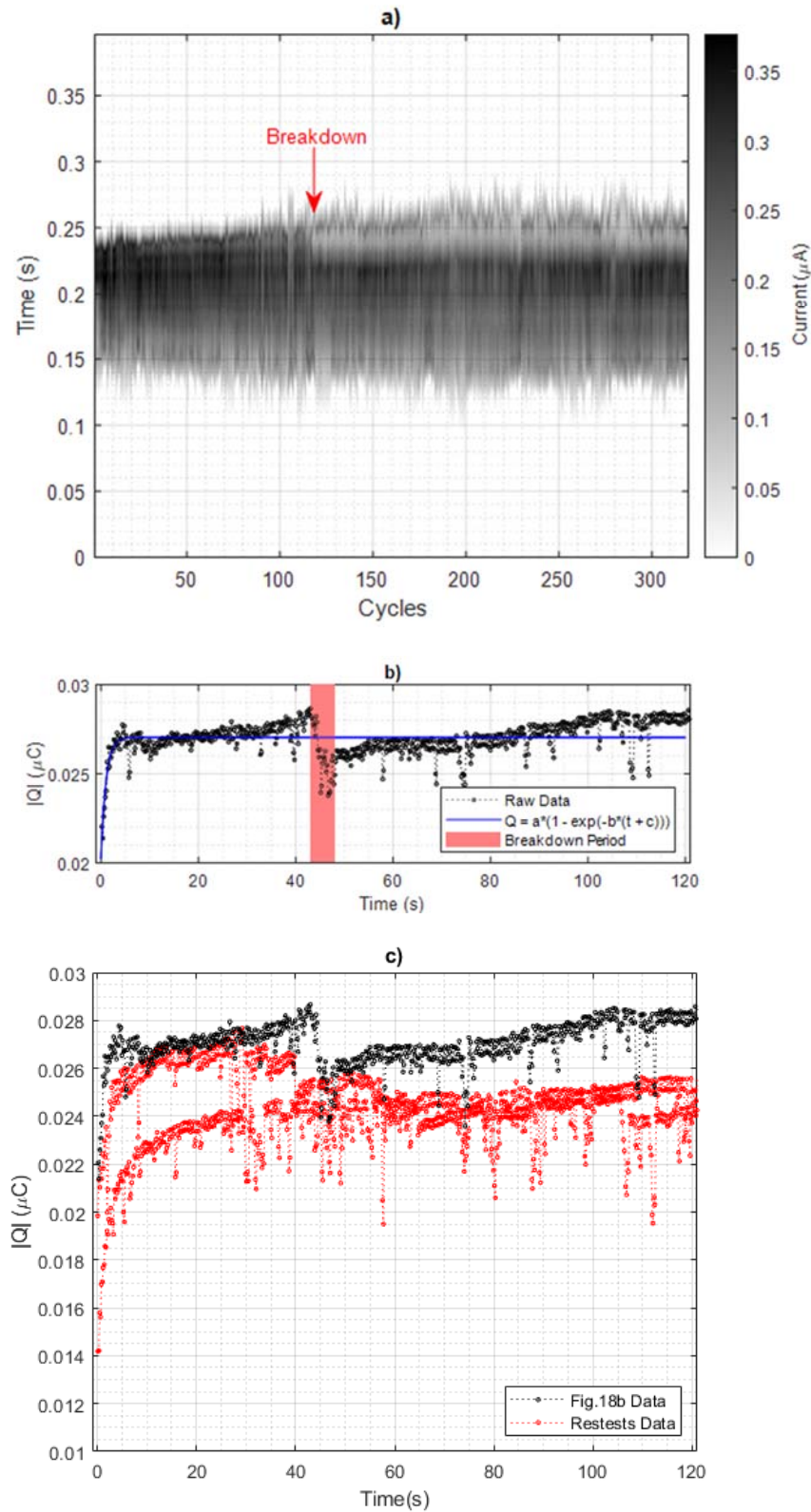


Figure 2-64 – a) 2D colour-scaled image depicting output current over time for each forward stroke of a Teflon on copper F-TENG contact across the duration of an example F-TENG test (cycles). b) Contact charge per cycle across the duration of the same test, highlighting an abrupt change in current waveform and contact charge during the 118th cycle of the test. c) Contact charge accumulation over time for three identical Teflon on copper contacts.

An additional test was conducted with the F-TENG apparatus in order to gauge the influence of lateral electrode spacing on the electric output of the device. The 2D projected current trace for this test are depicted in Figure 2-65 and shows how the current waveform becomes more concentrated towards the centre of the stroke as the electrode spacing is increased from 2mm to 20mm linearly across 100 cycles. This change in lateral electrode spacing did also cause a gradual decrease in time-integrated contact charge. The reason for this more spatially concentrated distribution of current output could be a result of the increasingly limited time that the polymer block spends in contact with both electrodes simultaneously whilst in motion. Therefore the higher current that passes through the ammeter during the middle section of each stroke could be explained by the fact that both electrodes are simultaneously experiencing a considerable change in electric field. It may be concluded that any changes in current waveform that do not coincide with a change in time-integrated contact charge is a result of a change in sample velocity profile, whereas those that do may be a result of electrostatic discharge within the contact or geometric change within the apparatus.

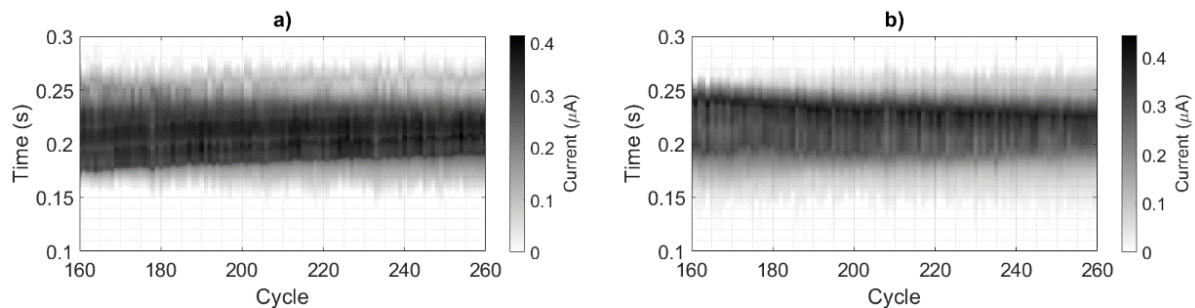


Figure 2-65 – 2D colour-scaled equivalent of Figure 2-45, depicting output current over time (samples) for each forward (a,) and reverse stroke (b) for 100 cycles of an example Delrin on Aluminium F-TENG contact; Depicting the changes in current waveform as the lateral electrode spacing is increased from 1mm to 10mm across the test cycles.

2.2.2.b Belt Driven Actuation and Electrometer

With the inclusion of the belt driven actuator, the controlled movement of the polymer block was able to reveal the origin of the previously mentioned waveform disparity to be mostly attributed to the velocity and position profile of the polymer block relative to the two lower electrodes. Whilst the waveform between individual tests still exhibited some variation, the variation across the duration of an individual test was shown to be more uniform, eluding to the expansion of existing sites for charge transfer due to surface deformation. Using consistently textured polymer and metal samples also allowed for surface topography to have less influence on the development of triboelectric charges. Therefore, the influence of surface composition could be investigated more thoroughly.

2.2.2.b.i Influence of Surface Composition

An interesting trend was found upon comparison of the different material pairings in the F-TENG apparatus. As expected, all material pairings with differing compositions exhibited not only different contact charges at the end of each test, but the pairings also reached these charges at differing rates. The charge accumulation data over time for a selection of tests comparing the three polymers are depicted in Figure 2-66. These data suggest that the surface composition of a material not only has an

influence on the maximum charge density it can attain against a given counter-material, but also the rate at which it can accumulate this charge via triboelectrification in a sliding environment.

Upon comparison of the three polymer surfaces it is clear that their chemical composition has a significant influence on the maximum amount of charge they can attain via triboelectric charge transfer, as well as the rate at which triboelectrification may occur. After 120 s of triboelectric charging under the aforementioned F-TENG testing procedure, the Delrin, Nylon and Teflon surfaces reached contact charges of approximately 25 nC, 49 nC and -23 nC respectively. Of the three polymers used in testing, Nylon accumulated the most charge within the given testing time. This emphasises the usefulness of electropositive insulating materials for triboelectric contacts in agreement with (Ding et al., 2018). Despite Teflon exhibiting a lower magnitude of saturation charge density than expected, the Teflon surfaces did all reach their respective charge saturation densities considerably faster than the Delrin and Nylon surfaces.

The charging rates for Teflon surfaces were also much more easily matched to the model for exponential charge accumulation than the Delrin and Nylon surfaces. The three coefficients (a , b , and c) used for exponential fitting to charge data for each material combination with respect to equation (2-8) are shown in Table 5. Coefficient a represents the contact saturation charge density ($|Q_{max}|$), above which further triboelectric charge transfer becomes energetically unfavourable. Coefficient b represents the inverse of the time constant (τ) describing the rate at which charge is accumulated via triboelectrification. Coefficient c is introduced as a means of separating the charge accumulation time constant (τ) from any potential offsets in test start (t_0) or the presence of pre-existing charges on some polymer sample surfaces prior to test initiation.

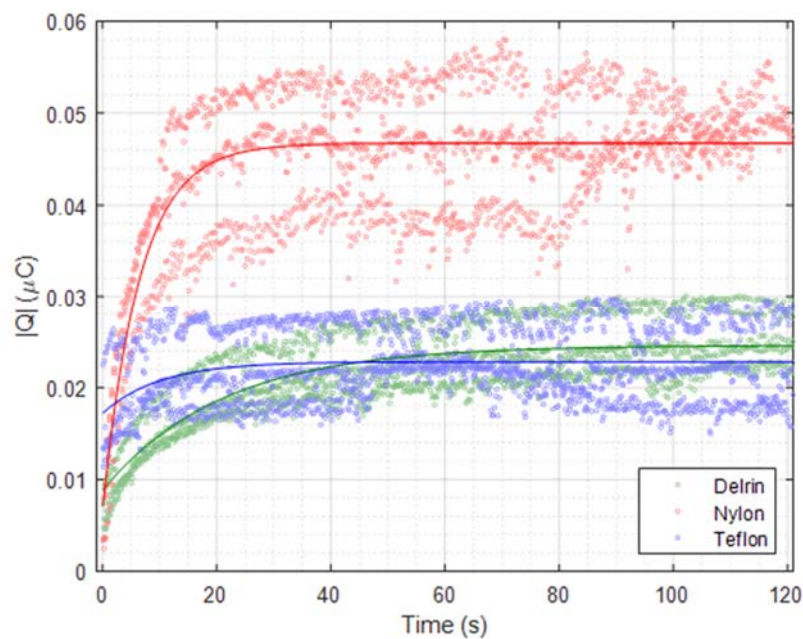


Figure 2-66 – Contact charge accumulation over time for Delrin (green), Nylon (red), and Teflon (blue) on Aluminium F-TENG contacts. Three example tests were taken from each material pairing in order to exhibit the level of consistency and repeatability achieved.

Table 5– Average coefficients for exponential fittings of charge accumulation data for Delrin, Nylon, and Teflon on Aluminium F-TENG tests.

Polymer	$a (Q_{max} , nC)$	$b (1/\tau, s)$	$c (t_0, s)$
Delrin	24.6	0.048	9.3
Nylon	46.7	0.154	0.9
Teflon	-22.8*	0.1	14

* All Teflon surfaces developed a negative surface polarity, indicating the accumulation of surface electrons.


Table 6– Average coefficients for exponential fittings of charge accumulation data for Delrin, Nylon, and Teflon on Copper F-TENG tests.

Polymer	$a (Q_{max} , nC)$	$b (1/\tau, s)$	$c (t_0, s)$
Delrin	27.8	0.076	2.2
Nylon	57.5	0.146	0.8
Teflon	-25.2*	0.167	1.5

* All Teflon surfaces developed a negative surface polarity, indicating the accumulation of surface electrons.

In terms of electrode composition, the copper electrodes consistently produced a larger charge density on all counter-materials than the aluminium electrodes. This increase in charge between copper and aluminium electrodes was approximately 10% for Delrin counter-surfaces, 22% for Nylon counter-surfaces, and 25% for Teflon as shown in Figure 2-67a, b and c respectively. This is partially contradictory to what was expected of the F-TENG tests. In this case one would expect a copper surface to charge electropositive surfaces such as Nylon and Delrin to a greater extent than an aluminium surface would, owing to its higher work function. This higher work function would also however predict copper to charge a Teflon counter surface to a lesser degree than aluminium, which is not observed. This reinforces the idea that there are more factors to consider than surface active groups and chemical composition when considering the effectiveness of triboelectric contacts.

Table 7 – Calculated triboelectric series for the tested metals and polymers.

Electron Donor (+ve)	Nylon 6-6
	Delrin
	Aluminium
	Stainless Steel
	Copper
Electron Acceptor (-ve)	Teflon

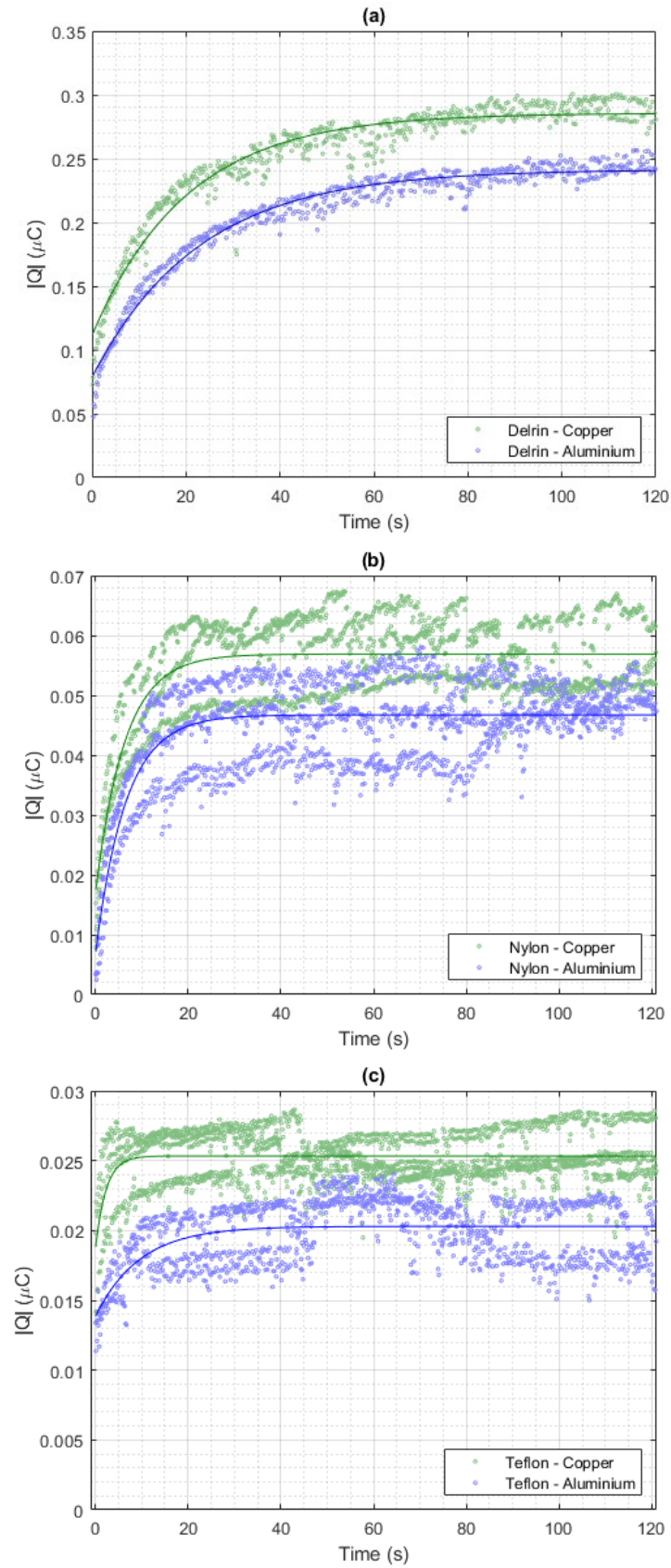


Figure 2-67 – Charge accumulation over time for Delrin (a), Nylon (b), and Teflon (c) on Aluminium (blue) and Copper (green) F-TENG contacts; demonstrating the difference in charge accumulation rates between contacts involving the two conductive counter-materials.

2.2.2.b.ii Influence of Surface Roughness

The primary mechanical factor to consider for TENG contacts is the real contact area between the two interacting surfaces are their respective topographies. In order to maximise the charge accumulating within a TENG contact it is important to both maximise the charge density per unit surface area within the contact, as well as the real surface area in mechanical contact. The consequence of microscale variations in surface topography is that the real contact area between two surfaces may be significantly smaller than the apparent nominal contact area (Avlonitis and Kalaitzidou, 2015). This effect is amplified if the two surface topographies conform less so to one another. Materials with higher hardness values and elastic moduli are prone to deform less under contact pressure. This implies that for two polymer surfaces that are generally soft, their low elastic moduli allow them to deform elastically more easily to allow their surfaces to conform with any counter material to a greater extent under the same contact pressure.

F-TENG tests were conducted using Nylon samples of differing surface topographies, produced via the aforementioned grinding technique. The surface topographies of the textured Nylon samples, in addition to the topographies of both electrode materials after being polished, were recorded as previously described using a Bruker NPFLEX white-light interferometer. The height maps for these surfaces are given in Figure 2-68, with the roughness parameters of the electrodes and Nylon samples also given in Table 10 and Table 8 respectively.

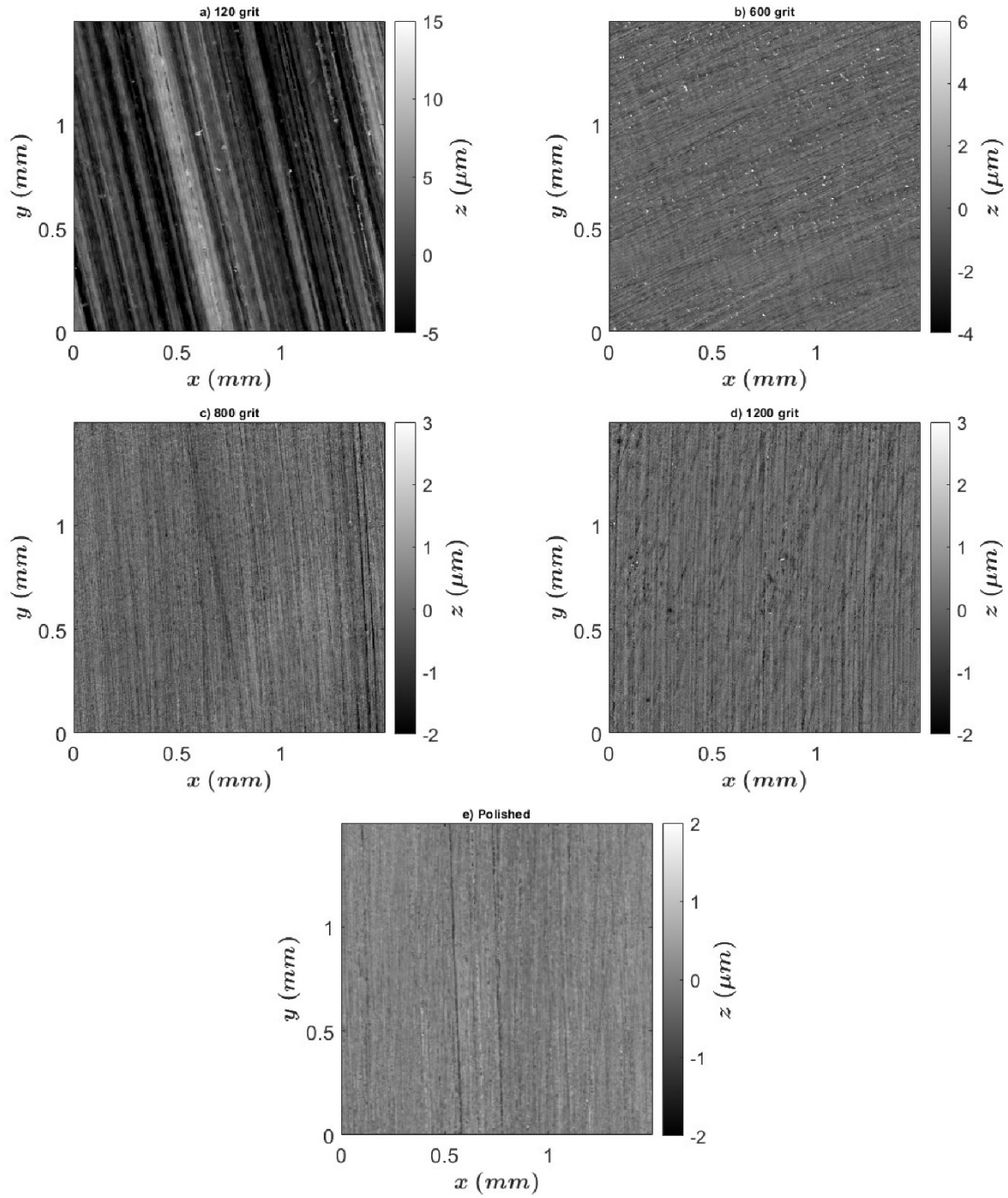


Figure 2-68 – Surface height maps for Nylon surfaces ground using SiC grinding pads of varying grit values.

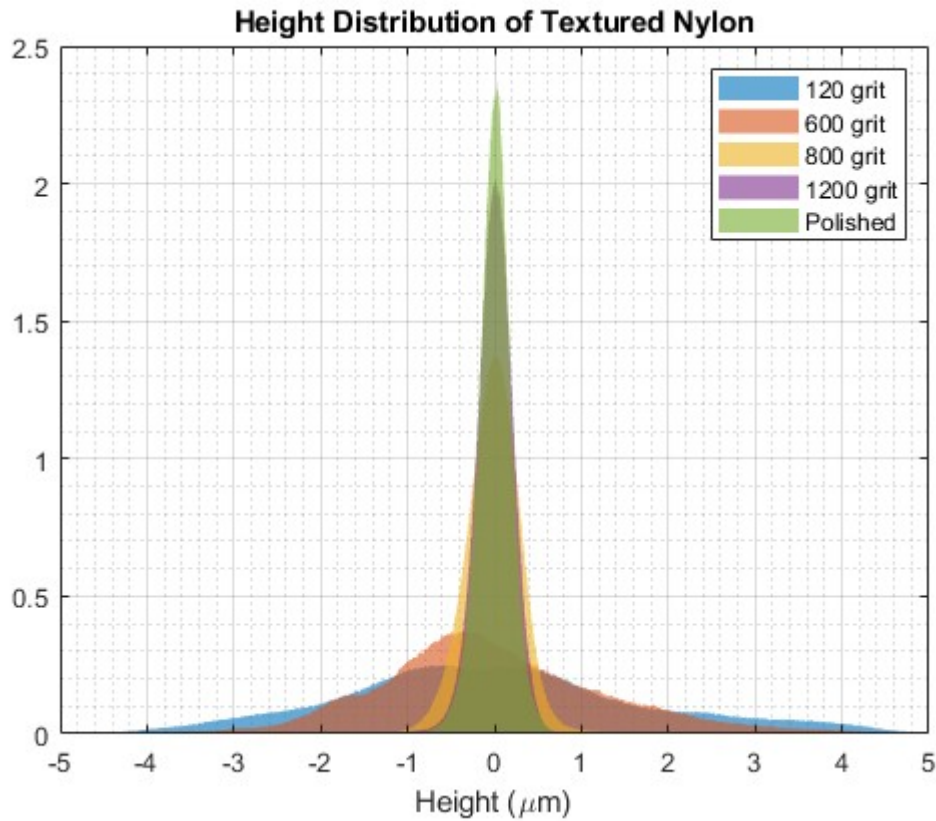


Figure 2-69 – Surface height histogram for Nylon surfaces ground using SiC grinding pads of varying grit values.

Upon inspection of the polished electrode topographies, the aluminium samples exhibited an almost doubled surface roughness (S_a) and rms slope ($S_{\Delta q}$) values in comparison to the copper samples. These differences in metal topography may constitute towards a smaller true contact area between the aluminium surfaces and an arbitrary counter-surface. This in turn may also explain the lower contact charge values across all counter-materials for the aluminium samples. The copper electrode surfaces also exhibit a positive skewness, implying that peaks and asperities are their most prominent features. These peaks and asperities may penetrate and deform the polymer counter-surface more easily due to higher localised contact pressures, resulting in a higher real area of contact. The aluminium surface scans also exhibit a high surface kurtosis, implying that the asperities on the copper surface are generally sharper than features on the aluminium surface. This high kurtosis value combined with a positive skewness would normally insinuate that the copper surface would have a smaller true contact area when pressed against a hypothetical counter-surface that is perfectly flat and infinitely hard (Sedlaček et al., 2012). However, the low moduli and viscoelastic nature of polymers instead implies that these sharp asperities would instead penetrate the polymer counter-surface and produce a larger contact area across the contact in general (Abdelbary, 2015).

Upon examination of the polymer surfaces, the grit value for the SiC grinding pads used in the grinding process correlates inversely with the centre-line roughness and negatively with the rms slope of the resulting Nylon surface topographies. The roughness parameters for each Nylon surface are displayed in Table 8.

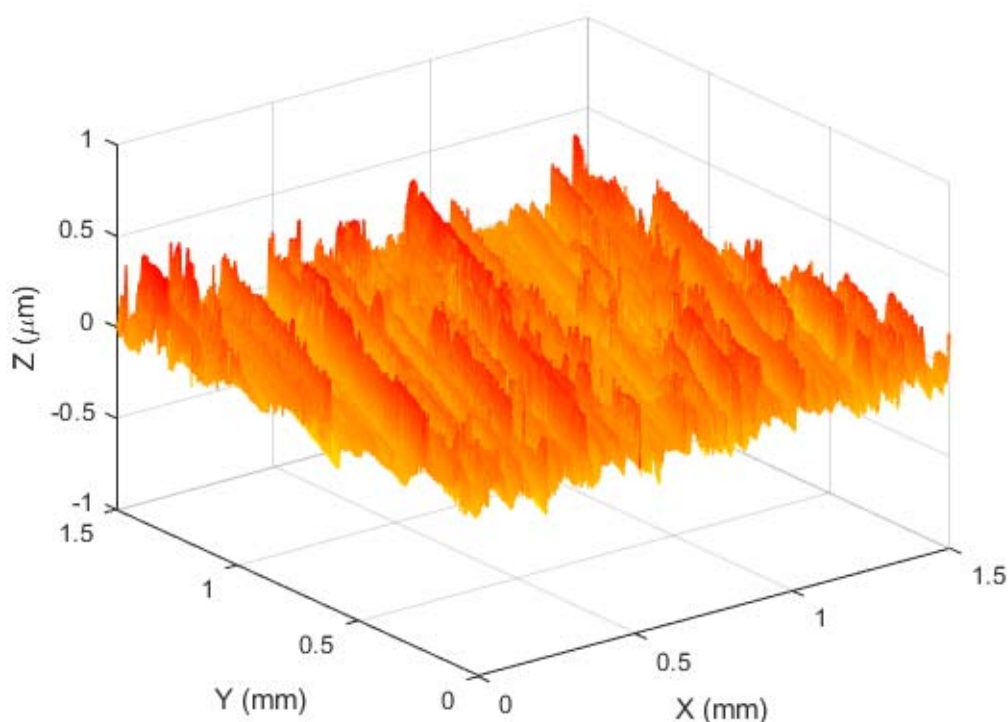


Figure 2-70 – Sample 1.5 mm x 1.5 mm surface topography of the Delrin surface after being subjected to a grinding process using 120 grit SiC pads.

Table 8 – Surface roughness parameters for insulating triboelectric layers using a Bruker NPFLEX white light interferometer.

Material	S_a (μm)	$S_{\Delta q}$	S_{sk}	S_{ku}
Nylon 120 grit	1.56	0.40	-0.08	3.89
Nylon 600 grit	0.61	0.23	0.82	15.90
Nylon 800 grit	0.41	0.22	-0.20	4.69
Nylon 1200 grit	0.24	0.11	2.95	131.31
Nylon Polished	0.13	5.6e^{-2}	-0.78	8.04

Upon comparing the charge accumulation data for the Nylon surfaces of differing roughness, a correlation between the 600, 800 and 1200 grit charge accumulation is difficult to discern. However the 120 grit surfaces were shown to consistently accumulate charge at a considerably lower rate than any other surface topography; to the point where they do not appear to reach a saturation charge density after two minutes of testing. The polished Nylon surfaces also accumulated charge consistently faster – and to a higher saturation density – than any surface that had only undergone a grinding process. These two cases are true not only for the pairing of Nylon and Aluminium, but for every pairing between the three polymers and two electrode materials.

An example comparison between tests using Nylon samples of varying roughness parameters is displayed in Figure 2-71. These data may imply that surfaces of lower surface roughness parameters – predominantly rms slope – inherently develop larger charge densities via triboelectrification. However, it may be more accurate to state that the case in fact applies to surfaces that topographically conform to a greater extent with their relative counter-surfaces, owing to the low roughnesses of the electrode surfaces. In turn this may confirm that the larger charge densities are in-fact a partial result of there being a greater real contact area within the F-TENG contact. The rms slope values for each surface were plotted against the charge densities they had accumulated over the initial 35 seconds of testing using the F-TENG apparatus. These data are displayed in Figure 2-72 and suggest that a linear relationship exists between these two variables; as opposed to the inverse square-root relationship theorised by Vasandani et al. (Vasandani et al., 2017). The values of the constants used for these linear fits are displayed in Table 9.

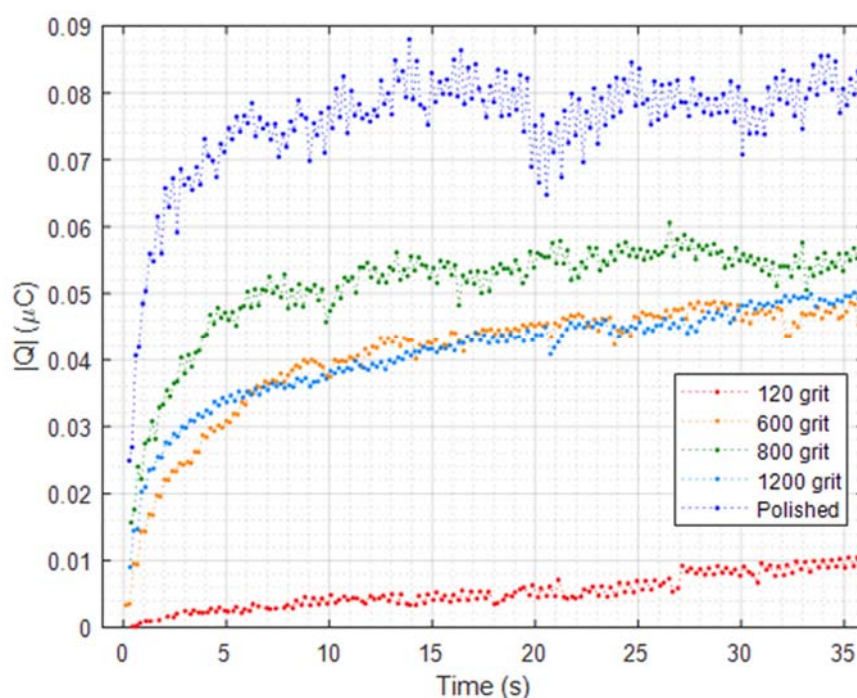


Figure 2-71 – Contact charge accumulation over time for Nylon on Aluminium F-TENG contacts using Nylon samples of differing surface roughness.

Table 9 – Linear fit constants used in Figure 2-72. for the linear equation $|Q| = m \cdot R_{\Delta q} + c$ with error margins included and R^2 values.

<i>Material Combination</i>	<i>m</i>	<i>c</i>	<i>R²</i>
Nylon - Aluminium	-0.21 (± 0.09)	0.096 (± 0.022)	0.97
Nylon - Copper	-0.20 (± 0.10)	0.111 (± 0.024)	0.98

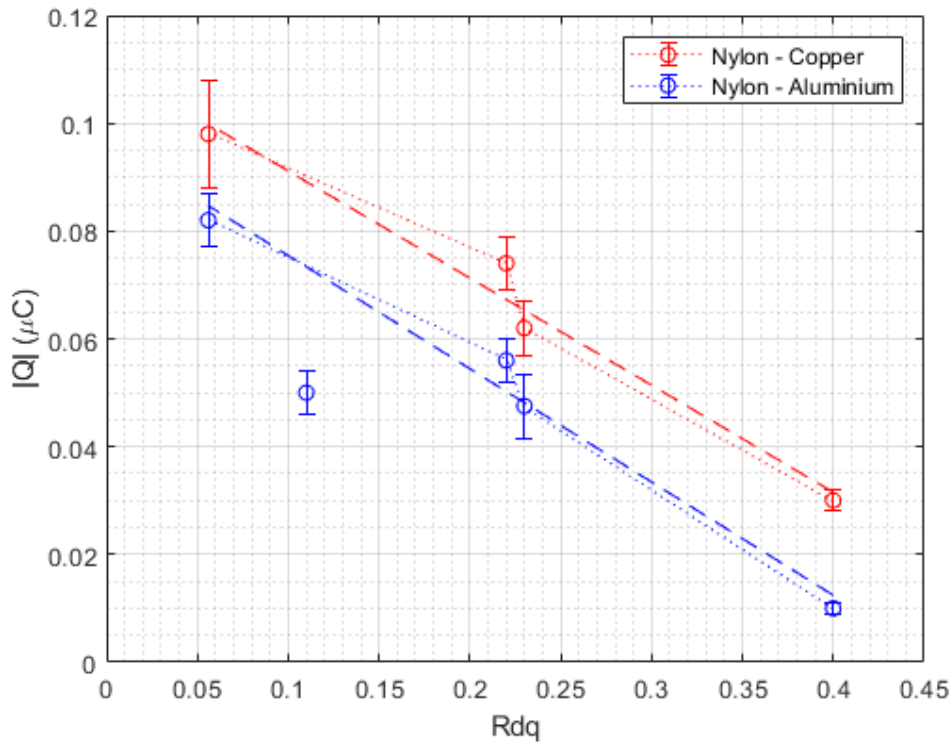


Figure 2-72 – Contact charge accumulated over 35 seconds (Q) plotted against polymer surface rms slope (R_{dq}) for Nylon on Aluminium (blue) and Copper (red) F-TENG tests. The data for each material combination are fitted to a linear expression with constants described in Table 9.

2.3 Conclusions

The feedback ammeter F-TENG apparatus has been proven to be a cost-effective method for analysing both the output current, and charging characteristics of macroscale sliding triboelectric applications, in addition to measuring the ohmic response of the F-TENG device under low external resistive loads. This methodology has provided results in agreement with existing research, whilst also describing the tribological viewpoint from which future triboelectric data can be interpreted.

The data collected using the F-TENG apparatus have shown that charge accumulation for a sliding triboelectric contact loosely resembles the exponential charging behaviour of a traditional capacitor, with the exception of additional complicating tribological factors. Both the saturation triboelectric charge density and charge accumulation rates are shown to be dependent on both the surface compositions and surface roughness parameters of the contacting materials. Teflon freestanding layers were shown to accumulate charge initially at a faster rate than ones composed of Delrin, up to a similar magnitude of saturation charge density; whereas Nylon layers accumulated charge at a similar initial rate but up to a higher charge density. These data also show that freestanding layers that were polished to low S_a and S_{dq} values produced a significantly higher charge density and at faster rates than those grinded to high S_a and S_{dq} values using low grit grinding pads.

The F-TENG methodology involved does not require the use of specialised contact materials or surface treatment in terms of TENG optimisation, beyond that of grinding and polishing and the cleaning of samples of surface contaminants through the use of heptane. In reinforcing the dependence of material chemical composition and surface roughness parameters on contact charging behaviour, these tests have served as a stepping stone towards fully understanding the complex role of tribology in triboelectric contacts and devices.

It is clear upon examining these data that longer duration tests are required in order to further study how electrostatic charge is generated and retained within material contacts, in addition to how long-term wear can affect these charging mechanisms. These results also provide little insight into the tribological aspects of these contacts. The utilisation of a tribometer can therefore significantly aid in revealing how contact charge accumulation can change with traction and contact force in sliding contacts. Ultimately, these tests have provided valuable insight into better developing an effective methodology for investigating the tribological aspects of triboelectric charging to a consistently reliable standard.

Chapter 3 – The UMT-TENG Apparatus: Tribological and Electronic Response

Using the data provided from the initial F-TENG study, a new methodology was constructed as to better understand the tribological factors that influence triboelectric charge transfer. Upon analysis of results from the F-TENG study, it becomes clear that a precise method for both controlling and measuring the physical movement of the contacting surfaces over significantly longer test durations is required in order to correlate tribological properties with triboelectric charging.

This chapter presents the configuration of the UMT-TENG apparatus. A universal mechanical tester that has been modified in order to measure electronic device outputs which are then correlated directly with tribological data in-situ. The capabilities of this apparatus are highlighted, alongside results of a series of tests conducted to determine the influence of certain tribological parameters on triboelectric charging within macroscale sliding contacts. The results in this chapter specifically describe in greater detail the influences of surface composition, surface texture, applied load, and material wear on the electronic response of a polymer on metal F-TENG contact.

3.1 Methodology

A Bruker Universal Mechanical Tester (UMT) TriboLab tribometer has been modified in order to accommodate and investigate various forms of TENG device. Electrically insulating plate-on-plate sample holders were additively manufactured for securing and electrically isolating metal electrodes and triboelectric layers within the UMT testing unit. These holders allow for the geometries of various TENG contacts devices to be replicated within the tribometer. The testing unit itself provides the controlled 3 dimensional actuation of both contacting surfaces, which allows for the replication of the varying forms of motion that occur within TENG devices. The positional encoding of these actuators, in addition to an LVDT sensor and a 2 dimensional load cell, allows for the precise measurement of sample position and contact forces within the TENG device. Two Keithley 6517B/E electrometers were also integrated into the data acquisition unit of the UMT for the purpose of providing high resolution high impedance electronic measurements in parallel with the UMT's existing measurement capabilities. A simplified schematic of the full UMT-TENG apparatus for laterally sliding TENG contacts is given in Figure 3-2a.

3.1.1 UMT-TENG Contact

The UMT TriboLab was chosen specifically for its modularity in terms of configuration. The UMT testing unit consists of two main sections; an upper sample suspension which hosts the load cell and is capable of being actuated linearly in the z and y directions, and a lower drive section, which can accommodate varying forms of motion, dependant on the drive unit being utilised. This particular iteration of UMT has three drive units available; two of which allow for the reciprocating actuation of samples within varying frequency ranges, whereas the third provides rotational motion. The high-speed reciprocating (REC) drive was specifically chosen as the drive unit for UMT-TENG testing as it allows for reciprocating frequencies between 0.1 and 10 Hz, at a stroke length of 27 mm, which is ideal for replicating the movements and

geometries of sliding TENG contacts. The REC drive is capable of higher reciprocating frequencies provided that the stroke length is reduced, but 10 Hz is the maximum reciprocating frequency used for this study. The specific device geometry being replicated for this study resembles that of the previous F-TENG configuration, being a laterally sliding freestanding triboelectric layer TENG device. This form of TENG contact comprises of an insulating upper sample being reciprocated across the surface of two conductive lower samples. This configuration of sliding-mode TENG is the easiest to accommodate within a reciprocating tribometer as it allows for the consistent measurement of friction under a constant applied load, throughout the full range of movement of the device. A side-on visual representation of an F-TENG contact is given in Figure 3-1. An insulating sample holder was additively manufactured in an acrylonitrile-butadiene-styrene copolymer (ABS) in order to secure the conductive elements of the F-TENG contact to the lower REC drive unit without any leakage of charge to the surrounding environment. An image of this arrangement is given in Figure 3-2c.

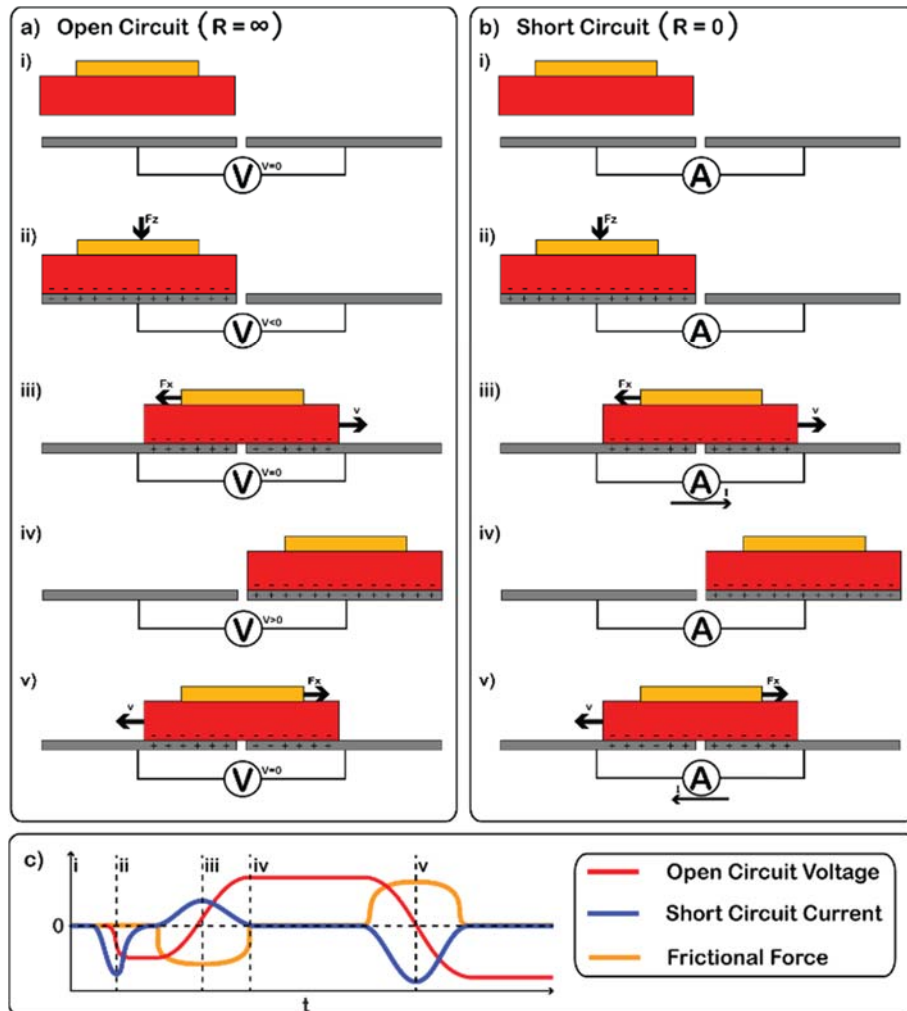


Figure 3-1 – Side-on diagram of a polymer-on-metal laterally-sliding freestanding-triboelectric-layer triboelectric nanogenerator (F-TENG) at subsequent stages of operation (i) before contact, (ii) first contact, (iii) mid-first-stroke, (iv) end-stroke, (v) and mid-stroke. The positions of trapped and mobile charges are given for open circuit (a) and short circuit (b) configuration, and the respective electronic outputs (c). Depicting the output voltage (red) and current (blue) for both (c). The red block represents an electronegative material, whereas the grey blocks denote an electropositive conductor, and the gold block denotes the UMT-TENG 2D load cell.

An additional sample holder, machined from stainless steel, was designed to attach to the UMT's upper sample suspension. This holder can accommodate insulated samples of varying sizes and geometries due to the adjustable nature of its clamping capability. An image of this arrangement is given in Figure 3-2b. 3D representations of the F-TENG contact within the UMT-TENG sample holders is given in Figure 3-2. For this particular study the influence of surface composition and contact topography on triboelectric charging is investigated within sliding contacts. Therefore the sliding polymer on metal F-TENG configuration used in the preliminary investigations remains the optimal choice of arrangement for this study.

A 0.5 mm thin Nylon film was also prepared via an extrusion process and implemented as an electrode coating for an additional series of tests. This layer was vertically clamped onto the electrodes and served as an intermediary triboelectric layer for the F-TENG device to create a polymer on polymer contact. The presence of this additional triboelectric layer changes the output of the TENG device to a small degree. The introduction of an insulating coating to these electrodes introduces a factor by which the measured current passing through the measurement circuit would be reduced with respect to the trapped charges on the freestanding surface. This is mainly due to the electric field being emitted by trapped charges within the contact needing to propagate through the insulating coating in order to influence mobile charges within the electrodes. Therefore, the electronic output of the device would also be dependent on the permittivity and thickness of this layer, in addition to the spatial charge density within the contact. This Nylon layer is specifically used in conjunction with a Teflon upper sample block due to the contrasting triboelectric properties of the two polymers. This material combination is theorised to substantially increase the triboelectric charge density within the F-TENG contact, therefore increasing the electronic output of the F-TENG device. As electrons become trapped on the Teflon surface, surface states are also vacated on the Nylon counter surface. These Nylon surface states are only negligibly repopulated when not in contact with the Teflon surface due to interactions with ambient air particles. Instead of directly measuring the presence of trapped charges on the upper Teflon surface, the electric field experienced by the mobile charges in each electrode is the sum of trapped charges on both the Teflon and Nylon surfaces. When the Teflon block is fully encompassing the projected surface of an electrode, the total field experienced by that electrode is roughly equal to zero, since the fields generated by trapped charges on both surfaces act to cancel each other out. As the Teflon block is moved away, the electrode experiences the electric field solely resulting from the trapped charges by the Nylon surface, thereby inducing the movement of mobile charges to cancel the presence of this field. The polarity of the open circuit voltage and short circuit traces should remain identical to that of the initial F-TENG device with a Teflon block directly contacting the electrode surface. The surface of this Nylon triboelectric layer did however exhibit an increased surface roughness relative to the metal electrodes, with topographical parameters given in Table 11 and height maps given in Figure 4-3. The secondary purpose that this interstitial Nylon layer serves is to mitigate the fluctuation in friction response as the polymer block slides over the edge of an electrode. Whilst great care has been taken to ensure that the two electrode surfaces are level with each other, there will always exist some sample deflection caused by the presence of the spacing.

The UMT-TENG apparatus is also capable of testing the operation other laterally sliding TENG configurations, such as attached-electrode and single-electrode devices. Contact-separation configuration TENG devices may also be investigated through the actuation of the upper sample along the z axis. The testing of the F-TENG configuration has however been prioritised for the aforementioned reasons of consistent friction measurement and increased output capability. Non-contact testing is also accommodated by this apparatus as a way of measuring the dissipation of electrostatic charge from insulating surfaces. This is accommodated by holding the charge-holding insulator surface a small distance away from the conductive electrodes as it is oscillated between them.

3.1.2 Tribological Measurements

The REC drive was used to move the lower conductive samples relative to the upper insulating sample and is shown in Figure 3-2c. The mechanism controlling this motion is a form of reverse-piston, where the rotational motion of the UMT motor is translated to a reciprocating motion via an adjustable piston rod. This gives the relative movement of the samples a sinusoidal velocity profile, where the largest velocities are observed in the middle of the stroke. A linear variable differential transformer (LVDT) sensor is used in conjunction with the REC drive in order to accurately measure the relative position of the samples over time ($x(t)$). The LVDT sensor was calibrated to give $x = 0$ at the centre-stroke, where the upper sample is equally in contact with both lower electrodes. The position resolution of the LVDT sensor is $1\text{ }\mu\text{m}$.

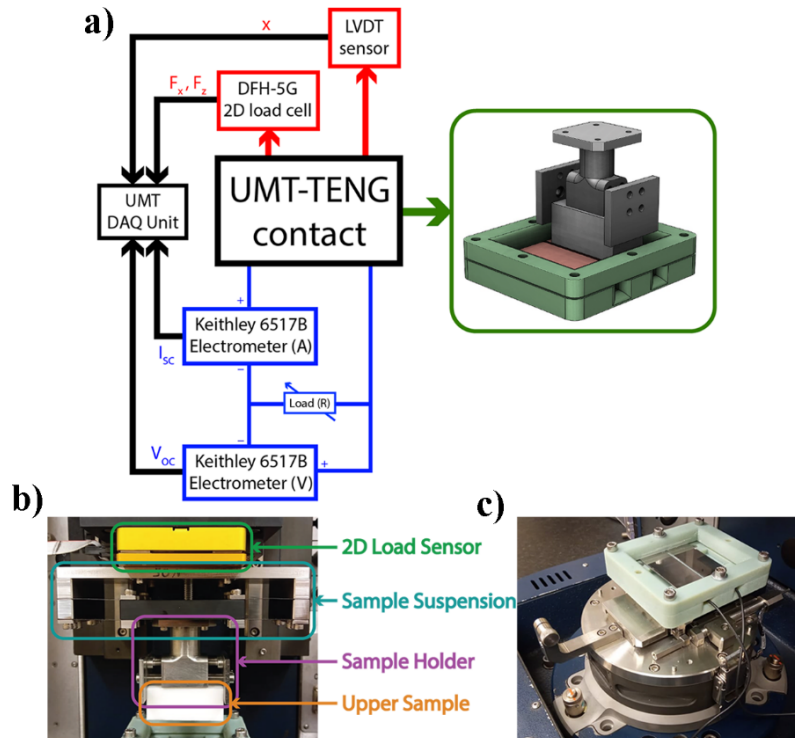


Figure 3-2 – (a) Schematic representation of the full UMT-TENG testing apparatus (left) accompanied by a 3D model of the assembled UMT-TENG contact itself (right). Elements highlighted in blue represent elements that constitute the electronic measurement circuit, whereas elements highlighted in red contribute to tribological measurements. (b) Photograph of the UMT-TENG upper sample holder assembly. (c) Image of the UMT's reciprocating drive module with the UMT-TENG lower sample holder attached.

A vertical force (F_z) is applied to the UMT-TENG contact by lowering the upper sample with a screw-driven linear actuator. The position resolution of this actuator is also 1 μm , with a minimum speed of 1 μms^{-1} , which allows for a precise control over the vertically applied load. A suspension system is also affixed between the upper sample and sensor in order to mitigate any acoustic vibrations and protect the load cell from potential damage. As the upper and lower samples are moved relative to each other by the REC drive whilst a vertical force is applied with the upper sample actuator, frictional resistance within the TENG contact works to impede this movement. The friction coefficient for such a mechanical contact (μ) is estimated as the force imparted by friction (F_x) divided by F_z .

$$\mu = \frac{F_x}{F_z} \quad (3-1)$$

A two-dimensional force sensor, connected to the upper sample suspension, is used to measure both F_z and F_x during testing. The resolution of this load cell is 2.5 mN, with an operating range of 0.5 to 50 N in both z and x directions, which accommodates most realistic TENG device applications. An alternative load cell is however available, with an operating range of 5 to 500 N and a lower resolution of 25 mN. Both the vertical and lateral forces are measured in-situ throughout each test using the UMT's data acquisition unit. The vertical force is also monitored throughout the test through a feedback loop in order to maintain a constant applied load throughout each test. This feature is exceptionally useful for mitigating the influence of geometric misalignments of the contact, where otherwise the contact force would differ across the length of the stroke. This is also helpful for maintaining a constant applied load in the presence of material removal and wear within the contact.

These load cells and positional sensors allow for the correlation of tribological data with the electrical output of the F-TENG device. This combination of mechanical and electronic outputs allows for the plotting of friction, output current, and output voltage over both time and relative sample position during tests. Being able to plot the electrical output of a TENG device over relative sample position allows for the influence of system geometry to be investigated in greater detail. This in-turn will provide experimental validation for existing models that describe the operation of TENG devices. The measurement of both friction coefficient and triboelectric charge across the duration of an extended tribological test may also provide insight into how both values evolve in relation to one another, in addition to whether one influences the other in any way.

3.1.3 Electronic Measurements

The finalised measurement circuit for the UMT-TENG apparatus consists of a Keithley 6517B/E electrometer connected in series with the F-TENG electrodes and a switchable resistor array, identical to the one previously mentioned as within the feedback ammeter device. A second Keithley electrometer is placed in parallel with this resistor array as a way to measure the voltage across it, with the first electrometer being used to directly measure the output current between the array and a single electrode. This arrangement is similar to the measurement configuration previously described in Figure 2-40, with the substitution of the feedback ammeter and myDAQ input channel both with these high resolution electrometers.

In principle it is impossible to measure both short-circuit and open-circuit properties simultaneously. The former requires the measurement circuit to have effectively zero load resistance whereas the latter requires an infinitely high load resistance. One solution to this problem is to measure the two characteristics independently during separate identical tests. This however would require twice as many tests to be conducted, with measurements relying heavily on the exact repeatability of said tests.

One advantage of using an F-TENG configuration is that both electrodes can be treated as single electrode TENGs for the purposes of measuring open-circuit and short-circuit properties for similar devices within a single test. The issue that arises with this form of measurement is that any inhomogeneity in σ_T along the x axis will cause a deviation in the electric potential experienced by each electrode along the stroke. This may cause a difference in recorded output between the two single electrodes. The effect of this can be measured simply by connecting one electrometer to each electrode via identical connectors, with the other side of the electrometers' differential inputs connected to electrical ground. This method also mitigates the movement of charges to ground during open circuit measurements, and is recommended as the best methodology for accurately measuring open circuit voltage (Zhang et al., 2020; W. Zhang et al., 2021).

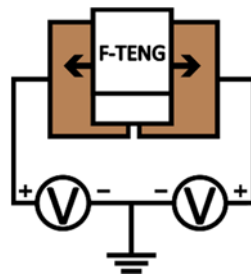


Figure 3-3 – Open circuit measurement configuration for a sliding freestanding triboelectric layer TENG device.

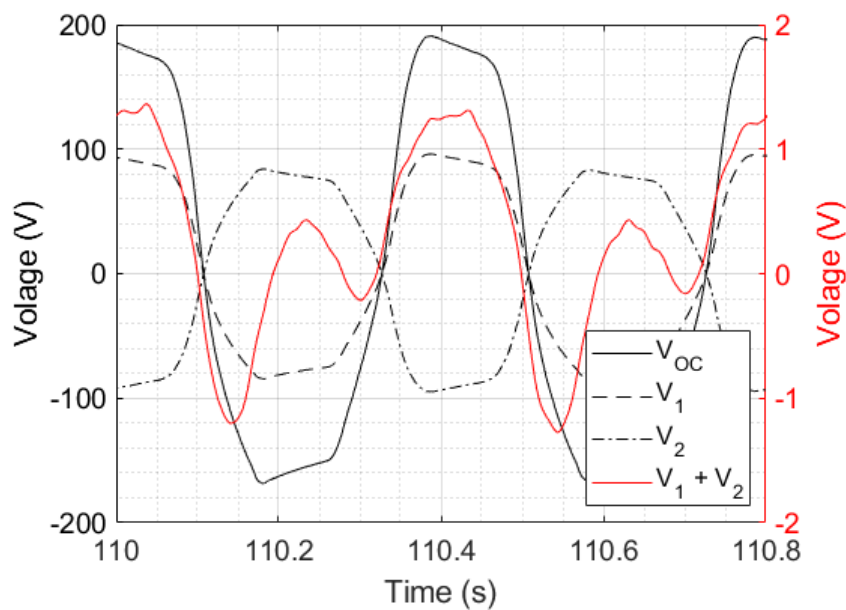


Figure 3-4 – Open circuit voltage trace of a Teflon on Nylon F-TENG contact as recorded by both electrometers in the configuration outlined in Figure 3-3, with V_{oc} being calculated as the subtraction of V_2 from V_1 .

Another solution is to measure the voltage across and current passing through a measurement circuit of a known finite resistance. This may not be a measurement of short-circuit and open-circuit characteristics but it provides a practical method for measuring the output power of the TENG device. The resistance value for this circuit can be changed in order to examine how the power output for the TENG varies with external load resistance (Niu, 2015).

The final configuration of the measurement circuit is as described in Figure 3-5. This configuration allows for the measurement and recording of both the output current and voltage of the TENG device with regards to a specific load resistance; which can subsequently be changed in order to optimize the output power. The resistor array is described as a variable resistor in this schematic since it serves a similar purpose over a wider range of resistances. The resistor array also has a bypass switch, which converts the measurement circuit to short circuit configuration. The two resistors used in addition to the bypass for testing at finite resistances were the 10 M Ω and 1 G Ω resistors. Elements of the electronic measurement system were connected via shielded copper wiring as a way of mitigating the influence of external electrical fields. This wiring was connected via conductive aluminium tape to the geometric centre of the rear face of each electrode to ensure a stable connection without the need for permanent mechanical attachment. A visual representation of the case for measurement of both friction (μ), open circuit voltage (V_{oc}) and short circuit current (I_{sc}) over time and relative sample position (x) is given in Figure 3-1.

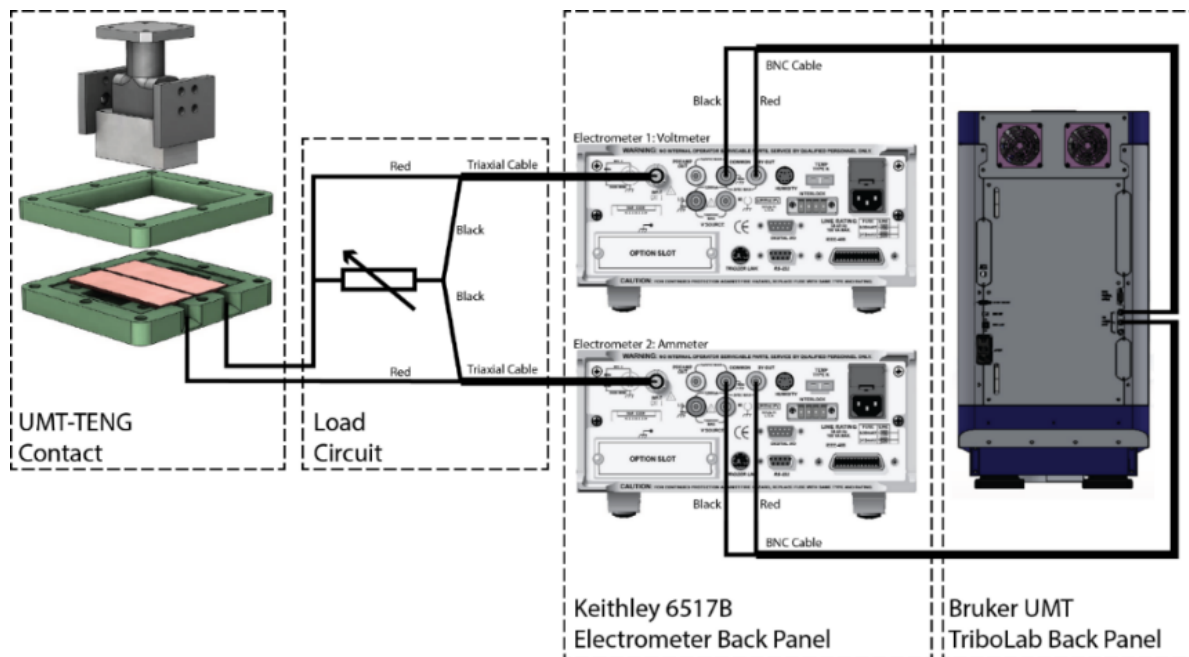


Figure 3-5 – Wiring schematic of the UMT-TENG apparatus set-up. Indicating the exact connections used to integrate the Keithley 6517B electrometers with the data acquisition unit of the UMT. Please note that the BNC ports on the back panel of the UMT have been internally connected to pins 15 and 16 of junction 15 on the UMT data acquisition unit.

3.1.4 Data Processing

Data from the 2D load cell, LVDT positional sensor, and both electrometers are collected and recorded by the UMT's in-built data acquisition unit; which is capable of sampling data from the five channels (x, F_x, F_z, I , and V) simultaneously up to a rate of 8 kHz. The resulting data are flagged for anomalies and cleaned, using a virtual notch filter at 50 Hz and 100 Hz in order to mitigate any external electrical interference. An additional band stop filter was implemented, centred on 70 Hz and with a bandwidth of 5 Hz, in order to mitigate the presence of acoustic vibrations that are caused by the stick-slip nature of the contact.

A modified iteration of the previously used MATLAB program is also implemented for the calculation of triboelectric charge, in addition to estimating the energy dissipated via friction using a similar integration method, for each forward and reverse stroke. Whilst the electrometers are both capable of directly measuring the induced flow of charge passing through them, measuring the induced conduction current over time across the resistor array still allows for this charge value to be calculated via integration over time. A similar integration method to the one used for the calculation of triboelectric charge can be used to estimate the energy dissipated via friction for each forward and reverse stroke of the relative sample movement. This is a common procedure for tribological testing, and be used as an indicator for the presence of frictional heating (Dini and Hills, 2009). The work imparted by a moving object to overcome friction (E_μ) is treated as the integral of the resistive frictional force (F_x) over the total distance travelled (x). Because of this relation it is possible to define the total energy dissipated via friction across this movement.

$$E_{\mu_n} = \int_{x_n}^{x_{n+1}} F_x(x) dx \quad (3-2)$$

A time-averaged value for friction coefficient is also calculated for each forward and reverse stroke to give a clearer view of how it evolves over the duration of contact testing. The integrated nature of this value also corrects for any systematic asymmetries or fluctuations across the length of the stroke. This value is calculated using only friction data collected from the middle 20% of the stroke, as to ensure that a full sliding contact is being exhibited with no stick-slip motion causing an increase in friction response.

$$\mu_n = \frac{\int_{t_n}^{t_{n+1}} F_x(t) dt}{\int_{t_n}^{t_{n+1}} F_z(t) dt} \quad (3-3)$$

3.1.5 Sample Preparation

This particular configuration of F-TENG contact requires one upper insulating sample and two lower conductive samples for each test as previously explained. To maximise the efficiency of the device whilst retaining a simple device construction, the lateral length of the upper and lower samples should be equal to the longest possible stroke length of the REC drive, minus the lateral spacing between the lower samples. This is in order to maximise the projected contact area between the upper and respective lower sample at either end of the reciprocating stroke. The stroke length of the UMT reciprocating drive is set at its maximum of 27 mm for the purpose of UMT-TENG testing, and the lateral spacing is kept at 2 mm

to maximise the apparent area of contact within the apparatus, as well as the portion of electronic output dependant on device geometry.

The widths of the upper and lower samples in the y direction (orthogonal to the stroke direction and parallel to the plane of contact) are 50 mm and 70 mm respectively. The higher width of the lower samples is purely to accommodate them within the clamping mechanism of the lower sample holder as with the F-TENG apparatus. The lower conductive samples were identical to the ones used for the F-TENG apparatus with the exception of being 23 mm wide in the x direction as opposed to 50 mm, due to the limited stroke length of the REC drive. The thickness of the upper samples in the z direction is set at 25 mm for ease of construction and ease of accommodation within the upper sample holder. The upper polymer blocks were therefore 25 x 25 x 50 mm in dimension.

All three polymers were used in conjunction with the UMT-TENG apparatus. The polymer samples were given differing surface texture parameters to investigate the influence of both material composition and surface texture on triboelectric charge transfer within a more controlled environment. Only the ground 120 grit and polished samples were used in these tests as either extremes in terms of topography. Aluminium and stainless steel were chosen as electrode materials for this study due to their differences in mechanical moduli, despite exhibiting similar work functions and both materials developing surface oxide layers when exposed to air. These metals were once again polished to a mirror like finish in order to minimise the effects of their topographies on contact geometry and real contact area.

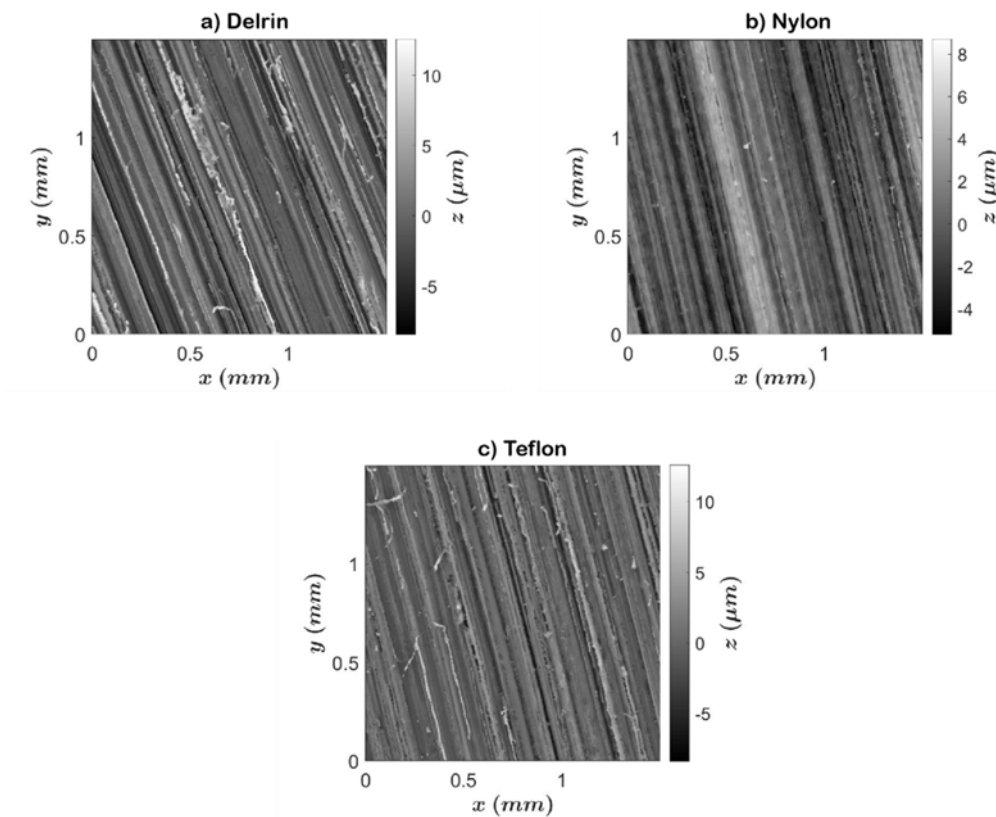


Figure 3-6 - Surface height maps for Polymer surfaces ground using 120 grit SiC grinding pads.

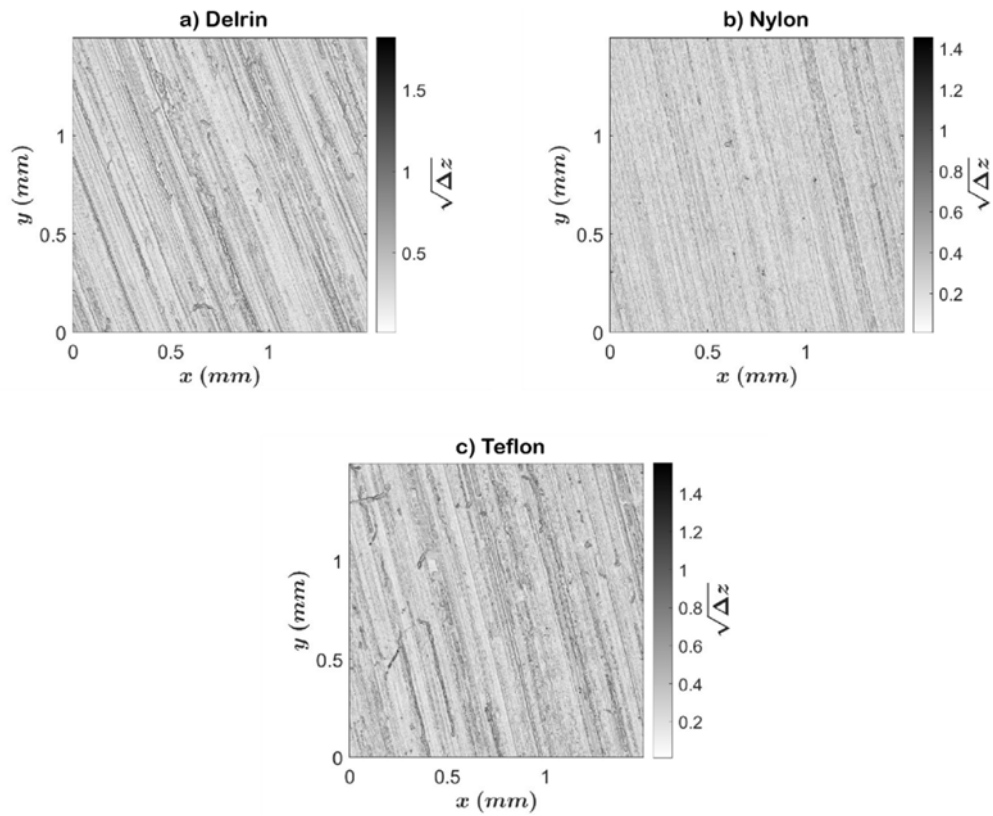


Figure 3-7 – Surface gradient maps for Polymer surfaces ground using 120 grit SiC grinding pads.

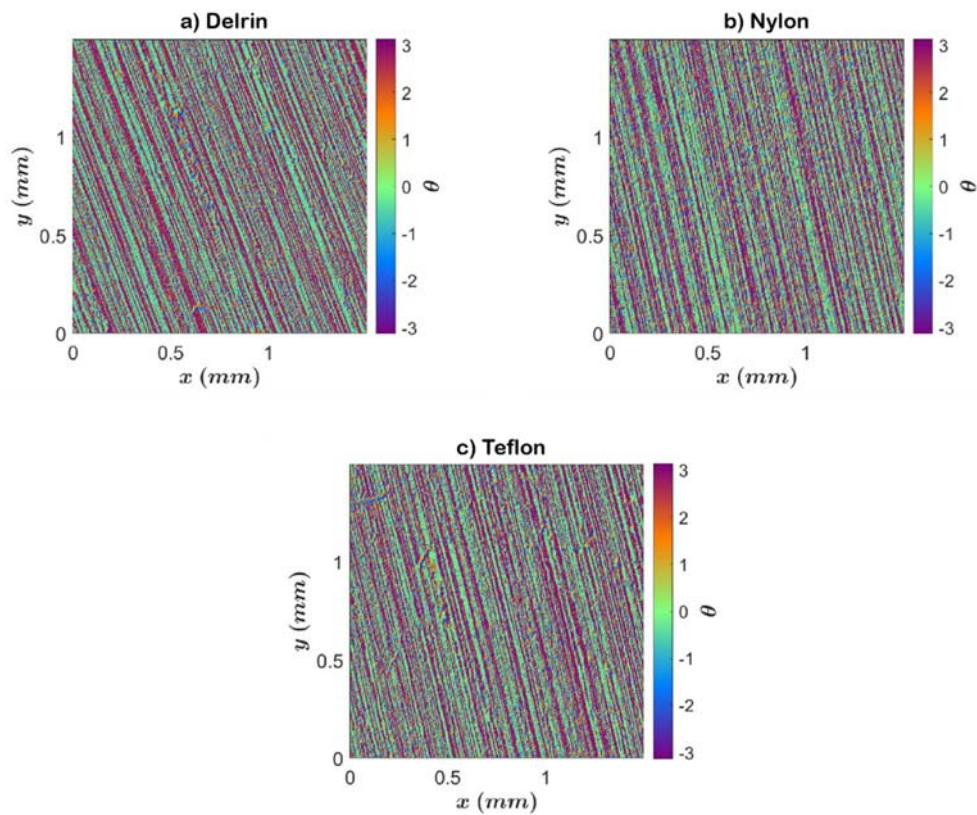


Figure 3-8 – Surface gradient direction maps for Polymer surfaces ground using 120 grit SiC grinding pads.

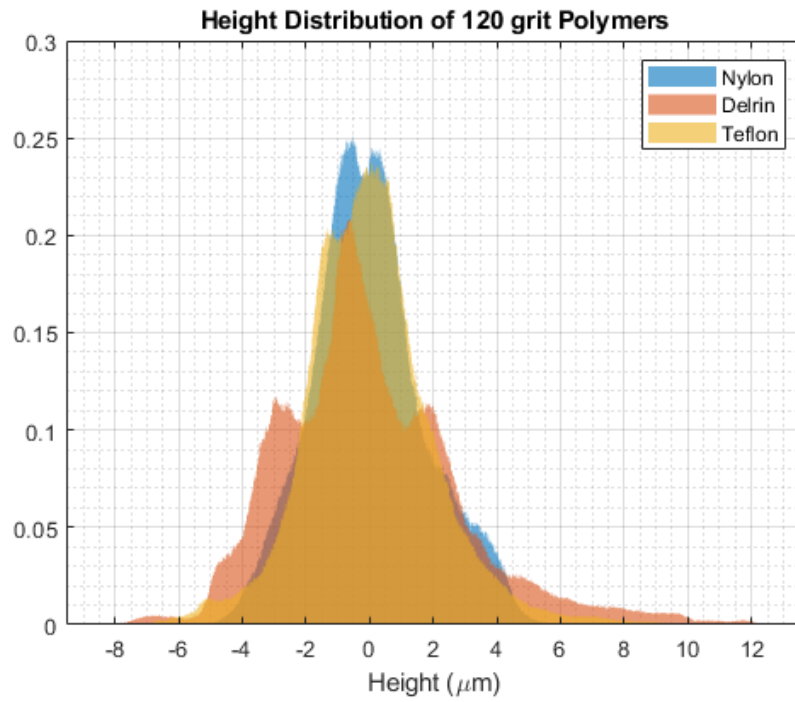


Figure 3-9 – Surface height histogram for Polymer surfaces ground using 120 grit SiC grinding pads.

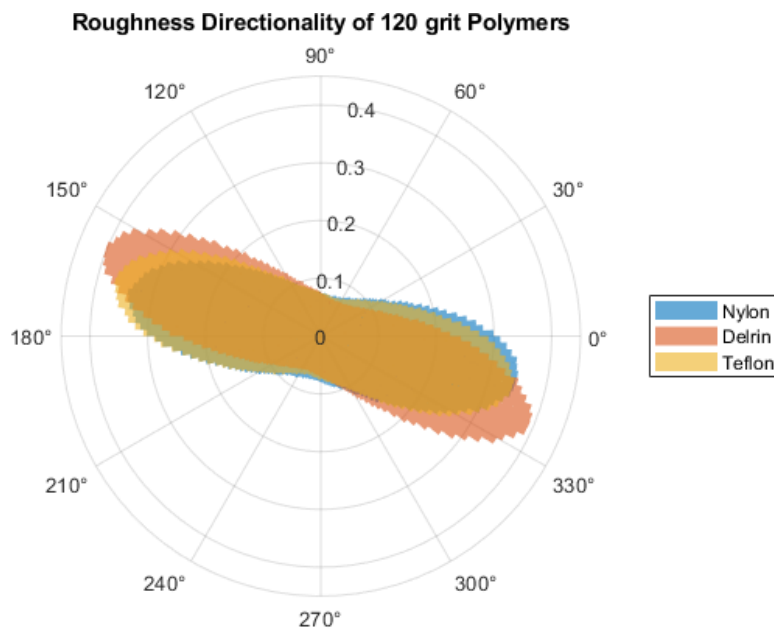


Figure 3-10 – Surface gradient direction polar histogram for the polished polymer surfaces.

3.1.6 Testing Procedure

A series of reciprocating tests using the UMT-TENG apparatus were conducted in order to investigate the influence of sliding friction and material wear on triboelectric charging for triboelectric contacts of differing compositions and topographies. The testing procedure was designed to replicate the operation of an F-TENG contact, consisting of differing material combinations and under varying tribological parameters.

The procedure itself consisted of bringing the upper sample into contact with one lower sample at the beginning of its stroke until the desired contact force is reached. This amount of stationary contact time is kept at a constant 1 minute for all tests as a way of systematically mitigating the influence of any initial stationary contact electrification when comparing test data. The two lower samples are then reciprocated back and forth at the desired frequency for 10 minutes, bringing each one into and out of contact with the upper sample surface in an oscillating fashion. The contact force is kept at a constant throughout this stage of testing via the force tracking and feedback loop feature of the UMT. Testing was conducted under applied loads of both 5 N and 10 N as a way for investigating the influence of contact force on triboelectric charge transfer. The reciprocating stroke length was set to its maximum of 27 mm and a reciprocating frequency of 2.5 Hz was used for tribological testing.

An additional series of tests were conducted at reciprocating frequencies of 1 Hz and 10 Hz in order to more accurately illustrate into how friction response and electronic output changed across the length of the stroke and under different resistive loads. These reciprocating frequencies correlate to maximum velocities of 0.17 and 0.42 ms⁻¹ respectively under a sinusoidal velocity profile. The 0.5 mm Nylon triboelectric layer was also implemented for this series of tests, both to optimise device output and provide a smooth friction response.

3.2 Results and Discussion

3.2.1 Friction measurements

Under correct interpretation, the UMT-TENG friction output can be used to identify the physical and mechanical processes that occur within the material interface. In conjunction with the electrical output, these data can also be used to detect the presence of transfer films, third-body particles, and wear debris. The generalised form of friction response from the UMT-TENG contact remains identical between all material pairings and tribological parameters.

As is to be expected from reciprocating tribological tests the friction trace for the UMT-TENG contact approximates that of a square wave over time. The frequency of this wave matches that of the relative reciprocating motion of the upper and lower samples and is also in phase with the relative velocity of the upper and lower samples, as to be expected from a typical reciprocating tribometer output. A 3D depiction of the cleaned data is presented in Figure 3-11a, while Figure 3-11b shows the cleaned and raw data against sample position over a single half-oscillation at 1 Hz.

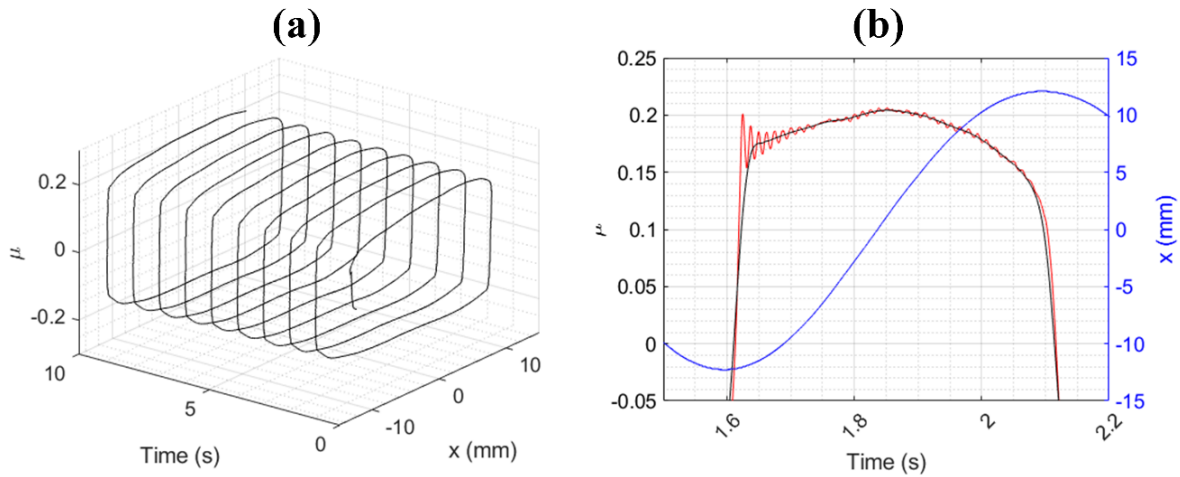


Figure 3-11 – (a) Cleaned friction coefficient against relative sample position and time for a polished Teflon on Nylon film F-TENG contact. (b) Cleaned (black) and raw (red) friction coefficient (μ) against relative sample position (blue) over time for the same contact. Samples were reciprocated at 1 Hz under an applied load of 40 N with a stroke length of 27 mm and a 2 mm lateral spacing of the lower samples. The apparent area of the contact is 23 mm by 50 mm.

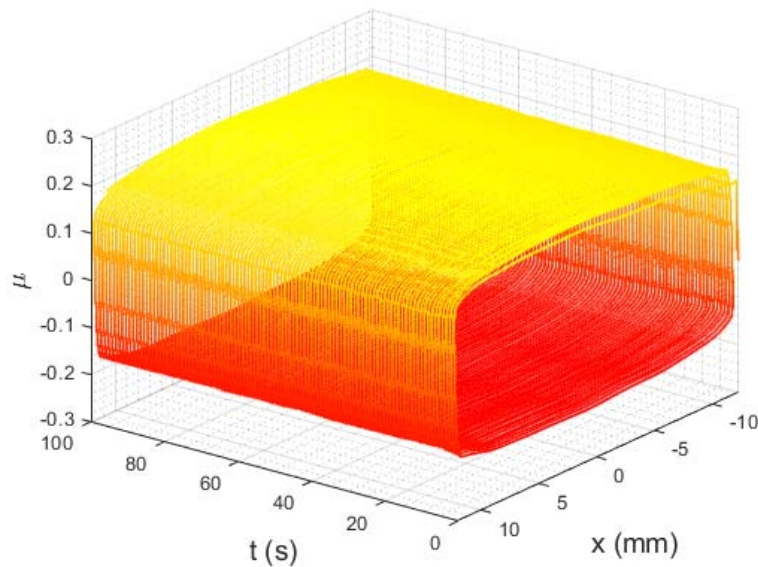


Figure 3-12 - Cleaned friction coefficient against relative sample position and time for a polished Teflon on nylon film F-TENG contact.

Due to the high apparent surface area plate-on-plate nature of the UMT-TENG contact, artefacts of a high stick-slip friction regime are seen at the beginning of each stroke and reverse stroke. These artefacts take the form of high frequency oscillations in F_x and F_z , as shown in Figure 3-11b, which are caused by acoustic vibrations occurring within the contact. These vibrations are caused by a difference between the static and dynamic friction coefficients for the contact, causing the surfaces to intermittently 'stick' to and 'slip' across each other (Viswanathan and Sundaram, 2017). This difference is known to be exhibited for almost all material pairings and manifests itself as an energy barrier, which must first be overcome if relative motion is to be initiated. Because of this energy barrier, the static friction coefficient for any contact is normally higher than the dynamic friction coefficient for the same contact.

The previously described time-averaged friction coefficient is shown to evolve over the duration of every test, indicating that tribological mechanisms cause the conditions within the contact to change dynamically over time. The presence of different mechanisms are dependent on the mechanical properties of both materials, as well as the tribological parameters that describe the form of contact. Comparisons of example friction responses from the UMT-TENG apparatus are given in Figure 3-13.

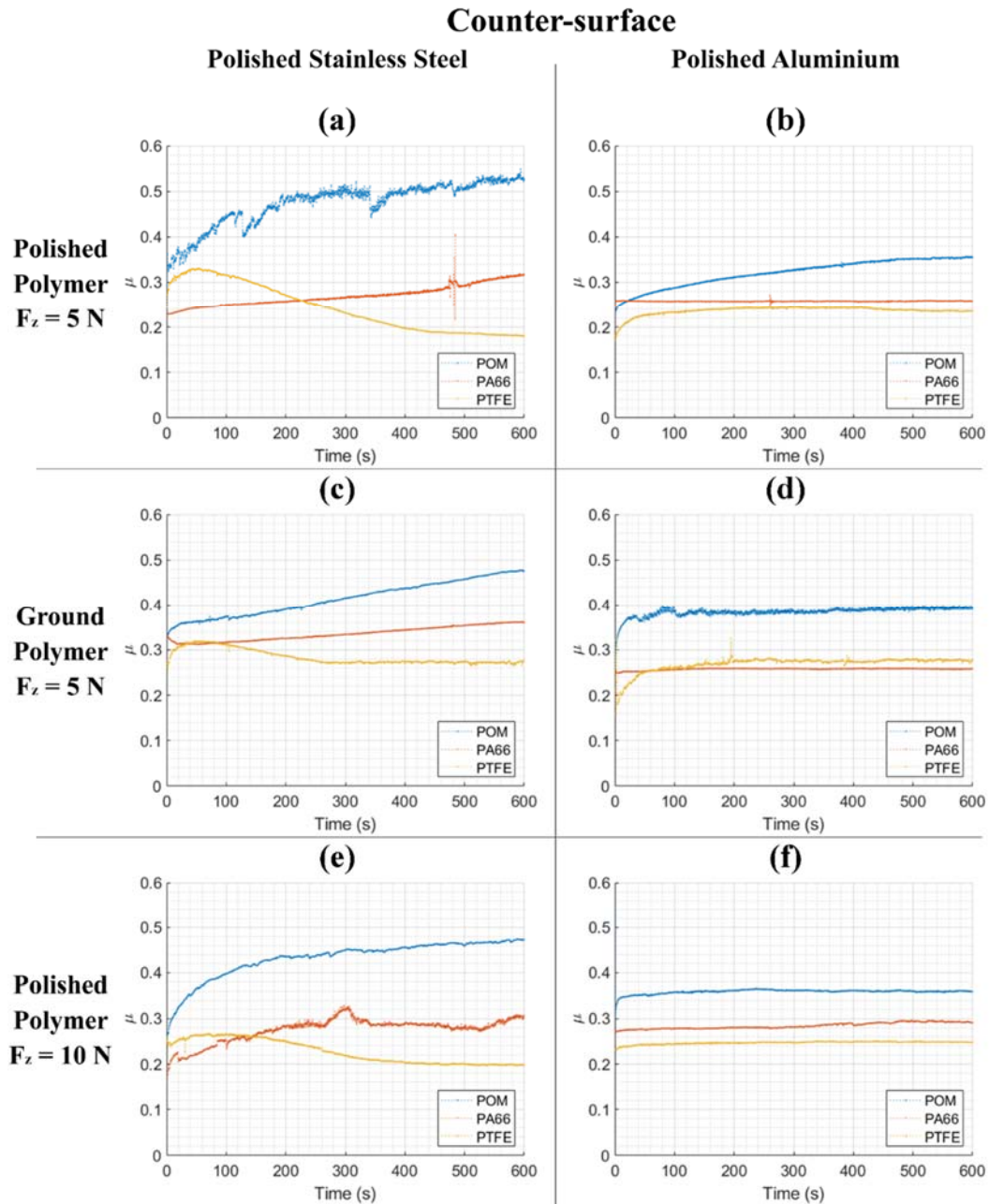


Figure 3-13 – Friction coefficient over time for (a) polished polymers on polished stainless steel F-TENG contacts under an applied load of 5 N, (b) polished polymers on polished aluminium F-TENG contacts under an applied load of 5 N, (c) ground polymers on polished stainless steel F-TENG contacts under an applied load of 5 N, (d) ground polymers on polished aluminium F-TENG contacts under an applied load of 5 N, (e) polished polymers on polished stainless steel F-TENG contacts under an applied load of 10 N, (f) polished polymers on polished aluminium F-TENG contacts under an applied load of 10 N. Samples were reciprocated at 2.5 Hz with a stroke length of 27 mm and a 2 mm lateral spacing of the lower samples. The apparent area of the contact is 23 mm by 50 mm when the upper sample fully encompasses a lower sample.

3.2.1.a Influence of Polymer Composition

Upon comparing the friction response of the three differing polymers, it becomes clear that they each exhibit unique tribological characteristics. The Delrin samples consistently exhibited the highest friction coefficient throughout testing against both stainless steel and aluminium counter-surfaces. The friction response from the Delrin samples show an initial high rise in friction coefficient, which gradually lessens in gradient over time. The Delrin samples exhibited their lowest end-of-test friction coefficient of 0.36 when polished and tested against an aluminium counter-surface. The Nylon samples exhibit the lowest friction coefficient for approximately the first minute of testing against stainless steel counter-surfaces. This friction response then gradually rises over the duration of each test up to a value between the friction coefficients of Delrin and Teflon. The Delrin samples exhibited their lowest end-of-test friction coefficient of 0.26 when tested against an aluminium counter-surface under an applied load of 5 N. The Teflon samples also exhibit this initial rise in friction coefficient. This response generally peaks between the first 50 to 100 s of testing against stainless-steel counter surfaces but then gradually lowers over time and levels out to a value more consistent with existing friction data for Teflon contacts (Biswas and Vijayan, 1992). This lowering of friction coefficient over time may be attributed to the development of a low-friction PTFE transfer film on the counter-surface. The Teflon samples achieved the lowest friction coefficient of all three polymers for the majority of testing conditions by the end of each test. The lowest friction coefficient of 0.18 was achieved by the polished Teflon samples against stainless steel counter-surfaces under an applied load of 10 N.

3.2.1.b Influence of Electrode Composition

The mechanical properties of the counter-surface are shown to have a strong influence on friction response. Figure 3-13a, 6c, and 6e show the response of polymer samples tested against the stainless steel counter-surfaces, whereas Figure 3-13b, 6d, and 6f show the response of samples tested against the aluminium counter-surfaces. Testing against the softer aluminium counter-surface yielded lower friction coefficients for Delrin and Nylon samples. The Teflon samples exhibited higher friction coefficients overall against aluminium. They also lacked the initial rise and fall in friction coefficient that is evident during the initial stages of tests against stainless steel. Both these trends in friction coefficient may be attributed to the relative softness of the aluminium surface in comparison to the stainless steel. The aluminium surface is more able to deform in response to applied pressure and therefore would be less abrasive on the polymer surfaces. This would ultimately lead to a lower friction coefficient for Delrin and Nylon, but would slow down the process of PTFE transfer film formation since less material would be removed from the Teflon surface.

3.2.1.c Influence of Surface Roughness

Upon comparing the response of differing roughness parameters for otherwise identical polymers, it becomes clear that the roughness of the polymer samples also influences the friction response and how it evolves over time. Figure 3-13a and b show the response of polished polymer samples under an applied load of 5N, whereas Figure 3-13c and d show the response of samples that had been ground using 120

grit SiC pads prior to testing. For Delrin, the polished samples exhibited a higher friction coefficient up to a value of 0.52 after 10 minutes of testing, whereas the friction coefficient for the ground samples after 10 minutes of testing was 0.47. This may be attributed to an increased adhesion between the two more conformal surfaces. The polished Nylon samples generally exhibited a lower friction coefficient than the ground ones across testing. The ground, Nylon surfaces also exhibit an initial drop in friction coefficient prior to this steady rise. This initial high friction coefficient and subsequent drop is an indicator of abrasive wear, as it truncates the surface profile of the Nylon samples to one which conforms better to the harder metal counter-surface. Both the polished and ground Teflon topographies peaked at approximately the same time and friction coefficient. However, the polished Teflon samples gave substantially lower and more stable friction responses after this point, giving steady state μ values of ~ 0.18 as opposed to ~ 0.27 for the ground samples.

3.2.1.d Influence of Applied Load

Friction coefficients remained similar for most material pairings under higher applied loads. Figure 3-13a and Figure 3-13b, show the response of polished polymer samples tested under an applied load of 5 N, whereas Figure 3-13e and Figure 3-13f show the response of identical samples tested under an applied load of 10 N. The friction coefficients for the Delrin contacts reach similar values, but reach those values at a faster rate, which is best shown against the aluminium counter-surfaces. The Nylon samples exhibited higher and less stable friction responses under the higher applied load, with these instabilities in friction response indicating the removal of material from the contact. The Teflon samples reached a similar friction coefficient under higher loads. Similarly to the Delrin samples, the Teflon samples reached these values at a faster rate. In addition the characteristic initial rise and fall in friction coefficient is lessened in magnitude when tested under higher loads against the stainless steel counter-surface. It is important to note that even an accurate measure of contact force still cannot provide an insight into the distribution of contact pressures within the plate-on-plate F-TENG contact, because an accurate model of how the topographies and mechanical properties of the involved materials interact in sliding motion remains to be developed.

3.2.1.e Wear Analysis

An important factor to consider with regards to the application and use of polymers within a tribological contact is that polymers often exhibit low mechanical moduli (Crawford and Martin, 2020). This in turn may lead to significant material wear within polymer contacts, most notably against harder counter-surfaces (Briscoe and Sinha, 2002). The unfortunate phenomenon that accompanies higher applied loads in dry friction is an increase in these material wear rates (Dangnan et al., 2020). The polymer samples used in testing were analysed using a Bruker NPFLEX white-light interferometer to accurately measure their roughness parameters before and after tribological testing. These parameters were measured from 3D surface topography maps taken across 3 separate $500\text{ }\mu\text{m}$ by $500\text{ }\mu\text{m}$ sample areas per sample surface and are displayed in Table 10. Evidence of material removal is evident on all post-tested polymer surfaces through distinct changes in their topographies. Evidence of abrasive wear along the axis of reciprocation is seen on the polished polymer samples, leading to a significant increase in their

mean arithmetic roughness's (S_a). An example of these changes in topography is given in Fig. 7a and Fig. 7b. The ground samples exhibit lower rms slope ($S_{\Delta q}$) values after tribological testing, despite similar R_a values, which imply a profile truncation caused by the removal of asperities. Both Nylon and Delrin are known to exhibit relatively high mechanical moduli in comparison to Teflon and thus exhibit less severe signs of material wear.

Table 10 – Surface topography parameters for all sample surfaces used in UMT-TENG testing.

<i>Material</i>	<i>S_a (nm)</i>	<i>$S_{\Delta q}$</i>	<i>S_{sk}</i>	<i>S_{ku}</i>
Stainless Steel (polished)	8.4	0.008	-3.2	22
Aluminium (polished)	21.3	0.024	-1.9	4.1
Copper (polished)	11.7	0.010	0.2	14
Delrin (polished)	260	0.17	-0.6	3.7
Nylon (polished)	290	0.17	-0.2	3.4
Teflon (polished)	170	0.09	-0.5	3.9
Delrin (120 grit)	1700	0.57	-0.7	4.3
Nylon (120 grit)	1900	0.67	-0.3	4.4
Teflon (120 grit)	1500	0.48	0.1	3.1
Delrin (Polished, Worn)	2000	0.47	1.4	9.9
Nylon (Polished, Worn)	1500	0.31	-1.9	11.4
Teflon (Polished, Worn)	1200	0.27	-1.2	5.4
Delrin (120 grit, worn)	3500	0.32	-0.4	2.1
Nylon (120 grit, Worn)	2400	0.36	-1.2	6.9
Teflon (120 grit, Worn)	1300	0.38	0.6	4.4

The polymer samples were also analysed using attenuated total reflection Fourier-transform infrared spectroscopy (ATR-FTIR) before and after tribological testing as a method for gauging any potential changes in surface composition during tests. FTIR spectroscopy operates by illuminating a section of a sample surface with varying spectra of infrared photons. A portion of these photons become absorbed by the material by exciting the vibrational modes of chemical bonds and creating phonons, depending on their respective energies. The fraction of photons absorbed by the material for every given spectra combination is then converted into an absorption spectra of the material using a Fourier transform. FTIR analysis is useful for identifying the composition of polymeric materials due to the varying responses of different polymeric functional groups (Kuptsov and Zhizhin, 1998; Jung et al., 2018).

The wear debris from any test that produced a sufficient amount was also analysed in a similar fashion. The composition of the aforementioned transfer films, generated by testing Teflon samples against both metal counter-surfaces, is confirmed to be PTFE under FTIR analysis as shown in Figure 3-14d. Wear debris was also observed from Delrin samples against aluminium counter-surfaces under an applied load of 10 N, but not against stainless steel. The composition of this wear debris was also different to that of Delrin, which is confirmed via ATR-FTIR in Figure 3-14f. One identifiable and prominent feature of this FTIR spectra is a sharp peak at 1730cm^{-1} , indicating the presence of ester groups within the wear debris (Kuptsov and Zhizhin, 1998). The Nylon samples deposited very little wear debris onto any counter-surface, however an amount of optically reflective and non-reflective wear debris was instead observed to become embedded into the Nylon surface under higher loads as shown in Figure 3-14g.

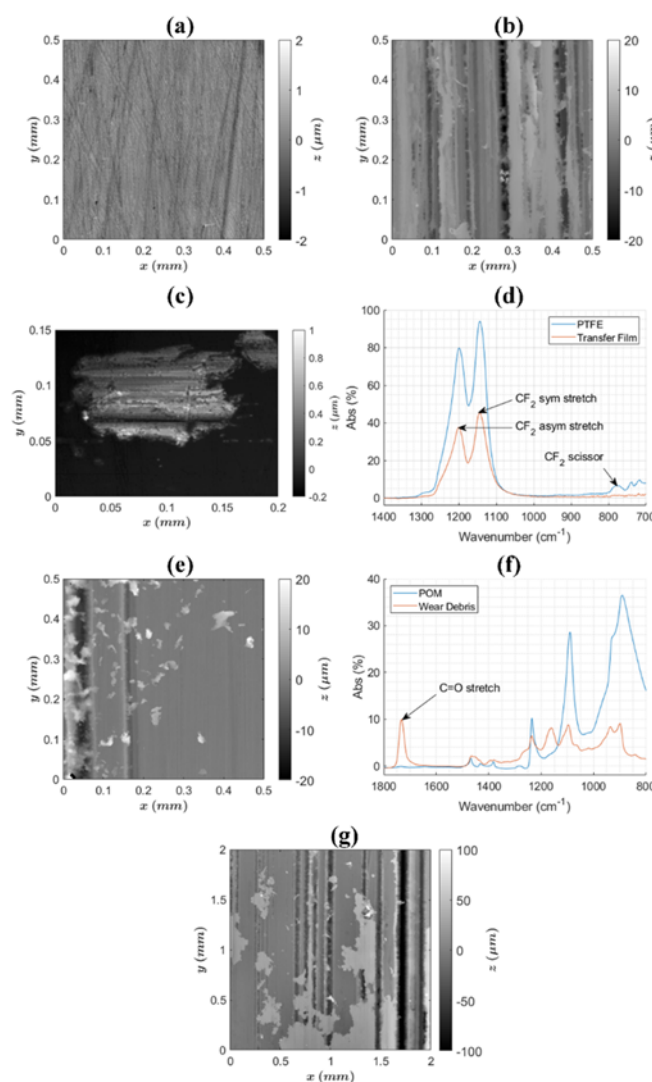


Figure 3-14 – (a) Example topography of unworn polished Teflon sample. (b) Example topography of worn Teflon sample. (c) Example topography of PTFE wear debris on a stainless steel counter-surface after contact testing against Teflon, measured using a Bruker NPFLEX white-light interferometer. (d) ATR-FTIR spectra of the Teflon surface prior to testing (blue) and the observed transfer film (orange). (e) Example topography of wear debris on an aluminium counter-surface after contact testing against Delrin, measured using a Bruker NPFLEX white-light interferometer. (f) ATR-FTIR spectra of the Delrin surface prior to testing (blue) and the observed wear debris (orange). (g) Example topography of embedded wear debris on a Nylon surface after contact testing against Aluminium.

3.2.2 Electronic Output Measurements

3.2.2.a Current and Voltage Measurements

3D depictions of a typical voltage and current response from high and low-impedance UMT-TENG contact tests are respectively given in Figure 3-15a and Figure 3-15b. Simultaneous measurements of output voltage and current over external load of 10 M Ω and 1 G Ω are also given in Figure 3-15c and Figure 3-15d respectively. Upon measurement of the electronic output properties of the UMT-TENG contact under open-circuit, short-circuit, and finite impedance measurement modes; alternating voltage and current traces are observed similarly to as observed with the F-TENG apparatus.

Under high impedance measurements (≥ 1 G Ω) the voltage trace accurately reflects the physical movement of trapped charges on the upper sample surface, as shown in Figure 3-15a Figure 3-15c, and Figure 3-16b. The current trace at such high impedances reflects the capacitive reactance of the TENG device; being proportional to the time differential of the voltage trace and therefore dependant on the relative velocity of the upper and lower samples, as shown in Figure 3-15b, Figure 3-15c, Figure 3-17b, Figure 3-19, and Figure 3-20.

At lower impedances (≤ 10 M Ω) the device response is shown to be ohmic in nature, where the voltage trace is equal to the current trace multiplied by the resistive impedance of the external measurement circuit, as shown in Figure 3-15d, Figure 3-16a and Figure 3-17a, Figure 3-21, and Figure 3-22. This confirms that the measured current trace is the free movement of mobile charges between the lower electrodes to accommodate for the change in local electric field, which in turn is caused by the physical movement of the charged upper sample surface. The magnitude and polarity of the tribocharges on the upper sample surface are also shown to influence the polarity and magnitude of the current output.

Both current and voltage outputs under high and low resistive loads are shown to increase throughout the initial stages of each test, indicating an accumulation of triboelectric charges on the insulating upper sample surface over time. These characteristics for each trace are preserved at reciprocating frequencies of 1 Hz, 2.5 Hz, and 10 Hz. One exception to this is the observation of a slight phase difference in voltage and current trace observed at 10 Hz under a resistive load of 10 M Ω as shown in Figure 3-22. This indicates that the capacitive reactance of the TENG device begins to dominate at increasing reciprocating frequencies.

Multiplying the current and voltage traces gives a representation of the electric power generated by the TENG through the measurement circuit, a visual representation of this power output under varying external resistances is given in Figure 3-18.

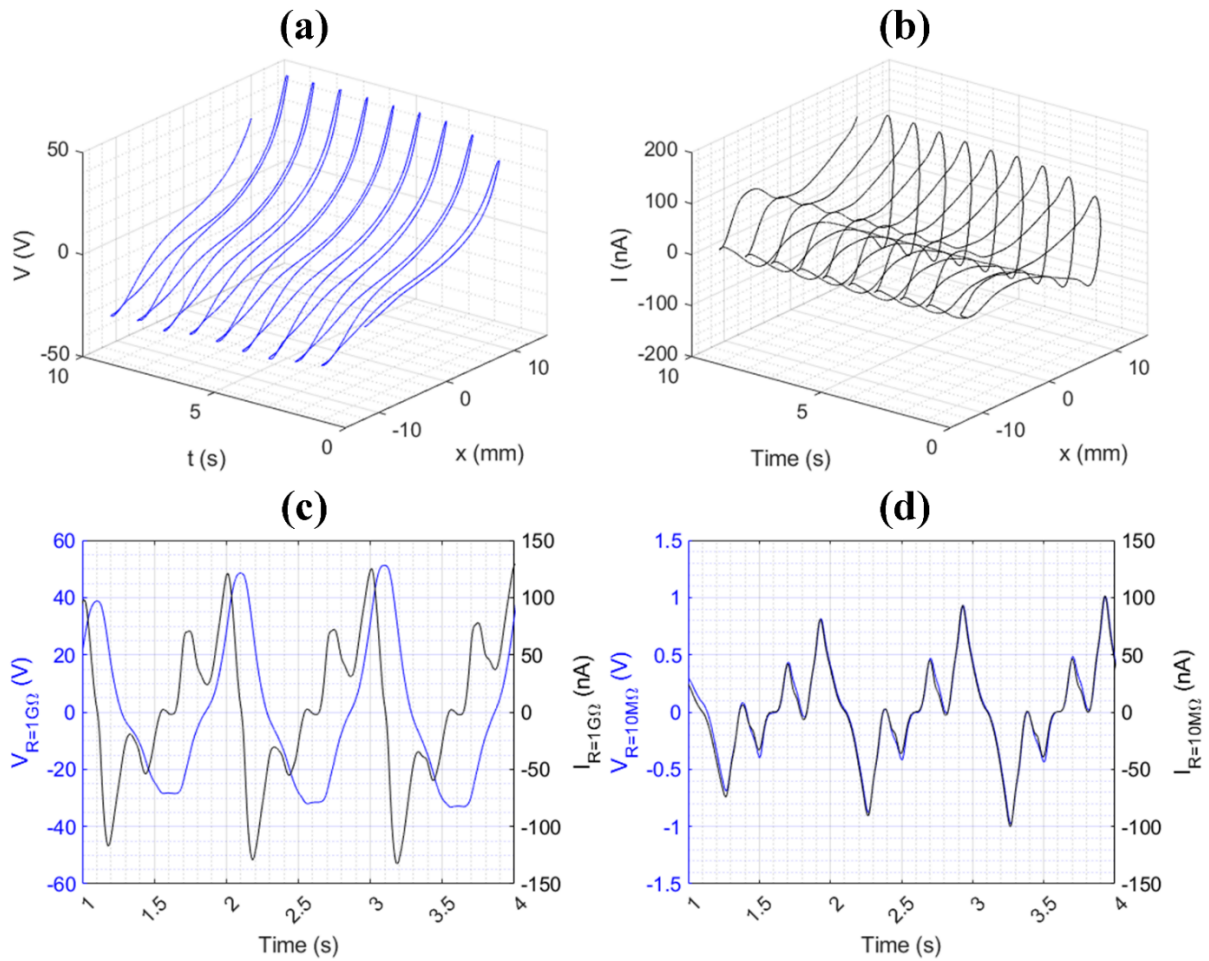


Figure 3-15 – (a) Output voltage against relative sample position and time for a polished Teflon on Nylon film F-TENG contact under an external resistance of approximately $> 2e^{14} \Omega$ (the input resistances of the two 6517B electrometers in series). (b) Output current against relative sample position and time for an identical contact under an external resistance of $\ll 1 \Omega$ (6517B connected as an ammeter with negligible voltage burden). (c) Output voltage (blue) and current (black) over time for an identical contact under an external resistance of $1 \text{ G}\Omega$. (d) Output voltage (blue) and current (black) over time for an identical contact under an external resistance of $10 \text{ M}\Omega$. Samples were reciprocated at 1 Hz under an applied load of 40 N with a stroke length of 27 mm and a 2 mm lateral spacing of the lower samples. The apparent area of the contact is 23 mm by 50 mm .

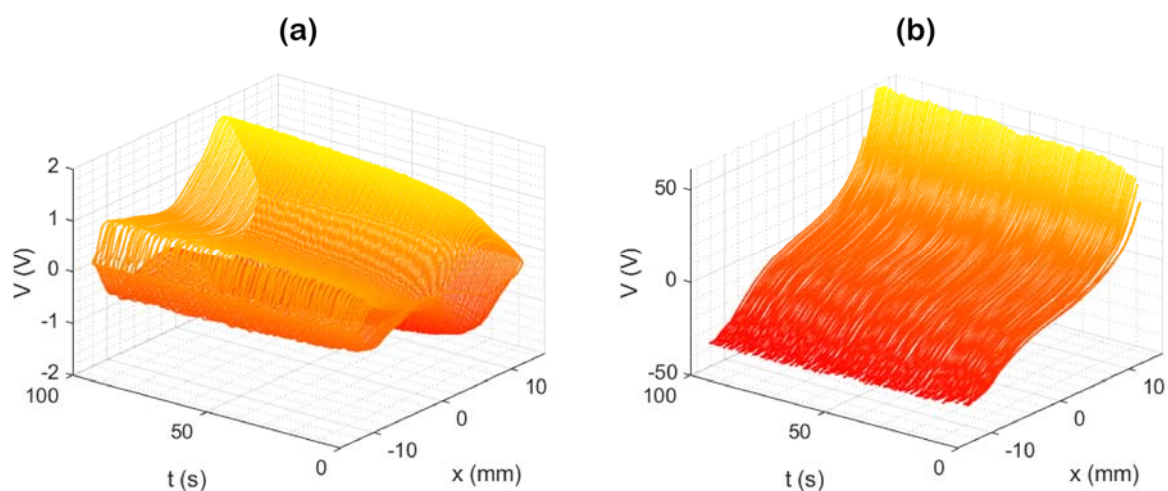


Figure 3-16 – Output voltage against relative sample position and time for a polished Teflon on Nylon film F-TENG contact under an external resistance of 10 M Ω (a) and 1 G Ω (b).

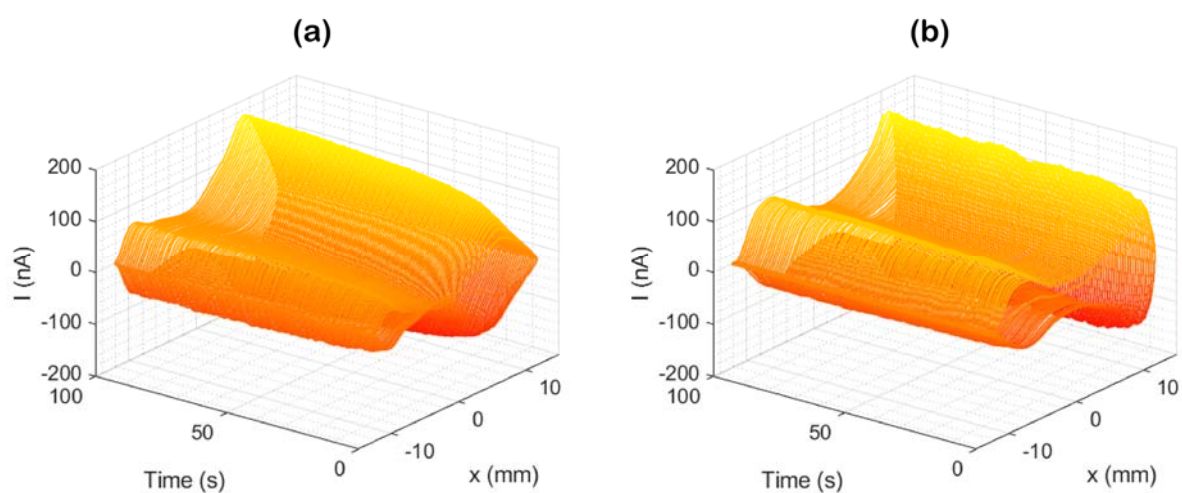


Figure 3-17 – Output current against relative sample position and time for a polished Teflon on Nylon film F-TENG contact under an external resistance of 10 M Ω (a) and 1 G Ω (b).

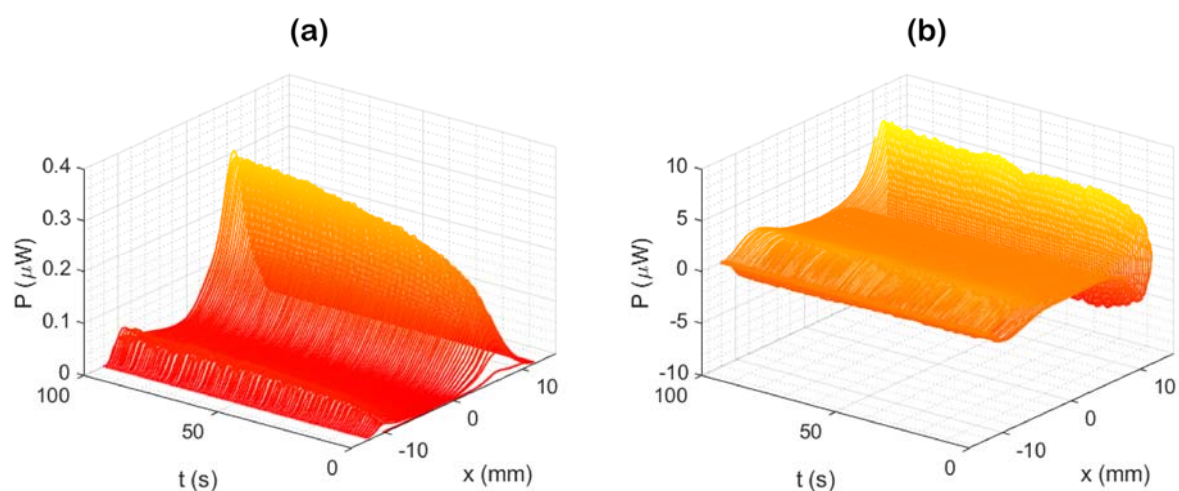


Figure 3-18 – Output power (current multiplied by voltage) against relative sample position and time for a polished Teflon on Nylon film F-TENG contact under an external resistance of 10 M Ω (a) and 1 G Ω (b).

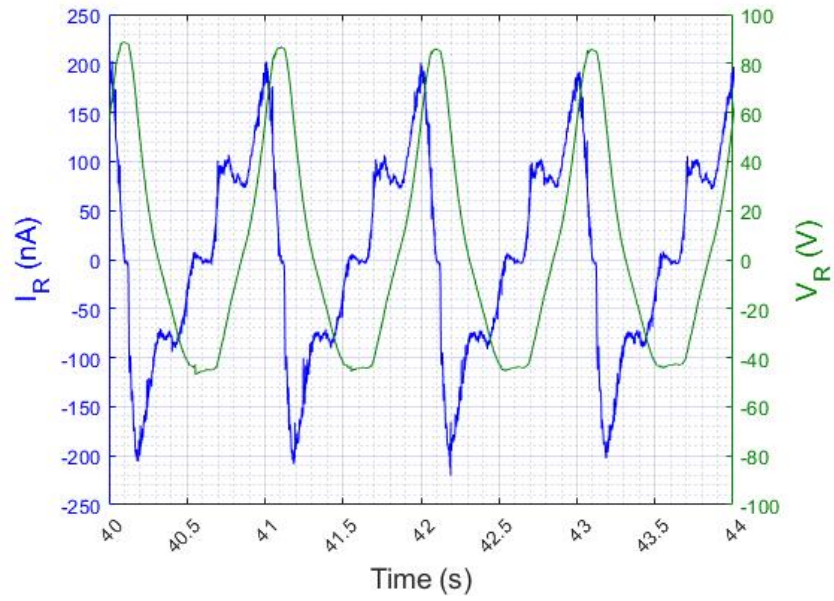


Figure 3-19 – Current (blue) and voltage (green) output for a Teflon on Nylon F-TENG contact oscillating at 1 Hz, under an external resistive load of 1 G Ω .

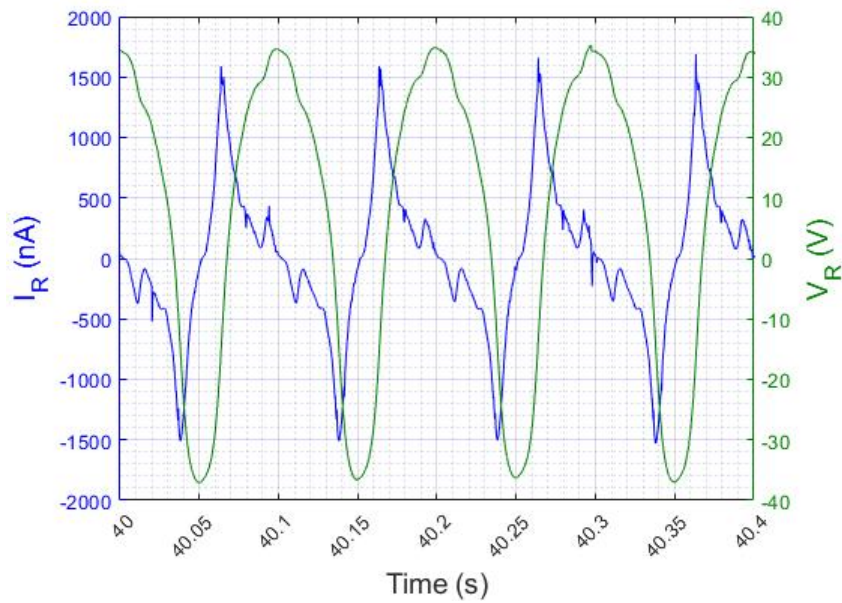


Figure 3-20 – Current (blue) and voltage (green) output for a Teflon on Nylon F-TENG contact oscillating at 10 Hz, under an external resistive load of 1 G Ω .

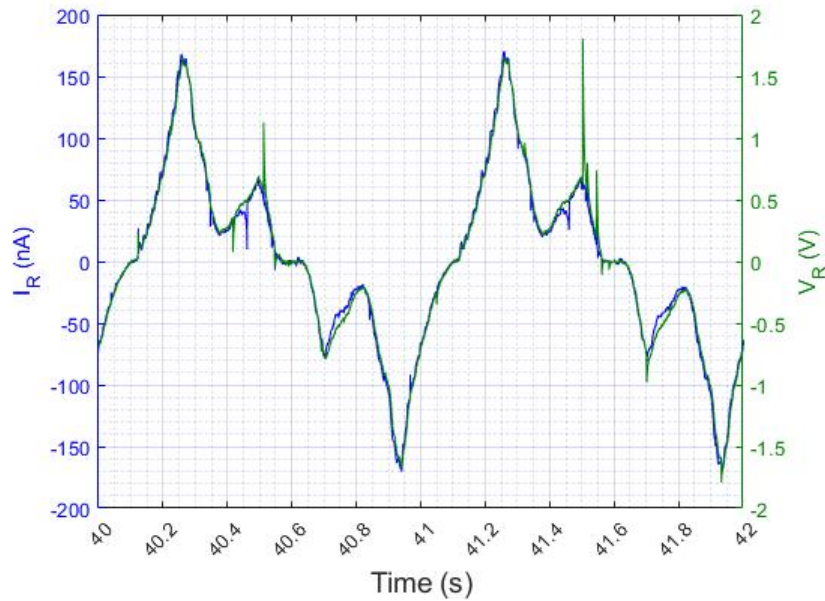


Figure 3-21 – Current (blue) and voltage (green) output for a Teflon on Nylon F-TENG contact oscillating at 1 Hz, under an external resistive load of 10 M Ω .

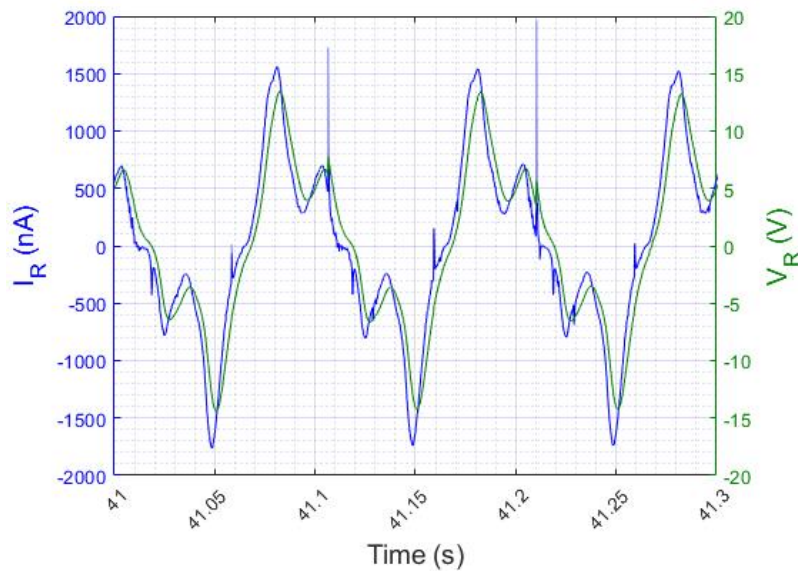


Figure 3-22 – Current (blue) and voltage (green) output for a Teflon on Nylon F-TENG contact oscillating at 10 Hz, under an external resistive load of 10 M Ω .

Tests were also conducted with both electrometers in open circuit voltage measurement configuration, placed in opposing polarities and connected to each respective electrode of the F-TENG device as depicted in Figure 3-3. The current output was measured in short circuit mode for the F-TENG apparatus with two electrometers connected in series with reversed polarities between the two electrodes. This configuration is also identical to the method used for measuring open circuit voltage of the F-TENG device as previously mentioned. The two electrodes were then disconnected from each other mid-test, and their respective single-electrode (SE) current outputs were compared to the initial differential outputs. This comparison is given in Figure 3-23, where the differential configuration is shown to yield a greater current output than a single electrode configuration.

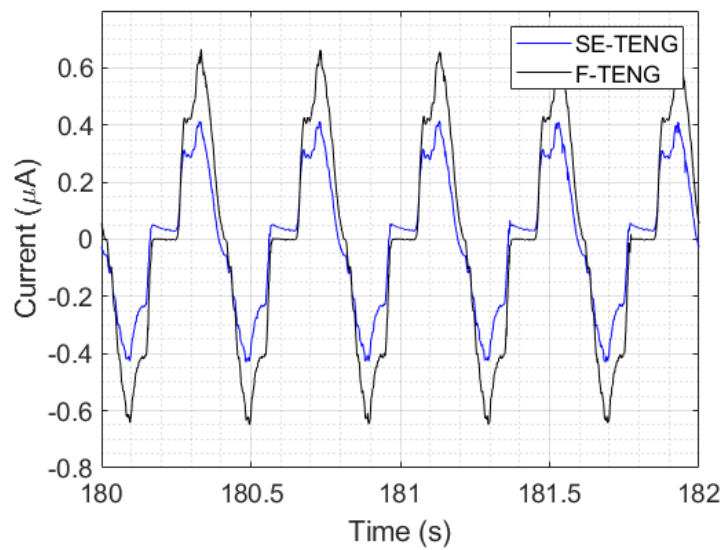


Figure 3-23 – Short circuit current output for a sliding reciprocating Teflon on Nylon UMT-TENG contact, configured in a) single electrode (SE) and b) freestanding triboelectric layer (F) mode.

3.2.2.b Microscale ESD Observations

The time resolution for the UMT data acquisition unit is 8 kHz, which allows for the observation of mechanical and electronic phenomena across the TENG device on a timescale of a millisecond. At these measurement resolutions, one particular electronic phenomenon becomes observable. Short and abrupt fluctuations in both current and voltage are observed across the measurement circuit during sliding contact tests. These fluctuations are shown to last several milliseconds and correspond to sharp spikes in current output or step changes in high impedance voltage response. Examples of current fluctuation are given in Figure 3-24 and Figure 3-25, alongside their respective changes in voltage. These spikes represent a sharp rise in current, followed by a corresponding decay over a slightly longer timescale.

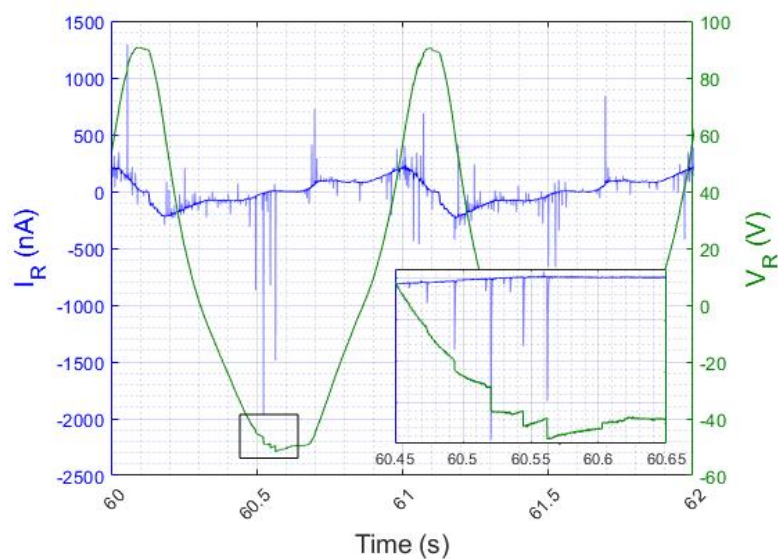


Figure 3-24 – Un-flagged current (blue) and voltage (green) output for a Teflon on Nylon F-TENG contact oscillating at 1 Hz, under an external resistive load of 1 GΩ.

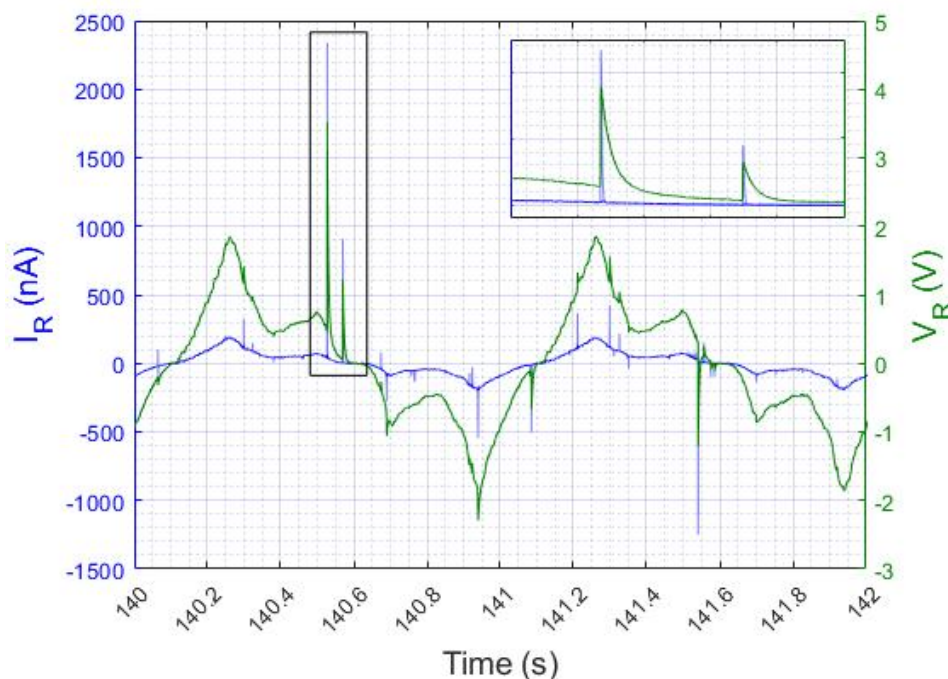


Figure 3-25 – Un-flagged current (blue) and voltage (green) output for a Teflon on Nylon F-TENG contact oscillating at 1 Hz, under an external resistive load of 10 M Ω .

An important aspect of these phenomena is that they are solely observed during sliding contact. During non-contact reciprocating tests the current and voltage traces resemble that of the F-TENG contact without the presence of these fluctuations; with the exception of an exponentially decaying response as expected from typical thermionic charge dissipation, rather than a triboelectric accumulation of charge. Because of this behaviour, these phenomena must be directly linked to physical mechanisms within the contact, rather than an artefact of measurement or other potential interferences.

A likely cause of these observed phenomena is the abrupt movement of a large number of electrons across the contact itself. Integrating a single spike in current over time yields a charge value that corresponds to a movement of charge in the magnitude of several thousand electrons. These abrupt movements of charge could be fundamentally linked to the phenomenon of triboluminescence, where the recombination of triboelectrically separated charges occurs on large scales in the form of lightning. These charge movements could be the recombination of triboelectrically generated charges across the contact. These charges may find it energetically favourable to recombine in such an abrupt manner as a result of an equally abrupt change in surface potential, combined with suitably high spatial charge densities within the contact.

Another possible cause for these fluctuations could be the delamination and subsequent adsorption of small charged particulate matter across the contact. This hypothesis is however less plausible due to the lack of observable embedded wear debris on sample surfaces after short duration testing. The assumption is therefore made that these phenomena are observations of microscale electrostatic discharge (ESD) events across the contact as previously explained. These ESD events may be linked to the nucleation and propagation of microscale cracks on the insulating polymer acceptor surfaces. If a

sufficiently high spatial charge density is reached, the formation of a crack can lead to a sharp increase in surface potential due to both geometric and flexoelectric factors. This abrupt increase in surface potential can make it energetically favourable for electrons in high energy trap states to tunnel back to their original donor surface. The MATLAB code was modified to identify these ESD events in the current trace and remove them from the data as shown in Figure 3-26.

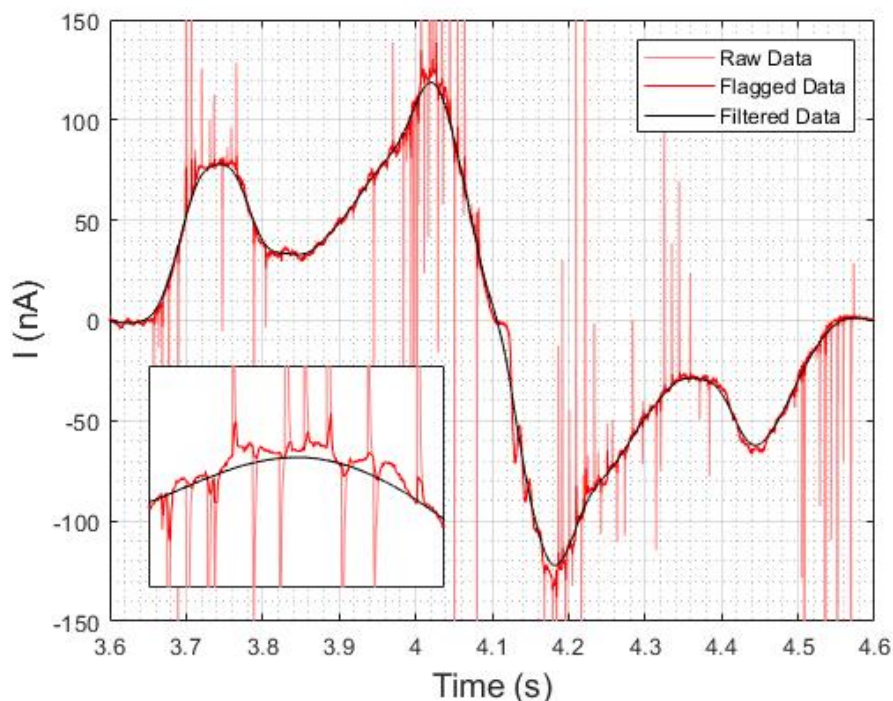


Figure 3-26 – Raw (light red), Flagged (red), and filtered (black) current output for a Teflon on Nylon F-TENG contact oscillating at 1 Hz.

Removing the background current trace and integrating under each isolated ESD event over time gives an estimation of the charge dissipated during each event. These charge values are added up across each forward and reverse stroke and plotted across the duration of each test to give an intriguing relationship. The ESD events were also separated depending on the direction of charge transfer as measured by the electrometers. The ESD events should generate a change in electric field that is experienced by both electrodes. The polarity of this experienced change in electric field should be identical for both electrodes, since the ESD events are only occurring across the contact.

The relative magnitudes of this change in electric field experienced by each electrode should however be dependent on the location of the ESD along the stroke. For example, an ESD event that occurs directly over one electrode at the end of the stroke would be experienced more strongly by that particular electrode, and would therefore register on the measurement circuit as a brief fluctuation in potential difference between the two electrodes. Alternatively, an ESD event that occurs directly between the two electrodes would be equally experienced by both of them, therefore would not be measured by the measurement circuit. By this logic, the polarity of current spike as measured by the external circuit is a representation of both the direction of charge movement across the contact, as well as the location of the ESD event along the stroke.

If a collection of electrons were to be transferred from the Teflon block to the Nylon sheet (back-tunnelling, in the reverse direction to triboelectric charge transfer) whilst the Teflon block was directly over the electrode at the forward end of its stroke (where $x = +12.5$ mm), the forward electrode would experience a lowering of electrostatic potential due to the approach of negative charge. The reverse electrode would feel a similar decrease in electrostatic potential, but to a significantly lesser degree due to its increased distance from the ESD site. A potential difference would therefore be experienced between the two electrodes, which would be measured as a positive voltage due to the positive terminal of the voltage-measuring electrometer being connected to the reverse electrode. A positive current would also be registered by the measurement circuit due to the positive terminal of the current-measuring electrometer being connected directly to the forward electrode.

Each ESD event of a particular polarity is then summed up across each forward and reverse stroke, giving four separate measurements of ESD per full cycle of the UMT-TENG apparatus. These values are then plotted across the test duration as given in Figure 3-27 in order to determine any time dependency between cycle number and total charge transferred via ESD. Upon examination of Figure 3-27, a clear time dependency can be seen for the total charge transferred via ESD

The intriguing aspect of this observation is that the time dependency is specifically experienced during the forward stroke. This implies a directional dependency for the tendency for ESD along the stroke, being more likely to occur with the upper sample moving in a specific direction. This could be explained by some inherent directional configuration characteristic of the surfaces which may elude to the preferential direction of surface crack propagation. However, the simpler and more likely cause could be the presence of an anisotropy in applied load along the cycle of the contact. This anisotropy is likely caused by a misalignment in height of the lower samples along the stroke length, leading to a higher applied load as the upper sample block travels in one specific direction as shown in Figure 3-28. The parameters of the UMTs aforementioned vertical force feedback loop were therefore recalibrated to a more sensitive response in order to eliminate this discrepancy before the primary series of tests were conducted.

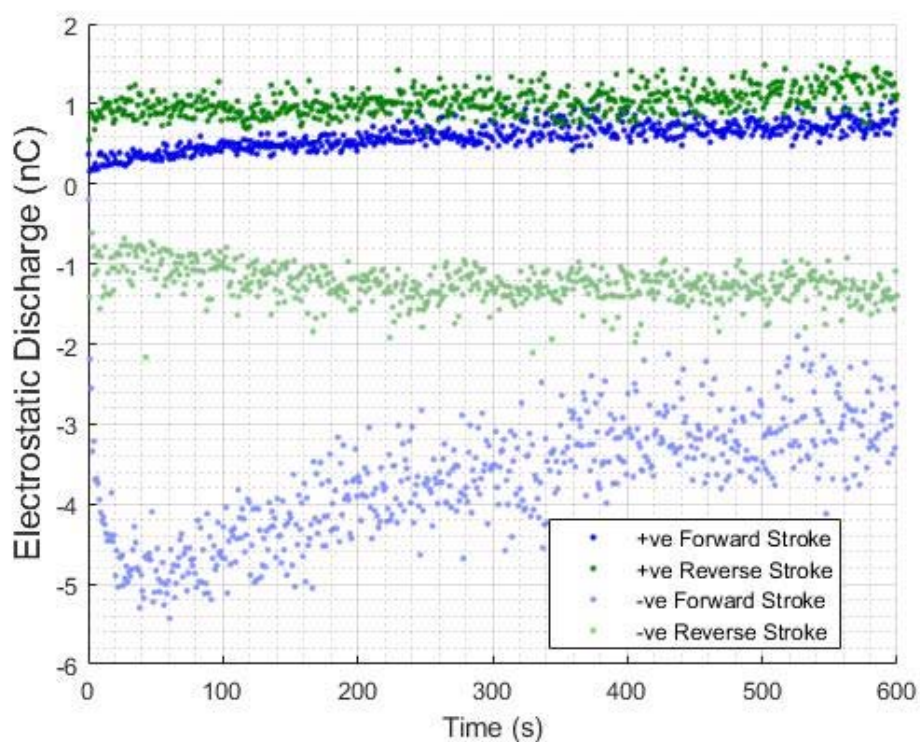


Figure 3-27 – Integrated electrostatic discharge per forward (blue) and reverse (green) stroke for an example Teflon on Nylon F-TENG contact. Each data point represents the total charge discharged across a single stroke, rather than an individual ESD event.

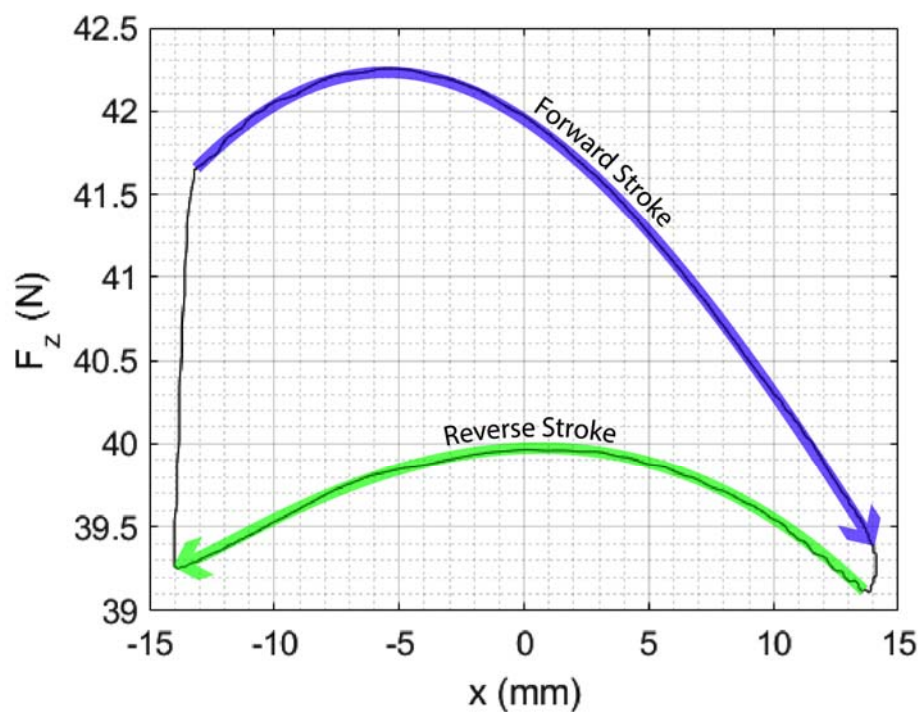


Figure 3-28 – Vertical force across the full reciprocation cycle of an example F-TENG apparatus, without the force feedback loop being implemented.

3.2.2.c Triboelectric Charge Measurements

The current output from each forward and reverse stroke across the duration of each test is integrated over time as described by equation (2-6). This returns the total amount of charge that has passed through the ammeter during each movement, and thus gives an estimation of the total amount of tribocharge present on the insulating polymer surface. Analysis of contact charge over time for each material pairing firstly reveals its transient nature. An initial stage of charge accumulation is shown to occur when previously uncharged and dissimilar surfaces are brought into contact. The exact formulation of how electrostatic charge accumulates within tribological contacts is the subject of further discussion. Previous research has concluded that an exponential model for charge accumulation fits well for contacts that have negligible changes in real contact area or pressure (Armitage et al., 2021). The maximum charge density, as well as the rate at which this charge accumulation occurs, is shown to be dependent on both material pairing and contact topography. These relationships are depicted in Figure 3-29 in the same layout as previously described for Figure 3-13.

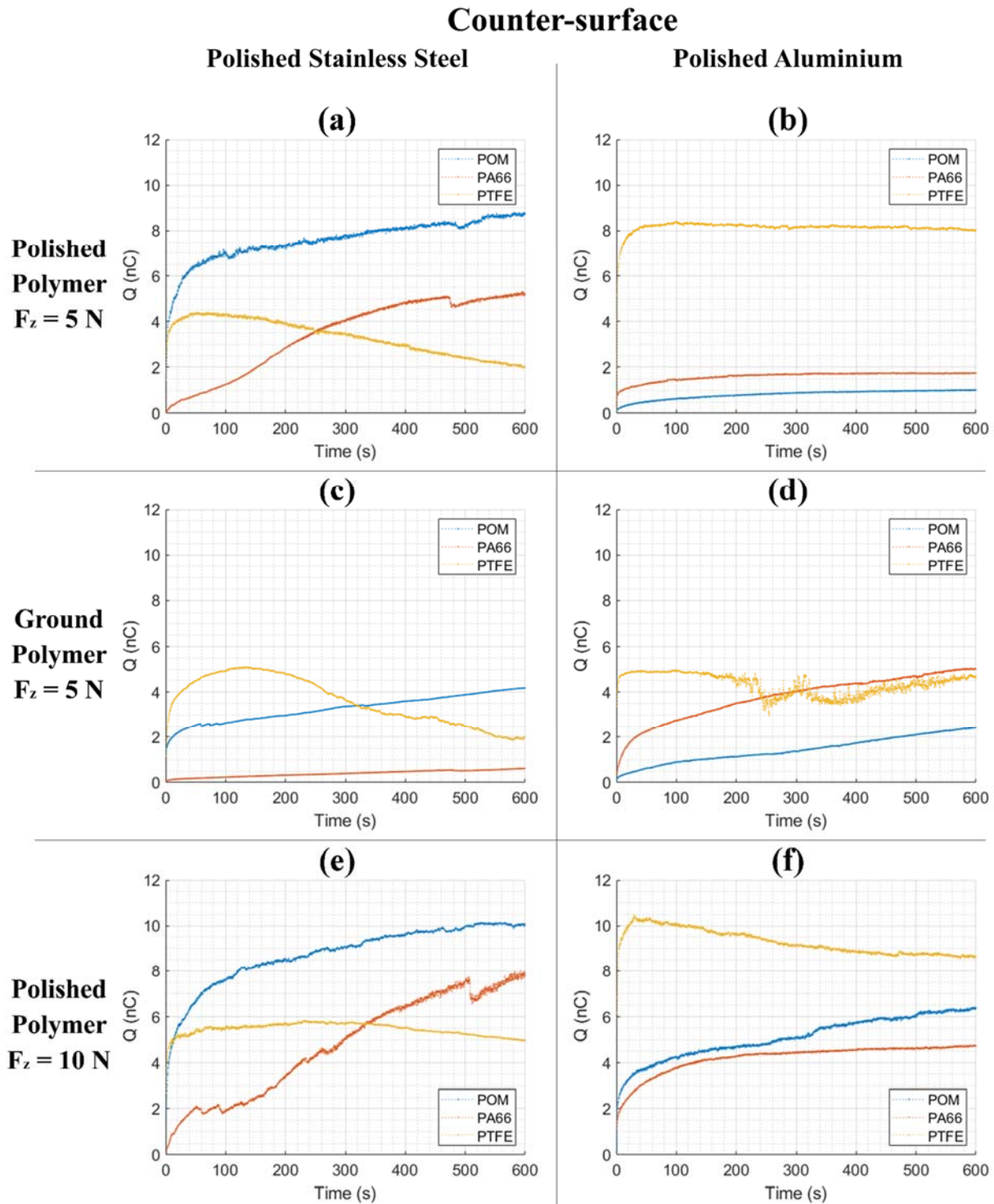


Figure 3-29 – Contact charge over time for (a) polished polymers on polished stainless steel F-TENG contacts under an applied load of 5 N, (b) polished polymers on polished aluminium F-TENG contacts under an applied load of 5 N, (c) ground polymers on polished stainless steel F-TENG contacts under an applied load of 5 N, (d) ground polymers on polished aluminium F-TENG contacts under an applied load of 5 N, (e) polished polymers on polished stainless steel F-TENG contacts under an applied load of 10 N, (f) polished polymers on polished aluminium F-TENG contacts under an applied load of 10 N. Samples were reciprocated at 2.5 Hz with a stroke length of 27 mm and a 2 mm lateral spacing of the lower samples. The apparent area of the contact is 23 mm by 50 mm when the upper sample fully encompasses a lower sample.

3.2.3.c.i Influence of Polymer Composition

It is known that some polymers are known to generally accumulate surface electrons when in contact with other materials by having low-energy unoccupied molecular orbitals (Shirakawa et al., 2010), whereas some polymers generally donate electrons to their respective counter-surfaces from high-energy occupied states (Zhou et al., 2020). Teflon has seen much use as an electronegative material choice in TENG contacts owing to its exceptional performance as an electron acceptor (Chen et al., 2019). Nylon and Delrin are two polymers that have been proven in literature to donate electrons to most counter-surfaces (Diaz and Felix-Navarro, 2004). Nylon in particular has seen extensive use in TENG contacts as an electropositive contact surface (Wang et al., 2013). The Teflon surfaces all accumulated a negative charge throughout the initial stages of contact testing, indicating the acceptance of electrons from both the aluminium and stainless-steel counter-surfaces as predicted. The Delrin and Nylon surfaces all accumulated a positive charge during the initial stages of contact testing, indicating the donation of electrons to both the aluminium and stainless-steel counter-surfaces, also in accordance with previous literature (Diaz and Felix-Navarro, 2004). The Delrin samples were shown to accumulate the highest magnitude of charge against stainless steel counter-surfaces, whereas the Teflon samples accumulated the highest magnitude of charge against the aluminium counter-surfaces. These data indicate that the work functions of both metal surfaces lie between the 'effective' work functions of Teflon and Nylon due to the polarity of the charges being accumulated on the polymer surfaces.

3.2.3.c.ii Influence of Electrode Composition

The composition of the conductive counter-surface was shown to have an influence on the magnitude and polarity of charges being transferred via triboelectric charging. Both the Delrin and Nylon surfaces accumulated less charge against aluminium than against stainless steel, whereas the Teflon surfaces accumulated more charge against aluminium. The polished Delrin samples are shown to accumulate a greater amount of charge than the polished Nylon samples, whereas this is reversed when the samples are tested against aluminium surfaces. This indicates that the 'effective' work function for Delrin is lower than that of Nylon, meaning that the highest occupied molecular orbital for Delrin is likely to be at a higher energy than that of Nylon. These data also indicate that the work function of the aluminium counter-surfaces is lower than that of the stainless steel counter-surfaces. Both metals are known to produce passive oxide surface layers, in the order of several nm thick, due to the high reactivity of their exposed metallic surfaces. The oxide layers that form on stainless steel surfaces however are mostly composed of iron oxides, molybdenum oxides and chromium oxides due to the composition of the alloy.

3.2.2.c.iii Influence of Surface Roughness

Previous research has suggested that increasing the real contact area of a TENG contact increases the total surface area through which triboelectric charging can occur (Armitage et al., 2021). Ultimately this implies that two smooth and conformal surfaces should accumulate a greater amount of charge via triboelectric charging than two, otherwise identical, non-conformal surfaces. The ground Delrin and Nylon surfaces are shown to accumulate more charge against aluminium counter-surfaces than their polished

equivalents, which can also be said for the Teflon samples being tested against stainless steel. However, for the remaining material pairings the ground surfaces accumulated a greater charge than their polished counterparts. This implies that there are more complex processes occurring within the TENG contact that affect triboelectric charging.

3.2.2.c.iv Influence of Applied Load

Increasing the applied load to the UMT-TENG contact is shown to increase both the rate of charge accumulation and the saturation charge density within it for all material pairings. Extensive tribological research has previously concluded that increasing the applied load to a typical mechanical contact increases the proportional area of real contact within the apparent area of contact (Xu et al., 2020). Whilst this increase in real contact area may contribute to triboelectric charging, as explained previously, it is also possible that the increase in energy dissipated into the contact via friction may enhance triboelectric charging through phonon-electron interactions (Pan and Zhang, 2017).

3.2.3 Comparison of Tribological & Electronic Measurement Results

The ability to simultaneously measure both the friction response and electrical output of the UMT-TENG contact gives an insight into how tribology influences triboelectric charging within it. Contact testing reveals that the amount of charge accumulated within the UMT-TENG contact, as well as the rates at which this charge accumulates and dissipates, is dependent on a multitude of tribological processes, in addition to the difference in surface electronic structures. Friction coefficient is plotted alongside triboelectric contact charge as a way of better highlighting this synergistic relationship between sliding friction and triboelectric charge accumulation. Examples of these plots are given in Figure 3-30 and Figure 3-31 for a Teflon-aluminium and Nylon-aluminium contact respectively.

For Teflon contacts, a maximum charge density is reached within the first few minutes of contact testing. After this point, the charge within the contact then begins to diminish. The data presented in Figure 3-13 and Figure 3-29 indicate that the amount of electrostatic charge trapped within the contact diminishes in a similar fashion to the friction coefficient over the duration of testing. This relationship is more clearly depicted in Figure 3-30. This reduction in contact charge could therefore be attributed to the PTFE transfer film formation within the contact. PTFE wear particles are removed from the bulk material and deposited on the counter-surface during transfer film formation. Further triboelectric charge transfer is inhibited in these areas due to the contact potential difference between the Teflon surface and the newly formed PTFE transfer film becoming substantially smaller than the CPD between the Teflon and the previously exposed counter-surface. Previously accumulated triboelectric charges on the Teflon surface may also be removed through contact with the PTFE transfer film on the counter-surface via tribo 'de-electrification' between the similar materials (Soh et al., 2012). The formation of PTFE transfer-films is beneficial in some circumstances where a self-replenishing solid lubricant is needed. PTFE transfer films in particular are known to lower the friction coefficient within contacts by covering any asperities to reduce abrasive wear, in addition to reducing adhesive forces between the Teflon surface and the newly generated PTFE counter-surface. This tribological behaviour can be explained by the loosely bonded rod-like molecular

structure of PTFE (Holt et al., 1996). This friction behaviour, explained by the development of a low friction transfer film, is seen to progress more expediently when tested against the harder stainless steel counter surface. This behaviour is also reflected in the electronic output, where the contact charge diminishes more noticeably over time against the stainless steel counter surfaces. These data combined indicate that a PTFE transfer film is slower to develop across the aluminium counter surfaces under the same contact force and relative motion.

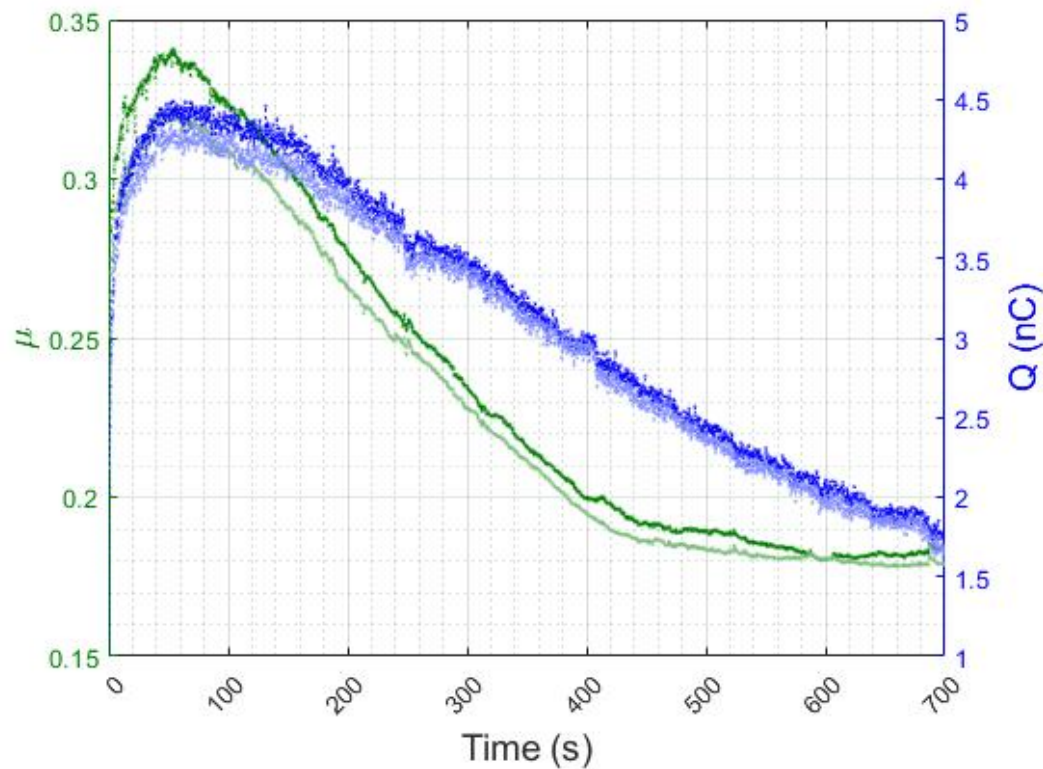


Figure 3-30 – Friction (green) and triboelectric charge (blue) for each forward (blue, green) and reverse (light blue, light green) stroke of a polished Teflon on polished Stainless Steel F-TENG contact over time, reciprocating at 2.5 Hz under an applied load of 5 N.

This similarity between friction coefficient and contact charge continues for both Delrin and Nylon contacts, where an increasing friction coefficient over time is followed by an increase in contact charge as shown in Figure 3-31. The exact underlying mechanisms behind this relationship are in need of further investigation. It is plausible that an increase in contact charge is caused by electron excitation, via phonons created by friction and material deformation (Pan and Zhang, 2017). Research also suggests that ‘Coulomb adhesion’ caused by the electrostatic attraction of the charged contacting surfaces may increase the friction coefficient between them (Sayfidinov et al., 2018; Luo et al., 2021). Abrupt reductions in contact charge are also occasionally observed during contact testing, which coincide with an associated change in friction coefficient, as highlighted in Figure 3-31. These combined phenomena indicate the removal of charged wear debris from the contact.

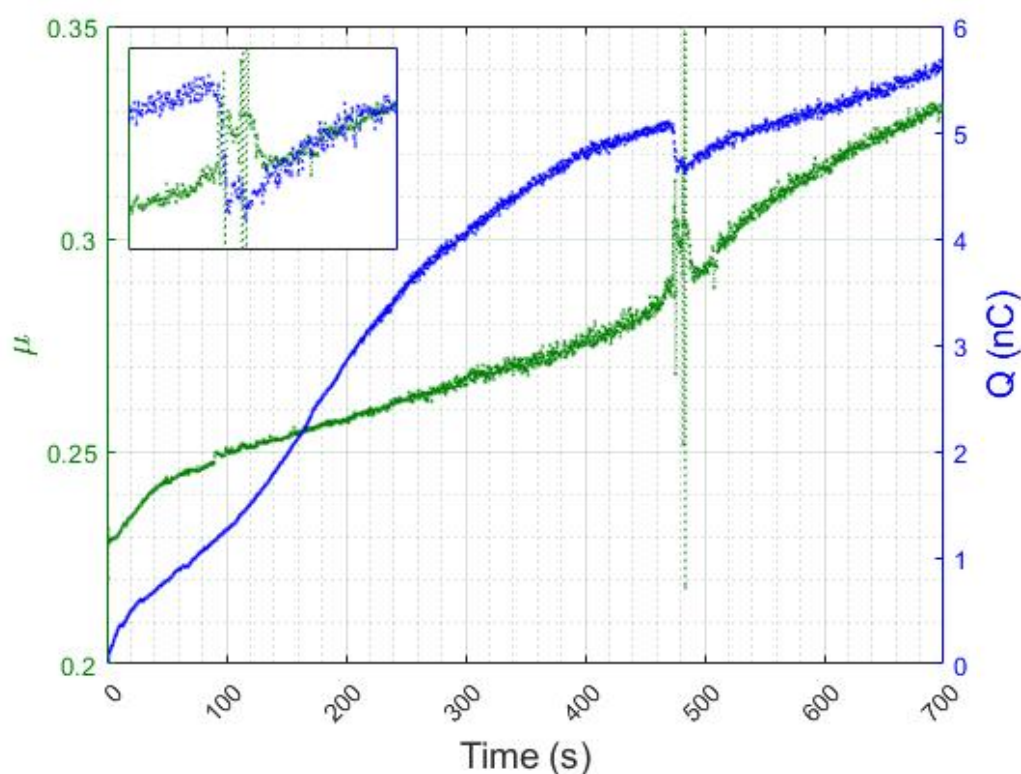


Figure 3-31 – Friction (green) and triboelectric charge (blue) for each forward stroke of a polished Nylon on polished Stainless Steel F-TENG contact over time, reciprocating at 2.5 Hz under an applied load of 5 N.

This correlation between friction coefficient and triboelectric charging continues for the case of an example lubricant being introduced to the contact during sliding motion. An additional test was conducted for the Teflon on Nylon F-TENG contact at 2.5 Hz and under 40 N applied load. 1 mL of heptane was added mid-test to the Nylon surface and entrained into the sliding contact by its relative motion to the Teflon block. The presence of the heptane within the contact noticeably lowered the friction coefficient from 0.27 to 0.1 across the span of approximately ten cycles. All triboelectric charge that had been previously generated within the contact was also subsequently removed by interactions with the entrained heptane as is reflected in Figure 3-32. As the heptane gradually evaporated from the contact, a resulting gradual increase in both friction coefficient and triboelectric charge is seen. The UMT-TENG apparatus was therefore able to detect the entrainment and subsequent starvation of the lubricating heptane from the sliding contact in both friction and electrostatic response.

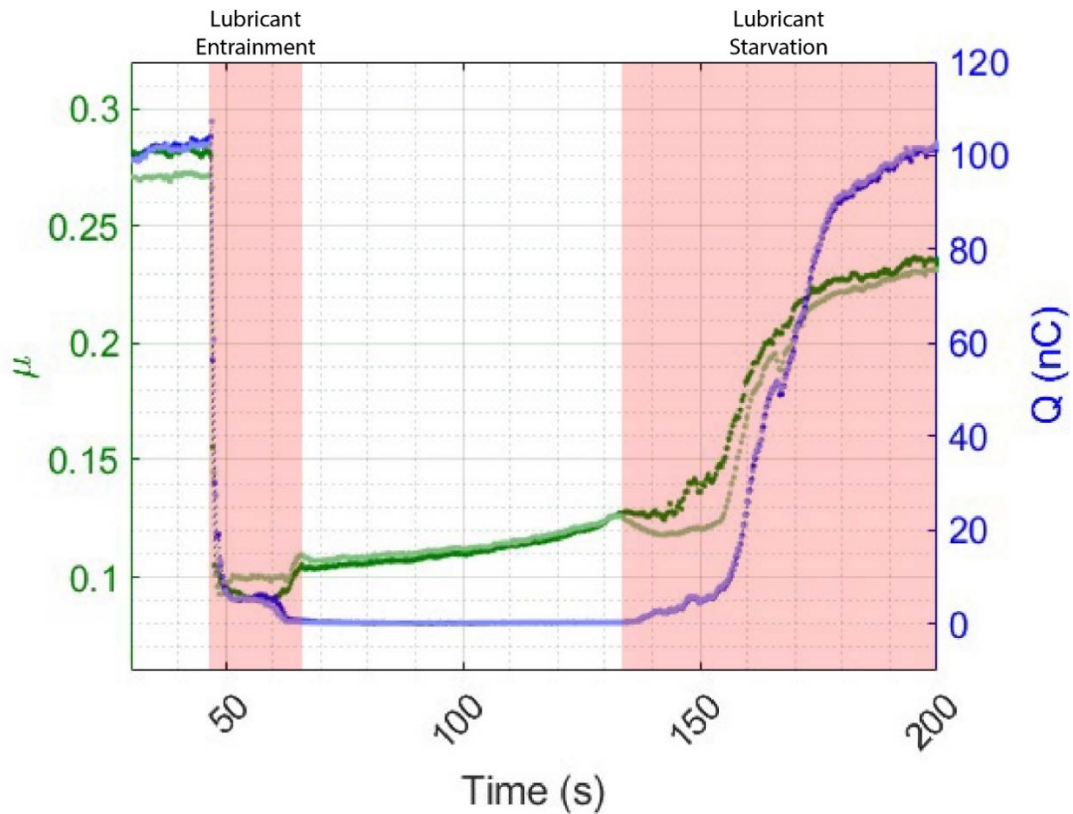


Figure 3-32 - Friction (green) and triboelectric charge (blue) for each forward (blue, green) and reverse (light blue, light green) stroke of a polished Teflon on Nylon F-TENG contact over time, reciprocating at 2.5 Hz under an applied load of 40 N, with heptane introduced as a lubricant mid-test.

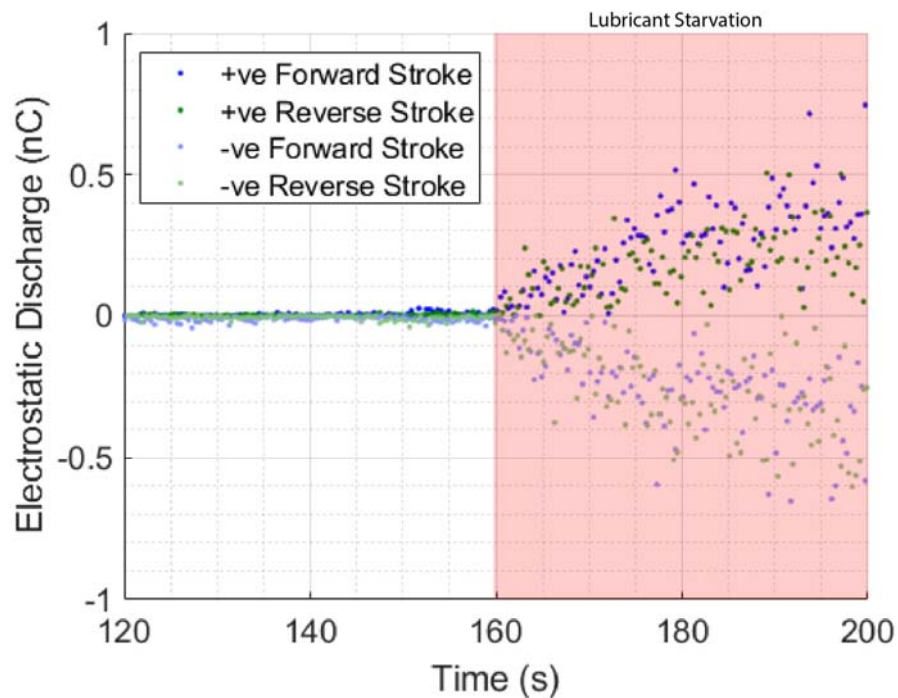


Figure 3-33 – Integrated electrostatic discharge per forward (blue) and reverse (green) stroke for the same Teflon on Nylon F-TENG contact as depicted in Figure 3-32, indicating the increase in ESD events after the onset of lubricant starvation. Each data point represents the total charge discharged across a single stroke, rather than an individual ESD event.

3.3 Conclusions

The UMT-TENG has proven to be a capable and effective apparatus for correlating tribological and triboelectric phenomena. The influences of surface composition and contact topography are further investigated, alongside the effects of applied load and material wear on triboelectric charging. The following findings can be drawn from this study.

- ❖ The triboelectric charging within a metal on polymer contact is shown to be dependent on the surface compositions of both the metal and polymer.
- ❖ Experimental data has been presented which reinforces existing theory on the increase of triboelectric contact charge density as a result of increasing real contact area under higher applied loads.
- ❖ The triboelectric charge within an F-TENG contact is shown to have a synergistic relationship with friction coefficient, with multiple mechanisms acting to bring the two values into good correlation with one another during contact testing.
- ❖ The accumulation of triboelectric charge is shown to increase with increasing friction coefficients across contact tests.
- ❖ Similarly, the diminishment of triboelectric charge densities within sliding contacts has been directly attributed to material wear mechanisms and the development of low-friction transfer layers within polymer-metal contacts.
 - The presence of a lubricant is also shown to reduce both friction and triboelectric charge.
- ❖ Microscale electrostatic discharges are also observed to occur within sliding triboelectric contacts as a result of stick-slip friction and surface crack propagation.
 - The prominence of these ESD events are shown to change across the duration of contact testing, in addition to being influenced by the presence of a charge dissipating lubricant.
- ❖ The effects of external circuit properties and reciprocating frequency are also related to electronic output F-TENG characteristics.
 - A clear correlation between relative sample position and open circuit voltage is observed.
 - Similarly, a correlation between relative sample velocities and short circuit current is observed.
 - The short circuit current response of an F-TENG device is shown to be greater than that of an equivalent single electrode TENG device, also with distinct differences in current waveform that relate to device geometry.
 - Under a finite resistive load of 10 M Ω , the output characteristics of the F-TENG device is purely ohmic in accordance with Ohm's law.
 - Under a higher finite resistance of 1 G Ω , the capacitive nature of the F-TENG device dominates, where the current output directly correlates to the time differential of voltage.

Chapter 4 – The UMT-TENG Apparatus: Friction and Semi-Analytical Model

In order to substantiate the contribution of friction and surface shear strains to triboelectric charging, both must be measured under controlled conditions. The previously demonstrated UMT-TENG methodology has provided a macroscale method for correlating the friction response and electric output for sliding TENG devices, whilst precisely monitoring and controlling the tribological parameters. In this chapter, the influence of sliding speed and frictional energy dissipation on triboelectric charging under varying applied loads is investigated using the UMT-TENG apparatus. A semi-analytical equation for describing triboelectric charging in sliding macroscale contacts is then derived using the insights provided by this investigation.

4.1 Methodology

The UMT-TENG apparatus is once again utilised as a valuable methodology for correlating the friction and electronic responses of a specific configuration of sliding F-TENG contact under varying tribological parameters.

4.1.1 Contact Geometry

An insulator-on-insulator freestanding triboelectric layer TENG device was replicated within the UMT-TENG test apparatus for this particular study. This iteration of F-TENG contact consisted of a Teflon block being reciprocated across the surface of a 0.5 mm thick Nylon sheet, under which two stainless steel electrodes were spaced apart laterally by 2 mm and connected electronically via an external measurement circuit. This configuration of F-TENG is identical to that which is used above in terms of dimensions; with the upper polymer block being 25 x 25 x 50 mm in dimension, and the lower electrodes being 25 x 2 x 70 mm. The relevant dimensions of this F-TENG device are displayed below in Figure 4-1. The introduction of the Nylon sheet between the Teflon block and conductive electrodes mitigates sample deflection arising from the lateral spacing of the two conductive electrodes. This also ensures that projected area of contact (denoted as A_n) between the Teflon block and Nylon sheet remains consistently 25 x 50 mm across the stroke length, regardless of the lateral spacing of the lower electrodes.

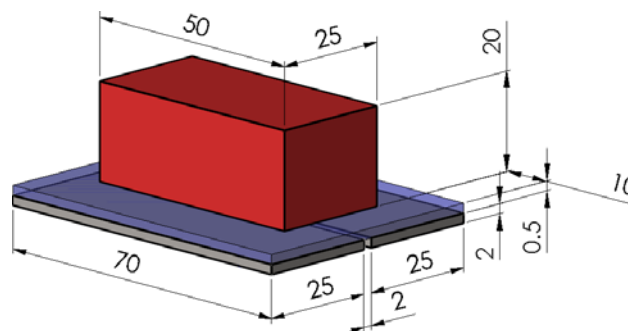


Figure 4-1 – Device geometry and sample dimensions in millimetres for the insulator-on-insulator freestanding-triboelectric-layer TENG. The Teflon block is coloured in red, whereas the Nylon sheet is blue, and the stainless steel plates are grey. The thickness of the Nylon sheet has been scaled up for it to be easily seen in this figure.

4.1.2 Electronic Measurements

The two conductive plates under the Nylon sheet are each connected to a Keithley 6517B electrometer for the purpose of measuring the electrostatically induced current produced by the movement of the Teflon block. The two electrometers are also connected in series as to provide a low resistance path through which current can flow between the two electrodes. In order to minimise file output size, a sampling rate of 110 Hz is used for the UMT data acquisition procedure in order to accommodate the longer duration 12 hr tests. This sampling rate was also used for the shorter 1 hr tests in order to maintain consistency. This sampling rate is more than adequate for collecting the necessary data as it is sufficiently higher than the Nyquist criterion of 5 Hz for a reciprocation frequency of 2.5 Hz and through Fourier transform analysis of the relevant waveform harmonics. Any phenomena that occur on smaller timescales - such as the previously mentioned ESD events - are considered to be negligible for the purpose of these measurements. As previously mentioned, the in-house MATLAB code was used to calculate the per stroke triboelectric charge and frictional energy dissipation, in addition to the time averaged friction coefficient. A diagram of the typical expected output from this configuration of the UMT-TENG apparatus is given in Figure 3-1.

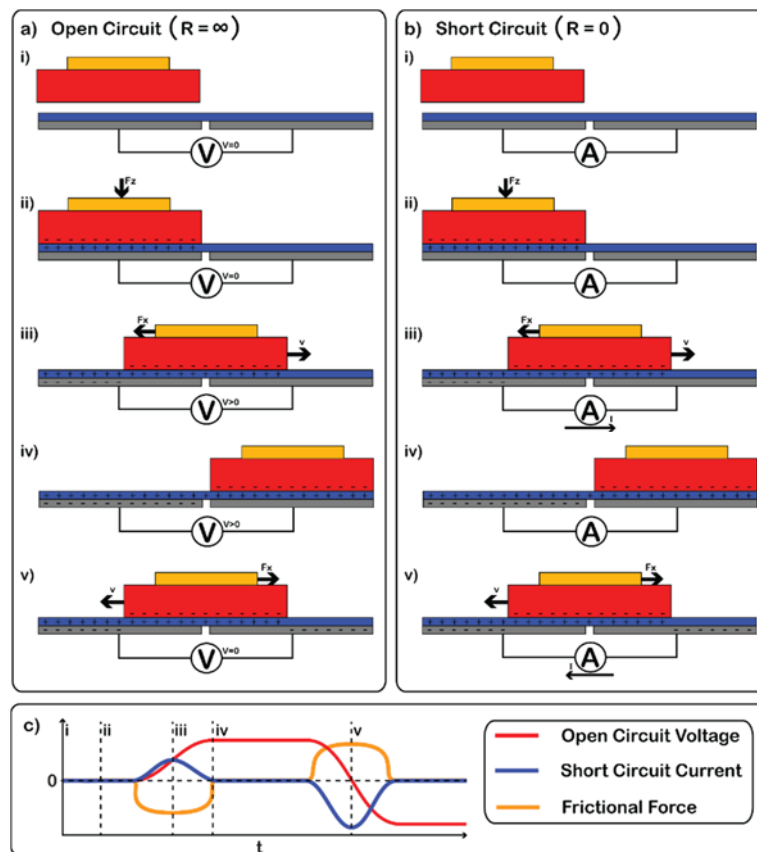


Figure 4-2 – Side-on diagram of a polymer-on-metal laterally-sliding freestanding-triboelectric-layer triboelectric nanogenerator (F-TENG) at subsequent stages of operation (i) before contact, (ii) first contact, (iii) mid-first-stroke, (iv) end-stroke, (v) and mid-stroke. The positions of trapped and mobile charges are given for open circuit (a) and short circuit (b) configuration, and the respective electronic outputs (c). Depicting the output voltage (red) and current (blue) for both (c). The red block represents an electronegative material, whereas the grey blocks denote an electropositive conductor, the blue layer represents an electropositive insulator, and the gold block denotes the UMT-TENG 2D load cell.

4.1.3 Sample Preparation

The Teflon samples for this study were textured using the aforementioned grinding process with 600 grit SiC grinding pads. The topographical parameters of the resulting surfaces are given in Table 11, with height maps provided in Figure 4-3. The Nylon sheet samples were manufactured using an extruding process and were provided by Goodfellow (product code AM30-FM-000300 as of publication). These sheets remained untextured for the testing procedure, with topographical parameters and height maps given in Table 11 and Figure 4-4 respectively.

Table 11 – Sample Surface Topographies for the Polymer on Polymer F-TENG contact

<i>Material</i>	<i>S_a (nm)</i>	<i>S_q (nm)</i>	<i>S_{Δa}</i>	<i>S_{Δq}</i>	<i>S_{sk}</i>	<i>S_{ku}</i>
Teflon (600 grit)	1238	1630	0.29	0.40	- 0.12	5.66
Nylon Sheet	278	353	0.05	0.07	- 0.49	3.87

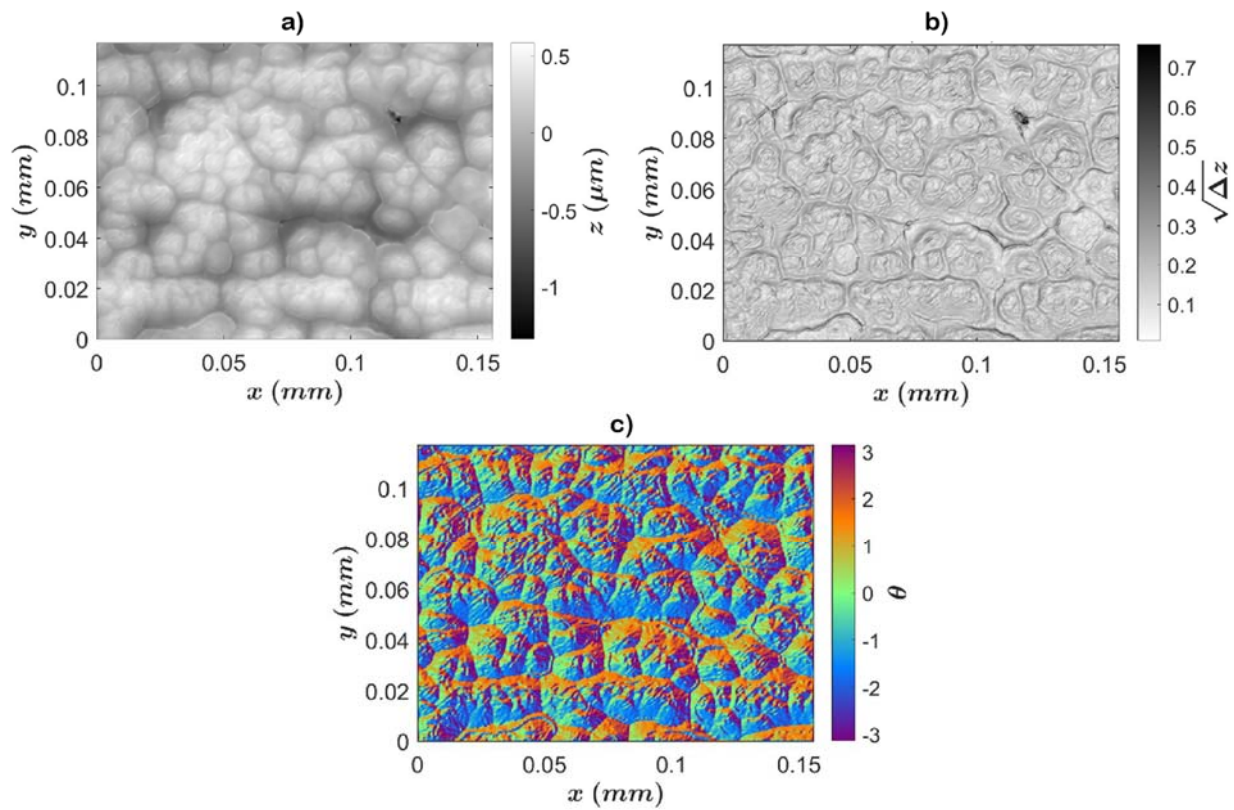


Figure 4-3 – Example topography of the Nylon Film surface, measured using white light interferometry.

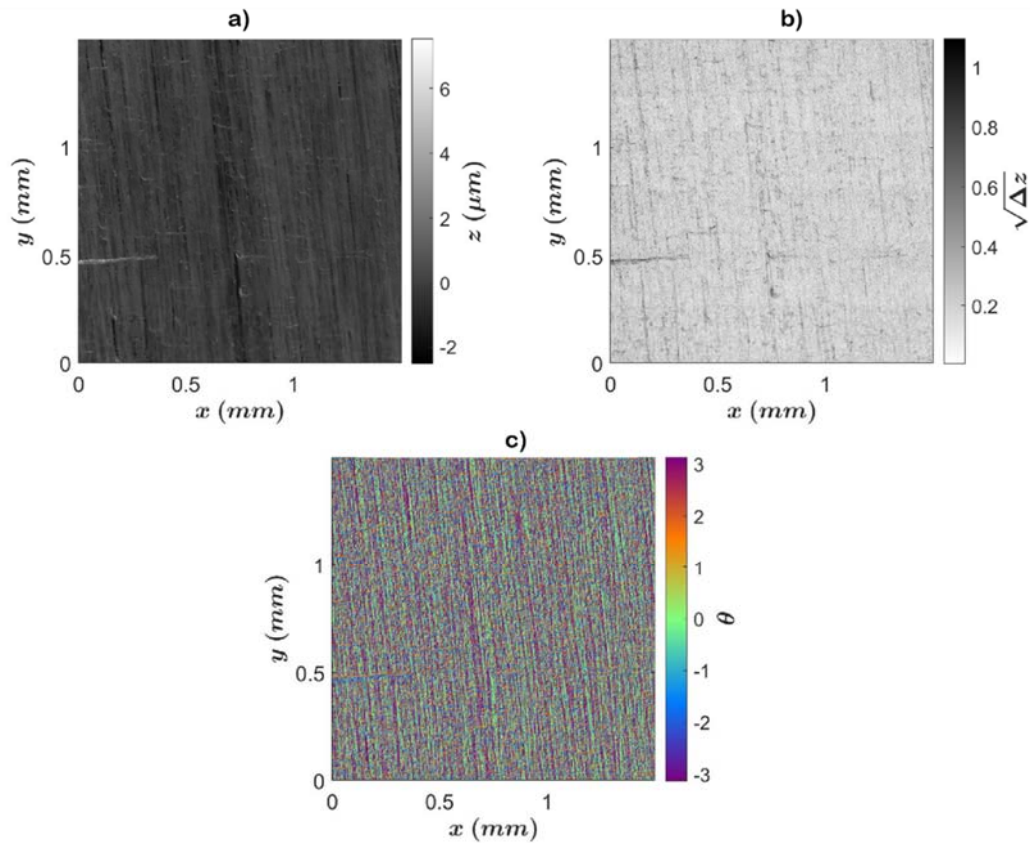


Figure 4-4 – Example topography of the ground Teflon surface, measured using white light interferometry.

Before examination and testing, the relevant Teflon surfaces were textured using a rotary grinding rig and 600 grit silicon carbide abrasive paper. This texturing was performed in order for them to exhibit consistent roughness parameters and to eliminate the influence of surface texturing between tests. The texture of the Nylon sheets were left unaltered from their manufactured state as upon examination they exhibited a suitably consistent topography between individual samples. The relevant mechanical and electronic properties for these polymers are given in Table 2.

4.1.4 Testing Procedure

Different reciprocating frequencies were used for this study as a method for investigating the influence of lateral sliding speed on triboelectric charging. The lower assembly – containing the electrodes and Nylon layer – was reciprocated using the UMT's REC drive at both 0.1 Hz and 2.5 Hz at a stroke length of 27 mm during tests, giving mid-stroke maximum velocities of 17 mms^{-1} and 424 mms^{-1} respectively. A stroke length of 27 mm was used in order to account for the 2 mm lateral spacing of the 25 mm electrodes. Samples were reciprocated for 28.8 minutes for each 2.5 Hz test and for 12 hours for each 0.1 Hz test, each lasting 4320 cycles. The total travel distances of these tests are 216 m. A two-dimensional load cell was used to monitor both the applied load and frictional force during tests. The feedback loop was also used to keep the applied load constant through each test, accounting for both material wear and sample deflection. These tribological tests were conducted under applied loads of 5 N, 10 N, 20 N, and 40 N as a method to investigate the relationship between applied load and triboelectric charging in greater detail.

The friction and current responses for the F-TENG contact under all combinations of tribological conditions were then examined and compared.

4.2 Results and Discussion

Upon comparison of the friction and electric responses it becomes clear that both applied load and lateral sliding speed have a strong influence on both. The following section displays the friction response and electric response for tests under varying applied load and sliding reciprocating frequency, as well as describing the relationships that are observed.

4.2.1 Friction Response

It is evident that both the applied load and reciprocating frequency affects the friction response over time for these contacts upon comparing the friction responses from the aforementioned tribological tests. The friction responses for tests at 0.1 Hz and 2.5 Hz are given in Figure 4-5a and Figure 4-5b respectively. The trends that are generally observed across all tests are first described, followed by the specific trends that result from the influence of applied load and lateral sliding speed. The most notable characteristic is the time-dependent nature of these friction responses. The majority of tests under all conditions exhibit an initial stage where the friction coefficient changes notably within the first few minutes of testing, followed by a second stage where the friction coefficient tends back towards its initial value to a small degree. These stages indicate an initial wear-in phase of the contact, where surface deformation and material wear occurs at an expedited rate until a more stable state is reached within the contact and these processes tend to decelerate. The only exception to this particular trend is the friction response from the 0.1 Hz test under 10 N normal load. This test instead exhibits an initial increase in friction coefficient which decelerates over time until a more stable value is reached. This friction coefficient value of 0.22 is higher than the values taken at similar times for tests under 5, 20, and 40 N; which range between 0.12 - 0.17.

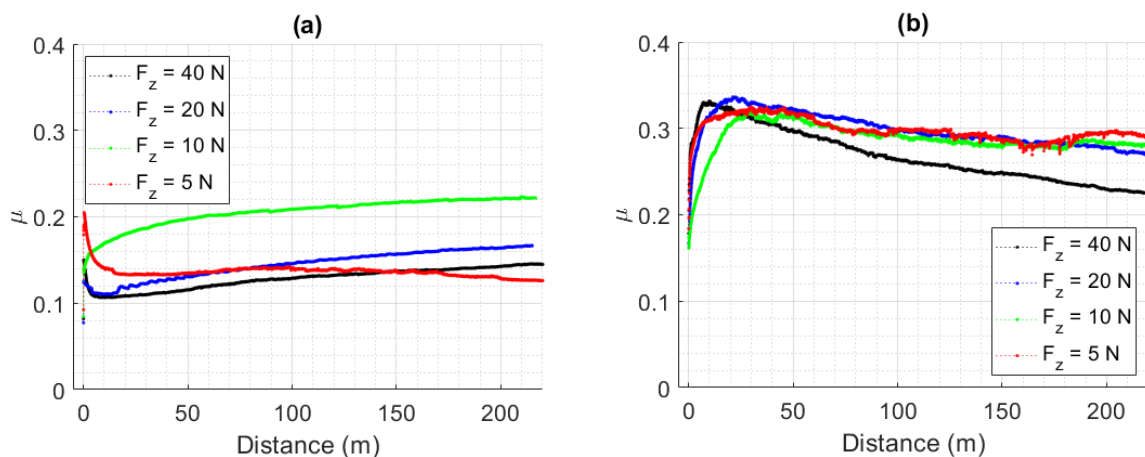


Figure 4-5 – Friction coefficient over time for the Teflon-Nylon UMT-TENG contacts, reciprocated at 0.1 Hz (a) and 2.5 Hz (b) under varying applied loads.

An estimation of the energy imparted to the contact via friction for every stroke across the test duration can be calculated by integrating the frictional force across F_x the stroke displacement $x(t)$ as shown below. These energy values were plotted across the total sliding distance for each test in a similar fashion to friction coefficient, and are displayed in Figure 4-6. Upon examination of the data it is clear that the energy imparted via friction across every half-cycle (forward or reverse stroke) increases with both applied load and lateral sliding speed. The energy imparted also evolves in an identical fashion to friction coefficient with respect to sliding distance.

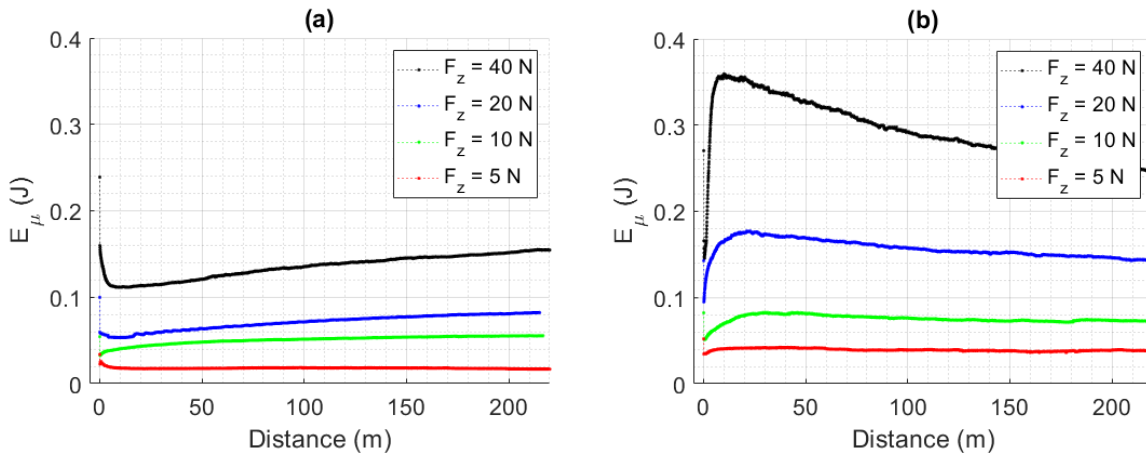


Figure 4-6 – Energy dissipated via friction per stroke over time for the Teflon-Nylon UMT-TENG contacts, reciprocated at 0.1 Hz (a) and 2.5 Hz (b) under varying applied loads.

4.2.1.a Reciprocating Frequency

The frequency at which the Teflon sample is reciprocated across the Nylon surface is shown to have a profound effect on the friction response. Tests conducted at 0.1 Hz exhibited a lower friction coefficient than those conducted at 2.5 Hz, implying that the Teflon-Nylon contact gives less frictional resistance at slower lateral sliding speeds. The lowest friction coefficient of 0.106 was achieved by the test conducted at 0.1 Hz under a 40 N applied load after 12 m of sliding, whereas the highest friction coefficient of 0.337 was observed during the test conducted at 2.5 Hz under a 20 N load after 42 m of sliding. The lower friction coefficients observed for tests at lower sliding speeds may also be evidence of reduced rates of material wear due to its strong dependence on sliding speed (Biswas and Vijayan, 1992).

The friction coefficient also evolved in a different fashion over tests conducted at 0.1 Hz to tests conducted at 2.5 Hz. At 2.5 Hz reciprocation frequency all contacts exhibited an initial rise in friction coefficient, reaching a similar maximum value of 0.32 ± 0.015 within the first 50 m of sliding. After reaching this peak value, the friction coefficient was shown to lower gradually over the remainder of each test. This has previously been observed in our previous research in linking material wear to triboelectric charging (Armitage et al., 2022). At 0.1 Hz reciprocation frequency all contacts exhibited an initial drop in friction coefficient, followed by a more gradual rise for the remaining test duration.

These contacts do not appear to reach a steady-state after the full 12 hours of testing and indicate that the friction coefficient will continue to rise at a decreasing rate over time beyond this point. These two-stage friction responses are evidence of a mechanism becoming activated during the initial stages of

testing. The particular mechanism in question is that of PTFE transfer layer formation on the Nylon surface. The energy imparted via friction per stroke is shown to be influenced by reciprocating frequency and sliding speed in an identical fashion to the friction coefficient for each test, with tests conducted at lower sliding speeds exerting less energy into the contact per stroke than tests at higher sliding speeds.

4.2.1.b Applied Load

The most notable influence of applied load on the friction response of the 2.5 Hz contacts was that higher applied forces expedited the decrease in friction coefficient after the initial peak value is reached. The contacts under the highest applied load of 40 N also reached a peak value of friction coefficient earlier than tests at lower applied loads. Under a reciprocating frequency of 0.1 Hz, the applied load also influenced the friction response of the contact. Under a low load of 5 N, the friction coefficient stabilises around 0.13 rather than increasing over time. Under higher applied loads, the initial drop and subsequent increase in friction coefficient becomes exaggerated. It is clear that the energy imparted into the contact is directly proportional to the applied load to the contact, with tests being conducted under higher loads being shown to exert more energy to the contact than tests under lower loads.

4.2.2 Electric Response

Firstly, upon examining the polarity of current with respect to relative sample velocity, it was clear that a negative charge had developed on the Teflon surface for all contacts. This charge polarity is in agreement with previous research into triboelectric charging with Teflon and Nylon, both against control counter surfaces and each other (Diaz and Felix-Navarro, 2004).

The total charge that passes through the electrometer during each stroke is measured and plotted against the stroke number across the duration of each test. The stroke numbers for these data were then translated into the equivalent total distance travelled by the Teflon block across the Nylon surface up to that particular stroke. The resulting data are now presented in Figure 4-7 to describe the evolution of contact charge over sliding distance for each test.

The triboelectric charge density present within the contact, as well as the rate at which it varies in magnitude across the duration of each test, is shown to also be dependent on various tribological factors in addition to surface composition. Triboelectric charge accumulation over time was observed under all testing conditions. Every test exhibited an initial phase of charge accumulation within the contact, the rate of charge accumulation and the maximum charge accumulated being dependant on the sliding speed and applied load respectively.

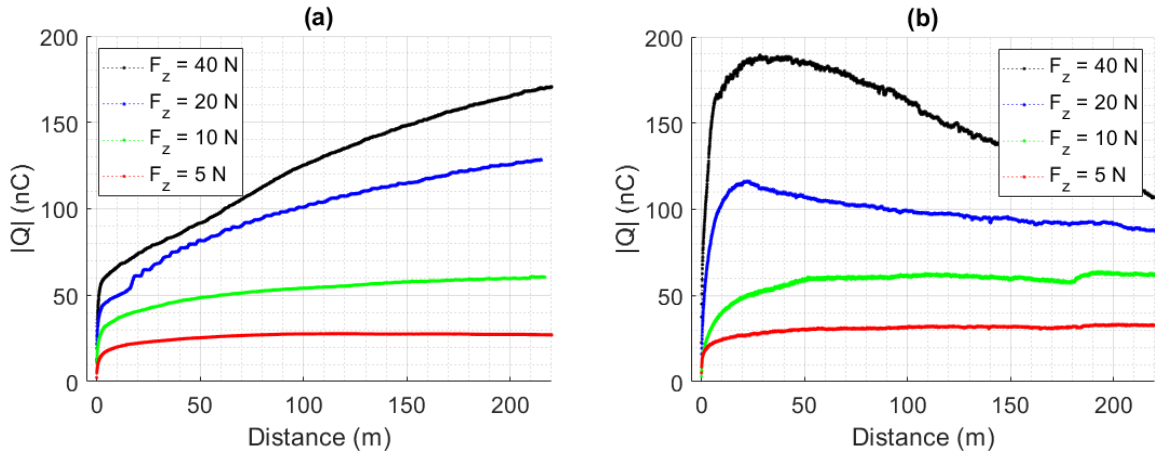


Figure 4-7 – Contact charge over time for the Teflon-Nylon UMT-TENG contacts, reciprocated at 0.1 Hz (a) and 2.5 Hz (b) under varying applied loads.

4.2.2.a Reciprocating Frequency

Tests conducted at 2.5 Hz all exhibit a charge accumulation and dissipation pattern that correlates with the frictional energy dissipation, which can be seen upon comparison of Figure 4-6 and Figure 4-7. The reason behind this particular phenomenon has previously been explained by our previous findings as being caused by the formation of a PTFE transfer layer on the Nylon counter surface. However, tests conducted at 0.1 Hz show a steady accumulation of charge over a significantly longer amount of time. A saturation charge density is only reached under 5 N after 2000 cycles and 200 m of sliding, whereas the charge density continues to grow beyond 4320 cycles under higher loads.

Upon comparing tests at 0.1 Hz and 2.5 Hz it becomes clear that increasing the reciprocating frequency of the Teflon block, and therefore the average relative sliding speed, increases the rate at which triboelectric charge is accumulated within the contact. The reasoning behind this could be one of two things. The first possibility is that the exposed Nylon surface is quickly able to regain surface electrons upon being exposed to air, after donating them to the Teflon counter-surface. This implies that a faster reciprocating frequency would lead the Nylon surface to be able to donate electrons at a faster rate, provided that the timescale of electron replenishment is significantly smaller than the reciprocation period.

4.2.2.b Electrostatic Charge Dissipation

To investigate the plausibility of this mechanism of charge replenishment, a non-contact reciprocating test was conducted with the apparatus. The previously triboelectrically charged Nylon surface was held 0.5 mm out of contact from the conductive electrodes and reciprocated at 2.5 Hz for 1 minute. The findings from this test are shown in Figure 4-8, where an exponential decay in surface charge is shown with a timescale of 16.5 ± 1 s. The equation used to describe this exponential decay in charge is stated in (4-1).

$$Q(t) = Q_0 e^{-\frac{t}{\tau}} \quad (4-1)$$

These findings eliminate the possibility that electron replenishment is the cause for the acceleration of triboelectric charging, purely as the observed charge replenishment timescale is too large to significantly affect contact testing. This test was also repeated for triboelectrically charged Teflon and Delrin surfaces

to find that the time constant for charge dissipation differs between each material. Teflon was shown to retain surface charges for a considerably longer amount of time than both Nylon and Delrin. The measured charge dissipation time constants for each material are displayed in Table 12.

Table 12 – Measured electrostatic charge dissipation time constants for polymer surfaces.

<i>Material</i>	τ (s)
Nylon	16.5 ± 1
Delrin	120 ± 5
Teflon	3360 ± 30

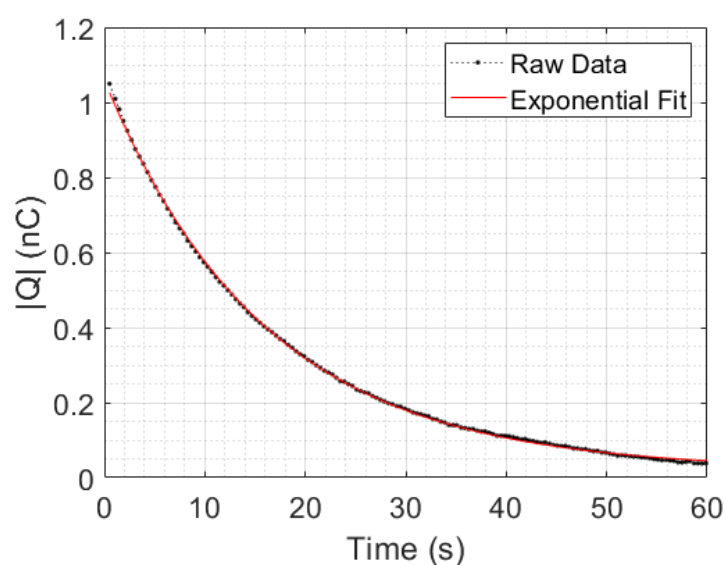


Figure 4-8 – Electrostatic surface charge over time for an example Nylon surface exposed to the ambient atmosphere.

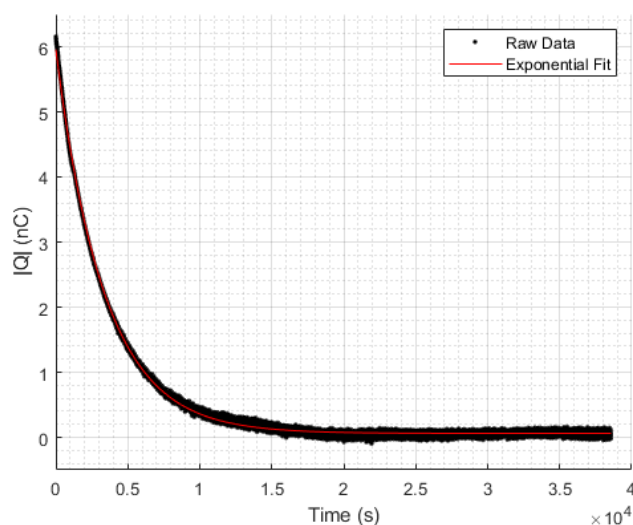


Figure 4-9 – Electrostatic surface charge over time for an example Teflon surface exposed to the ambient atmosphere.

The alternative cause for this acceleration of charge accumulation could be the dissipation of kinetic and thermal energy through the contact via the generation of phonon wavelets during sliding friction. The creation of these phonon wavelets causes surface electron-phonon interactions, which in turn gives electrons in high energy states an additional amount of energy to assist with overcoming the energy barrier of the material interface. This would imply that the nature of the contact itself is expediting triboelectric charge transfer rather than the replenishment of triboelectrically vacated donor states. A further detailed explanation of this is given in accompaniment with the analytical model in 4.3.1.c Friction Contribution.

4.2.2.c Applied Load

The applied load to the contact is also shown to influence the accumulation of triboelectric charge. Existing theories on the modelling of TENG devices have predicted that increasing the applied load results in an increase in real contact area within the nominal contact in accordance to the aforementioned Persson's contact theory (Xu et al., 2020). This predicted increase in real contact area with applied load increases the area within the contact across which triboelectric charging can occur. It not only increases the number of available electron acceptor sites on the Teflon surface, but also brings more donor sites on the Nylon surface into real contact across the stroke length. The equivalent elastic modulus (Y^*) for the Nylon-Teflon contact is calculated to be 551 MPa through substituting the mechanical properties listed in Table 11 into equation (1-120). Values for the real areas of contact under each applied load are calculated using equation (1-123) and displayed in Table 13.

Table 13 – Real contact area values for the Teflon – Nylon F-TENG interface.

<i>Applied Load (N)</i>	<i>Real Area of Contact (A_r, m^2)</i>	<i>Real Area of Contact Ratio (A_r/A_n, %)</i>
40	2.8e-7	0.0226
20	1.4e-7	0.0113
10	7.1e-8	0.0056
5	3.5e-8	0.0028

It is important to note that these values for real contact area are calculated for the case of a static contact with no sliding motion involved. The introduction of sliding motion will act to significantly increase the total real area of contact on the Nylon surface as the Teflon surface slides across it, therefore the number of donor sites are also significantly increased. Sliding motion may also increase the total real area of contact across the Teflon surface due to variations in the topography of the Nylon surface across the stroke causing new asperities on both surfaces to come into and out of contact. The static values for real area of contact are plotted against the maximum measured charge under each corresponding applied load in Figure 4-10.

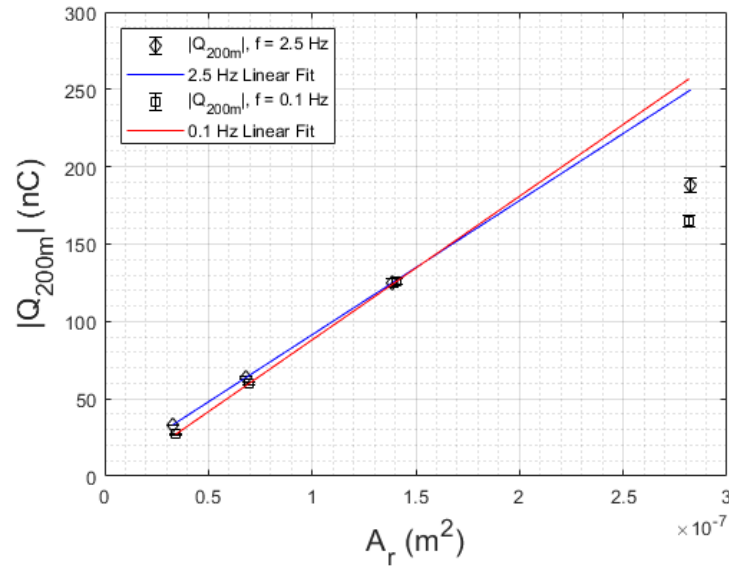


Figure 4-10 – Maximum contact charge achieved during the first 200 m of sliding plotted against calculated static real contact area for Teflon-Nylon UMT-TENG tests conducted at 2.5 Hz and 0.1 Hz under applied loads of 5 N, 10 N, 20 N, and 40 N.

A linear relationship between A_r and Q_{200m} is observed between 5 N and 20 N, with a gradient of $0.90 \pm 0.04 \text{ Cm}^{-2}$ and intercept of $0 \pm 5 \text{ nC}$. At 40 N, a lower charge is observed than what would be expected if charge density within the real area of contact is assumed to be independent of applied load. This implies that the maximum charge density arising from an increase in applied load is more than just a result of a resulting increase in real contact area.

4.3 Semi-Analytical Model

Combining the observed relationships between contact charge, reciprocating frequency, and applied load; it is possible to derive a semi-analytical model that may predict the outcome of future tests on frictional electrification.

This model is dependent on the following criteria being met.

1. The contact is assumed as occurring in vacuo, in order to avoid complications introduced by triboelectric charge transfer between a charge carrying or conductive ambient medium.
2. Electrons are the only triboelectric charge carrier, implying that no triboelectric ion transfer occurs across the contact.

As per our second criteria, the primary mechanism for triboelectric charge transfer for these contacts is hypothesised to be the quantum tunnelling of electrons from high energy ‘donor’ molecular orbitals within the Nylon surface to unoccupied low energy ‘acceptor’ orbitals within the Teflon surface as a method of establishing local thermodynamic equilibrium across the contact. Since the driving force behind triboelectric electron transfer between conductors is known to be the difference in respective fermi energies of the contacting surfaces, it is reasonable to assume that the driving force behind triboelectric charge transfer between insulating polymers is the difference in energy between the relevant acceptor and donor orbitals and their respective state densities.

We hypothesise that triboelectric charge transfer is expedited by the injection of kinetic energy to the relevant electron donor orbitals. We predict this energy to be provided by electron-phonon interactions with friction produced phonon wavelets. Additionally, the maximum triboelectric charge density that can be achieved within the contact may also be enhanced by strain gradients within the contact through a flexoelectric material response (Mizzi and Marks, 2022). This may possibly explain the larger observed charge densities that can be explained through solely an increase in real contact area. In order to produce a model which can affectively predict triboelectric charge densities in the presence of tribological mechanisms, it is important to first understand the individual contributing roles of unperturbed charge accumulation as well as the ramifications of friction and wear involvement.

4.3.1 Theory

Historically, since it has been reasonable to assume that triboelectrification between surfaces could effectively be modelled in a similar fashion to a traditional linear capacitor (Harper, 1951b). The magnitude of triboelectric charge present on an insulating surface during non-sliding mechanical contact with another surface over time may be hereby expressed as in equation (1-2). The equation is exponential in form, denoting a build-up of triboelectric charge density up to a critical saturation value Q_{max} , above which it is no longer energetically favourable for triboelectric charge transfer to occur. As charge is transferred across the contact, an electric field is generated by the growing charge densities on the contacting surfaces. As more charges are transferred, a greater a Coulomb repulsion is experienced which acts to inhibit further charge transfer until no further charge may be transferred.

Localised triboelectric transfer for each individual charge carrier can be treated as instantaneous, with a probability of occurrence being dependant on the overlapping of the relevant donor and acceptor electron orbital wavefunctions and their relevant energies. As this mechanism is scaled up to the macroscale, its probabilistic nature can be treated as a time constant τ_0 . This constant must account for the timescale over which charge transfer across a single site would occur, as well as the rates at which transfer sites are introduced and removed.

4.3.1.a Charge Saturation Value

The maximum charge value can be seen as a function of the contact capacitance C_c and the contact potential difference V_c . The contact capacitance can then be expressed as a function of the geometry of the contact as well as its electric permittivity, and the contact potential difference can be expressed in terms of the relevant energies involved.

$$Q_{max} = C_c V_c = \frac{\epsilon A_r \Delta\phi^*}{z_0 e} \quad (4-2)$$

$\Delta\phi^*$ is expressed as the difference in 'effective' work function between the two contacting mediums, ϵ is the permittivity of the ambient medium through which the charge is being transported, A_r is the real area of contact between the two surfaces, through which triboelectric charge transfer can occur, z_0 is the separation distance across which the charge is being transported, and e is the elementary electronic charge of $1.6e^{-19}$ C.

The nature of $\Delta\phi^*$ can be expressed in terms of the energy barriers they must first overcome to leave the donor surface, subtracted from the energies they then release once they relax into the acceptor state of the counter-surface. These terms can be treated as an 'effective work function' of the respective donor and acceptor surfaces to give a difference in electrochemical potential ($\Delta\bar{\mu}$) in the absence of external electric fields.

$$\Delta\bar{\mu} = \phi_D^* - \phi_A^* \quad (4-3)$$

These terms can be expressed as their respective differences in energy level. The work function of an insulator can be treated as the difference in energy between the vacuum state directly outside the surface, and the highest occupied molecular orbital (HOMO). The electron affinity of an insulator can be treated as the energy difference between the vacuum state and the lowest unoccupied molecular orbital (LUMO).

4.3.1.b Flexoelectric Contribution

The presence of inhomogeneous stress fields within contacting surfaces have been shown to drive triboelectric charge transfer within static contacts. Therefore it is reasonable to assume that within sliding contacts, the presence of significant tangential stresses and shear strains in addition to existing normal stresses can significantly alter surface electron states. The strain fields in the presence of both normal and tangential applied loads are yet to be mathematically calculated. However, a crude approximation can at least be made in order to give an estimation for the contribution of tangential loads.

$$F = \sqrt{F_z^2 + F_x^2} = \sqrt{F_z^2(1 + \mu^2)} \quad (4-4)$$

F_z and F_x are the normal and tangential components of the applied load, and μ is the friction coefficient of the contact. The two contacting surfaces can be treated as a collection of contacting asperities, which in turn can be treated as a collection of individual Hertzian contacts of varying radii. The two contacting asperities for each contact can be treated as a sphere-on-sphere contact rather than the previously mentioned sphere-on-flat for flexoelectric models. The Hertzian radii used here is therefore an effective average radius, averaged across the possible values across the contact and treated as a composite 'effective' radius of the contact geometry (R^*).

$$\frac{1}{R^*} = \frac{2}{\langle R_D \rangle} + \frac{2}{\langle R_A \rangle} \quad (4-5)$$

$\langle R_D \rangle$ and $\langle R_A \rangle$ are the average asperity radii for the donor and acceptor surfaces respectively. These radii can be roughly approximated by dividing the mean arithmetic roughness for each surface (S_{a_i}) by its respective mean arithmetic gradient ($S_{\Delta a_i}$).

$$R_i \approx \frac{S_{a_i}}{S_{\Delta a_i}} \quad (4-6)$$

$$\therefore \frac{1}{R^*} = 2 \left(\frac{S_{\Delta a_D}}{S_{a_D}} + \frac{S_{\Delta a_A}}{S_{a_A}} \right) \quad (4-7)$$

The elastic moduli of the two contacting surfaces are also condensed into an equivalent elastic modulus Y^* which is previously expressed in (1-120). The force applied to each asperity within the contact (F_a) can

be related to the total applied load to the contact (F) by relating both to the average pressure across the contact ($\langle P \rangle$).

$$\langle P \rangle = \frac{F}{A_r} = \frac{F_a}{\pi a^2} \therefore F_a = \frac{F \pi a^2}{A_r} \quad (4-8)$$

Rearranging equation (1-99) for F_a yields the following expression.

$$F_a = \frac{4Y^* a^3}{3R^*} \quad (4-9)$$

The dependency on Poisson's ratio is eliminated through the definition of equivalent elastic modulus. Equating (4-8) to (4-9) yields the following expression for a .

$$a = \frac{3\pi F R^*}{4A_r Y^*} \quad (4-10)$$

Substituting (4-10) back into (4-8) yields a final definition for F_a , dependant purely on macroscale properties.

$$F_a = \left(\frac{3R^*}{4Y^*} \right)^2 \left(\frac{\pi F}{A_r} \right)^3 \quad (4-11)$$

This definition is in turn substituted into Mizzi and Marks' original equation (1-107) to give an expression for the flexoelectric perturbation in surface potential.

$$V_{FxExi} = -\xi V_f \sqrt[3]{\frac{F_a}{(1-\nu^2)R^2Y}} = -\xi V_{fi} \frac{F\pi}{A_r Y^*} \sqrt[3]{\frac{9}{16} R^*} \quad (4-12)$$

V_{fi} is the flexoelectric voltage of the material being considered, and ξ is a dimensionless constant to account for the graphical nature of (1-107), which may be incorporated into V_{fi} . This particular model however does not take into account the relevant shear moduli (G_i) of the materials involved, which is a key characteristic to be considered for sliding contacts. Therefore a more complete model that accounts for the presence of a tangential load and the respective shear moduli of the contacting materials would provide a considerably more accurate approximation of the flexoelectric perturbations that are present within sliding contacts. The perturbations can be included into the contact potential difference term in equation (4-2), giving the definition of a flexoelectrically perturbed $\Delta\bar{\mu}'$ to be as expressed below.

$$\Delta\bar{\mu}' = \phi_D^* + V_{FxExD} - \phi_A^* - V_{FxExA} \quad (4-13)$$

4.3.1.c Friction Contribution

Upon inspection of our charge accumulation data for contacts under varying reciprocating frequencies, it appears to be plausible that the rate at which triboelectric charge accumulation occurs can be stated as a function of the energy flux density imparted into the donor surface via sliding friction. This allows for expedition of charge accumulation to be attributed to the generation of friction phonon wavelets. The total energy imparted via friction to the contact per stroke is the integral of the frictional force F_x across the stroke, as previously explained. If the assumption is made that a constant frictional resistance is met, and that pure sliding friction occurs across the entirety of the stroke with a constant friction coefficient, this

energy can then be approximated as the product of the applied load F_z , friction coefficient μ and stroke length Δx .

$$E_\mu \approx \mu F_z \Delta x \quad (4-14)$$

The resulting flux density of energy imparted via friction can then be approximated by dividing this energy value by the real area of contact and the time taken for this energy to be imparted. The expedited triboelectric charging, resulting from the introduction of this additional energy via electron-phonon interactions, may be represented as a modification of Harper's original time constant τ_0 for charge accumulation. This perturbed time constant (τ') for triboelectric charge accumulation can therefore be expressed as below.

$$\tau' = \tau_0 \left(1 - \beta \frac{2\mu F_z \Delta x f}{A_r} \right) \quad (4-15)$$

τ_0 is the unperturbed timescale constant that represents triboelectric charge transfer under static contact, β is introduced as a dimensionless proportionality factor. The influence of friction on the saturation charge density value is negligible within the context of this model, however it is important to note the influence of frictional heating on the Fermi-Dirac distribution of electrons and resulting thermionic emission (Wang et al., 2020). The charge saturation value can now also be viewed from a more dynamic perspective. At the saturation value, the mechanisms of triboelectric charge transfer and electrostatic discharge are in equilibrium. If frictional excitation causes the triboelectric transfer of additional charge, said charge is expected to be discharged back to its surface of origin. Conversely, if electrostatic discharge occurs within the contact, triboelectric charge transfer is expected to occur between the newly-formed acceptor-donor site pairs to regain local thermodynamic equilibrium.

4.3.1.d Material Wear Contribution

The effects of material wear are far too significant to be ignored when considering the plausibility and longevity of industrial triboelectric applications. These effects have been observed experimentally, both in this study and in previous investigations (Armitage et al., 2022). The results of which give insight into how they may be incorporated into a model such as this. Firstly, the context of polymer tribology the development of a transfer layer within the contact will diminish over sliding distance the total area across which triboelectric charge transfer may occur (Wang and Yan, 2006). According to previous research into the development of these films it can be reasonable to approximate this reduction in available area as an exponential decay. An exponential function is chosen as it is in reasonable agreement with existing research into zinc dialkyl dithiophosphate (ZDDP) tribofilm growth (Ghanbarzadeh et al., 2016).

$$A_r(|x|) = A_r e^{-C_{wear}|x|} \quad (4-16)$$

$|x|$ is the total sliding distance travelled and is in itself a function of time, dependent on the relative sliding velocity profile of the contact. The velocity profile of the UMT-TENG tribometer is sinusoidal, therefore it is difficult to express this distance as a discrete function since the indefinite integral of the magnitude of a trigonometric function such as $|\sin(t)|$ cannot be defined in terms of regular functions, without the creation of a Taylor or Fourier series. Instead, the assumption is made that the velocity profile comes in

the form of a square-wave as a way to simplify this equation and give a linear relationship between time, number of cycles N , and sliding distance.

$$|x| = 2\Delta x N = 2\Delta x f t \quad (4-17)$$

W is an arbitrarily defined wear constant, representing the sliding distance across which the contact must travel to exhibit a reduction in effective contact area by a factor of Euler's constant e . Incorporating this exponential representation of A_r into the previously derived equations for τ' (4-15) and Q_{max} (4-2) gives an exponential function, which in turn has an exponentially increasing time constant. This can instead be approximated by the combination of two separate exponential functions, one to represent the capacitive accumulation of triboelectric charge without the influence of wear, and the second to describe any changes in effective contact area resulting from material wear.

$$Q(t) = Q_{max} \left(1 - e^{\frac{-t}{\tau'}} - \zeta \left(1 - e^{\frac{-t}{\tau_{wear}}} \right) \right) \quad (4-18)$$

C_{wear} is now redefined as the wear-dependent time constant τ_{wear} , which can be expressed in terms of C_{wear} through the relationship between distance travelled over time, described in equation (4-17).

$$\frac{-t}{\tau_{wear}} = -C_{wear}|x| \div \tau_{wear} = C_{wear} \frac{d|x|}{dt} = 2\Delta x f C_{wear} \quad (4-19)$$

ζ is introduced as the dimensionless proportion of maximum transfer film coverage. This is included to account for the rate at which the transfer layer is also worn away, revealing new sites for triboelectric charge transfer. τ' is once again treated as though A_r is independent of time and purely a product of Persson's contact theorem.

4.3.1.e Full Equation

Combining the factors that account for flexoelectric perturbations, frictional excitation, and material wear, a final form of equation (4-18) can be presented as a function of measurable mechanical properties and their respective scaling coefficients.

$$Q(t) = \frac{\varepsilon A_r}{e z_0} \left(\phi_D^* - \phi_A^* + \xi (V_{fA} - V_{fD}) \left(\frac{\pi}{A_r Y^*} \right) (F_z^2 (1 + \mu^2))^{\frac{1}{2}} \left(\frac{9}{8} \left(\frac{S_{\Delta a_D}}{S_{a_D}} + \frac{S_{\Delta a_A}}{S_{a_A}} \right) \right)^{\frac{1}{3}} \right) \cdot \left(1 - \exp \left(\frac{-t}{\tau_0 \left(1 - \beta \frac{2\mu F_z \Delta x f}{A_r} \right)} \right) - \zeta \left(1 - \exp \left(\frac{-t}{2\Delta x f C_{wear}} \right) \right) \right) \quad (4-20)$$

4.3.2 Data Fitting

The dual exponential function as described by equation (4-18) has been fitted to the existing charge accumulation data to evaluate the validity of this model. Example raw data for each combination of testing parameter are plotted alongside their respective best exponential fits in Figure 4-11 and Figure 4-12, with the relevant fitting parameters presented in Table 14.

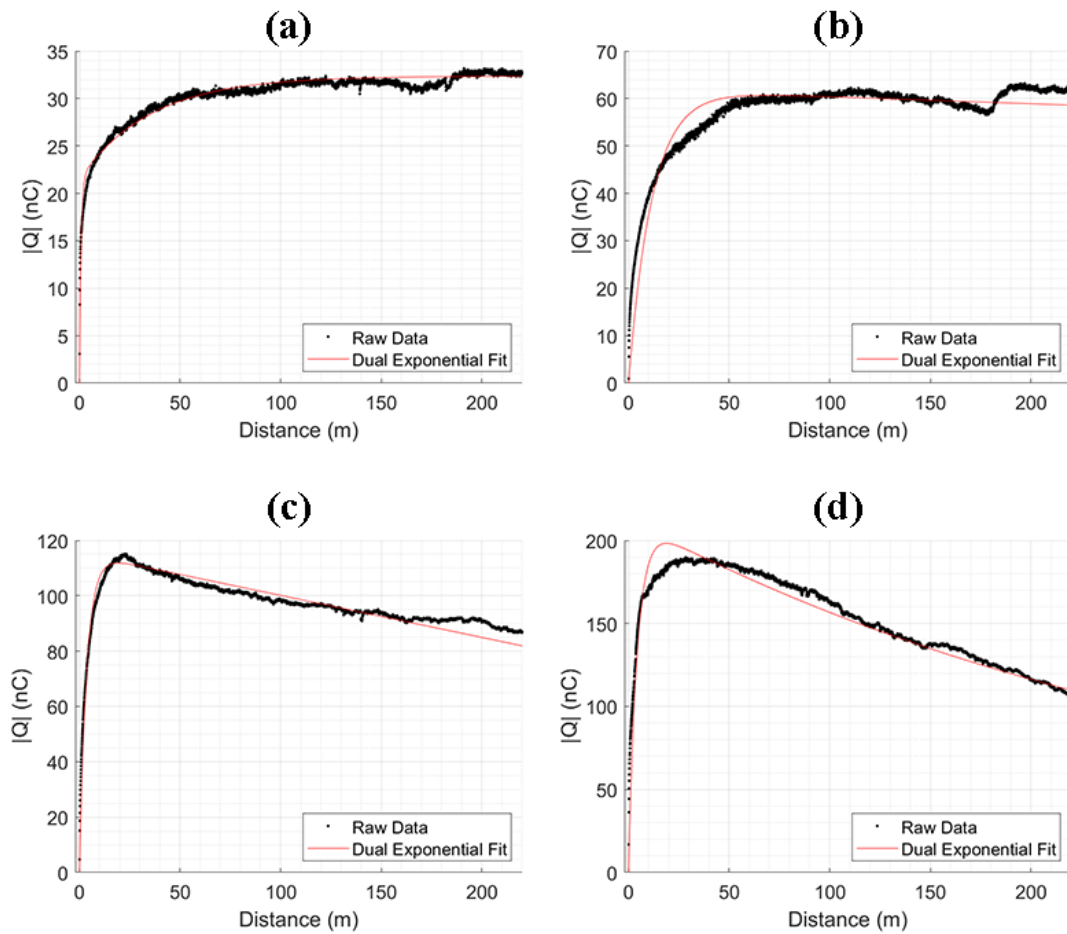


Figure 4-11 - Contact charge data (black) and exponential fit (red) over total sliding distance for tests conducted at 2.5 Hz under 5 N (a), 10 N (b), 20 N (c) and 40 N (d) applied load.

The exponential trend of charge accumulation becomes apparent upon examination of charge generation under higher sliding speeds. It becomes clear that a saturation charge density is reached at a certain point, and accumulation up to said point is shown to fit a single exponential term within a reasonable margin for error. At higher loads it is shown that the inclusion of a second exponential term can be used to describe the decay in charge density as the Teflon transfer film increases coverage on the Nylon counter-surface. The values of γ for tests conducted at 2.5 Hz and under applied loads of 10, 20, and 40 N are all close to or slightly less than 1. A γ value of 1 would imply that the total charge within the contact would completely vanish after an infinite amount of time as a total transfer film coverage is achieved. A γ value between zero and unity would imply that a steady state is reached where the rate of transfer film development is equal to the rate of its subsequent removal, giving a constant area of contact where triboelectric charges may be accumulated and retained.

Under the lowest applied load of 5 N, the charge accumulation trend can no longer be effectively modelled by a single exponential term. A more accurate estimation is given upon the introduction of a second exponential term, this second term contrasts with testing at higher applied loads however in the sense that it represents a secondary mechanism for charge accumulation rather than that of charge dissipation due to transfer film coverage. Another explanation for this deviation from perfectly capacitive charge accumulation may recall to the dependence of both A_r and μ on distance travelled within contact.

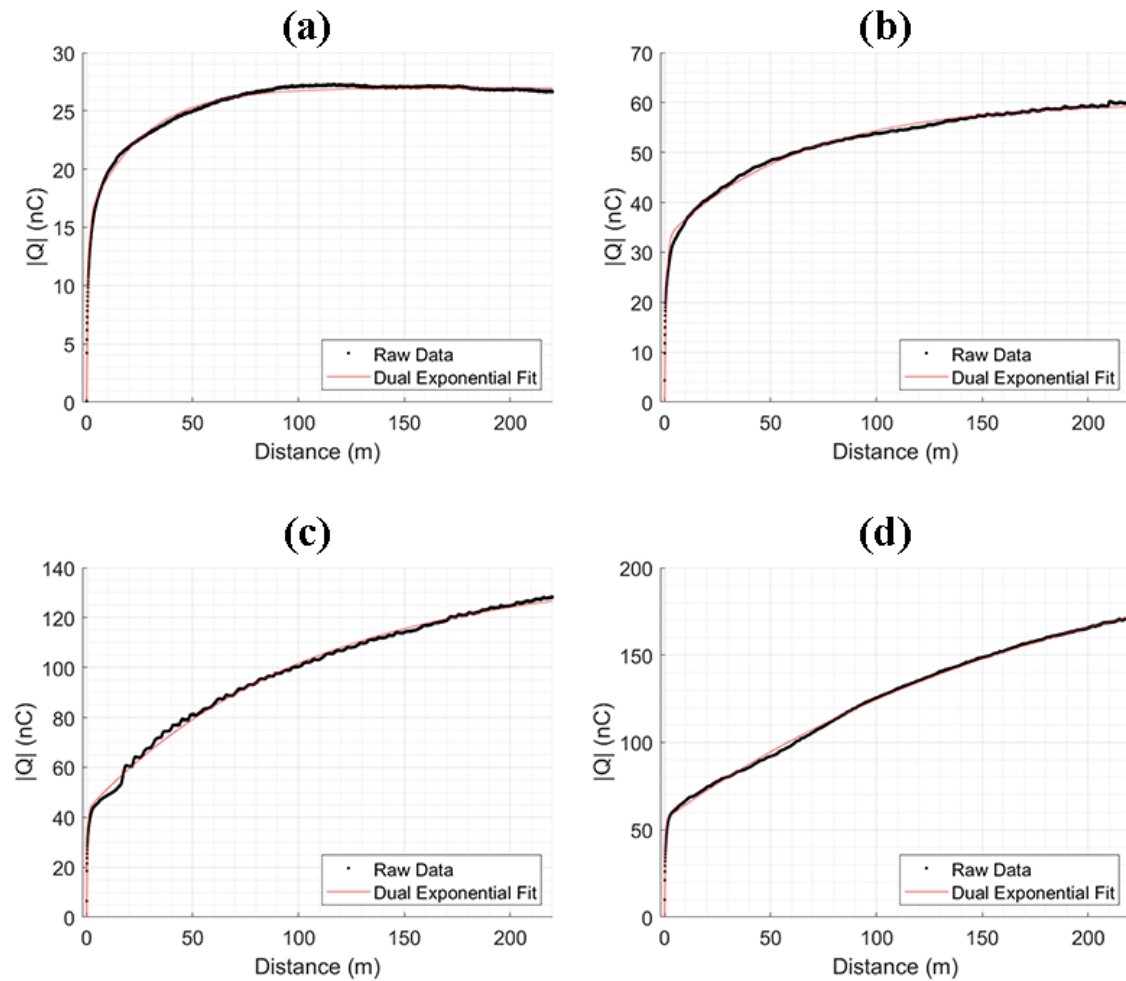


Figure 4-12 - Contact charge data (black) and dual exponential fit (red) over total sliding distance for tests conducted at 0.1 Hz under 5 N (a), 10 N (b), 20 N (c) and 40 N (d) applied load.

Upon initial examination of tests conducted at 0.1 Hz it becomes clear that although charge is accumulated over both time and sliding distance at a decreasing rate, the overall trend for charge accumulation does not appear to be easily described by a single exponential term to represent capacitive charging. Similarly to the 5 N test data at 2.5 Hz, the addition of a second exponential term can help to better describe this trend. These findings further suggest that a secondary mechanism affecting charge accumulation, operating over a separate timescale to triboelectric charging within a static contact, may be present within the sliding contact. The second exponential term included in these fits may still be used to represent a change in real contact area. Rather than describing a reduction in effective area of contact over time, due to an increase in transfer film coverage, the same term for these tests conducted under lower loads and sliding speed instead elude to an increase in real area of contact. The γ value for these fits are all less than zero, which implies that material wear is instead somehow contributing to charge accumulation.

When considering that these tests are conducted under lower applied loads and under lower sliding speeds, it is reasonable to assume that considerably less extreme material wear will be exhibited during these tests. This is validated by the complete lack of PTFE transfer film presence observed on all post-testing Nylon surfaces under these conditions, despite the presence of PTFE wear debris outside of the

contact. Therefore, the supposed increase in real area of contact during these tests may arise from a truncation of the contact topography as a result of abrasive wear and the subsequent removal of protruding asperities (Jeng and Gao, 2008). Since the Teflon surface is markedly rougher and softer than the Nylon counter-surface, it is reasonable to assume that it is the topography of the Teflon surface that becomes truncated more so than the Nylon surface. This explains the presence of PTFE wear debris despite the absence of a PTFE transfer film within the contact. From these findings it is reasonable to assume that the milder tribological conditions within these contacts produce far fewer phonon wavelets through friction, and therefore exhibit a lower increase in local temperature which has been shown to contribute to PTFE transfer film adhesion and growth (Wang and Yan, 2006).

Table 14 – Exponential fitting parameters for contact charge accumulation tests under varying tribological conditions

f (Hz)	F_z (N)	Q_{max} (nC)	τ' (s)	γ	τ_w (s)	R^2
0.1	5	15.7	171	- 0.7	$0.5e^4$	0.98
0.1	10	19.6	165	- 0.8	$1.2e^4$	0.99
0.1	20	35.7	81.1	- 3	$2.1e^4$	0.83
0.1	40	55.8	80	- 3	$3.7e^4$	0.99
2.5	5	21.5	6.3	- 0.5	270	0.93
2.5	10	86.6	90.1	1	$3.2e^4$	0.83
2.5	20	121	32.1	0.95	$3.7e^4$	0.96
2.5	40	214	33.5	0.9	$2.3e^4$	0.98

Upon examination of the fitting parameters for each test, the first observed relationship is the correlation between A_r and the theoretical enhanced saturation charge value, Q_{max}' . γ is only included in the calculation of Q_{max}' if the second exponential term contributes to charge accumulation as shown below.

$$Q_{max}' = \begin{cases} Q_{max} & \text{if } \gamma < 0 \\ (1 + \gamma)Q_{max} & \text{if } \gamma \geq 0 \end{cases} \quad (4-21)$$

This value for Q_{max}' is plotted against its corresponding value for calculated real area of contact (A_r) using Persson's contact theorem (1-123) and is displayed in Figure 4-13. The average gradient between the linear fits of the 0.1 and 2.5 Hz data is similar that of the peak contact charge trend in the experimental data, being $0.77 \pm 0.05 \text{ Cm}^{-2}$ with an intercept of $10.3 \pm 3 \text{ nC}$. This reinforces the notion that the contact charge is accumulating exponentially up to a peak value, and implies that material wear is the cause of the deviation observed at 40 N for the experimental data in Figure 4-10. The existence of an intercept value for this relationship however implies that triboelectric charge transfer may still occur across an interface that has no real area of contact, i.e. no available sites for charge transfer to occur. This may be an artefact arising from the relatively short test duration. An element of difficulty is introduced in accurately measuring the maximum charge value, since most tests conducted at 0.1 Hz do not reach a saturation charge by the test termination and significant material wear quickly diminishes the charge during tests conducted at 2.5 Hz.

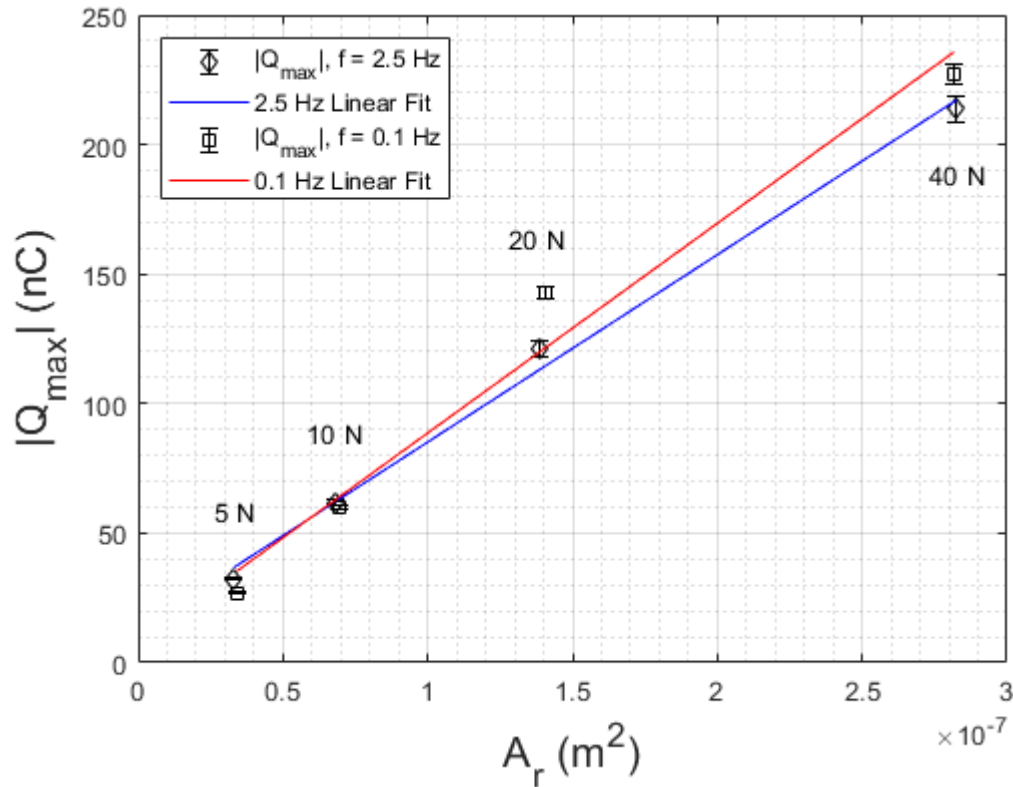


Figure 4-13 – Exponential fitting parameter Q_{\max} versus calculated A_r for Teflon-Nylon UMT-TENG tests conducted at 2.5 Hz and 0.1 Hz under applied loads of 5 N, 10 N, 20 N, and 40 N.

Although no linear relationship can be gauged between sliding speed and the charge accumulation time constant, all tests conducted at 2.5 Hz exhibit smaller time constants than their respective tests at 0.1 Hz. Upon examination of tests conducted at 2.5 Hz it may be possible to draw a relationship where a higher applied load yields a smaller time constant, although testing at a wider range of reciprocating frequencies would be needed to verify this claim.

4.4 Conclusions

To summarise our findings,

- ❖ Experimental evidence has been provided that the introduction of energy via electron-phonon interactions from friction-produced phonon wavelets can expedite triboelectric charge transfer between insulating polymers in sliding contact.
- ❖ Evidence has also been provided that the maximum charge density that can be accumulated within such a contact is dependent on the real area of contact (A_r) across which triboelectric charge transfer can occur, as well as a separate factor hypothesised to be attributed to flexoelectric perturbations in surface potential induced by the presence of strain gradients across the depth of contacting asperities (V_{FxE}).
- ❖ Using these data a semi-analytical model and associated equation has been derived to describe frictional electrification between insulating polymers in sliding contact.
 - The basis of the model describes a time dependant aspect of triboelectric charging of macroscale contacts, made probabilistic in nature by the availability of electron

state energies relevant to charge transfer. The equation for charge accumulation is therefore given an exponential form due to this nature.

- The influence of frictional excitation and electron phonon interactions on the expedition of triboelectric charging is represented in the perturbed time constant for charge accumulation (τ').
 - The effects of material wear are effectively modelled as an exponential term within this model, with a time constant corresponding to material wear rates (τ_w).
 - The introduction of this second exponential term represents the trends observed for cases where material wear both inhibits and enhances triboelectric charge transfer.
 - The influence of flexoelectric perturbations in surface potential are also accounted for through the introduction of a perturbed triboelectric electrochemical potential $\Delta\bar{\mu}'$.
 - All the above terms have their respective dependencies on the average pressure exerted onto the contact $\langle P \rangle$, which is expressed as the ratio of applied force (F) to real contact area (A_r) and follows Persson's equation for randomly rough planar contacts to give a $\langle P \rangle \propto F/\text{erf}(F)$ relationship.
- ❖ The intent of this model is to provide a stepping stone towards a comprehensive yet simplistic understanding of the phenomenon that is frictional electrification between complex surface structures and within complex tribological environments.

Chapter 5 – Summary

The primary conclusion of these studies is that tribology has a significant influence on the triboelectric charging behaviour of macroscale sliding contacts. The development of an apparatus capable of correlating tribological and triboelectric data from a TENG contact – in-situ and under precisely controlled tribological conditions – has yielded data that has highlighted this significant relationship. An initial freestanding apparatus was also proven to be a cost effective methodology for determining triboelectric performance.

The output current and voltage characteristics of the sliding freestanding layer triboelectric nanogenerator (F-TENG) were measured for a multitude of tribological parameters, material combinations and external circuit impedances. The short and open circuit output characteristics were shown to correlate with existing models, based on time varying and distance dependant electric fields.

Firstly, the macroscale nature of triboelectric charging within sliding contacts is shown to be time dependant, and can be approximated using the combination of two exponential terms. The first term representing the capacitive charging of the triboelectric contact, and the second term representing tribological mechanisms such as contact profile truncation or wear debris and transfer layer development. The time dependency of the first term contradicts the instantaneous quantum nature of triboelectric charge transfer, but can be explained through the probabilistic nature of available energy state transitions when expanded to the macroscale. The influence of friction is introduced through the generation of phonon-electron interactions acting to diversify this energy state distribution, and therefore expedite triboelectric charge transfer.

The unperturbed dissipation of electrostatic charges from insulating surfaces when exposed to ambient air is also shown to follow a single exponential term exactly. Insulating surfaces of differing composition are shown to exhibit different timescales for charge dissipation. Microscale electrostatic discharge (ESD) events were also observed during dry sliding contact for all material combinations. The prominence of these ESD events are shown to change across the duration of tests, in addition to exhibiting a dependence on tribological parameters such as applied load.

Initial investigations yielded results in agreement with previous studies on triboelectric charging within contact separation TENG devices. Nylon 6-6 and Delrin have been confirmed as electron donating polymers whereas Teflon is confirmed as electron accepting. The triboelectric charging behaviour of the Delrin surfaces were shown to be of identical polarity to that of Nylon, in addition to being greater in magnitude for identically rough surfaces.

It is interpreted from the data collected from these studies that the work functions of all metals involved in testing lie between the effective work functions of Nylon and Teflon, which is in agreement with previous studies that use methodologies separate from triboelectric charging. This was gauged by observing that Teflon samples always exhibit a reversed current and voltage output to identical contact involving either of alternative polymers, indicating a reversed polarity of triboelectric charging with all metal counter surfaces.

It is also interpreted from these results that the metals can be arranged by their triboelectric behaviours as they would be by their respective work functions. Aluminium on average accumulated the smallest charges against Nylon and Delrin, but the largest against Teflon, whereas stainless steel exhibited the reverse. It was shown that the Teflon on Nylon sliding contacts accumulated a considerably larger triboelectric charge density than any polymer on metal equivalent.

The friction response of sliding contacts for all of the observed material pairings correlate well with the triboelectric charge development within said contacts. It is hypothesised that numerous tribological mechanisms contribute towards this synergy in different ways. Friction coefficient and contact charge are both shown to rise and eventually stabilise over time for dry contacts where material wear is negligible. The presence of material wear, transfer films, and even an interfacial lubricant are shown to inhibit triboelectric charge transfer. The removal of charged wear debris from a dry sliding contact is directly observed in both friction and contact charge measurements as a reduction in contact charge and abrupt fluctuations in measured forces. The development of Teflon transfer layers were shown to gradually inhibit the development of triboelectric charge against all counter surfaces with increasing coverage over sliding distance. The introduction of heptane as an example lubricant was also observed to temporarily reduce both friction and charge response within a Teflon on Nylon sliding contact; until evaporation and subsequent lubricant starvation caused both values to rise again as though the two materials were being brought into contact for the first time once more.

In addition to the influence of surface mechanical properties and chemical composition, the role of contact topography was also confirmed to be in agreement with existing theories. Higher triboelectric charge densities were observed for contacts with more conformal topographies. For the specific case of this study, smoother polymer surfaces were found to conform better with polished metal counter surfaces and yield electric outputs of greater magnitude regardless of charging polarity. The magnitude of charge accumulated within these sliding contacts was found to be linearly dependant on the calculated real area of contact within them, which in turn was inversely proportional to the composite root mean square slope of the two contacting surfaces.

Tests conducted under a range of applied loads are also shown to further reinforce this dependency on real contact area on triboelectric charging. This has previously only been confirmed for contact electrification in the absence of lateral motion. This relationship can however be extended to sliding contacts if the real area of contact is assumed to follow a linear relationship with increasing lateral displacement from the static position. The application of higher applied loads is also shown to expedite material wear mechanisms. Increased rates of low-friction transfer film development and subsequent contact charge reduction is observed within Teflon contacts against all counter materials under higher applied loads.

The relative velocities of sliding contacting surfaces is shown to influence the development of triboelectric charge within said contacts. Higher relative sliding speeds are shown to expedite the process of triboelectric charging. An important factor to note is that the reciprocating nature of these tests eliminates the plausibility of Volta's original hypothesis – that the contribution of sliding motion to triboelectric

charging is solely through the introduction of new sites for charge transfer within the contact. Teflon on Nylon sliding contacts are also shown to exhibit higher friction coefficients at higher relative sliding speeds, in addition to the expedition of Teflon transfer layer development.

Ultimately, a semi-analytical model is constructed from the combined findings of this study. The following equation has therefore been derived to estimate the total triboelectric charge within a macroscale sliding contact; accounting for the contact geometry of rough surfaces, flexoelectric perturbations in surface potential that arise from stress fields and resulting strain gradients, frictional excitation from sliding contact and electron-phonon interactions, and material wear causing profile truncation and the development of material transfer layers.

$$Q(t) = \frac{\varepsilon A_r}{e z_0} \left(\phi_D^* - \phi_A^* + \xi (V_{fA} - V_{fD}) \left(\frac{\pi}{A_r Y^*} \right) (F_z^2 (1 + \mu^2))^{\frac{1}{2}} \left(\frac{9}{8} \left(\frac{S_{\Delta a_D}}{S_{a_D}} + \frac{S_{\Delta a_A}}{S_{a_A}} \right) \right)^{\frac{1}{3}} \right) \cdot \left(1 - \exp \left(\frac{-t}{\tau_0 \left(1 - \beta \frac{2\mu F_z \Delta x f}{A_r} \right)} \right) - \zeta \left(1 - \exp \left(\frac{-t}{2\Delta x f C_{wear}} \right) \right) \right)$$

In summary, it is clear that triboelectric charging within sliding contacts is an intensely dynamic phenomenon, with a multitude of contributing factors that synergise and interact with each other in different ways. The methodology presented in this work provides a pivotal stepping stone towards a more fundamental understanding of frictional electrification in macroscale contacts, highlighting how it significantly differs from static contact electrification and nanoscale phenomena.

Future works that I plan to pursue in this field involve the evolution of the previously mentioned semi-analytical model to include the skewness and kurtosis values for contacting topographies, in addition to the modified stress fields that arise from the presence of tangential loads and shear stresses within sliding contacts. I also aim to effectively characterise the surface electronic properties of common engineering materials using low-energy electron diffraction spectroscopy (conveniently abbreviated as LEEDS) to probe the lowest energy unoccupied surface electron states of materials. This analysis will be used in conjunction with ultraviolet photoelectron spectroscopy (UVPES) and thermionic photoemission spectroscopy (TIPES) to probe the highest energy occupied electron states of surfaces and interfaces. The influence of phonon generation and surface shear stresses will also be isolated in nanoscale atomic force microscopy (AFM) tests, using a combination of lateral force microscopy (LFM) and Kelvin probe force microscopy (KPFM) techniques. The Sessile drop technique for determining interfacial energies will also be investigated as a potential cost-effective methodology for predicting the triboelectric behaviour of engineering surfaces, without the need for the previously mentioned expensive characterisation techniques.

Appendix A: Additional Analysis Techniques

5.1 Atomic Force Microscopy Study

A minor complimentary study was conducted into the feasibility of using the previously mentioned LFM-AFM and FM-KPFM techniques for determining the mechanisms that dominate frictional electrification within nanoscale sliding contacts. This section will briefly describe the methodology used, alongside relevant findings and a final discussion of evaluation.

5.1.2 Methodology

To provide a suitable methodology for characterising the triboelectric properties of materials on the nanoscale a two-stage procedure is required. Firstly a contact mode scan is performed on the surface of the sample material. This scan transfers triboelectric charge between the AFM tip and the sample surface, depositing electrostatic charges onto the insulating sample surface.

The contact mode scan is performed using lateral force microscopy (LFM), providing topographical data as well as mapping traction force due to the lateral tip deflection. The RTESPA-300 silicon nitride (SiN) AFM cantilever by Bruker was selected for these tests due to its high spring constant of 40 Nm^{-1} , allowing for relatively high-load testing in future experiments. Silicon nitride is also one of the materials used for AFM contact electrification in previous literature (Zhou et al., 2013; Zhou et al., 2014). A grid is first patterned onto the substrate surface using a micro-indenter. The grid consists of $9 \times 15 \mu\text{m}$ by $15 \mu\text{m}$ squares within which the contact mode scans are performed. The contact mode raster scans were $5 \mu\text{m}$ by $5 \mu\text{m}$, consisting of 256 lines and 256 lines per sample and giving a spatial resolution of $\sim 20 \text{ nm}$. The scan rate was set to 0.5 Hz , indicating a sliding speed of $5 \mu\text{ms}^{-1}$ for the tip across the sample surface. A deflection set-point of 1 V was used, implying a normal contact force of $2.4 \mu\text{N}$ since the inverse optical lever amplification for this set-up was 60 nm/V . Contact force for contact mode AFM scans are generally calculated using the product of the deflection set-point, inverse optical lever amplification and cantilever spring constant. The nominal and maximum tip radii quoted by Bruker are 30 and 36 nm respectively. Once the LFM scan is completed, the SiN RTESPA-300 AFM cantilever is replaced with a Bruker conductive SCM-PIT V2 cantilever for electrostatic force measurements.

A $10 \mu\text{m}$ by $10 \mu\text{m}$ AM-KPFM scan is then performed on the contacted area – with aid from the micro-indented grid for location – to measure the surface potential of the contacted area and surrounding surface. Since these tests are performed in air rather than a vacuum, the potential for charge dissipation due to interactions with air particles is a factor that should be considered. Therefore the sample substrate is undisturbed between the LFM and KPFM measurements as to retain any static charges deposited onto the surface as much as possible. The time between the two scans is also measured and kept constant for each procedure as a way of keeping charge dissipation constant relative with regards to time across the tests. The SCM-PIT V2 probe is a Platinum-coated probe doped with Iridium to increase durability of the tip. It has a resonant frequency around 63 kHz for the purpose of these KPFM tests, with a variation of 2 kHz found during calibration dependent on the exact tip being used as well as the potential presence

of contaminant particles. The spring constant of these probes are significantly lower than that of the RTESPA-300 probes at approximately 1.5 Nm^{-1} . The purpose of these preliminary scans is to evaluate the effectiveness of the experimental procedure; therefore the lift scan height, drive amplitude, lock-in bandwidth and gain values were varied in order to obtain the highest quality images.

5.1.2 Results and Discussion

Preliminary tests in using the previously explained testing procedure have varied levels of success. Initial tests were conducted on $25 \text{ }\mu\text{m}$ thin polymer films of various compositions without any conductive backing or being grounded to the AFM base. Low-force tests conducted at 120 nN yielded no results via KPFM, partially due to errors in finding the correct location for the LFM scan without any significant visual markers as well as having inconsistencies in the motors moving the sample along the AFM base.

This lack of change in contact potential difference could also be caused by the polymer samples not being backed and grounded sufficiently. Since these measurements are intended to detect the presence of isolated surface charges on the polymer, backing the polymer samples should have little effect other than essentially changing the mode of detection for the charge from working in a similar fashion to a single-electrode TENG to an attached-electrode TENG instead. The roughnesses of the polymer films were also considerably high in relation to the AFM tip geometry due to the nature of polymers, which further complicated the process of taking KPFM measurements. Another potential cause for error is the intermediate contact nature of the AM-KPFM tapping-mode scans. For a small period of time the conductive AFM probe is in electrical contact with the sample surface in order to map topography. During this brief period there is the possibility of electrical discharge of the isolated tribo-charges into the AFM tip, as a form of forced triboelectric transfer, in order to reach thermodynamic equilibrium. This time period of contact should be on an order of magnitude smaller than microseconds.

Tests are then carried out on an atomically flat silicon oxide (SiO_2) surface as a way of evaluating the replicability of results in the literature (Zhou et al., 2013). The elastic modulus of the silicon samples was taken as 165 GPa from literature (Dolbow and Gosz, 1996) so are only used as an estimation. Using Hertzian analysis the contact pressure within the tip-sample contact can also be estimated. The real contact area was derived to be approximately $2.5\text{e-}16 \text{ m}^2$ with a diameter of 18 nm . The maximum contact pressure was estimated to be approximately 14 GPa , although this is heavily dependent on the accuracy of the contact force calculation as well as assumptions being made for both the elastic modulus of both the tip and sample. This calculation also estimated an unusually large deformation in the z axis normal to the sample surface, which raises the question of the validity of Hertzian contact analysis under such extreme conditions on the nanoscale. The semi-conductive nature of silicon was proposed to provide a more reliable backing and ground for the oxide layer upon which the tests were performed, as well as providing an insight into the replicability of tests performed in literature (Zhou et al., 2013).

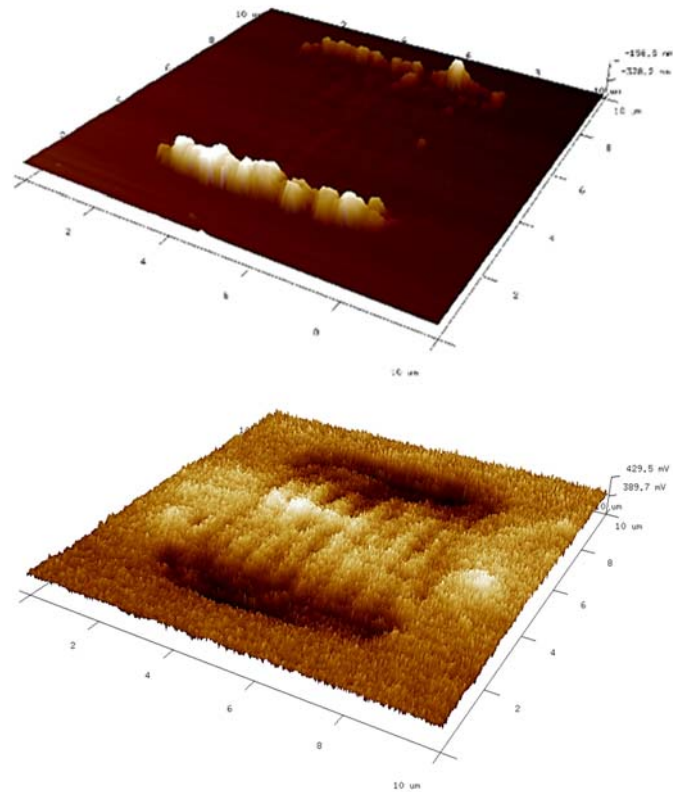


Figure 5-1 - Topographical (top) and surface potential (bottom) maps for AM-KPFM tests on 10 μm by 10 μm on a SiO substrate, with the centre portion being raster scanned using LFM with a SiN probe at 2.4 μN contact force and a sliding speed of 5 μms^{-1} .

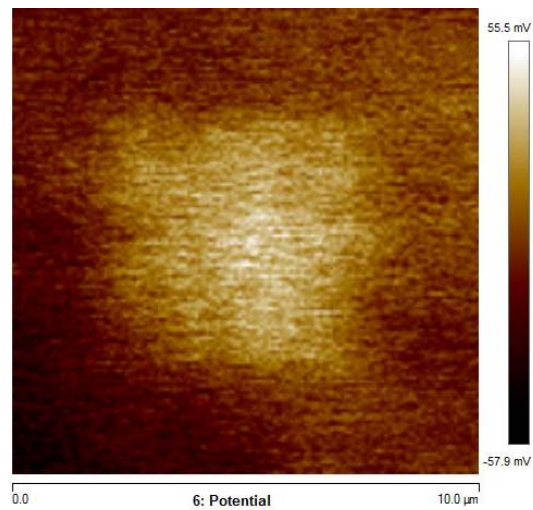


Figure 5-2 - Surface potential map for AM-KPFM tests on 10 μm by 10 μm on a SiO substrate, with the centre portion being raster scanned using LFM with a SiN probe at 0.6 μN contact force and a sliding speed of 1 μms^{-1} .

The resulting maps provided by these tests on the silicon oxide substrate show a distinct collection of wear particles at either end of the stroke due to the high-load nature of the test. The surface potential image of the same scan indicate the wear particles having a lower surface energy than the surrounding material. This could be caused by several physical phenomena. Either the very geometrical nature of the

collection of wear particles lowers the surface potential of that specific area (Yilbas et al., 2017) or the wear particles carry an electrostatic charge which would cause or amplify a change in surface potential.

There also resides a significant chance that these large changes in surface potential are due to limitations in the measurement capabilities of the Dimension Icon AFM. Since these collections of wear particulate stand at a significant height above the sample surface in relation to the surface roughness itself, there is a chance for the AFM tip to not anticipate these large changes in height if the gain levels are not set high enough. This can be seen in the 'Height Error' maps produced by the NanoScope software alongside the topography and surface potential maps.

Despite these potential causes in error, there is a distinct pattern in surface potential within the worn area itself. The surface potential map shows a series of grooves running parallel to the stroke of the AFM tip. The width of these grooves average at around 500nm in width and run across the full 5 μ m stroke length. This is interesting as the width of these grooves is substantially larger than both the cross-sectional area of the tip-sample contact as well as the lateral spacing between individual strokes. These patterns in surface potential also have no correlation to the topography of the worn area apart from this correlation with stroke angle.

As well as these grooves, there are areas within the worn area that have a higher surface potential than the surrounding non-contacted area. The most plausible cause for these specific changes in surface potential is triboelectrification, however more tests are required to evaluate the repeatability of these results. When examining outside of the worn area there are also some changes in surface potential, albeit smaller than the changes generated as a result of contact with the AFM tip.

With regards to the LFM data the NanoScope software associated with the Bruker Dimension Icon AFM does not allow for the calibration of the torsional spring constant of a cantilever, meaning all friction data collected using this methodology is unfortunately qualitative and only usable for comparison with tests using an identical cantilever. Another thing to consider is that the AFM cantilever may not be perfectly perpendicular to the sample surface due to the way it is loaded into the module. This – alongside any internal stresses within the cantilever – may cause a natural directional bias in the friction mapping data.

The normal contact force for these tests was substantially higher than the force of 120nN used for triboelectrification in literature (Zhou et al., 2013). The reasoning behind this was due to a lack of availability in AFM cantilevers, leading to the selection of the RTESPA-300 tip having a spring constant more than a magnitude larger than the 1.46 Nm⁻¹ AC240TM Olympus tip used in literature.

5.1.3 Conclusions

The resulting maps from these tests demonstrate that there is a potential for developing a unified methodology for characterising the triboelectric and surface potential properties of surfaces on the nanoscale. More tests are needed, experimenting with different sample materials and sample preparation techniques, in order to develop a methodology that produces sufficiently replicable results.

In addition, frequency modulated KPFM is proven in literature to be the favoured KPFM measurement method for isolated surface charges. This is due to the higher spatial resolution and single-pass procedure that FM measurements can provide.

Once this particular methodology has been proven and used to characterise the triboelectric properties of a range of materials, research will be conducted into the significance of tribological factors and their contribution to triboelectric charge transfer on the nanoscale. This will involve LFM tests with a range of deflection set-points and scan rates to influence the normal contact force and sliding speed of the AFM tip as it contacts the sample surface and replicates a single material asperity.

Appendix B: The Terminologies of Potential

This appendix is purposed to highlight the often conflicting definitions of different forms of potential. Most importantly the distinction between electrochemical, chemical, and electric potentials are given, and their properties correlating to triboelectric charge transfer are also described. Boston-based physicist Steve Byrnes has previously produced a useful guide for distinguishing these particular terms. Material from this guide is shown in Table 15 and further elaborated on in this section.

Table 15 – Differing concepts relating to electrochemical potential.

Label	Concept	Electrochemical Terminology	Solid-state Physics Terminology	Semiconductor Physics Terminology
A	Total chemical potential of electrons	Electrochemical potential (of electrons)	Electrochemical potential	Fermi level / Fermi energy
B	Internal chemical potential of electrons	Chemical potential (of electrons)	Chemical potential	Fermi level (relative to vacuum / conduction band minimum)
C	Electric potential	Galvani potential	Electric potential, Voltage	Electric potential, Voltage, Difference in vacuum level
D	Internal chemical potential of electrons at absolute zero temperature	n/a	Fermi energy	Fermi level (at absolute zero temperature)

Firstly, electrons may possess potential energy from both their chemical environment as well as from any external electrical influences. The total electrochemical potential is therefore stated as the sum of its chemical and electric components respectively.

$$A_i = B_i + eC_i \quad (5-1)$$

Physicists frequently use the terms ‘voltage’ and ‘potential difference’ interchangeably, which gives rise to the common misconception that voltage as measured by a voltmeter is electric potential difference. The introduction of electronvolts as a unit of energy helps in allowing for the interchangeability of these concepts. The electronvolt is described as the amount of kinetic energy gained by an electron accelerating from rest through an electric potential difference of one volt in vacuum. The value of one electronvolt as stated in terms of Joules is therefore equal to the value of elemental charge as it would be stated in terms of Coulombs.

$$1 \text{ eV} = 1 \text{ Joule} \cdot e = 1.6e^{-19} \text{ Joules}$$

It is important to note that the physical quantity measured by a voltmeter is actually the total electrochemical potential between two points (A/e), rather than solely electric potential (C). From a purely thermodynamic viewpoint, electrons will always attempt to reduce their total electrochemical potential

energy and will therefore travel from a state of high A to low A until local thermodynamic equilibrium is reached and A is constant throughout the system being considered.

The Aluminium-Gold contact previously described in 1.4.1.b Fermi Gas Model will now be used as an example to better define these different – and often mistaken – definitions of potential. The Aluminium (Al) and Gold (Au) surfaces have work functions of 4.08 and 5.10 eV respectively. These workfunctions correlate inversely to the internal chemical potential of electrons within their respective surfaces, meaning that electrons in the Aluminium surface have a higher internal chemical potential than those in the Gold surface. One can assume that $B_{Al} - B_{Au} = 1.02$ eV before *and* after the two surfaces contacting, since internal chemical potential is not influenced by external electrical potentials.

Upon initial contact there is no electric field or electric potential between the two surfaces, making $C_{Au} = C_{Al} = 0$. Due to the relationship stated in (5-1) and the two previously mentioned initial conditions, the total electrochemical potential of the two contacting surfaces must initially be different, meaning $A_{Au} < A_{Al}$ which reflects their respective internal chemical potentials. Electrons are then triboelectrically transferred from the Aluminium surface to the Gold counter-surface until $A_{Au} = A_{Al} = A'$ and thermodynamic equilibrium is reached.

Once equilibrium is reached, a difference in internal chemical potential remains between the two contacting surfaces. This implies that an electric field and corresponding electric potential must exist across the contact in order for (5-1) to hold true. The resulting electric potential would be such that $C_{Au} - C_{Al} = 1.02$ V. Another definition subject to contention is the definition of the term ‘vacuum level’. Byrnes uses a simple yet imperfect definition for this concept, describing the difference in vacuum level between two points as the difference in electric potential multiplied by -1. The vacuum energy at a given point is often treated as the difference in electric potential between that given point and a reference point infinitely far away.

Several misconceptions also arise from the definitions of different named forms of potential. These terms include the Galvani and Volta potentials. Firstly, a Galvani potential is as described in Table 15 as the electric potential difference between two points in the bulk of two phases. The Galvani potential is also often referred to as the ‘inner’ potential which is the source of much misguided correlation with internal chemical potential. The Volta potential is also referred to as the contact potential difference (CPD), or ‘outer’ potential. A Volta potential is defined as the electric potential between two metals that are in contact and are in thermodynamic equilibrium. The Volta potential is also measured between two points close to but on opposing sides of the contact interface. Because of this definition, a Volta potential can be treated as a specific form of Galvani potential that can prove useful for describing problems that involve triboelectric charge transfer.

Index of Figures

Figure 1-1 – Visual representation of the splitting of valence electron states for carbon atoms as they are brought into proximity to form a diamond crystal.	1-25
Figure 1-2 – Electron potential energy at a metal-metal contact as depicted by Matsusaka (Matsusaka and Masuda, 2003).	1-28
Figure 1-3 – Energy diagram for electron transport across an Aluminium-Gold contact. Denoting the electron state densities ($g_i(E)$, red lines), unperturbed and perturbed Fermi Dirac distributions ($f_i(E)$ and $f_i'(E)$ respectively, blue lines), vacuum state energies (E_{vac} , green line), conduction band ground state energies (E_{0i}), work functions (ϕ_i), Fermi energies (E_{Fi}) and Fermi energy / vacuum potential perturbations (ΔE_{Fi}) of the donor (D) and acceptor (A) surfaces, in addition to the final balanced electrochemical potential (ϕ') across the contact.	1-31
Figure 1-4 – Charge on a chromium sphere - 4mm in diameter - in contact with another sphere - 13mm in diameter - as a function of the CPD of chromium against each metal as stated and depicted by Harper (Harper, 1951a).	1-32
Figure 1-5 – Illustrating the mechanisms that underlie ultraviolet photoelectron spectroscopy, using a metal collector material and a semiconductor emitter. Depicting an incident photon of energy $\hbar\omega$ equal to the work function of the emitter material (ϕ_e) plus the kinetic energy of the resulting emitted electron (E_k). The electric potential in the vacuum (eV , green line) is equal to the cut-off voltage (V) multiplied by the electron charge (e), which in turn is equal to the highest attainable kinetic energy for the emitted electrons. ..	1-34
Figure 1-6 – Schematic description of amplitude modulated (a) and frequency modulated (b) non-contact mode AFM and their respective feedback systems for mapping topography and maintaining a constant sample-tip separation as depicted by (Melitz et al., 2011).	1-36
Figure 1-7 – Schematic diagram for an AFM system configured for EFM measurements.	1-37
Figure 1-8 – Schematic diagram of an AFM system for both AM (bold line) and FM (dotted line) KPFM measurements. The lower section is an FM system for mapping topography and the upper section is the KPFM system for surface potential measurements (Melitz et al., 2011).	1-39
Figure 1-9 – Energy band diagrams for an example conductor, semi-metal, semi-conductor, and insulator at an arbitrary non-zero temperature. Denoting the vacuum energy (E_{vac}), state density ($g(E)$), Fermi-Dirac distribution ($f(E)$), Fermi level (μ), Fermi energy (E_f), work function (ϕ), ionisation potential (E_{IP}), electron affinity (E_{EA}), highest occupied molecular orbital (E_{HOMO}), lowest unoccupied molecular orbital (E_{LUMO}), conduction band bottom (E_c), valence band top (E_v), and band gap energy (E_{gap}). Note that the example semi-conductor purposefully exhibits an unusually small band-gap and in some situations may be considered a semi-metal, allowing for valence electrons to be thermally excited into the conduction band.	1-41
Figure 1-10 – Example energy band structures for a semi-metal, and indirect and direct bandgap semi-conductors plotted as wave-vector against energy.	1-42
Figure 1-11 – Energy band diagrams for example intrinsic, n-type, and p-type semi-conductors. Denoting the vacuum energy (E_{vac}), Fermi-Dirac distribution ($f(E)$), Fermi level (μ), work function (ϕ), ionisation potential (E_{IP}), electron affinity (E_{EA}), conduction band bottom (E_c), valence band top (E_v), and band gap energy (E_{gap}).	1-45
Figure 1-12 – Energy band diagrams for separate n-type and p-type semi-conductors (left), and a p-n junction diode (right). Denoting the built-in potential (V_{b-in}), vacuum energy (E_{vac}), Fermi-Dirac distribution ($f(E)$), Fermi level (μ), work function (ϕ), ionisation potential (E_{IP}), electron affinity (E_{EA}), conduction band bottom (E_c), valence band top (E_v), and band gap energy (E_{gap}).	1-47
Figure 1-13 – Example energy band diagrams for an n-type semi-conductor and a metal (left), and a Schottky diode (right). Denoting the built-in potential (V_{b-in}), vacuum energy (E_{vac}), Fermi-Dirac distribution ($f(E)$), Fermi level (μ), work function (ϕ), ionisation potential (E_{IP}), electron affinity (E_{EA}), conduction band bottom (E_c), valence band top (E_v), and band gap energy (E_{gap}).	1-48
Figure 1-14 – Depicting example Brillouin zones (light red) and irreducible Brillouin zones (dark red) for example 2D square (a) and hexagonal (b) lattices.	1-49
Figure 1-15 – Surface states model for metal-polymer contact charging as shown by Lee (Lee, 1994). ϕ_m and ϕ_p are the work function of the metal and the effective work function of the polymer respectively, LUMO is known as the lowest unoccupied molecular orbital, and HOMO is known as the highest occupied molecular orbital.	1-50
Figure 1-16 – Energy level diagram for insulator-insulator contact as depicted by Matsusaka (Matsusaka et al., 2010). The horizontal dashed depict set surface states for each insulator and the large dots indicate which states are filled.	1-51
Figure 1-17 – Photograph of example menisci within a glass test tube for mercury (left) and water (right).	1-52
Figure 1-18 – Sessile drop method for the measurement of contact angle between three sample liquids and substrate.	1-52
Figure 1-19 – Du Noüy ring method for measuring the surface tension of a sample liquid.	1-53
Figure 1-20 – Molecular ion state model for a metal-insulator contact. Specifically for the injection of electrons into the acceptor states of the insulator as depicted (Matsusaka et al., 2010). Depicting the electron state densities (referred to as piE by Fabish and Duke, using A and D to denote acceptor and donor states for the insulator, but traditional notation defines these as giE instead), Fermi-Dirac distributions fiE , electron state energy distribution centroids (Ei) of the metal-donor (M) and insulating-acceptor (I) surfaces.	1-58
Figure 1-21 – Molecular ion state model for an insulator-insulator contact as shown in (Matsusaka et al., 2010). Depicting the electron state densities (referred to as piE by Fabish and Duke, using A and D to denote acceptor and donor states for the insulators) but traditional notation defines these as giE instead), Fermi-Dirac distributions fiE , electron state energy distribution centroids (Ei) of the two insulating surfaces (I and 2).	1-58
Figure 1-22 – Changes in phonon energy corresponding from changes in vibrational modes from frictional contact as shown by Pan & Zhang (Pan and Zhang, 2017).	1-60
Figure 1-23 – Lattice deformation and vibration mode change when two surfaces are in frictional contact as depicted by Pan & Zhang (Pan and Zhang, 2017). (a) represents the equilibrium vibration modes whereas (b) represents the friction-induced lattice vibration modes.	1-61
Figure 1-24 – Changes in lattice spacing resulting from frictional contact as shown by Pan & Zhang (Pan and Zhang, 2017).	1-61
Figure 1-25 – Visual depictions of charge transfer mechanisms for contact electrification between Teflon and water (a), a sodium chloride solution in water (b), a sodium hydroxide solution in water (c), and hydrochloric acid (d) as depicted by (Nie et al., 2020).	1-68
Figure 1-26 – A visual depiction of surface skewness R_{sk} and kurtosis R_{ku} , as given by (Zeng et al., 2018). The left side of the four example plots are direct height maps, whereas histograms of their height distributions are placed to the right of each plot.	1-73
Figure 1-27 – Temperature dependence on output Voltage and Current of an Aluminium-PFA (50mm x 50mm apparent contact area, PFA film thickness not stated but constant) oscillating triboelectric contact, attached to a 5M Ω load resistance as depicted by (Wen et al., 2014).	1-76
Figure 1-28 – Experimental setup used by Nguyen & Yang (Nguyen and Yang, 2013) to investigate the effects of humidity and ambient pressure on PDMS-Al contact-separation mode triboelectric nanogenerators (TENGs).	1-77

Figure 1-29 – Peak current and voltage output (left) and power output (right) for generic TENG applications with varying external resistances as calculated using finite element analysis (FEA) techniques (Niu, 2015).	1-81
Figure 1-30 – Comparison of TENG technology with the electromagnetic (EM) generator, highlighting the advantages and disadvantages of both with regards to applications.	1-82
Figure 1-31 – Example configurations of contact separation TENG devices. Depicting the <i>conductive electrodes</i> , and respective <i>electronegative</i> and <i>electropositive</i> triboelectric insulating layers. The white box represents an arbitrary load circuit.	1-85
Figure 1-32 – Example configurations of laterally sliding TENG devices. Depicting the <i>conductive electrodes</i> , and respective <i>electronegative</i> and <i>electropositive</i> triboelectric insulating layers. The white box represents an arbitrary load circuit.	1-85
Figure 1-33 – Example configuration for a laterally rolling TENG device. Depicting the <i>conductive electrodes</i> , and respective <i>electronegative</i> and <i>electropositive</i> triboelectric insulating layers. The white box represents an arbitrary load circuit.	1-85
Figure 1-34 – Example configurations for a solid-liquid single electrode (a) and freestanding triboelectric body (b) TENG device. Depicting the <i>conductive electrodes</i> , <i>electronegative</i> triboelectric insulating layers and <i>charge-carrying liquid</i> . The white box represents an arbitrary load circuit.	1-86
Figure 1-35 – First-order lumped-parameter equivalent circuit model of a typical triboelectric nanogenerator as shown by Niu (Niu, 2015).1-86	1-86
Figure 1-36 – Schematics for a double attached electrode contact-separation mode TENG (a) and an attached electrode contact-separation mode TENG (b) alongside a brief circuit section showing how the different sections of the device correlate to effective capacitances.1-87	1-87
Figure 1-37 – Schematics for a double attached electrode linear in-plane sliding mode TENG (a) and an attached electrode S-TENG (b) as shown by Niu & Wang (Niu, 2015).	1-88
Figure 1-38 – Illustrating how a contact-separation mode TENG operates in open circuit (a) and short circuit (b) mode as shown by Vasandani et al. (Zhu et al., 2015).	1-89
Figure 1-39 – A contact-separation mode single electrode TENG (C-SE-TENG) as described by Niu & Wang (Niu, 2015).	1-90
Figure 1-40 – Schematics for a contact-separation mode conducting F-TENG (a) and a dielectric C-F-TENG (c) as shown by Niu & Wang (Niu, 2015) with partial circuit diagram describing their capacitive behaviour (b).	1-90
Figure 1-41 – Schematics for a linear in-plane sliding mode dielectric F-TENG (a) and a metal-coated S-F-TENG (c) as shown by (Niu et al., 2015).	1-90
Figure 2-1 – Side-on diagram of a polymer-on-metal laterally-sliding freestanding-triboelectric-layer triboelectric nanogenerator (F-TENG) at subsequential stages of operation (i) before contact, (ii) first contact, (iii) mid-first-stroke, (iv) end-stroke, (v) and mid-stroke. The positions of trapped and mobile charges are given for open circuit (a) and short circuit (b) configuration, and the respective electronic outputs (c). Depicting the output voltage (red) and current (blue) for both (c). The red block represents an electronegative material, whereas the grey blocks denote an electropositive conductor.....	2-96
Figure 2-2 – Sample dimensions and configuration for the F-TENG apparatus.....	2-97
Figure 2-3 – Schematic representation of the F-TENG supporting structure without samples (a), and with samples (b), one upper clamp is removed here to show the lower sample holder and demonstrate how the lower samples sit within the supporting structure.	2-98
Figure 2-4 – Photograph of the F-TENG supporting structure.....	2-98
Figure 2-5 – Solidworks model for the updated freestanding rig apparatus, following the addition of a belt driven linear actuator.....	2-99
Figure 2-6: Circuit diagram for a generic feedback ammeter.....	2-101
Figure 2-7 – Circuit diagram for a feedback ammeter with selectable sensitivity.....	2-101
Figure 2-8 – Image of a circuit board section from the manufactured low current amplifier, showing the multiple resistive ranges of the device with multiple resistors in parallel.....	2-101
Figure 2-9 – Final Circuit diagram for the low current feedback ammeter, excluding external circuits.	2-102
Figure 2-10 – Image of the low current feedback amplifier, manufactured by the Electronic Services Workshop at the University of Leeds School of Mechanical Engineering.....	2-102
Figure 2-11 – Circuit diagram of the 50Hz notch filter implemented within the F-TENG apparatus. $R = 160 \Omega$, and $C = 10 \mu F$	2-103
Figure 2-12 – F-TENG measurement circuit configurations for a) the initial feedback ammeter and oscilloscope series of tests, b) the feedback ammeter and myDAQ series, and c) the electrometer and myDAQ configuration series.	2-104
Figure 2-13 – Raw induced background current (red) over time, alongside fitted data produced by the four-stage notch filter (blue) and the final filtered data (black).	2-105
Figure 2-14 – Raw induced current (red) over several oscillations during an example test, alongside fitted data produced by the four-stage notch filter (blue) and filtered data (black) to show how the filter discerns between the signal and background noise.....	2-105
Figure 2-15 – Fourier transform of a generic initial 10 s of background raw current (red) induced by external interference; illustrating significant interference at 50 Hz and its even harmonic frequencies. These data were processed through a four-stage notch filter to remove interference at 50Hz and its first three harmonics (black).	2-105
Figure 2-16 – Molecular diagrams of a) Delrin, b) Teflon, and c) Nylon 6-6; with functional groups highlighted. Delrin is intentionally terminated differently to how one would expect – by its manufacturer DuPont – in order to prevent breakdown of the polymer into trioxane ($C_3H_6O_3$). Nylon may also be terminated differently to how it is depicted in this diagram due to the presence of terminal hydroxyl and amine groups.	2-107
Figure 2-17 – Molecular diagrams for the monomers of a) Delrin, and b) Teflon, and the two monomers of Nylon 6-6 (c and d). Formaldehyde is depicted in both its reduced form and with the carbon and hydrogen atoms shown in order to better display its structure.	2-108
Figure 2-18 – Depicting the intermolecular hydrogen bonds in Nylon 6-6. The blue regions approximate the skewed distribution of electron densities.....	2-109
Figure 2-19 – Depicting the hypothetical hydrogen bonds in Delrin. The blue regions approximate the skewed distribution of electron densities.	2-110
Figure 2-20 – Surface height maps for the untextured metal surfaces.	2-111
Figure 2-21 – Surface gradient maps for the untextured metal surfaces.....	2-112
Figure 2-22 – Surface gradient direction maps for the untextured metal surfaces.....	2-112
Figure 2-23 – Surface height histogram for the untextured metal surfaces.....	2-113
Figure 2-24 – Surface gradient direction polar histogram for the untextured metal surfaces.	2-113
Figure 2-25 – Surface height maps for the untextured polymer surfaces.	2-114
Figure 2-26 – Surface gradient maps for the untextured metal surfaces.....	2-114
Figure 2-27 – Surface gradient direction maps for the untextured metal surfaces.....	2-115

Figure 2-28 – Surface height histogram for the untextured metal surfaces.....	2-115
Figure 2-29 – Surface gradient direction polar histogram for the untextured metal surfaces.	2-116
Figure 2-30 – Surface height maps for the polished metal surfaces.	2-117
Figure 2-31 – Surface gradient maps for the polished metal surfaces.	2-117
Figure 2-32 – Surface gradient direction maps for the polished metal surfaces.	2-118
Figure 2-33 – Surface height histogram for the polished metal surfaces.	2-118
Figure 2-34 – Surface gradient direction polar histogram for the polished metal surfaces.	2-119
Figure 2-35 – Surface height maps for the polished polymer surfaces.	2-119
Figure 2-36 – Surface gradient maps for the polished polymer surfaces.	2-120
Figure 2-37 – Surface gradient direction maps for the polished polymer surfaces.	2-120
Figure 2-38 – Surface height histogram for the polished polymer surfaces.	2-121
Figure 2-39 – Surface gradient direction polar histogram for the polished polymer surfaces.	2-121
Figure 2-40 – F-TENG measurement circuit for finite resistive load voltage and current output configuration.	2-123
Figure 2-41 – Induced voltage output of the low current feedback ammeter for an example material pairing (Nylon on Copper). The initial pattern is the result of oscillating motion from electrode to electrode, the second is slow pulsed movement from electrode to electrode, and the third is a result of faster pulsed movement.	2-124
Figure 2-42 – An example of how current waveform can change across the duration of a typical F-TENG test.	2-127
Figure 2-43 – Example plots for induced current over time for the Delrin block reciprocating over aluminium (red), copper (green) and stainless steel (blue) electrodes.	2-127
Figure 2-44 – Example plots for induced current over time for the Delrin (red), Nylon (green) and Teflon (blue) blocks reciprocating over aluminium electrodes.	2-128
Figure 2-45 – 3D colour-scaled line-plot depicting output current over time for each forward (a) and reverse stroke (b) of a Delrin on Aluminium F-TENG contact over the duration of the test (cycles); Depicting the changes in current waveform as the test progressed.....	2-128
Figure 2-46 – 2D colour scaled images depicting output current (a & b) and voltage (c & d) over time (measured in samples at 1 kHz, directly corresponding to 1 ms) for each forward (a & c) and reverse (b & d) stroke of a Teflon on Copper F-TENG contact over the duration of the test (cycles); depicting the changes in current and voltage waveform as the test progressed.	2-129
Figure 2-47 – Peak induced current over time for 50x50mm Delrin (red), Nylon (green) and Teflon (blue) on aluminium contacts sliding with a stroke length of 50mm and a frequency of 2.5 Hz. Electrodes were spaced 1mm apart laterally.	2-130
Figure 2-48 – Peak induced current over time for 50x50mm Delrin (red), Nylon (green) and Teflon (blue) on copper contacts sliding with a stroke length of 50mm and a frequency of 2.5Hz. Electrodes were spaced 1mm apart laterally.	2-131
Figure 2-49 – Peak induced current over time for 50x50mm Delrin (red), Nylon (green) and Teflon (blue) on mild steel contacts sliding with a stroke length of 50mm and a frequency of 2.5Hz. Electrodes were spaced 1mm apart laterally.	2-131
Figure 2-50 – Peak induced current over time for 50x50mm Nylon on aluminium (red), copper (green) and mild steel (blue) contacts sliding with a stroke length of 50mm and a frequency of 2.5Hz. Electrodes were spaced 1mm apart laterally.	2-131
Figure 2-51 – Peak induced current over time for 50x50mm Delrin on aluminium (red), copper (green) and mild steel (blue) contacts sliding with a stroke length of 50mm and a frequency of 2.5Hz. Electrodes were spaced 1mm apart laterally.	2-132
Figure 2-52 – Peak induced current over time for 50x50mm Teflon on aluminium (red), copper (green) and mild steel (blue) contacts sliding with a stroke length of 50mm and a frequency of 2.5Hz. Electrodes were spaced 1mm apart laterally.	2-132
Figure 2-53 – Output current (green, top) and voltage (blue, bottom) for 50 x 50 mm Nylon on Copper F-TENG contact reciprocating at 2.7 (±0.3) Hz for 2.5 s with a stroke length of 50 mm and a 1 mm lateral electrode spacing.	2-133
Figure 2-54 – Comparison for output current (solid red), peak output current (dotted red) and contact charge (blue) over time for 50x50mm Delrin and aluminium contact reciprocating at 2.5Hz with a stroke length of 50mm and electrodes spaced 1mm apart laterally at the middle of the stroke.....	2-133
Figure 2-55 – Maximum output current per half-oscillation (green, left), and contact charge per stroke (blue, right) for a generic F-TENG contact.	2-134
Figure 2-56 – Integrated contact charge over time for 50x50mm Delrin (red), Nylon (green) and Teflon (blue) on aluminium contacts sliding with a stroke length of 50mm and a frequency of 2.5Hz. Electrodes were spaced 1mm apart laterally.	2-134
Figure 2-57 – Integrated contact charge over time for 50x50mm Delrin (red), Nylon (green) and Teflon (blue) on copper contacts sliding with a stroke length of 50mm and a frequency of 2.5Hz. Electrodes were spaced 1mm apart laterally.	2-135
Figure 2-58 – Integrated contact charge over time for 50x50mm Delrin (red), Nylon (green) and Teflon (blue) on mild steel contacts sliding with a stroke length of 50mm and a frequency of 2.5Hz. Electrodes were spaced 1mm apart laterally.	2-135
Figure 2-59 – Integrated contact charge over time for 50x50mm Nylon on aluminium (red), copper (green) and mild steel (blue) contacts sliding with a stroke length of 50mm and a frequency of 2.5Hz. Electrodes were spaced 1mm apart laterally.	2-135
Figure 2-60 – Integrated contact charge over time for Delrin on aluminium (red), copper (green) and mild steel (blue) contacts sliding with a stroke length of 50mm and a frequency of 2.5Hz. Electrodes were spaced 1mm apart laterally.	2-136
Figure 2-61 – Integrated contact charge over time for Teflon on aluminium (red), copper (green) and mild steel (blue) contacts sliding with a stroke length of 50mm and a frequency of 2.5Hz. Electrodes were spaced 1mm apart laterally.	2-136
Figure 2-62 – Contact charge per half-oscillation (black) fitted against an exponential (red) charging function for a generic F-TENG contact, exhibiting a more exponential charging pattern with an R^2 value of 87.89. The coefficients for the exponential function are as follows: $a = 0.04637 \pm 0.0019$, $b = 0.1849 \pm 0.011$, $c = 0.9141 \pm 0.2591$	2-137
Figure 2-63 – An extreme-case example of how contact charge can abruptly drop and attempt to rise back up several times during F-TENG testing. The material combination used for this specific test was Nylon on Copper.	2-138
Figure 2-64 – a) 2D colour-scaled image depicting output current over time for each forward stroke of a Teflon on copper F-TENG contact across the duration of an example F-TENG test (cycles). b) Contact charge per cycle across the duration of the same test, highlighting an abrupt change in current waveform and contact charge during the 118 th cycle of the test. c) Contact charge accumulation over time for three identical Teflon on copper contacts.	2-140
Figure 2-65 – 2D colour-scaled equivalent of Figure 2-45, depicting output current over time (samples) for each forward (a,) and reverse stroke (b) for 100 cycles of an example Delrin on Aluminium F-TENG contact; Depicting the changes in current waveform as the lateral electrode spacing is increased from 1mm to 10mm across the test cycles.	2-141
Figure 2-66 – Contact charge accumulation over time for Delrin (green), Nylon (red), and Teflon (blue) on Aluminium F-TENG contacts. Three example tests were taken from each material pairing in order to exhibit the level of consistency and repeatability achieved.	2-142

Figure 2-67 – Charge accumulation over time for Delrin (a), Nylon (b), and Teflon (c) on Aluminium (blue) and Copper (green) F-TENG contacts; demonstrating the difference in charge accumulation rates between contacts involving the two conductive counter-materials.	2-144
Figure 2-68 – Surface height maps for Nylon surfaces ground using SiC grinding pads of varying grit values.	2-146
Figure 2-69 – Surface height histogram for Nylon surfaces ground using SiC grinding pads of varying grit values.	2-147
Figure 2-70 – Sample 1.5 mm x 1.5 mm surface topography of the Delrin surface after being subjected to a grinding process using 120 grit SiC pads.	2-148
Figure 2-71 – Contact charge accumulation over time for Nylon on Aluminium F-TENG contacts using Nylon samples of differing surface roughness.	2-149
Figure 2-72 – Contact charge accumulated over 35 seconds (Q) plotted against polymer surface rms slope (R_{dq}) for Nylon on Aluminium (blue) and Copper (red) F-TENG tests. The data for each material combination are fitted to a linear expression with constants described in Table 9.	2-150
Figure 3-1 – Side-on diagram of a polymer-on-metal laterally-sliding freestanding-triboelectric-layer triboelectric nanogenerator (F-TENG) at subsequent stages of operation (i) before contact, (ii) first contact, (iii) mid-first-stroke, (iv) end-stroke, (v) and mid-stroke. The positions of trapped and mobile charges are given for open circuit (a) and short circuit (b) configuration, and the respective electronic outputs (c). Depicting the output voltage (red) and current (blue) for both (c). The red block represents an electronegative material, whereas the grey blocks denote an electropositive conductor, and the gold block denotes the UMT-TENG 2D load cell.	3-153
Figure 3-2 – (a) Schematic representation of the full UMT-TENG testing apparatus (left) accompanied by a 3D model of the assembled UMT-TENG contact itself (right). Elements highlighted in blue represent elements that constitute the electronic measurement circuit, whereas elements highlighted in red contribute to tribological measurements. (b) Photograph of the UMT-TENG upper sample holder assembly. (c) Image of the UMT's reciprocating drive module with the UMT-TENG lower sample holder attached.	3-155
Figure 3-3 – Open circuit measurement configuration for a sliding freestanding triboelectric layer TENG device.	3-157
Figure 3-4 – Open circuit voltage trace of a Teflon on Nylon F-TENG contact as recorded by both electrometers in the configuration outlined in Figure 3-3, with V_{oc} being calculated as the subtraction of V_2 from V_1 .	3-157
Figure 3-5 – Wiring schematic of the UMT-TENG apparatus set-up. Indicating the exact connections used to integrate the Keithley 6517B electrometers with the data acquisition unit of the UMT. Please note that the BNC ports on the back panel of the UMT have been internally connected to pins 15 and 16 of junction 15 on the UMT data acquisition unit.	3-158
Figure 3-6 – Surface height maps for Polymer surfaces ground using 120 grit SiC grinding pads.	3-160
Figure 3-7 – Surface gradient maps for Polymer surfaces ground using 120 grit SiC grinding pads.	3-161
Figure 3-8 – Surface gradient direction maps for Polymer surfaces ground using 120 grit SiC grinding pads.	3-161
Figure 3-9 – Surface height histogram for Polymer surfaces ground using 120 grit SiC grinding pads.	3-162
Figure 3-10 – Surface gradient direction polar histogram for the polished polymer surfaces.	3-162
Figure 3-11 – (a) Cleaned friction coefficient against relative sample position and time for a polished Teflon on Nylon film F-TENG contact. (b) Cleaned (black) and raw (red) friction coefficient (μ) against relative sample position (blue) over time for the same contact. Samples were reciprocated at 1 Hz under an applied load of 40 N with a stroke length of 27 mm and a 2 mm lateral spacing of the lower samples. The apparent area of the contact is 23 mm by 50 mm.	3-164
Figure 3-12 – Cleaned friction coefficient against relative sample position and time for a polished Teflon on nylon film F-TENG contact.	3-164
Figure 3-13 – Friction coefficient over time for (a) polished polymers on polished stainless steel F-TENG contacts under an applied load of 5 N, (b) polished polymers on polished aluminium F-TENG contacts under an applied load of 5 N, (c) ground polymers on polished stainless steel F-TENG contacts under an applied load of 5 N, (d) ground polymers on polished aluminium F-TENG contacts under an applied load of 5 N, (e) polished polymers on polished stainless steel F-TENG contacts under an applied load of 10 N, (f) polished polymers on polished aluminium F-TENG contacts under an applied load of 10 N. Samples were reciprocated at 2.5 Hz with a stroke length of 27 mm and a 2 mm lateral spacing of the lower samples. The apparent area of the contact is 23 mm by 50 mm when the upper sample fully encompasses a lower sample.	3-165
Figure 3-14 – (a) Example topography of unworn polished Teflon sample. (b) Example topography of worn Teflon sample. (c) Example topography of PTFE wear debris on a stainless steel counter-surface after contact testing against Teflon, measured using a Bruker NPFLX white-light interferometer. (d) ATR-FTIR spectra of the Teflon surface prior to testing (blue) and the observed transfer film (orange). (e) Example topography of wear debris on an aluminium counter-surface after contact testing against Delrin, measured using a Bruker NPFLX white-light interferometer. (f) ATR-FTIR spectra of the Delrin surface prior to testing (blue) and the observed wear debris (orange). (g) Example topography of embedded wear debris on a Nylon surface after contact testing against Aluminium.	3-169
Figure 3-15 – (a) Output voltage against relative sample position and time for a polished Teflon on Nylon film F-TENG contact under an external resistance of approximately $> 2e^{14} \Omega$ (the input resistances of the two 6517B electrometers in series). (b) Output current against relative sample position and time for an identical contact under an external resistance of $\ll 1 \Omega$ (6517B connected as an ammeter with negligible voltage burden). (c) Output voltage (blue) and current (black) over time for an identical contact under an external resistance of 1 G Ω . (d) Output voltage (blue) and current (black) over time for an identical contact under an external resistance of 10 M Ω . Samples were reciprocated at 1 Hz under an applied load of 40 N with a stroke length of 27 mm and a 2 mm lateral spacing of the lower samples. The apparent area of the contact is 23 mm by 50 mm.	3-171
Figure 3-16 – Output voltage against relative sample position and time for a polished Teflon on Nylon film F-TENG contact under an external resistance of 10 M Ω (a) and 1 G Ω (b).	3-172
Figure 3-17 – Output current against relative sample position and time for a polished Teflon on Nylon film F-TENG contact under an external resistance of 10 M Ω (a) and 1 G Ω (b).	3-172
Figure 3-18 – Output power (current multiplied by voltage) against relative sample position and time for a polished Teflon on Nylon film F-TENG contact under an external resistance of 10 M Ω (a) and 1 G Ω (b).	3-172
Figure 3-19 – Current (blue) and voltage (green) output for a Teflon on Nylon F-TENG contact oscillating at 1 Hz, under an external resistive load of 1 G Ω .	3-173
Figure 3-20 – Current (blue) and voltage (green) output for a Teflon on Nylon F-TENG contact oscillating at 10 Hz, under an external resistive load of 1 G Ω .	3-173
Figure 3-21 – Current (blue) and voltage (green) output for a Teflon on Nylon F-TENG contact oscillating at 1 Hz, under an external resistive load of 10 M Ω .	3-174
Figure 3-22 – Current (blue) and voltage (green) output for a Teflon on Nylon F-TENG contact oscillating at 10 Hz, under an external resistive load of 10 M Ω .	3-174
Figure 3-23 – Short circuit current output for a sliding reciprocating Teflon on Nylon UMT-TENG contact, configured in a) single electrode (SE) and b) freestanding triboelectric layer (F) mode.	3-175

Figure 3-24 – Un-flagged current (blue) and voltage (green) output for a Teflon on Nylon F-TENG contact oscillating at 1 Hz, under an external resistive load of 1 GΩ.	3-175
Figure 3-25 – Un-flagged current (blue) and voltage (green) output for a Teflon on Nylon F-TENG contact oscillating at 1 Hz, under an external resistive load of 10 MΩ.	3-176
Figure 3-26 – Raw (light red), Flagged (red), and filtered (black) current output for a Teflon on Nylon F-TENG contact oscillating at 1 Hz.	3-177
Figure 3-27 – Integrated electrostatic discharge per forward (blue) and reverse (green) stroke for an example Teflon on Nylon F-TENG contact. Each data point represents the total charge discharged across a single stroke, rather than an individual ESD event.	3-179
Figure 3-28 – Vertical force across the full reciprocation cycle of an example F-TENG apparatus, without the force feedback loop being implemented.	3-179
Figure 3-29 – Contact charge over time for (a) polished polymers on polished stainless steel F-TENG contacts under an applied load of 5 N, (b) polished polymers on polished aluminium F-TENG contacts under an applied load of 5 N, (c) ground polymers on polished stainless steel F-TENG contacts under an applied load of 5 N, (d) ground polymers on polished aluminium F-TENG contacts under an applied load of 5 N, (e) polished polymers on polished stainless steel F-TENG contacts under an applied load of 10 N, (f) polished polymers on polished aluminium F-TENG contacts under an applied load of 10 N. Samples were reciprocated at 2.5 Hz with a stroke length of 27 mm and a 2 mm lateral spacing of the lower samples. The apparent area of the contact is 23 mm by 50 mm when the upper sample fully encompasses a lower sample.	3-181
Figure 3-30 – Friction (green) and triboelectric charge (blue) for each forward (blue, green) and reverse (light blue, light green) stroke of a polished Teflon on polished Stainless Steel F-TENG contact over time, reciprocating at 2.5 Hz under an applied load of 5 N.	3-184
Figure 3-31 – Friction (green) and triboelectric charge (blue) for each forward stroke of a polished Nylon on polished Stainless Steel F-TENG contact over time, reciprocating at 2.5 Hz under an applied load of 5 N.	3-185
Figure 3-32 – Friction (green) and triboelectric charge (blue) for each forward (blue, green) and reverse (light blue, light green) stroke of a polished Teflon on Nylon F-TENG contact over time, reciprocating at 2.5 Hz under an applied load of 40 N, with heptane introduced as a lubricant mid-test.	3-186
Figure 3-33 – Integrated electrostatic discharge per forward (blue) and reverse (green) stroke for the same Teflon on Nylon F-TENG contact as depicted in Figure 3-32, indicating the increase in ESD events after the onset of lubricant starvation. Each data point represents the total charge discharged across a single stroke, rather than an individual ESD event.	3-186
Figure 4-1 – Device geometry and sample dimensions in millimetres for the insulator-on-insulator freestanding-triboelectric-layer TENG. The Teflon block is coloured in red, whereas the Nylon sheet is blue, and the stainless steel plates are grey. The thickness of the Nylon sheet has been scaled up for it to be easily seen in this figure.	4-188
Figure 4-2 – Side-on diagram of a polymer-on-metal laterally-sliding freestanding-triboelectric-layer triboelectric nanogenerator (F-TENG) at subsequent stages of operation (i) before contact, (ii) first contact, (iii) mid-first-stroke, (iv) end-stroke, (v) and mid-stroke. The positions of trapped and mobile charges are given for open circuit (a) and short circuit (b) configuration, and the respective electronic outputs (c). Depicting the output voltage (red) and current (blue) for both (c). The red block represents an electronegative material, whereas the grey blocks denote an electropositive conductor, the blue layer represents an electropositive insulator, and the gold block denotes the UMT-TENG 2D load cell.	4-189
Figure 4-3 – Example topography of the Nylon Film surface, measured using white light interferometry.	4-190
Figure 4-4 – Example topography of the ground Teflon surface, measured using white light interferometry.	4-191
Figure 4-5 – Friction coefficient over time for the Teflon-Nylon UMT-TENG contacts, reciprocated at 0.1 Hz (a) and 2.5 Hz (b) under varying applied loads.	4-192
Figure 4-6 – Energy dissipated via friction per stroke over time for the Teflon-Nylon UMT-TENG contacts, reciprocated at 0.1 Hz (a) and 2.5 Hz (b) under varying applied loads.	4-193
Figure 4-7 – Contact charge over time for the Teflon-Nylon UMT-TENG contacts, reciprocated at 0.1 Hz (a) and 2.5 Hz (b) under varying applied loads.	4-195
Figure 4-8 – Electrostatic surface charge over time for an example Nylon surface exposed to the ambient atmosphere.	4-196
Figure 4-9 – Electrostatic surface charge over time for an example Teflon surface exposed to the ambient atmosphere.	4-196
Figure 4-10 – Maximum contact charge achieved during the first 200 m of sliding plotted against calculated static real contact area for Teflon-Nylon UMT-TENG tests conducted at 2.5 Hz and 0.1 Hz under applied loads of 5 N, 10 N, 20 N, and 40 N.	4-198
Figure 4-11 – Contact charge data (black) and exponential fit (red) over total sliding distance for tests conducted at 2.5 Hz under 5 N (a), 10 N (b), 20 N (c) and 40 N (d) applied load.	4-204
Figure 4-12 – Contact charge data (black) and dual exponential fit (red) over total sliding distance for tests conducted at 0.1 Hz under 5 N (a), 10 N (b), 20 N (c) and 40 N (d) applied load.	4-205
Figure 4-13 – Exponential fitting parameter Q_{max} versus calculated A_r for Teflon-Nylon UMT-TENG tests conducted at 2.5 Hz and 0.1 Hz under applied loads of 5 N, 10 N, 20 N, and 40 N.	4-207
Figure 5-1 – Topographical (top) and surface potential (bottom) maps for AM-KPFM tests on 10 μm by 10 μm on a SiO substrate, with the centre portion being raster scanned using LFM with a SiN probe at 2.4 μN contact force and a sliding speed of 5 $\mu\text{m s}^{-1}$	5-214
Figure 5-2 – Surface potential map for AM-KPFM tests on 10 μm by 10 μm on a SiO substrate, with the centre portion being raster scanned using LFM with a SiN probe at 0.6 μN contact force and a sliding speed of 1 $\mu\text{m s}^{-1}$	5-214

Index of Tables

Table 1 – Measured material parameters and calculated triboelectric interfacial properties of an Aluminium-Gold contact	1-30
Table 2 – Mechanical properties for all sample materials used in F-TENG testing.....	2-110
Table 3 – Surface topographies of untextured samples.....	2-111
Table 4 – Maximum induced current magnitudes from oscillating the polymer block by hand.....	2-125
Table 5– Average coefficients for exponential fittings of charge accumulation data for Delrin, Nylon, and Teflon on Aluminium F-TENG tests.	2-143
Table 6– Average coefficients for exponential fittings of charge accumulation data for Delrin, Nylon, and Teflon on Copper F-TENG tests.....	2-143
Table 7 – Calculated triboelectric series for the tested metals and polymers.	2-143
Table 8 – Surface roughness parameters for insulating triboelectric layers using a Bruker NPFLEX white light interferometer.	2-148
Table 9 – Linear fit constants used in Figure 2-72. for the linear equation $ Q = m \cdot R_{\Delta q} + c$ with error margins included and R^2 values.....	2-149
Table 10 – Surface topography parameters for all sample surfaces used in UMT-TENG testing.....	3-168
Table 11 – Sample Surface Topographies for the Polymer on Polymer F-TENG contact.....	4-190
Table 12 – Measured electrostatic charge dissipation time constants for polymer surfaces.....	4-196
Table 13 – Real contact area values for the Teflon – Nylon F-TENG interface.	4-197
Table 14 – Exponential fitting parameters for contact charge accumulation tests under varying tribological conditions.....	4-206
Table 15 – Differing concepts relating to electrochemical potential.....	5-217

Index of Equations

(Equation number) Page number

(1-1) 1-21	(1-62) 1-47	(1-123)..... 1-74
(1-2) 1-22	(1-63) 1-49	(1-124)..... 1-87
(1-3) 1-22	(1-64) 1-50	(1-125)..... 1-87
(1-4) 1-22	(1-65) 1-51	(1-126)..... 1-88
(1-5) 1-23	(1-66) 1-53	(1-127)..... 1-88
(1-6) 1-23	(1-67) 1-54	(1-128)..... 1-88
(1-7) 1-25	(1-68) 1-54	(1-129)..... 1-88
(1-8) 1-26	(1-69) 1-55	(1-130)..... 1-89
(1-9) 1-26	(1-70) 1-55	(1-131)..... 1-89
(1-10) 1-26	(1-71) 1-55	(1-132)..... 1-89
(1-11) 1-26	(1-72) 1-57	(1-133)..... 1-89
(1-12) 1-26	(1-73) 1-57	(1-134)..... 1-91
(1-13) 1-27	(1-74) 1-57	(1-135)..... 1-91
(1-14) 1-27	(1-75) 1-58	(1-136)..... 1-91
(1-15) 1-27	(1-76) 1-59	(1-137)..... 1-91
(1-16) 1-27	(1-77) 1-60	(1-138)..... 1-91
(1-17) 1-27	(1-78) 1-60	(1-139)..... 1-92
(1-18) 1-28	(1-79) 1-60	(1-140)..... 1-92
(1-19) 1-28	(1-80) 1-60	(1-141)..... 1-92
(1-20) 1-28	(1-81) 1-63	(1-142)..... 1-92
(1-21) 1-29	(1-82) 1-63	(1-143)..... 1-92
(1-22) 1-29	(1-83) 1-63	(1-144)..... 1-92
(1-23) 1-29	(1-84) 1-64	(1-145)..... 1-92
(1-24) 1-29	(1-85) 1-64	(1-146)..... 1-92
(1-25) 1-29	(1-86) 1-64	(2-1) 2-99
(1-26) 1-30	(1-87) 1-64	(2-2) 2-100
(1-27) 1-30	(1-88) 1-64	(2-3) 2-101
(1-28) 1-31	(1-89) 1-64	(2-4) 2-103
(1-29) 1-31	(1-90) 1-64	(2-5) 2-103
(1-30) 1-31	(1-91) 1-64	(2-6) 2-106
(1-31) 1-31	(1-92) 1-64	(2-7) 2-136
(1-32) 1-31	(1-93) 1-65	(2-8) 2-137
(1-33) 1-32	(1-94) 1-65	(3-1) 3-156
(1-34) 1-32	(1-95) 1-65	(3-2) 3-159
(1-35) 1-33	(1-96) 1-65	(3-3) 3-159
(1-36) 1-35	(1-97) 1-65	(4-1) 4-195
(1-37) 1-35	(1-98) 1-65	(4-2) 4-199
(1-38) 1-35	(1-99) 1-65	(4-3) 4-200
(1-39) 1-36	(1-100)..... 1-65	(4-4) 4-200
(1-40) 1-37	(1-101)..... 1-65	(4-5) 4-200
(1-41) 1-38	(1-102)..... 1-65	(4-6) 4-200
(1-42) 1-38	(1-103)..... 1-65	(4-7) 4-200
(1-43) 1-38	(1-104)..... 1-66	(4-8) 4-201
(1-44) 1-38	(1-105)..... 1-66	(4-9) 4-201
(1-45) 1-39	(1-106)..... 1-66	(4-10) 4-201
(1-46) 1-39	(1-107)..... 1-66	(4-11) 4-201
(1-47) 1-39	(1-108)..... 1-66	(4-12) 4-201
(1-48) 1-41	(1-109)..... 1-68	(4-13) 4-201
(1-49) 1-41	(1-110)..... 1-69	(4-14) 4-202
(1-50) 1-42	(1-111)..... 1-69	(4-15) 4-202
(1-51) 1-43	(1-112)..... 1-72	(4-16) 4-202
(1-52) 1-43	(1-113)..... 1-72	(4-17) 4-203
(1-53) 1-43	(1-114)..... 1-72	(4-18) 4-203
(1-54) 1-43	(1-115)..... 1-73	(4-19) 4-203
(1-55) 1-44	(1-116)..... 1-73	(4-20) 4-203
(1-56) 1-45	(1-117)..... 1-73	(4-21) 4-206
(1-57) 1-45	(1-118)..... 1-73	(5-1) 5-217
(1-58) 1-46	(1-119)..... 1-74	
(1-59) 1-46	(1-120)..... 1-74	
(1-60) 1-46	(1-121)..... 1-74	
(1-61) 1-46	(1-122)..... 1-74	

Bibliography

- Abdelbary, A. 2015. *Wear of Polymers and Composites*. Woddhead publishing.
- Albrecht, T.R., Grütter, P., Horne, D. and Rugar, D. 1991. Frequency modulation detection using high-Q cantilevers for enhanced force microscope sensitivity. *Journal of Applied Physics*. **69**(2), pp.668–673.
- Aristotle 350BC. On the Soul. . **405a**, pp.19–21.
- Armitage, J.L., Ghanbarzadeh, A., Bryant, M.G. and Neville, A. 2022. Investigating the Influence of Friction and Material Wear on Triboelectric Charge Transfer in Metal–Polymer Contacts. *Tribology Letters* 2022 70:2. **70**(2), pp.1–17.
- Armitage, J.L., Ghanbarzadeh, A., Wang, C. and Neville, A. 2021. An investigation into the influence of tribological parameters on the operation of sliding triboelectric nanogenerators. *Tribology International*. **155**, p.106778.
- Arridge, R.G.C. 1967. The static electrification of nylon 66. *British Journal of Applied Physics*. **18**(9), pp.1311–1316.
- ASM Handbook Committee 1990. *ASM Handbook Volume 2: Properties and Selection: Nonferrous Alloys and Special-Purpose Materials* 10th ed. ASM International.
- Avlonitis, M. and Kalaitzidou, K. 2015. Estimating the real contact area between sliding surfaces by means of a modified OFC model. *Archives of Civil and Mechanical Engineering*. **15**(2), pp.355–360.
- Bardeen, J., Cooper, L.N. and Schrieffer, J.R. 1957. Theory of superconductivity. *Physical Review*. **108**(5), pp.1175–1204.
- Barrett, N., Renault, O., Lemaître, H., Bonnaillie, P., Barcelo, F., Miserque, F., Wang, M. and Corbel, C. 2014. Microscopic work function anisotropy and surface chemistry of 316L stainless steel using photoelectron emission microscopy. *Journal of Electron Spectroscopy and Related Phenomena*. **195**, pp.117–124.
- Baytekin, H.T., Patashinski, A.Z., Branicki, M., Baytekin, B., Soh, S. and Grzybowski, B.A. 2011. The Mosaic of Surface Charge in Contact Electrification. *Science*. **333**(6040), pp.308–312.
- Benabdallah, H. 2003. Friction and wear of blended polyoxymethylene sliding against coated steel plates. *Wear*. **254**(12), pp.1239–1246.
- Bhushan, B. 2012. Bioinspired structured surfaces. *Langmuir*. **28**(3), pp.1698–1714.
- Birdi, K.S. (ed.). 2021. Surface Tension and Interfacial Tension of Liquids *In: Handbook of Surface and Colloid Chemistry*. CRC Press, pp.81–132.
- Biswas, S.K. and Vijayan, K. 1992. Friction and wear of PTFE - a review. *Wear*. **158**(1–2), pp.193–211.
- Bloch, F. 1929. Über die Quantenmechanik der Elektronen in Kristallgittern. *Zeitschrift für Physik* 1929 52:7. **52**(7), pp.555–600.
- Boehm, A.M., Wieser, J., Butrouna, K. and Graham, K.R. 2017. A new photon source for ultraviolet photoelectron spectroscopy of organic and other damage-prone materials. *Organic Electronics*. **41**, pp.9–16.
- Böer, K.W. and Pohl, U.W. 2017. Photon–Phonon Interaction *In: Semiconductor Physics* [Online]. Springer, Cham, pp.1–36. [Accessed 17 November 2022]. Available from: https://link.springer.com/referenceworkentry/10.1007/978-3-319-06540-3_11-2.
- Brennan, K.F. 2005. *Introduction to Semiconductor Devices: For Computing and Telecommunications Applications*. Cambridge University Press.
- Briscoe, B.J. and Sinha, S.K. 2002. Wear of polymers. *Proceedings of the Institution of Mechanical Engineers, Part J: Journal of Engineering Tribology*. **216**(6), pp.401–413.
- Burgo, T.A.L., Ducati, T.R.D., Francisco, K.R., Clinckspoor, K.J., Galembeck, F. and Galembeck, S.E. 2012. Triboelectricity: Macroscopic charge patterns formed by self-arraying ions on polymer surfaces. *Langmuir*. **28**(19), pp.7407–7416.
- Burgo, T.A.L., Galembeck, F. and Pollack, G.H. 2016. Where is water in the triboelectric series? *Journal of Electrostatics*. **80**, pp.30–33.
- Bush, A.W., Gibson, R.D. and Thomas, T.R. 1975. The elastic contact of a rough surface. *Wear*. **35**(1), pp.87–111.
- Camara, C.G., Escobar, J. V., Hird, J.R. and Putterman, S.J. 2008. Correlation between nanosecond X-ray flashes and stick–slip friction in peeling tape. *Nature* 2008 455:7216. **455**(7216), pp.1089–1092.
- Chen, Aihua, Zhang, Chen, Zhu, Guang, Lin Wang, Z., Chen, A, Zhang, C, Zhu, G and Wang, Z.L. 2020. Polymer Materials for High-Performance Triboelectric Nanogenerators. *Advanced Science*. **7**(14), p.2000186.

- Chen, J. and Wang, Z.L. 2017. Reviving Vibration Energy Harvesting and Self-Powered Sensing by a Triboelectric Nanogenerator. *Joule*. **1**(3), pp.480–521.
- Chen, X., Zhao, A., Li, J., Deng, J., Zhang, G. and Zhao, X. 2019. First-principle investigation of the charge injection barriers of polyethylene and polytetrafluoroethylene oligomers. *Journal of Applied Physics*. **126**(3), p.035101.
- Cheung, Y.K., Zhao, Z. and Yu, H. 2022. Self-Powered Galvanic Vibration Sensor. *Micromachines*. **13**(4), p.530.
- Cilveli, G., Okur, A. and Sölar, V. 2020. Electrostatic Properties of Clothing Fabrics Suitable for Different End-Uses. *FIBRES & TEXTILES in Eastern Europe*. **28**(1(139)), pp.50–57.
- Compton, R.N. and Duncan, M.A. 2015. The Speed of Sound in Gases, Liquids, and Solids. *Laser Experiments for Chemistry and Physics*, pp.122–143.
- Cowley, A.M. and Sze, S.M. 1965. Surface States and Barrier Height of Metal-Semiconductor Systems. *Journal of Applied Physics*. **36**(10), pp.3212–3220.
- Cramer, S.D. 2005. Density of Metals and Alloys *In*: S. D. Cramer and B. S. J. Covino, eds. *Corrosion: Materials* [Online]. ASM International, pp.658–661. [Accessed 17 November 2022]. Available from: <https://dl.asminternational.org/handbooks/edited-volume/25/chapter/347147/Density-of-Metals-and-Alloys>.
- Crawford, R.J. and Martin, P.J. 2020. Mechanical behaviour of plastics. *Plastics Engineering*, pp.59–194.
- Danganan, F., Espejo, C., Liskiewicz, T., Gester, M. and Neville, A. 2020. Friction and wear of additive manufactured polymers in dry contact. *Journal of Manufacturing Processes*. **59**, pp.238–247.
- Dash, J.G. and Wettlaufer, J.S. 2011. The surface physics of ice in thunderstorms. *Canadian Journal of Physics*. **81**(1–2), pp.201–207.
- Dekker, A.J. 1960. *Solid State Physics*. London: Macmillan.
- Derry, G.N., Kern, M.E. and Worth, E.H. 2015. Recommended values of clean metal surface work functions. *Journal of Vacuum Science & Technology A: Vacuum, Surfaces, and Films*. **33**(6), p.060801.
- Dharmasena, R.D.I.G., Jayawardena, K.D.G.I., Mills, C.A., Deane, J.H.B., Anguita, J. V., Dorey, R.A. and Silva, S.R.P. 2017. Triboelectric nanogenerators: Providing a fundamental framework. *Energy and Environmental Science*. **10**(8), pp.1801–1811.
- Diaz, A.F. and Felix-Navarro, R.M. 2004. A semi-quantitative tribo-electric series for polymeric materials: the influence of chemical structure and properties. *Journal of Electrostatics*. **62**(4), pp.277–290.
- Ding, P., Chen, J., Farooq, U., Zhao, P., Soin, N., Yu, L., Jin, H., Wang, X., Dong, S. and Luo, J. 2018. Realizing the potential of polyethylene oxide as new positive tribo-material: Over 40 W/m² high power flat surface triboelectric nanogenerators. *Nano Energy*. **46**, pp.63–72.
- Dini, D. and Hills, D.A. 2009. Frictional energy dissipation in a rough Hertzian contact. *Journal of Tribology*. **131**(2), pp.1–8.
- Dolbow, J. and Gosz, M. 1996. Effect of out-of-plane properties of a polyimide film on the stress fields in microelectronic structures. *Mechanics of Materials*. **23**(4), pp.311–321.
- Dong, Y., Mallineni, S.S.K., Maleski, K., Behlow, H., Mochalin, V.N., Rao, A.M., Gogotsi, Y. and Podila, R. 2018. Metallic MXenes: A new family of materials for flexible triboelectric nanogenerators. *Nano Energy*. **44**, pp.103–110.
- Dorgham, A., Wang, C., Morina, A. and Neville, A. 2019. 3D tribo-nanoprinting using triboreactive materials. *Nanotechnology*. **30**(9), p.095302.
- Dransfeld, K. and Li-Jie 1995. Coherent Phonon Generation in the Process of Friction *In: Forces in Scanning Probe Methods* [Online]. Springer, Dordrecht, pp.273–283. [Accessed 17 November 2022]. Available from: https://link.springer.com/chapter/10.1007/978-94-011-0049-6_24.
- Eastment, R.M. and Mee, C.H.B. 1973. Work function measurements on (100), (110) and (111) surfaces of aluminium. *Journal of Physics F: Metal Physics*. **3**(9), p.1738.
- Ebnesajjad, S. 2011. Surface Tension and Its Measurement *In: Handbook of Adhesives and Surface Preparation: Technology, Applications and Manufacturing*. William Andrew Publishing, pp.21–30.
- Fabish, T.J. and Duke, C.B. 1977. Molecular charge states and contact charge exchange in polymers. *Journal of Applied Physics*. **48**(10), pp.4256–4266.
- Fan, F.-R., Tian, Z.-Q. and Lin Wang, Z. 2012. Flexible triboelectric generator. *Nano Energy*. **1**(2), pp.328–334.

- Feldman, B., Park, S., Haverty, M., Shankar, S. and Dunham, S.T. 2010. Simulation of grain boundary effects on electronic transport in metals, and detailed causes of scattering. *physica status solidi (b)*. **247**(7), pp.1791–1796.
- Francis, C.R. 1982. Electrostatic charging problems of spacecraft. *Journal of Electrostatics*. **11**(3), pp.265–280.
- Garcia, D. and Starkweather, H.W. 1985. Hydrogen bonding in nylon 66 and model compounds. *Journal of Polymer Science: Polymer Physics Edition*. **23**(3), pp.537–555.
- García, R. and Pérez, R. 2002. Dynamic atomic force microscopy methods. *Surface Science Reports*. **47**(6–8), pp.197–301.
- Ghanbarzadeh, A., Parsaeian, P., Morina, A., Wilson, M.C.T., Van Eijk, M.C.P., Nedelcu, I., Dowson, D. and Neville, A. 2016. A Semi-deterministic Wear Model Considering the Effect of Zinc Dialkyl Dithiophosphate Tribofilm. *Tribology Letters*. **61**(1), pp.1–15.
- Giessibl, F.J. 2003. Advances in atomic force microscopy. *Reviews of Modern Physics*. **75**(3), pp.949–983.
- Gilbert, W. 1600. *De Magnete* 1st ed. London: P. Short.
- Gillespie, R.J. and Robinson, E.A. 2007. Gilbert N. Lewis and the chemical bond: The electron pair and the octet rule from 1916 to the present day. *Journal of Computational Chemistry*. **28**(1), pp.87–97.
- Girardeaux, C. and Pireaux, J.-J. 2021. Analysis of Poly(tetrafluoroethylene) (PTFE) by XPS. *Surface Science Spectra*. **4**(2), p.138.
- Van De Graaff, R.J., Compton, K.T. and Van Atta, L.C. 1933. The Electrostatic Production of High Voltage for Nuclear Investigations. *Physical Review*. **43**(3), p.149.
- Gu, Z., Wei, W., Su, J. and Yu, C.W. 2013. The role of water content in triboelectric charging of wind-blown sand. *Scientific Reports* 2013 3:1. **3**(1), pp.1–6.
- von Guericke, O. 1672. *Experimenta Nova (ut vocantur) Magdeburgica de Vacuo Spatio*. Magdeburg: Apud Joannem Janssonium à Waesberge.
- Ha, M., Park, J., Lee, Y. and Ko, H. 2015. Triboelectric Generators and Sensors for Self-Powered Wearable Electronics. *ACS Nano*. **9**(4), pp.3421–3427.
- Harper, W.R. 1951a. Interpretation of experiments on frictional electrification. *Nature*. **167**(4245), pp.400–401.
- Harper, W.R. 1951b. The Volta Effect as a Cause of Static Electrification. *Proceedings of the Royal Society of London. Series A, Mathematical and Physical Sciences*. **205**, pp.83–103.
- Hasegawa, H. 1999. Fermi level pinning and schottky barrier height control at metal-semiconductor interfaces of InP and related materials. *Japanese Journal of Applied Physics, Part 1: Regular Papers and Short Notes and Review Papers*. **38**(2 B), pp.1098–1102.
- Hawksbee, F. 1709. *Physico-Mechanical Experiments on Various Subjects*. London: R. Brugis.
- Helander, M.G., Greiner, M.T., Wang, Z.B. and Lu, Z.H. 2010. Pitfalls in measuring work function using photoelectron spectroscopy. *Applied Surface Science*. **256**(8), pp.2602–2605.
- Henniker, J. 1962. Triboelectricity in Polymers. *Nature* 1962 196:4853. **196**(4853), pp.474–474.
- Hertz, H. 1882. Ueber die Berührung fester elastischer Körper. *Journal für die Reine und Angewandte Mathematik*. **1882**(92), pp.156–171.
- Holt, D.B., Farmer, B.L., Macturk, K.S. and Eby, R.K. 1996. Fluoropolymer force fields derived from semiempirical molecular orbital calculations. *Polymer*. **37**(10), pp.1847–1855.
- Hoshina, H., Kanemura, T. and Ruggiero, M.T. 2020. Exploring the Dynamics of Bound Water in Nylon Polymers with Terahertz Spectroscopy. *Journal of Physical Chemistry B*. **124**(2), pp.422–429.
- Hou, T.-C., Yang, Y., Zhang, H., Chen, J., Chen, L.-J. and Lin Wang, Z. 2013. Triboelectric nanogenerator built inside shoe insole for harvesting walking energy. *Nano Energy*. **2**(5), pp.856–862.
- Huber, K.P. and Herzberg, G. 1979. Constants of diatomic molecules *In: Molecular Spectra and Molecular Structure* [Online]. Boston: Springer, p.649. [Accessed 17 November 2022]. Available from: https://link.springer.com/chapter/10.1007/978-1-4757-0961-2_2.
- International Union of Pure and Applied Chemistry. Commission on Atomic Weights. 1976. *Atomic Weights of the Elements 1975* 1st ed.
- Iversen, P. and Lacks, D.J. 2012. A life of its own: The tenuous connection between Thales of Miletus and the study of electrostatic

- charging. *Journal of Electrostatics*. **70**(3), pp.309–311.
- Jarolimek, K., Hazrati, E., De Groot, R.A. and De Wijs, G.A. 2017. Band Offsets at the Interface between Crystalline and Amorphous Silicon from First Principles. *Physical Review Applied*. **8**(1), p.014026.
- Jason A. Wiles, Bartosz A. Grzybowski, *, Adam Winkleman, A. and Whitesides*, G.M. 2003. A Tool for Studying Contact Electrification in Systems Comprising Metals and Insulating Polymers.
- Jena, D. 2022. Taking the Heat: Phonons and Electron-Phonon Interactions *In: Quantum Physics of Semiconductor Materials and Devices* [Online]. Oxford University Press Oxford, pp.531–554. [Accessed 17 November 2022]. Available from: <https://academic.oup.com/book/43800/chapter/370781147>.
- Jeng, Y.R. and Gao, C.C. 2008. Changes of Surface Topography during Wear for Surfaces with Different Height Distributions. *Tribology Transactions*. **43**(4), pp.749–757.
- Jiang, Q., Wu, C., Wang, Z., Wang, A.C., He, J.-H., Wang, Z.L. and Alshareef, H.N. 2018. MXene Electrochemical Microsupercapacitor Integrated with Triboelectric Nanogenerator as a Wearable Self-charging Power Unit. *Nano Energy*.
- de Jong, M.P., Friedlein, R., Osikowicz, W., Salaneck, W.R. and Fahlman, M. 2006. Ultraviolet Photoelectron Spectroscopy of Polymers. *Molecular Crystals and Liquid Crystals*. **455**(1), pp.193–203.
- Jost, H.P. 1966. *Lubrication: Tribology; Education and Research; Report on the Present Position and Industry's Needs*. London: HM Stationery Office.
- Jung, M.R., Horgen, F.D., Orski, S. V., Rodriguez C., V., Beers, K.L., Balazs, G.H., Jones, T.T., Work, T.M., Brignac, K.C., Royer, S.-J., Hyrenbach, K.D., Jensen, B.A. and Lynch, J.M. 2018. Validation of ATR FT-IR to identify polymers of plastic marine debris, including those ingested by marine organisms. *Marine Pollution Bulletin*. **127**, pp.704–716.
- Kaelble, D.H. 2008. Dispersion-Polar Surface Tension Properties of Organic Solids. *The Journal of Adhesion*. **2**(2), pp.66–81.
- Keithley, J.F. 1999. The story of electrical and magnetic measurements : from 500 B.C. to the 1940s. , p.240.
- Khvolson, O.D., Cosserat, E., Cosserat, F. and Davaux, E. 1906. *Traité de Physique* [Online]. Paris: Librairie Scientifique A. Hermann & Fils. [Accessed 20 July 2022]. Available from: <https://link.springer.com/article/10.1007/BF01708143>.
- Kim, S. 2019. High-order calculation of triboelectric charge density using a transition matrix element in a triboelectric nanogenerator system. *Journal of Physics Communications*. **3**(9), p.095002.
- Kim, T., Kim, D.Y., Yun, J., Kim, B., Lee, S.H., Kim, D. and Lee, S. 2018. Direct-current triboelectric nanogenerator via water electrification and phase control. *Nano Energy*. **52**, pp.95–104.
- Kiss, I., Szedenik, N. and Berta, I. 2005. Electrostatic hazard and protection: Expert system for fuel delivery modules. *Journal of Electrostatics*. **63**(6–10), pp.495–499.
- Knoblauch, O. 1902. Versuche über die Berührungselektrizität. *Zeitschrift für Physikalische Chemie*. **39U**(1), pp.225–244.
- Kohan, M.I. 1986. HISTORY AND DEVELOPMENT OF NYLON-66. , pp.19–37.
- Kuptsov, A.H. and Zhizhin, G.N. (German N. 1998. Handbook of fourier transform Raman and infrared spectra of polymers. , p.536.
- Kutzelnigg, W. and Morgan, J.D. 1996. Hund's rules. *Zeitschrift für Physik D Atoms, Molecules and Clusters* 1996 36:3. **36**(3), pp.197–214.
- Lax, J.Y., Price, C. and Saaroni, H. 2020. On the Spontaneous Build-Up of Voltage between Dissimilar Metals Under High Relative Humidity Conditions. *Scientific Reports* 2020 10:1. **10**(1), pp.1–9.
- Lee, J.-W. and Hwang, W. 2018. Theoretical study of micro/nano roughness effect on water-solid triboelectrification with experimental approach. *Nano Energy*. **52**, pp.315–322.
- Lee, L.-H. 1994. Dual mechanism for metal-polymer contact electrification. *Journal of Electrostatics*. **32**(1), pp.1–29.
- Li, C., Dong, S. and Zhang, G. 2000. Evaluation of the root-mean-square slope of 3D surface topography. *International Journal of Machine Tools and Manufacture*. **40**(3), pp.445–454.
- Li, R., Cai, C., Hu, L., Wu, H., Zhang, W. and Zhu, J. 2013. Band alignment of ZnO/CdSe quantum dots heterojunction determined by ultraviolet photoelectron spectroscopy using synchrotron radiation. *Applied Surface Science*. **276**, pp.258–261.
- Libbrecht, K.G. 2012. Toward a Comprehensive Model of Snow Crystal Growth Dynamics: 1. Overarching Features and Physical Origins.
- Lu, S., Zhang, H., Hu, Q.-M., -, al, Khanna, A.J., Yamamura, M., Raghava Kakireddy, V., Mudhivarthi, S., Gitis, N., Kuiry, S. and

- Lowell, J. 1975. Contact electrification of metals. *Journal of Physics D: Applied Physics*. **8**(1), p.53.
- Luo, J. and Wang, Z.L. 2020. Recent progress of triboelectric nanogenerators: From fundamental theory to practical applications. *EcoMat*. **2**(4), p.e12059.
- Luo, N., Feng, Y., Zhang, L., Sun, W., Wang, D., Sun, X., Zhou, F. and Liu, W. 2021. Controlling the tribological behavior at the friction interface by regulating the triboelectrification. *Nano Energy*. **87**, p.106183.
- Luo, Y.R. 2002. Handbook of bond dissociation energies in organic compounds. *Handbook of Bond Dissociation Energies in Organic Compounds*, pp.1–380.
- Matsusaka, S., Maruyama, H., Matsuyama, T. and Ghadiri, M. 2010. Triboelectric charging of powders: A review. *Chemical Engineering Science*. **65**(22), pp.5781–5807.
- Matsusaka, S. and Masuda, H. 2003. Electrostatics of particles. *Advanced Powder Technology*. **14**(2), pp.143–166.
- Melitz, W., Shen, J., Kummel, A.C. and Lee, S. 2011. Kelvin probe force microscopy and its application. *Surface Science Reports*. **66**(1), pp.1–27.
- Mitcheson, P.D., Yeatman, E.M., Rao, G.K., Holmes, A.S. and Green, T.C. 2008. Energy Harvesting From Human and Machine Motion for Wireless Electronic Devices. *Proceedings of the IEEE*. **96**(9), pp.1457–1486.
- Mizes, H.A., Conwell, E.M. and Salamida, D.P. 1990. Direct observation of ion transfer in contact charging between a metal and a polymer. *Applied Physics Letters*. **56**(16), pp.1597–1599.
- Mizzi, C.A., Lin, A.Y.W. and Marks, L.D. 2019. Does flexoelectricity drive triboelectricity? *Physical Review Letters*. **123**(11), p.116103.
- Mizzi, C.A. and Marks, L.D. 2022. When Flexoelectricity Drives Triboelectricity. *Nano Letters*.
- Murata, Y. and Kittaka, S. 1979. Evidence of Electron Transfer as the Mechanism of Static Charge Generation by Contact of Polymers with Metals. *Japanese Journal of Applied Physics, Part 1: Regular Papers and Short Notes and Review Papers*. **18**(2), p.421.
- Murphy, L.R., Meek, T.L., Louis Allred, A. and Alien, L.C. 2000. Evaluation and test of Pauling's electronegativity scale. *Journal of Physical Chemistry A*. **104**(24), pp.5867–5871.
- Nan, Y., Shao, J., Willatzen, M. and Wang, Z.L. 2022. Understanding Contact Electrification at Water/Polymer Interface. *Research*. **2022**, pp.1–10.
- Newton, I. 1704. *Opticks*. London.
- Nguyen, V. and Yang, R. 2013. Effect of humidity and pressure on the triboelectric nanogenerator. *Nano Energy*. **2**(5), pp.604–608.
- Nguyen, V., Zhu, R. and Yang, R. 2015. Environmental effects on nanogenerators. *Nano Energy*. **14**, pp.49–61.
- Nie, J., Ren, Z., Xu, L., Lin, S., Zhan, F., Chen, X. and Wang, Z.L. 2020. Probing Contact-Electrification-Induced Electron and Ion Transfers at a Liquid–Solid Interface. *Advanced Materials*. **32**(2), p.1905696.
- Niu, S. 2015. Theoretical systems of triboelectric nanogenerators. *Nano Energy*. **14**, pp.161–192.
- Niu, S., Liu, Y., Chen, X., Wang, S., Zhou, Y.S., Lin, L., Xie, Y. and Wang, Z.L. 2015. Theory of freestanding triboelectric-layer-based nanogenerators. *Nano Energy*. **12**.
- Niu, S., Liu, Y., Wang, S., Lin, L., Zhou, Y.S., Hu, Y. and Wang, Z.L. 2013. Theory of Sliding-Mode Triboelectric Nanogenerators. *Advanced Materials*. **25**(43), pp.6184–6193.
- Niu, S., Wang, S., Lin, L., Liu, Y., Zhou, Y.S., Hu, Y. and Wang, Z.L. 2013. Theoretical study of contact-mode triboelectric nanogenerators as an effective power source. *Energy & Environmental Science*. **6**(12), p.3576.
- Nonnenmacher, M., O'Boyle, M.P. and Wickramasinghe, H.K. 1991. Kelvin probe force microscopy. *Applied Physics Letters*. **58**(25), pp.2921–2923.
- Owens, D.K. and Wendt, R.C. 1969. Estimation of the surface free energy of polymers. *undefined*. **13**(8), pp.1741–1747.
- Pan, S. and Zhang, Z. 2017. Triboelectric effect: A new perspective on electron transfer process. *Journal of Applied Physics*. **122**(14), p.144302.
- Pan Wong, D. 1979. Theoretical justification of Madelung's rule. *Journal of Chemical Education*. **56**(11), pp.714–717.
- Pancaldi, G. 2003. *Volta: Science and Culture in the Age of Enlightenment*. Princeton: Princeton Press.

- Pang, H., Tian, K., Li, Y., Su, C., Duan, F. and Xu, Y. 2021. Super-hydrophobic PTFE hollow fiber membrane fabricated by electrospinning of Pullulan/PTFE emulsion for membrane deamination. *Separation and Purification Technology*. **274**, p.118186.
- Park, B.S. and Stetten, D. 2001. A Principle Written in Diagrams: The Aufbau Principle for Molecules and Its Visual Representations, 1927–1932. , pp.179–198.
- Park, S., Schultz, T., Shin, D., Mutz, N., Aljarb, A., Kang, H.S., Lee, C.H., Li, L.J., Xu, X., Tung, V., List-Kratochvil, E.J.W., Blumstengel, S., Amsalem, P. and Koch, N. 2021. The Schottky-Mott Rule Expanded for Two-Dimensional Semiconductors: Influence of Substrate Dielectric Screening. *ACS Nano*. **15**(9), pp.14794–14803.
- Pashley, M.D., Haberern, K.W., Feenstra, R.M. and Kirchner, P.D. 1993. Different Fermi-level pinning behavior on n- and p-type GaAs(001). *Physical Review B*. **48**(7), p.4612.
- Pauli, W. 1925. Über den Zusammenhang des Abschlusses der Elektronengruppen im Atom mit der Komplexstruktur der Spektren. *Zeitschrift für Physik*. **31**(1), pp.765–783.
- Peckner, D. and Bernstein, I.M. 1977. *Handbook of Stainless Steels*. New York: McGraw-Hill Book Company.
- Pellissier, G. 1891. Théorie de la machine de Wimshurst. *Journal de Physique Théorique et Appliquée*. **10**(1), pp.414–419.
- Perucca, E. 1928. Ein gründliches Experiment über die Kontakttheorie der Triboelektrizität. — Voltaeffekt erster Art und elektrische Doppelschichten beim Kontakt. *Zeitschrift für Physik* 1928 51:3. **51**(3), pp.268–278.
- Plato 360BC. Timaeus 80c.
- Plutarch 100AD. Moralia XIII: Platonicae Quaestiones. . **13**(7), p.7.
- Poole, C. and Darwazeh, I. 2016. Microwave semiconductor materials and diodes *In: Microwave Active Circuit Analysis and Design*. Academic Press, pp.355–393.
- Popov, B.N. 2015. Galvanic Corrosion *In: Corrosion Engineering* [Online]. Elsevier, pp.239–287. [Accessed 17 November 2022]. Available from: <https://linkinghub.elsevier.com/retrieve/pii/B9780444627223000069>.
- Priestley, J. 1767. *he History and Present State of Electricity, with original experiments*. London: Printed for J. Dodsley, J. Johnson and T. Cadell.
- Qiu, X.H., Qi, G.C., Yang, Y.L. and Wang, C. 2008. Electrostatic characteristics of nanostructures investigated using electric force microscopy. *Journal of Solid State Chemistry*. **181**(7), pp.1670–1677.
- Racko, J., Grmanova, A. and Breza, J. 1996. Extended thermionic emission-diffusion theory of charge transport through a Schottky diode. *Solid-State Electronics*. **39**(3), pp.391–397.
- Richards, H.F. 1920. Electrification by Impact. *Physical Review*. **16**(4), p.290.
- Richards, H.F. 1923. The Contact Electricity of Solid Dielectrics. *Physical Review*. **22**(2), p.122.
- Richardson, O.W. 1912. The electron theory of contact electromotive force and thermoelectricity. *The London, Edinburgh and Dublin philosophical magazine and journal of science*. **23**(134), pp.263–278.
- Sadewasser, S. and Barth, C. 2012. Electrostatic Force Microscopy And Kelvin Probe Force Microscopy. *Characterization of Materials.*, pp.1–12.
- Sakaguchi, M., Makino, M., Ohura, T. and Iwata, T. 2014. Contact electrification of polymers due to electron transfer among mechano anions, mechano cations and mechano radicals. *Journal of Electrostatics*. **72**(5), pp.412–416.
- Sakaguchi, M., Shimada, S. and Kashiwabara, H. 1990. Mechanoions Produced by Mechanical Fracture of Solid Polymer. 6. A Generation Mechanism of Triboelectricity due to the Reaction of Mechanoradicals with Mechanoanions on the Friction Surface. *Macromolecules*. **23**(23), pp.5038–5040.
- Saurenbach, F., Wollmann, D., Terris, B.D. and Diaz, A.F. 1992. Force microscopy of ion-containing polymer surfaces: morphology and charge structure. *Langmuir*. **8**(4), pp.1199–1203.
- Sayfidinov, K., Cezan, S.D., Baytekin, B. and Baytekin, H.T. 2018. Minimizing friction, wear, and energy losses by eliminating contact charging. *Science Advances*. **4**(11), pp.3808–3824.
- Schroeder, L.R. and Cooper, S.L. 2008. Hydrogen bonding in polyamides. *Journal of Applied Physics*. **47**(10), p.4310.
- Sedlaček, M., Podgornik, B. and Vižintin, J. 2012. Correlation between standard roughness parameters skewness and kurtosis and tribological behaviour of contact surfaces *In: Tribology International*. Elsevier, pp.102–112.

- Seki, K., Tanaka, H., Ohta, T., Aoki, Y., Imamura, A., Fujimoto, H., Yamamoto, H., Inokuchi, H., Tanaka, H., Aoki, Y. and Yamamoto, H. 1990. Electronic structure of poly(tetrafluoroethylene) studied by UPS, VUV absorption, and band calculations. *Physica Scripta*. **41**(1), pp.167–171.
- Seol, M.-L., Han, J.-W., Moon, D.-I. and Meyyappan, M. 2017a. Hysteretic behavior of contact force response in triboelectric nanogenerator. *Nano Energy*. **32**, pp.408–413.
- Seol, M.-L., Han, J.-W., Moon, D.-I. and Meyyappan, M. 2017b. Triboelectric nanogenerator for Mars environment. *Nano Energy*. **39**, pp.238–244.
- Shaw, P.E. 1917. Experiments on tribo-electricity. I.—The tribo-electric series. *Proceedings of the Royal Society of London. Series A, Containing Papers of a Mathematical and Physical Character*. **94**(656), pp.16–33.
- Shaw, P.E. and Jex, C.S. 1928a. Tribo-electricity and friction. II.—Glass and solid elements. *Proceedings of the Royal Society of London. Series A, Containing Papers of a Mathematical and Physical Character*. **118**(779), pp.97–108.
- Shaw, P.E. and Jex, C.S. 1928b. Tribo-electricity and friction. III.—Solid elements and textiles. *Proceedings of the Royal Society of London. Series A, Containing Papers of a Mathematical and Physical Character*. **118**(779), pp.108–113.
- Shaw, P.E. and Jex, C.S. 1926. Tribo-electricity and friction. *Proceedings of the Royal Society of London. Series A, Containing Papers of a Mathematical and Physical Character*. **111**(758), pp.339–355.
- Shen, J., Goronkin, H., Dow, J.D. and Ren, S.Y. 1998. Tamm states and donors at InAs/AlSb interfaces. *Journal of Applied Physics*. **77**(4), p.1576.
- Shirakawa, Y., Li, N., Yoshida, M., Takashima, R., Shimosaka, A. and Hidaka, J. 2010. Quantum chemical calculation of electron transfer at metal/polymer interfaces. *Advanced Powder Technology*. **21**(4), pp.500–505.
- Soh, S., Kwok, S.W., Liu, H. and Whitesides, G.M. 2012. Contact De-electrification of electrostatically charged polymers. *Journal of the American Chemical Society*. **134**(49), pp.20151–20159.
- Sow, M., Widenor, R., Kumar, A., Lee, S.W., Lacks, D.J. and Sankaran, R.M. 2012. Strain-Induced Reversal of Charge Transfer in Contact Electrification. *Angewandte Chemie International Edition*. **51**(11), pp.2695–2697.
- Šupuk, E., Zarrebini, A., Reddy, J.P., Hughes, H., Leane, M.M., Tobyn, M.J., Timmins, P. and Ghadiri, M. 2012. Tribo-electrification of active pharmaceutical ingredients and excipients. *Powder Technology*. **217**, pp.427–434.
- Tcho, I.-W., Kim, W.-G., Jeon, S.-B., Park, S.-J., Lee, B.J., Bae, H.-K., Kim, D. and Choi, Y.-K. 2017. Surface structural analysis of a friction layer for a triboelectric nanogenerator. *Nano Energy*. **42**, pp.34–42.
- Tewari, U.S., Sharma, S.K. and Vasudevan, P. 2014. Polymer tribology *In: Wear of Polymers and Composites*. Woodhead Publishing, pp.1–36.
- Theophrastus 300BC. On Stones.
- Thomas III, S.W., Vella, S.J., Dickey, M.D., Kaufman, G.K. and Whitesides, G.M. 2009. Controlling the Kinetics of Contact Electrification with Patterned Surfaces. *Journal of the American Chemical Society*. **131**(25), pp.8746–8747.
- Trigwell, S., Grable, N., Yurteri, C.U., Sharma, R. and Mazumder, M.K. 2003. Effects of surface properties on the tribocharging characteristics of polymer powder as applied to industrial processes. *IEEE Transactions on Industry Applications*. **39**(1), pp.79–86.
- Tusche, C., Chen, Y.J., Schneider, C.M. and Kirschner, J. 2019. Imaging properties of hemispherical electrostatic energy analyzers for high resolution momentum microscopy. *Ultramicroscopy*. **206**, p.112815.
- Vasandani, P., Mao, Z.-H., Jia, W. and Sun, M. 2017. Relationship between triboelectric charge and contact force for two triboelectric layers. *Journal of Electrostatics*. **90**, pp.147–152.
- Vick, F.A. 1953. Theory of contact electrification. *British Journal of Applied Physics*. **4**(S2), p.S1.
- Viswanathan, K. and Sundaram, N.K. 2017. Distinct stick-slip modes in adhesive polymer interfaces. *Wear*. **376–377**, pp.1271–1278.
- Walton, A.J. 1977. Triboluminescence. *Advances in Physics*. **26**(6), pp.887–948.
- Wang, A.C., Zhang, B., Xu, C., Zou, H., Lin, Z. and Wang, Z.L. 2020. Unraveling Temperature-Dependent Contact Electrification between Sliding-Mode Triboelectric Pairs. *Advanced Functional Materials*. **30**(12), p.1909384.
- Wang, C., Duscher, G. and Paddison, S.J. 2014. Electron energy loss spectroscopy of polytetrafluoroethylene: experiment and first principles calculations. *Microscopy*. **63**(1), pp.73–83.

- Wang, S., Lin, L. and Wang, Z.L. 2015. Triboelectric nanogenerators as self-powered active sensors. *Nano Energy*. **11**, pp.436–462.
- Wang, S., Lin, L., Xie, Y., Jing, Q., Niu, S. and Wang, Z.L. 2013. Sliding-Triboelectric Nanogenerators Based on In-Plane Charge-Separation Mechanism. *Nano Letters*. **13**(5), pp.2226–2233.
- Wang, S., Xie, Y., Niu, S., Lin, L. and Wang, Z.L. 2014. Freestanding Triboelectric-Layer-Based Nanogenerators for Harvesting Energy from a Moving Object or Human Motion in Contact and Non-contact Modes. *Advanced Materials*. **26**(18), pp.2818–2824.
- Wang, Y. and Yan, F. 2006. Tribological properties of transfer films of PTFE-based composites. *Wear*. **261**(11–12), pp.1359–1366.
- Wang, Z.L. 2017a. On Maxwell's displacement current for energy and sensors: the origin of nanogenerators. *Materials Today*. **20**(2), pp.74–82.
- Wang, Z.L. 2017b. On Maxwell's displacement current for energy and sensors: the origin of nanogenerators. *Materials Today*. **20**(2), pp.74–82.
- Wang, Z.L., Jiang, T. and Xu, L. 2017. Toward the blue energy dream by triboelectric nanogenerator networks. *Nano Energy*. **39**, pp.9–23.
- Wang, Z.L. and Wang, A.C. 2019. On the origin of contact-electrification. *Materials Today*.
- Wen, X., Su, Y., Yang, Y., Zhang, H. and Wang, Z.L. 2014. Applicability of triboelectric generator over a wide range of temperature. *Nano Energy*. **4**, pp.150–156.
- Wilcke, J.C. 1757. *Disputatio Physica Experimentalis, De Electricitatibus Contrariis: Qvam Consentiente*. Rostock: Ioannis Iacobi Adleri.
- Wilcke, J.C. 1762. Ytterligare rön och försök om contraria electriciteterna vid laddningen och därtill hörande delar. *Kongliga Svenska Vetenskaps Academiens Handlingar*. **23**, pp.206–299.
- Willatzen, M., Lew Yan Voon, L.C. and Wang, Z.L. 2020. Quantum Theory of Contact Electrification for Fluids and Solids. *Advanced Functional Materials*. **30**(17), p.1910461.
- Willatzen, M. and Wang, Z.L. 2019. Contact Electrification by Quantum-Mechanical Tunneling. *Research*. **2019**, pp.1–11.
- Williams, M.W. 2012. Triboelectric charging of insulating polymers—some new perspectives. *AIP Advances*. **2**(1), p.010701.
- Wojciechowski, K.F. 1997. Work function of transition metals calculated from Brodie's expression (corrected values). *Vacuum*. **48**(11), pp.891–892.
- Xi, F., Pang, Y., Li, W., Bu, T., Zhao, J., Liu, G., Guo, T., Liu, W. and Zhang, C. 2018. Tribotronic bipolar junction transistor for mechanical frequency monitoring and use as touch switch. *Microsystems & Nanoengineering* **2018 4:1**. **4**(1), pp.1–8.
- Xi, F., Pang, Y., Li, W., Jiang, T., Zhang, L., Guo, T., Liu, G., Zhang, C. and Wang, Z.L. 2017. Universal power management strategy for triboelectric nanogenerator. *Nano Energy*. **37**, pp.168–176.
- Xia, X., Chen, J., Liu, G., Javed, M.S., Wang, X. and Hu, C. 2017. Aligning graphene sheets in PDMS for improving output performance of triboelectric nanogenerator. *Carbon*. **111**.
- Xie, Y., Wang, S., Niu, S., Lin, L., Jing, Q., Yang, J., Wu, Z. and Wang, Z.L. 2014. Grating-Structured Freestanding Triboelectric-Layer Nanogenerator for Harvesting Mechanical Energy at 85% Total Conversion Efficiency. *Advanced Materials*. **26**(38), pp.6599–6607.
- Xu, C., Zi, Y., Wang, A.C., Zou, H., Dai, Y., He, X., Wang, P., Wang, Y.-C., Feng, P., Li, D. and Wang, Z.L. 2018. On the Electron-Transfer Mechanism in the Contact-Electrification Effect. *Advanced Materials*. **30**(15), p.1706790.
- Xu, Y., Min, G., Gadegaard, N., Dahiya, R. and Mulvihill, D.M. 2020. A unified contact force-dependent model for triboelectric nanogenerators accounting for surface roughness. *Nano Energy*. **76**, p.105067.
- Yan, B., Stadtmüller, B., Haag, N., Jakobs, S., Seidel, J., Jungkenn, D., Mathias, S., Cinchetti, M., Aeschlimann, M. and Felser, C. 2015. Topological states on the gold surface. *Nature Communications* **2015 6:1**. **6**(1), pp.1–6.
- Yang, J., Yang, F., Zhao, L., Shang, W., Qin, H., Wang, S., Jiang, X., Cheng, G. and Du, Z. 2018. Managing and optimizing the output performances of a triboelectric nanogenerator by a self-powered electrostatic vibrator switch. *Nano Energy*. **46**, pp.220–228.
- Yang, Y., Zhang, H., Chen, J., Jing, Q., Zhou, Y.S., Wen, X. and Wang, Z.L. 2013. Single-Electrode-Based Sliding Triboelectric Nanogenerator for Self-Powered Displacement Vector Sensor System. *ACS Nano*. **7**(8), pp.7342–7351.

- Yilbas, B.S., Keles, O. and Toprakli, A.Y. 2017. Surface Engineering towards Self-Cleaning Applications: Laser Textured Silicon Surface. *Procedia Engineering*. **184**, pp.716–724.
- Young, R., Ward, J. and Scire, F. 1971. Observation of Metal-Vacuum-Metal Tunneling, Field Emission, and the Transition Region. *Physical Review Letters*. **27**(14), p.922.
- Yu, Z.-Z. and Watson, P.K. 1989. Contact charge accumulation and reversal on polystyrene and PTFE films upon repeated contacts with mercury. *Journal of Physics D: Applied Physics*. **22**(6), pp.798–801.
- Zakarian, D., Khachatryan, A. and Firstov, S. 2019. Universal temperature dependence of Young's modulus. *Metal Powder Report*.
- Zarrebini, A., Ghadiri, M., Dyson, M., Kippax, P. and McNeil-Watson, F. 2013. Tribo-electrification of powders due to dispersion. *Powder Technology*. **250**, pp.75–83.
- Zeng, Q., Qin, Y., Chang, W. and Luo, X. 2018. Correlating and evaluating the functionality-related properties with surface texture parameters and specific characteristics of machined components. *International Journal of Mechanical Sciences*. **149**, pp.62–72.
- Zhai, C., Chou, X., He, J., Song, L., Zhang, Z., Wen, T., Tian, Z., Chen, X., Zhang, W., Niu, Z. and Xue, C. 2018. An electrostatic discharge based needle-to-needle booster for dramatic performance enhancement of triboelectric nanogenerators. *Applied Energy*. **231**, pp.1346–1353.
- Zhang, J., Rogers, F.J.M., Darwish, N., Gonçalves, V.R., Vogel, Y.B., Wang, F., Gooding, J.J., Peiris, M.C.R., Jia, G., Veder, J.P., Coote, M.L. and Ciampi, S. 2019. Electrochemistry on Tribocharged Polymers Is Governed by the Stability of Surface Charges Rather than Charging Magnitude. *Journal of the American Chemical Society*. **141**(14), pp.5863–5870.
- Zhang, W., Diao, D., Sun, K., Fan, X. and Wang, P. 2018. Study on friction-electrification coupling in sliding-mode triboelectric nanogenerator. *Nano Energy*. **48**, pp.456–463.
- Zhang, W., Gu, G., Qin, H., Li, S., Shang, W., Wang, T., Zhang, B., Cui, P., Guo, J., Yang, F., Cheng, G. and Du, Z. 2020. Measuring the actual voltage of a triboelectric nanogenerator using the non-grounded method. *Nano Energy*. **77**, p.105108.
- Zhang, W., Gu, G., Shang, W., Luo, H., Wang, T., Zhang, B., Cui, P., Guo, J., Yang, F., Cheng, G. and Du, Z. 2021. A general charge compensation strategy for calibrating the voltage of a triboelectric nanogenerator measured by a capacitive circuit. *Nano Energy*. **86**, p.106056.
- Zhang, X., Scaraggi, M., Zheng, Y., Li, X., Wu, Y., Wang, D., Dini, D. and Zhou, F. 2022. Quantifying Wetting Dynamics with Triboelectrification. *Advanced Science*. **9**(24), p.2200822.
- Zhang, Z., He, T., Zhao, J., Liu, G., Wang, Z.L. and Zhang, C. 2021. Tribo-thermoelectric and tribovoltaic coupling effect at metal-semiconductor interface. *Materials Today Physics*. **16**, p.100295.
- Zhou, Y., Deng, W., Xu, J. and Chen, J. 2020. Engineering Materials at the Nanoscale for Triboelectric Nanogenerators. *Cell Reports Physical Science*. **1**(8), p.100142.
- Zhou, Y.S., Liu, Y., Zhu, G., Lin, Z.-H., Pan, C., Jing, Q. and Wang, Z.L. 2013. In Situ Quantitative Study of Nanoscale Triboelectrification and Patterning. *Nano Letters*. **13**(6), pp.2771–2776.
- Zhou, Y.S., Wang, S., Yang, Y., Zhu, G., Niu, S., Lin, Z.-H., Liu, Y. and Wang, Z.L. 2014. Manipulating Nanoscale Contact Electrification by an Applied Electric Field. *Nano Letters*. **14**(3), pp.1567–1572.
- Zhu, G., Lin, Z.-H., Jing, Q., Bai, P., Pan, C., Yang, Y., Zhou, Y. and Wang, Z.L. 2013. Toward Large-Scale Energy Harvesting by a Nanoparticle-Enhanced Triboelectric Nanogenerator. *Nano Letters*. **13**(2), pp.847–853.
- Zhu, G., Peng, B., Chen, J., Jing, Q. and Lin Wang, Z. 2015. Triboelectric nanogenerators as a new energy technology: From fundamentals, devices, to applications. *Nano Energy*. **14**, pp.126–138.
- Zisman, W.A. 1964. Relation of the Equilibrium Contact Angle to Liquid and Solid Constitution. . **18**, pp.1–51.
- Zou, H., Zhang, Y., Guo, L., Wang, P., He, X., Dai, G., Zheng, H., Chen, C., Wang, A.C., Xu, C. and Wang, Z.L. 2019. Quantifying the triboelectric series. *Nature Communications*. **10**(1).